



Lithium garnets: Synthesis, structure, Li⁺ conductivity, Li⁺ dynamics and applications



S. Ramakumar, C. Deviannapoorani, L. Dhivya, Lakshmi S. Shankar, Ramaswamy Murugan*

Department of Physics, Pondicherry University, Puducherry 605 014, India

ARTICLE INFO

Article history:

Received 3 April 2017

Accepted 6 April 2017

Available online 8 April 2017

Keywords:

Electrochemical energy storage devices

Rechargeable lithium battery technology

Solid fast Li⁺ conductors

Garnet structured fast Li⁺ conductors

ABSTRACT

Inorganic solid fast Li⁺ conductors based batteries are expected to overcome the limitations over safety concerns of flammable organic polymer electrolytes based Li⁺ batteries. Hence, an all-solid-state Li⁺ battery using non-flammable solid electrolyte have attracted much attention as next-generation battery. Therefore, in the development of all-solid-state lithium rechargeable batteries, it is important to search for a solid electrolyte material that has high Li⁺ conductivity, low electronic conductivity, fast charge transfer at the electrode interface and wide electrochemical window stability against potential electrodes and lithium metal. Hence, significant research effort must be directed towards developing novel fast Li⁺ conductors as electrolytes in all-solid-state lithium batteries. Among the reported inorganic solid Li⁺ conductive oxides, garnet-like structural compounds received considerable attention in recent times for potential application as electrolytes in all-solid-state lithium batteries. The focus of this review is to provide comprehensive overview towards the importance of solid fast lithium ion conductors, advantages of lithium garnets over other ceramic lithium ion conductors and understanding different strategies on synthesis of lithium garnets. Attempts have also been made to understand relationship between the structure, Li⁺ conduction and Li⁺ dynamics of lithium garnets. The status of lithium garnets as solid electrolyte in electrochemical devices like all-solid state lithium battery, lithium-air battery and sensor are also discussed.

© 2017 Elsevier Ltd. All rights reserved.

Contents

1. Electrochemical energy storage devices	326
1.1. Introduction	326
1.2. Lithium ion battery technology	327
1.2.1. Working principle of Li ⁺ battery technology	327
1.2.2. Disadvantages of present rechargeable Li ⁺ battery technology	327
1.2.3. Challenges for the improvement in the performance of rechargeable Li ⁺ battery	328
1.3. Electrolyte materials for rechargeable Li ⁺ battery	328
1.3.1. Liquid electrolytes	328
1.3.2. Ionic liquids	328
1.3.3. Polymer electrolytes	329
1.4. Expected advancements in Li ⁺ battery technology	329

* Corresponding author.

E-mail address: moranamurugan.phy@pondiuni.edu.in (R. Murugan).

<http://dx.doi.org/10.1016/j.pmatsci.2017.04.007>

0079-6425/© 2017 Elsevier Ltd. All rights reserved.

1.5.	Solid fast Li ⁺ conductors for the rechargeable all-solid-state lithium batteries.	329
1.5.1.	Inorganic solid fast Li ⁺ conductors	330
1.6.	Garnet-like structured solid Li ⁺ conductors.	333
1.6.1.	Conventional lithium garnet and stuffed lithium garnet	334
2.	Synthesis techniques for the preparation of lithium garnets	335
2.1.	Solid-state reaction	336
2.2.	Wet chemical techniques	344
2.2.1.	Sol-gel method	344
2.2.2.	Pechini method.	344
2.2.3.	Combustion method.	345
2.2.4.	Chemical co-precipitation method	345
2.3.	Growth of single crystal	346
2.4.	Thin film processing techniques.	348
2.4.1.	Radio-frequency (RF) magnetron sputtering.	348
2.4.2.	Pulsed laser deposition (PLD)	349
2.4.3.	Metal-organic chemical vapor deposition (MOCVD)	350
2.4.4.	Sol-gel spin coating method	350
2.5.	Nebulized spray pyrolysis (NSP) technique.	351
2.6.	Electrospinning technique	352
2.7.	Sintering of lithium garnets	353
2.7.1.	Densification by sintering agent	353
2.7.2.	Hot press technique	357
2.7.3.	Fast microwave-assisted synthesis	359
2.7.4.	Spark plasma sintering (SPS) process	359
2.7.5.	Field assisted sintering technology (FAST)	360
2.8.	3D Li ⁺ conducting ceramic nanofibre network	360
3.	Structural analysis of lithium garnets.	362
3.1.	X-ray and neutron diffraction analysis	362
3.2.	Nuclear magnetic resonance spectroscopy (NMR)	367
3.3.	Raman spectroscopy	368
4.	Li ⁺ conductivity of lithium garnets	371
5.	Li ⁺ dynamics in lithium garnets	379
6.	Application of lithium garnets in electrochemical devices	386
6.1.	All-solid-state lithium battery	387
6.1.1.	Interface engineering	387
6.2.	Fuel cell	401
6.3.	Li-air battery	401
6.4.	Sensors.	404
7.	Conclusions.	404
	Acknowledgements	405
	References	405

1. Electrochemical energy storage devices

1.1. Introduction

Energy plays an important role in many aspects of human lives. The demand for energy will continue to inflate as long as there is an increase in the population and an aspiration for a high standard of living. To meet this ever increasing energy demand, we mostly depend on fossil fuels such as coal, petroleum, natural gas and nuclear power. The limitation of the availability, access of natural resources and the climatic consequences arising due to continuous rise in CO₂ levels has made the focus of research towards renewable energy sources. Extensive research activities from various research groups, government agencies and industries had been initiated on renewable energy resources such as wind, solar, biomass, and hydropower. The major challenge of the efficient use of renewable energy includes the exploration of suitable electrical energy storage devices for both off-grid and on-grid schemes.

The CO₂ emission and the ensuing air pollution may be reduced by replacing internal combustion engine (ICE) with ideally, zero emission vehicles, i.e., electric vehicles (EVs) or at least, by controlled emission vehicles, i.e., hybrid electric vehicles (HEVs) and/or plug-in electric vehicles (PHEVs). The global market for electrical energy storage devices for portable electronic devices such as mobile phones and laptops is also expected to increase dramatically in the near future.

The most convenient form of electrical energy storage is electrochemical storage such as batteries and supercapacitors. Compared to supercapacitors, batteries continue to dominate the market of portable electronic systems. Batteries are electrochemical devices, which can convert electrical energy into chemical energy and store the energy. Conversely, it can

convert chemical energy into electrical energy through reduction-oxidation (redox) reaction while releasing the energy. Energy density (amount of energy stored per unit mass (Wh kg^{-1}) or volume (Wh l^{-1}) and power density (the maximum practical sustained power output per unit mass (W kg^{-1}) or volume (W l^{-1})) are the two key parameters of batteries. There have been significant efforts to improve the energy density of batteries, which is very crucial for most of the consumer electronics market and hybrid electric vehicle applications [1].

1.2. Lithium ion battery technology

Among the various electrochemical energy storage devices, rechargeable lithium ion (Li^+) batteries are attaining significant attention for various applications ranging from portable electronics to electric vehicle because of their high energy density compared to other battery systems. Lithium is the lightest metal with high electrochemical potential and thus enables to achieve high energy and power density. Initial attempts with pure lithium as negative electrode (anode) in lithium metal batteries failed because of safety problems due to dendrite formation. Further analysis on rechargeable lithium battery gave rise to a solution using non metallic Li^+ . This technology is named as Li^+ battery technology. Unlike lithium primary batteries, the specific energy of Li^+ battery technology is quite low but is relatively safer.

Rechargeable Li^+ batteries are considered widely as efficient energy storage device for portable electronic gadget because they have strong advantages in terms of higher gravimetric energy density of 150 Wh kg^{-1} [2–5] and deliver voltage in the order of 2.5–4.2 V depending on the selection of the electrode materials. In addition to the high energy density, Li^+ batteries are offering flexible light weight design, low self-discharge and relatively longer cycle life [2].

1.2.1. Working principle of Li^+ battery technology

The concept of rechargeable Li^+ batteries with LiCoO_2 as positive electrode (cathode) was proposed by Prof. John B. Goodenough [6]. The commercialized Li^+ batteries introduced in the year 1991 used coke (coal product) as the negative electrode; lithium metal oxide (e.g., LiCoO_2) as positive electrode and a lithium salt such as hexafluorophosphate (LiPF_6) dissolved in an organic solvent as liquid electrolyte [7]. Later coal has been replaced by graphite. This technology is also named as a “rocking-chair” battery as the Li^+ “rock” back and forth between the positive and negative electrodes during battery charging and discharging. The working principle of rechargeable Li^+ battery is shown in Fig. 1.1.

During the charging process, Li^+ are de-intercalated from the layered LiCoO_2 positive electrode, pass across the electrolyte and then inserted between the graphite layers in the negative electrode. At the same time, electrons flow from the positive electrode to the negative electrode through the external circuit. This process is completely reversed while discharging. The Li^+ battery operation is based on the reversible shuttling of Li^+ between the positive and negative electrode materials. As a result, the intrinsic properties of electrode materials will strongly confine the feat of batteries.

1.2.2. Disadvantages of present rechargeable Li^+ battery technology

The present rechargeable Li^+ battery technology has some disadvantages that need to be balanced against the benefits. The chief limiting factor of the rechargeable Li^+ battery is safety. The organic liquid electrolyte used in the present rechargeable Li^+ batteries is flammable and tends to leak and decompose under certain conditions (uncontrolled charging above 4.6 V) [8]. Hence Li^+ cells need electronic control to avoid such conditions. Short circuiting a rechargeable Li^+ battery results in overheating and causing fire.

During the charging process from the open circuit potential towards 0 V vs. Li/Li^+ , the Li^+ intercalate into the negative (carbon) electrode and the electrolyte solution and gets reduced to form a passivation film on the negative electrode, which

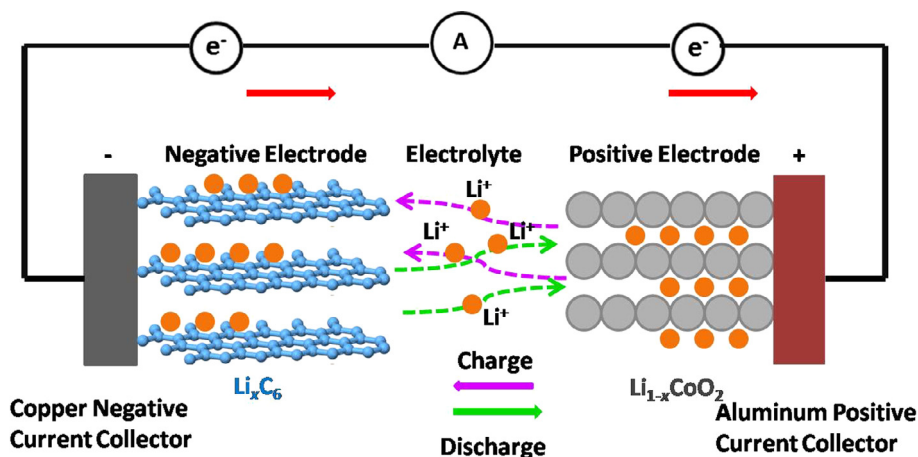


Fig. 1.1. Schematic representation for the working principle of rechargeable Li^+ battery.

is termed as the solid electrolyte interface (SEI). The formation of a solid electrolyte interface (SEI) at the negative electrode leads to a large irreversible capacity loss during the discharge cycles. The properties and the chemical composition of the solid electrolyte interface (SEI) layer have been a subject of intense scientific interest because the SEI layer determines the safety, power capability, shelf life and the cycle life of the rechargeable Li^+ batteries.

The working capacity is insufficient/moderate at higher cycling rates. At higher cycling rates, the energy efficiency is too low. This is due to large polarization losses during charge and discharge. The cost of Li^+ battery is relatively high compared to the other existing rechargeable batteries. This is a major issue while considering its use in large scale applications.

1.2.3. Challenges for the improvement in the performance of rechargeable Li^+ battery

The improvement in the performance of rechargeable Li^+ battery depends upon the development of suitable positive electrode, electrolyte and negative electrode materials. The open-circuit voltage of a cell is the difference between the electrochemical potentials μ_A and μ_C of the negative electrode and positive electrode, respectively:

$$V_{OC} = (\mu_A - \mu_C)/e \quad (1.1)$$

A right combination of negative electrode-electrolyte-positive electrode materials will help to attain high energy density light weight batteries. The high open-circuit voltage is achieved by the energy of both the electron transfer and Li^+ transfer. Li^+ transport also depends on the crystal structure and coordination geometry of the positive and negative electrode site. The extensive research work carried out on both positive and negative electrode material has helped to improve the performance as well as high energy density of Li^+ batteries.

The open-circuit voltage is limited by “window” of the electrolyte. The window of the electrolyte is the energy gap (E_g) between the lowest unoccupied and highest occupied molecular orbitals (LUMO and HOMO) of an electrolyte. When μ_A is located above LUMO, reduction of electrolyte takes place, whereas when μ_C is located below HOMO oxidation of the electrolyte takes place, unless the reaction is blocked by an SEI layer.

The ideal electrolyte should exhibit high ionic conductivity ($>10^{-2} \text{ S cm}^{-1}$ at room temperature) and low electronic conductivity. It should also be chemically and electrochemically compatible with the electrode materials. There were many attempts in the field of battery research to improve the performance of electrolytes.

1.3. Electrolyte materials for rechargeable Li^+ battery

The development of high energy density Li^+ battery technology truly depends on the development of robust electrolyte which can sustain with high performance electrodes. On that account the choice of electrolyte depends on the chemistry of electrodes. The electrolyte materials for rechargeable Li^+ battery may be broadly classified as

- Liquid electrolytes
- Ionic liquids
- Polymer electrolytes
- Solid electrolytes

1.3.1. Liquid electrolytes

Owing to their high ionic conductivity of $\sim 10^{-2} \text{ S cm}^{-1}$, the liquid electrolytes retains their importance in rechargeable Li^+ battery technology. In general liquid electrolytes are composed of lithium salts such as LiClO_4 , LiAsF_6 , LiPF_6 , LiSO_3CF_3 , and $\text{LiN}(\text{SO}_2\text{CF}_3)_2$ dissolved in solvents. Based on the solvent used, they are classified into aqueous (water), mixed aqueous (water mixed along with co-solvent) and non-aqueous (organic or inorganic solvent) electrolyte solutions. The non-aqueous aprotic organic solvent comprises of one or the mixture of the following: propylene carbonate (PC), diethyl carbonate (DEC), ethylene carbonate (EC), dimethyl carbonate (DMC), or ethyl methyl carbonate (EMC). These solvents have good electrochemical stability towards the highly oxidizing positive electrode. The initial Li^+ battery design was made using LiClO_4 as electrolyte. Later it was found that LiClO_4 lithium salt underwent violent decomposition, resulting in safety issues [9]. Hence, LiClO_4 was replaced by LiPF_6 . The major concern of using liquid electrolytes is that they are thermodynamically unstable in combination with negative electrode. Moreover, the formation of intermediate layers of reaction products (SEI) between the electrode and electrolyte reduces the kinetics of charge and discharge process and therefore results in capacity fading.

1.3.2. Ionic liquids

Ionic liquids are organic salts composed of ionic species [10]. Ionic liquids offer great advantages that include low volatility, high thermal stability, good electrochemical stability, recyclability and non flammability. These remarkable properties make ionic liquids as green solvents for Li^+ battery applications [11]. Based on the cation segment the ionic liquids are generally classified into alkylammonium, dialkylimidazolium, phosphonium and N-alkylpyridinium. Ammonium-based ethanolanionium nitrate (EOAN), was the first synthesized ionic liquid in 1888 by Gabriel et al. [12]. Comparison of few room temperature ionic liquid containing quaternary ammonium cation and imide anion revealed that quaternary ammonium cations, including EMI (1-ethyl-3-methylimidazolium) cation, TMPA (trimethylpropylammonium) cation, P13 (N-methyl-N-propylpyridinium) cation, PP13 (N-methyl-N-propylpiperidinium) cation and TFSI (bis(trifluoromethanesulfonyl)imide) cation, could form stable room temperature ionic liquid against the lithium metal [13]. The physico-chemical

properties of the ionic liquids, such as viscosity, melting point, glass transition temperature, surface tension and diffusion coefficients can be tailored by several possible substituent (hydrogen, aliphatic chains, ether based chains, etc.) with the cation [14]. The viscosity of ionic liquids are higher and thus the ionic conductivities of ionic liquids are three to four orders of magnitude lower, than those of liquid electrolytes [15,16].

1.3.3. Polymer electrolytes

Polymer electrolytes were first explored by Fenton, Parker and Wright in 1973 [17]. However, their prospective application in electrochemical devices was recognized by Armand in 1978 [18]. The polymer electrolytes are generally polymer-salt complexes formed between polymers and alkali metal salts (such as LiPF₆/LiCF₃SO₃). Various polymers such as polyethylene oxide (PEO), polypropylene oxide (PPO), polymethyl methacrylate (PMM), polyacrylonitrile (PAN), polyvinyl chloride (PVC), and polyvinylidene fluoride (PVdF), have been extensively studied as host polymer for the dissolution of alkali metal salts. The ion transport in these polymer electrolytes is governed by local relaxation as well as segmental motion of the polymer chains which are more favoured by high degree of amorphicity of the host polymers [18,19]. The most common type of polymer electrolyte studied is PEO₆:LiMF₆ (where M = P, Sb, As). PEO based lithium ion conductors have been preferred for its ability to solvate a wide range of anions such as ClO₄⁻, BF₄⁻, [N(SO₂CF₃)₂]⁻, PF₆⁻, and [N(SO₂C₂F₅)₂]⁻ [20]. However, PEO-based electrolytes exhibit a low ionic conductivity of 10⁻⁸–10⁻⁴ S cm⁻¹ at temperature between 40 °C and 100 °C owing to their high degree of crystallinity [21]. Later PEO was replaced by polyacrylonitrile (PAN). Nevertheless the usage of PAN results in an increase in internal resistance of the Li⁺ polymer battery. Polyvinylidene fluoride (PVdF) is the most common polymer used at present in Li⁺ polymer battery technology due to its strong electron withdrawing functional group (—C—F) and high dielectric constant. Although PVdF has greater tendency to attract Li⁺, the ionic conductivity is still lower than liquid electrolytes. Different approaches have been adapted in order to improve the conduction mechanism and thermal, interfacial and mechanical stability towards metallic lithium such as (i) addition of organic plasticizers [22], (ii) incorporation of inorganic fillers such as Al₂O₃, SiO₂, and TiO₂ [23–26], (iii) preparation of cross-linked network polymers and (iv) polymer blends [27].

Major advantages of polymer electrolytes based batteries. By configuring the electrolytes as very thin layer and large-area elements the internal resistance of the fabricated cell may be reduced into an acceptable range. Also, the cells can be operated at relatively low values of current density, while still permitting the battery at practical rates. It is the combination of a unique battery cell structure with the properties of these polymer electrolytes that can, in principle, permit high values of specific energy and power to be achieved [28].

The polymer electrolyte plays three important roles in the polymer electrolyte (PE) based battery.

- It is a Li⁺ carrier and can be formed into thin films to improve the energy density.
- It acts as an electrode spacer hence eliminates the need to incorporate an inert porous separator.
- It is a binder, which ensures good electrical contact with the electrodes. The flexibility and mechanical resilience are the major advantages.

Drawbacks of liquid and polymer electrolytes

- Major drawback of organic polymer electrolytes is their low ionic conductivity (10⁻⁶ S cm⁻¹) at ambient temperature.
- Poor interfacial stability i.e., formation of solid electrolyte interface (SEI).
- Liquid and polymer electrolytes are not stable with lithium metal; they cannot be used together with lithium negative electrode.

1.4. Expected advancements in Li⁺ battery technology

- The replacement of carbonaceous materials with alternative lithium accepting negative electrode compounds with the improved safety features.
- The replacement of suitable positive electrode structure with the aim of reducing the cost and environmental impact.
- The replacement of the liquid-like electrolyte with a solid state fast lithium ion conductor which may act as both the separator and the electrolyte with the aim of improving battery's design and reliability [29].

Despite the fact that solid electrolytes proffer many advantages, they display very low ionic conductivities compared to that of liquid electrolytes. Therefore, in the development of all-solid-state lithium rechargeable batteries, it is important to search for solid electrolyte materials with high Li⁺ conductivity and electrochemical stability.

1.5. Solid fast Li⁺ conductors for the rechargeable all-solid-state lithium batteries

Properties of solid Li⁺ conducting electrolytes required for the fabrication of all-solid-state lithium batteries are [30–33]:

- High Li⁺ conductivity at room temperature.
- Negligible electronic conductivity over the entire employed range of lithium activity and temperature.

- Negligibly small or no grain-boundary resistance.
- Stability against chemical reaction with both electrodes, especially with elemental Li or Li-alloys.
- High electrochemical decomposition voltage (preferably higher than 5 V vs. Li).
- Environmental benign, low cost and easiness of preparation.

Therefore, considerable research have been initiated in various laboratories towards developing solid fast Li⁺ conductors for potential application as electrolytes in all-solid-state lithium batteries and other high energy density battery architecture.

1.5.1. Inorganic solid fast Li⁺ conductors

A wide range of layered two-dimensional (2D) and three-dimensional (3D) inorganic solid Li⁺ conducting electrolytes (SLICEs) were investigated for possible application as solid electrolytes in all-solid-state lithium batteries. Among them Li₃N [34], Li-β-alumina [35,36], amorphous lithium phosphorus oxynitride (LIPON) [37], Li₄SiO₄ [30], Li₁₄ZnGe₄O₁₆ (lithium superionic conductors, LISICON) [38,39], Li_{1.3}Al_{0.3}Ti_{1.7}(PO₄)₃ (sodium superionic conductors, NASICON) [40,41], Li₃PO₄ and perovskite (Li, Ln)TiO₃ (Ln = rare earths) [42–44] had been widely investigated for possible application in rechargeable batteries.

1.5.1.1. Li₃N. The structural arrangement of Li₃N was first proposed by Zintl and Brauer [45] and later was reconfirmed by Rabinau and Schulz [46]. Li₃N consists of hexagonal structure connecting tightly bonded Li₂N layers with the nitrogen arranged in the centre. These layers are connected by the remaining 1/3 of the lithium ions, which bridge the nitrogen ions of adjacent layers. Single crystal Li₃N exhibited Li⁺ conductivity of about $1.2 \times 10^{-3} \text{ S cm}^{-1}$ perpendicular to c-axis and $1 \times 10^{-5} \text{ S cm}^{-1}$ along the c-axis at 27 °C [34]. The major disadvantage of Li₃N is that it exhibited very low thermodynamic decomposition voltage of 0.44 V at room temperature; moreover it is sensitive to air [47]. These characteristics restrict the practical implementation of Li₃N to all-solid-state batteries. The crystal structure of Li₃N is shown in Fig. 1.2 [48].

1.5.1.2. β-Alumina. Beta-alumina is an isomorphous form of aluminum oxide (Al₂O₃). They are good conductor of mobile ions and are complexed with Na⁺, K⁺, Li⁺, Ag⁺, H⁺, Pb²⁺, Sr²⁺ or Ba²⁺ for electrolyte applications. The beta alumina has an empirical formula Na₂O·11Al₂O₃ in which Na ions are situated perpendicular to c-axis and the oxygen atoms are arranged in the planes above and below the sodium ion conducting plane [35]. Beta-alumina exists in two different crystal structures viz. hexagonal β-Al₂O₃ (P6₃/mmc; a = 0.559 nm, c = 2.261 nm) [49,50] and rhombohedral β'-Al₂O₃ (R3m; a = 0.560 nm, c = 3.395 nm) [51,52]. They differ by stacking sequence of oxygen ions across the conduction plane as shown in Fig. 1.3 [53]. The single crystal lithium beta alumina exhibited conductivity of $3 \times 10^{-3} \text{ S cm}^{-1}$ at 25 °C [36]. The major drawback of beta alumina is that they are highly hygroscopic and difficult to prepare as pure phase.

1.5.1.3. NASICON-type Li⁺ conductors. Na super ionic conductor (NASICON) type phosphate exhibits a rhombohedral structure (R $\bar{3}C$) with a general formula A_xB₂(PO₄)₃. Where A corresponds to monovalent ion and B corresponds to one or more ions in trivalent, tetravalent or pentavalent state [40,41,54–59]. The structure can be described as a covalent skeleton [A₂P₃O₁₂]⁻ constituted by AO₆ octahedra and PO₄ tetrahedra, which forms 3D interconnected channels. Moreover, there exist two types of interstitial positions M1 located at an inversion centre (surrounded by six oxygen atoms) and M2 disposed symmetrically around the ternary axis (surrounded by ten oxygen atoms) for the distribution of mobile cations. A pair of near lying octahedra is linked through PO₄ tetrahedra. Both M1 and M2 sites are arranged in alternating way along the conducting channels.

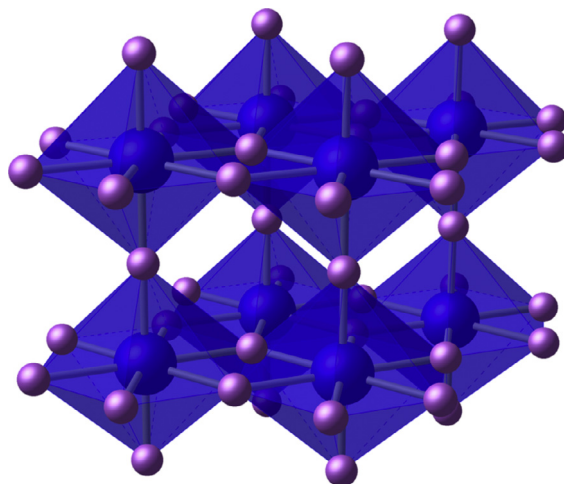


Fig. 1.2. Crystal structure of Li₃N. The blue and red spheres represent the nitrogen and lithium atoms, respectively [48].

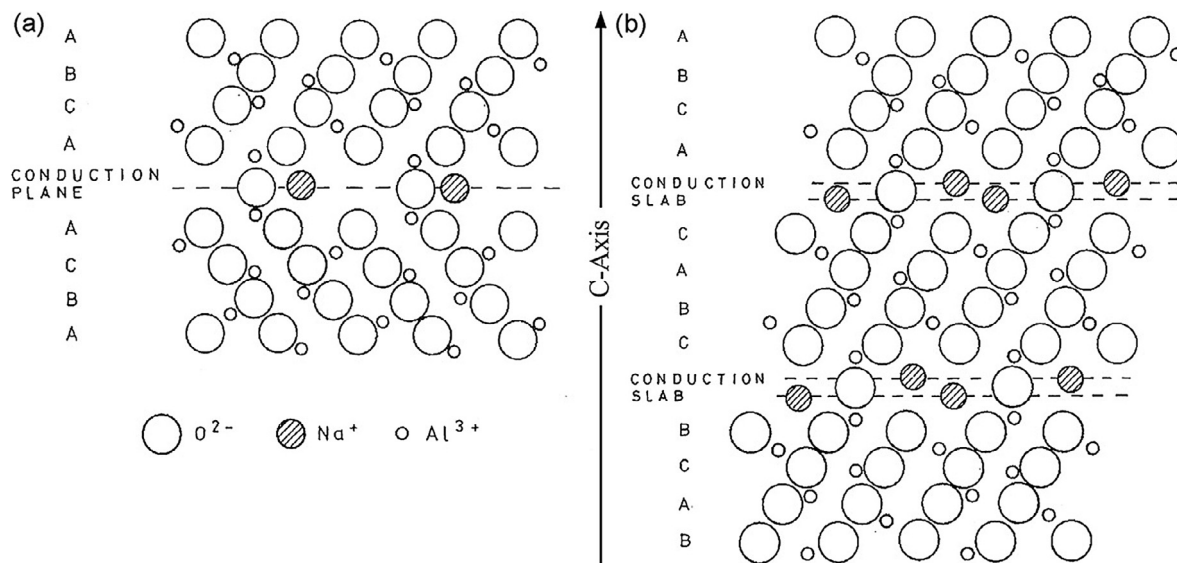


Fig. 1.3. Crystal structure of (a) β - Al_2O_3 and (b) β'' - Al_2O_3 [53].

The mobile cations move from one site to another through bottlenecks, the size of which depends on the nature of the skeleton ions and on the carrier concentration [60]. NASICON type $\text{NaA}^{\text{IV}}(\text{PO}_4)_3$ ($A^{\text{IV}} = \text{Ge}, \text{Ti}$ and Zr) was first reported in 1968 [54]. By partial substitution of the tetravalent metal cation (A^{4+}) with a trivalent dopant (e.g., $\text{Al}, \text{La}, \text{Y}, \text{Sc}$) [61] the ion conductivity of NASICON can be increased. NASICON-related $\text{Li}_{1.3}\text{Al}_{0.3}\text{Ti}_{1.7}(\text{PO}_4)_3$ (LATP) exhibits the highest Li^+ conductivity of $\sigma \approx 3 \times 10^{-3} \text{ S cm}^{-1}$ at 25°C [62]. The substitution of Ti^{4+} by smaller Al^{3+} cations reduces unit cell dimensions of the NASICON framework and enhances ionic conductivity by about three orders of magnitude. The crystal structure of NASICON-type $\text{LiA}_2^{\text{IV}}(\text{PO}_4)_3$ ($A^{\text{IV}} = \text{Ti}, \text{Zr}, \text{Ge}, \text{Hf}$) solid electrolyte is shown in Fig. 1.4 [63].

Unfortunately, the applicability of Ti containing NASICON-related Li^+ conductors as solid electrolyte is limited owing to the electrochemical instability with respect to the metallic lithium due to the reduction of Ti^{4+} to Ti^{3+} .

1.5.1.4. LISICON-type Li^+ conductors. $\text{Li}_{1.4}\text{Zn}(\text{GeO}_4)_4$ is the first material to give the name lithium super ionic conductor (LISICON). It is a member of the solid solutions of $\text{Li}_{2+2x}\text{Zn}_{1-x}\text{GeO}_4$ ($-0.36 < x < 0.87$), which is iso-structural with γ - Li_3PO_4

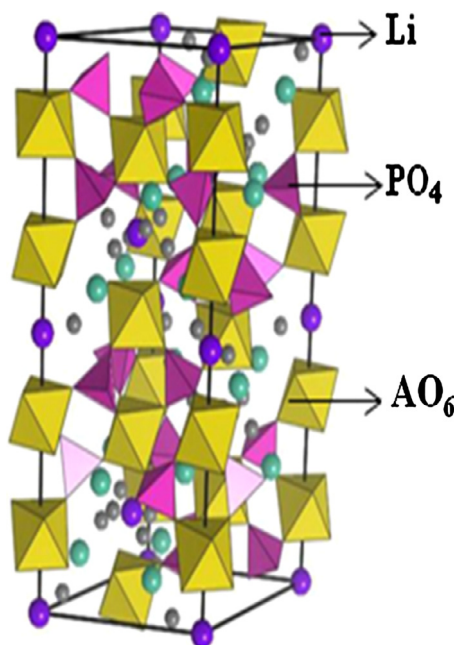


Fig. 1.4. Crystal structure of NASICON-type $\text{LiA}_2^{\text{IV}}(\text{PO}_4)_3$ ($A^{\text{IV}} = \text{Ti}, \text{Zr}, \text{Ge}, \text{Hf}$) solid electrolyte [63].

crystallizing in the *Pnma* orthorhombic space group [38,39,64–66]. The crystal structure of LISICON-type $\text{Li}_3\text{Zn}_{0.5}\text{GeO}_4$ solid electrolyte is shown in Fig. 1.5 [67]. The LISICON structure consists of cations that occupy half of the tetrahedral site with hexagonal close packed oxygen ion arrays. The Li^+ diffusion pathway is formed through the tetrahedral and interstitial octahedral sites [68,69]. The Li^+ distribution between tetrahedral and interstitial octahedral sites plays an important role to create Li^+ conduction pathway that affects their ionic conduction [33,70–76]. The room temperature Li^+ conductivity of $1 \times 10^{-7} \text{ S cm}^{-1}$ was achieved with $\text{Li}_{3.5}\text{Zn}_{0.25}\text{GeO}_4$ [77]. The Li^+ conductivity of $\text{Li}_{2+2x}\text{Zn}_{1-x}\text{GeO}_4$ tends to decrease with time at low temperature. $\text{Li}_{3.6}\text{Ge}_{0.6}\text{V}_{0.4}\text{O}_4$ exhibited highest room temperature Li^+ conductivity of $4 \times 10^{-5} \text{ S cm}^{-1}$ [78] which was highly reactive with lithium metal and atmospheric CO_2 [79,80].

The thio-LISICON (Li^+ conducting sulfide compounds) $\text{Li}_{4-x}\text{M}_{1-y}\text{M}'_y\text{S}_4$ ($\text{M} = \text{Si}, \text{Ge}$ and $\text{M}' = \text{P}, \text{Al}, \text{Zn}, \text{Ga}$) exist in the structure similar to $\gamma\text{-Li}_3\text{PO}_4$ [33]. $\text{Li}_{3.25}\text{Ge}_{0.25}\text{P}_{0.75}\text{S}_4$ exhibited the highest Li^+ conductivity of $2.17 \times 10^{-3} \text{ S cm}^{-1}$ at room temperature [77]. The drawback of this material is the instability in ambient condition. Like other amorphous or polycrystalline sulfide solid electrolytes, this material needs to be synthesized and handled in a dry environment [81].

1.5.1.5. Perovskite-type Li^+ conductors. Due to its various functional properties like electronic, magnetic and ion conducting properties [42–44,82–84], intensive research has been carried out in perovskites with general formula ABO_3 (where A

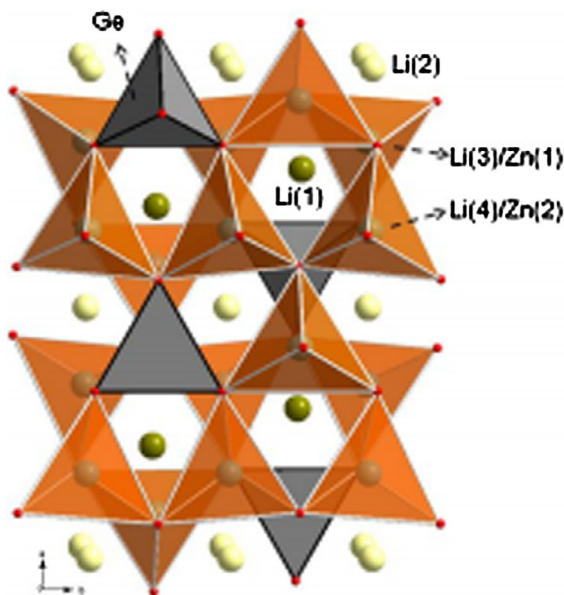


Fig. 1.5. Crystal structure of LISICON-type $\text{Li}_3\text{Zn}_{0.5}\text{GeO}_4$ [66,67].

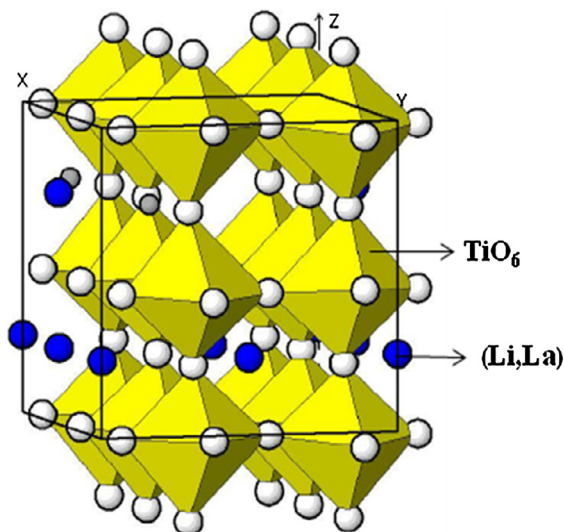


Fig. 1.6. Crystal structure of perovskite-type $(\text{Li}, \text{La})\text{TiO}_3$ (LLTO) [87].

and B are 12 and 6-fold coordinated cations, respectively). The structure of perovskite is portrayed by corner-shared BO_6 octahedra enclosing 12 coordinated A-site ions. $(\text{Li, La})\text{TiO}_3$ (LLTO) exhibits high bulk Li^+ conductivity in the order of $10^{-3} \text{ S cm}^{-1}$ and total (bulk + grain-boundary) Li^+ conductivity of $7 \times 10^{-5} \text{ S cm}^{-1}$ at 27°C , which is two orders of magnitude lower than that of the bulk Li^+ conductivity [85–87]. The disordered distributions of Li^+ and reasonable vacancies in the structure are accountable for the high bulk Li^+ conductivity in LLTO. The major limitation of LLTO as electrolyte for battery application is the high reducibility of Ti^{4+} in direct contact with metallic lithium. The crystal structure of perovskite-type $(\text{Li, La})\text{TiO}_3$ (LLTO) Li^+ conductor is shown in Fig. 1.6 [87].

1.5.1.6. Lithium phosphorus oxynitride (LIPON). Lithium phosphorus oxynitride (LIPON) is an amorphous glass electrolyte commonly used for the fabrication of an all-solid-state thin film type lithium battery. LIPON films were fabricated using sputtering method from Li_3PO_4 target under a N_2 atmosphere [88]. LIPON has a Li^+ conductivity of about $3.3 \times 10^{-6} \text{ S cm}^{-1}$ at 25°C and good electrochemical stability with both metallic lithium positive electrode and transition metal negative electrode with a cell potential of 5.5 V versus Li. The electronic resistivity of LIPON film is $>10^{14} \Omega \text{ cm}$ which minimizes the short circuit self-discharge of the battery [89]. The major drawback of LIPON system is that the films can be fabricated only by means of sputtering method in controlled N_2 atmosphere. Moreover, the LIPON exhibits a poor ionic conductivity [37].

The above discussed inorganic compounds had either high ionic conductivity or high electrochemical stability, but not the both. In order to develop high-energy density all-solid-state lithium batteries the electrolyte must possess both high Li^+ conductivity as well as high electrochemical stability. Comparisons of Li^+ conductivity and electrochemical stabilities of few important solid fast Li^+ conducting electrolytes are shown in Fig. 1.7 [90]. Fig. 1.7 illustrates that the reported solid electrolytes exhibit either high Li^+ conductivity or high electrochemical stability, but not the both. Except $\text{Li}_{2.88}\text{PO}_{3.73}\text{N}_{0.14}$ (LIPON) [37], prepared by means of a sputtering technique in controlled N_2 atmosphere using a target of Li_3PO_4 [88], others are not suitable for the fabrication of an all-solid-state lithium battery with metallic lithium as negative electrode. The properties of typical crystalline Li^+ conductors reported in the literature are provided in Table 1.1 [35–37,40,41,47,62,79–81,85–88].

1.6. Garnet-like structured solid Li^+ conductors

Although Li^+ conduction has been reported for a wide range of crystalline metal oxides and sulfides, in general, the oxides are believed to be superior due to its ease in preparation, mechanical properties and thermal stability. Most of the inorganic oxide Li^+ conductors have had either high lithium ion conductivity or high electrochemical stability but not the both. There was a strong search for materials with similar constituents, like the best lithium ion conductor $(\text{Li, La})\text{TiO}_3$, but without lithium-reducible titanium. It has been attempted to replace the transition metal titanium in $(\text{Li, La})\text{TiO}_3$ with fixed valent and most stable (against chemical reaction with elemental Li) zirconium. However, the attempt was unsuccessful owing to the ready formation of thermodynamically favorable $\text{La}_2\text{Zr}_2\text{O}_7$ pyrochlore phase.

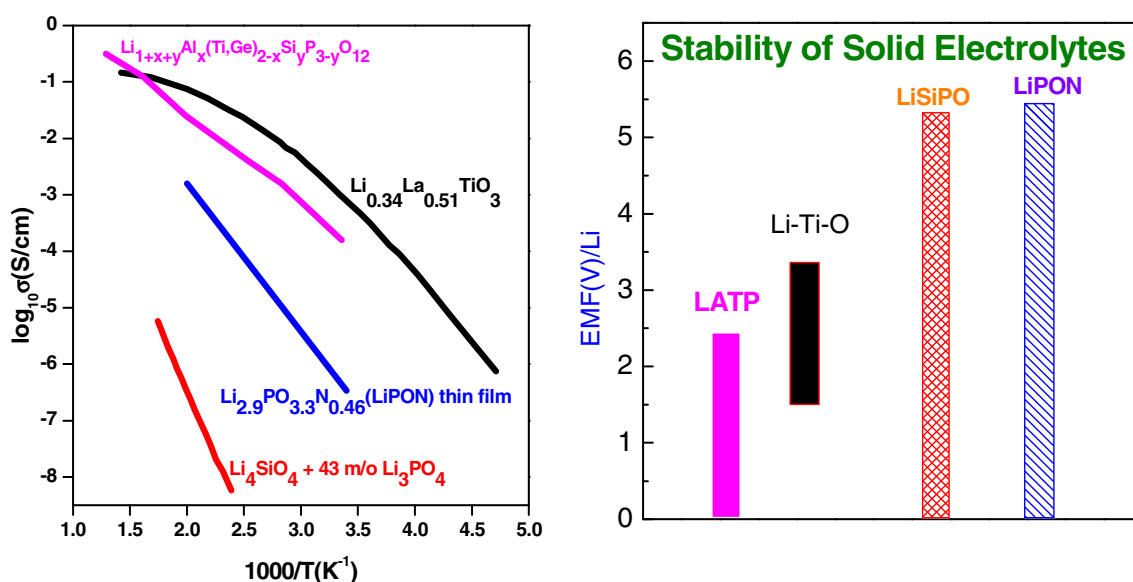


Fig. 1.7. Comparisons of Li^+ conductivity and electrochemical stabilities of few important solid fast Li^+ conducting electrolytes [90].

Table 1.1Properties of typical inorganic crystalline Li⁺ conductors reported in the literature [35–37,40,41,47,62,79–81,85–88].

Electrolytes	Limiting factors in solid-state battery application
Li ₃ N	Very low decomposition voltage (0.44 V)
Li-β-alumina	Highly hygroscopic, difficult to prepare as pure phase
Li ₁₄ ZnGe ₄ O ₁₆ (LISICON)	Highly reactive with lithium metal and atmospheric CO ₂ ; conductivity decreases with time
Li _{1.3} Ti _{1.7} Al _{0.3} (PO ₄) ₃ (NASICON)	Unstable with lithium metal because of facile Ti ⁴⁺ reduction
(Li, La)TiO ₃ (Perovskite)	Unstable with lithium metal, because of facile Ti ⁴⁺ reduction, High temperature required for preparation, high loss of Li ₂ O, variance of conductivity with lithium concentration, difficulty in controlling lithium content. Large grain-boundary resistance
Li _{2.88} PO _{3.86} N _{0.14} (LiPON)	Moderate conductivity, only used in development of thin-film battery using sputtering method

The first report of fast Li⁺ conduction in novel garnet-type lithium containing transition metal oxides with nominal chemical composition Li₅La₃B₂O₁₂ (B = Nb, Ta) reported from Prof. Werner Weppner's laboratory [90] stimulated extensive investigations on synthesis, structure and Li⁺ conducting properties of several lithium stuffed garnets by various groups.

Garnets are orthosilicates with general formula A₃B₂(SiO₄)₃ in which A and B refer to eight- and six-coordinated cation sites, respectively, which crystallizes in a face centered cubic structure with *Ia* $\bar{3}$ *d* space group [91]. It consists of a 3D framework with BO₆ octahedra and BO₄ tetrahedra, where each octahedron is joined to six corner-sharing tetrahedral, meanwhile each tetrahedron shares each corner with four octahedral [91]. The ideal garnet contains mixture of cations on filled square antiprismatic, octahedral and tetrahedral sites in 3:2:3 to provide a stoichiometry A₃B₂Si₃O₁₂. The structure of such ideal garnet Ca₃Al₂Si₃O₁₂ is shown in Fig. 1.8 [92].

A large variety of garnet-like structured complex oxides have been achieved with replacing silicon by other elements, e.g., A₃B₅O₁₂ (where A = Ca, Mg, Y or Ln = La or other rare earth elements and B = Al, Fe, Ga, Ge, Mn, Ni, V). The basic and most widely studied garnet material is yttrium aluminum garnet (YAG, having chemical formula Y₃Al₅O₁₂). The crystal structure of YAG is shown in Fig. 1.9 [93].

1.6.1. Conventional lithium garnet and stuffed lithium garnet

Lithium containing garnets are obtained by replacing silicon with lithium in A₃^{II}B₂^{III}(SiO₄)₃ to provide the general composition of A₃^{II}B₂^{III}(LiO₄)₃. It is possible to increase the lithium content in A₃^{II}B₂^{III}(LiO₄)₃ by partial replacement of either A or B cations with higher or lower oxidation state. The doping of larger ionic radii elements will increase the lattice parameter and leads to the fast movement of Li⁺ in the crystal structure. Conversely some doping elements may introduce vacancies

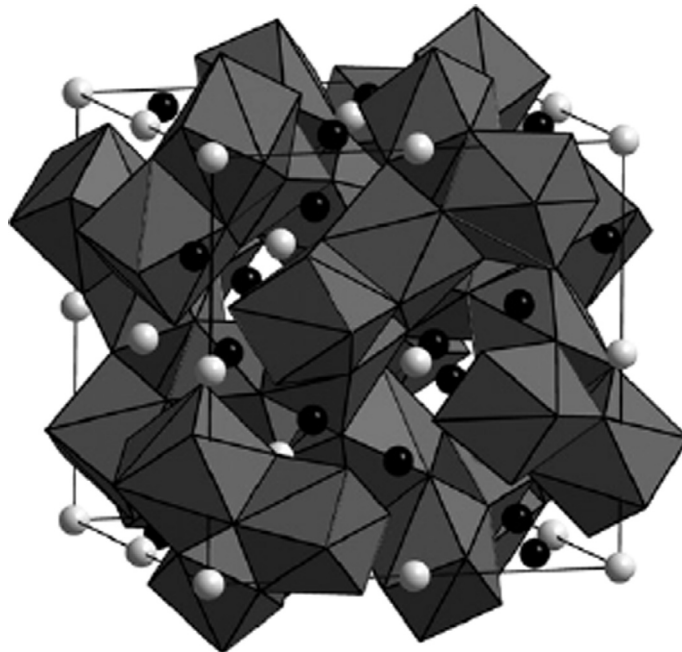


Fig. 1.8. Crystal structure of Ca₃Al₂Si₃O₁₂ constituting a body-centered network of CaO₈ units including aluminum (gray spheres) and silicon (black spheres) on the interstitial sites [92].

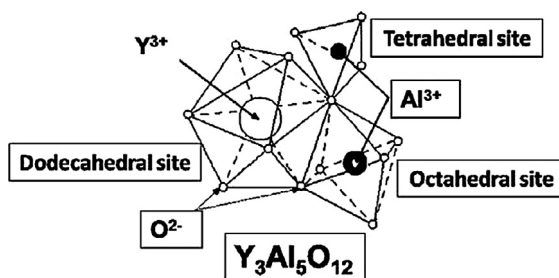
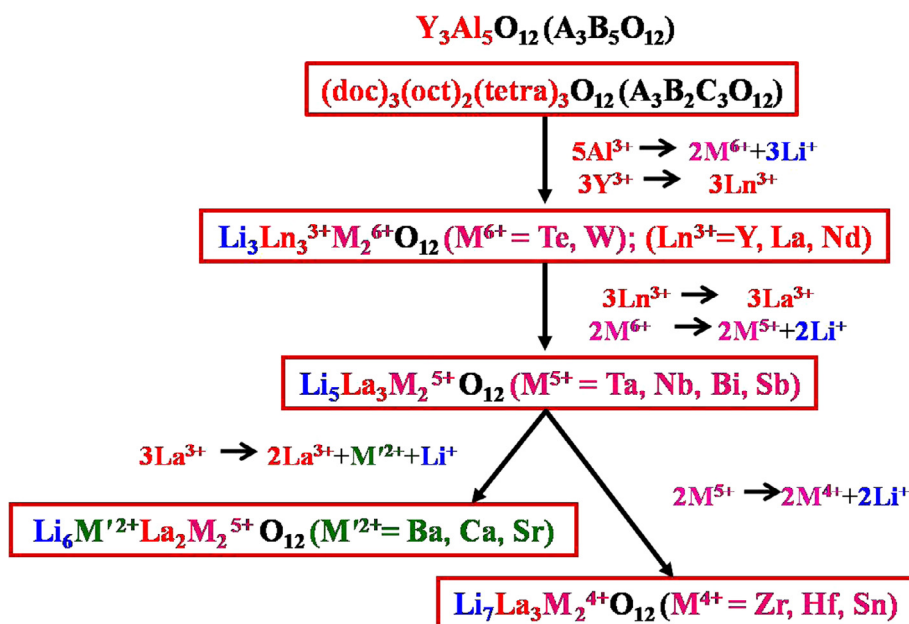


Fig. 1.9. Crystal structure of YAG [93].

Fig. 1.10. The evolution of family of garnet structured solid Li⁺ conductors.

to increase the mobility of Li⁺. Garnets with lithium concentration >3 are identified as stuffed lithium garnets. Fig. 1.10 shows the evolution of family of garnet structured solid Li⁺ conductors.

The similarity between the conventional lithium garnet and that of stuffed lithium garnet is that, in both cases the rare earth ions occupy 8-fold coordination site and B atom occupy 6-fold coordination site. The major difference is that in conventional garnet, Li⁺ occupy the tetrahedral coordination exclusively whereas, in stuffed lithium garnet, Li⁺ occupies both tetrahedral and highly distorted octahedral coordination sites [94–96]. A general comparison of the structure of conventional lithium garnet Li₃Nd₃Te₂O₁₂ with that of stuffed lithium garnet Li₅La₃Ta₂O₁₂ is shown in Fig. 1.11 [96].

Among the related lithium garnets, Li₆BaLa₂Ta₂O₁₂ and Li₇La₃Zr₂O₁₂ (LLZO) exhibited a Li⁺ conductivity of ~10⁻⁵ and 10⁻⁴ S cm⁻¹ at RT [97,98]. LLZO has been widely investigated since its discovery because of its superior ionic conductivity and excellent stability with metallic lithium. Moreover LLZO has been successfully applied in a handful of publications to fabricate rechargeable all-solid-state batteries. In order to increase the Li⁺ conductivity of the garnet-type LLZO, a large number of studies on the chemical substitution using various cation species have been reported.

2. Synthesis techniques for the preparation of lithium garnets

Lithium garnets can be obtained by different synthesis methods, such as solid-state reactions from mixtures of oxide, carbonate and hydroxide, single crystal growth technique, sol-gel method based on hydrolysis and condensation of alkoxide and nitrates, pechini, thin film processing techniques (radio-frequency (RF) magnetron sputtering, pulsed laser deposition, metal-organic chemical vapor deposition (MOCVD) and sol-gel spin coating), spray pyrolysis and electrospinning technique.

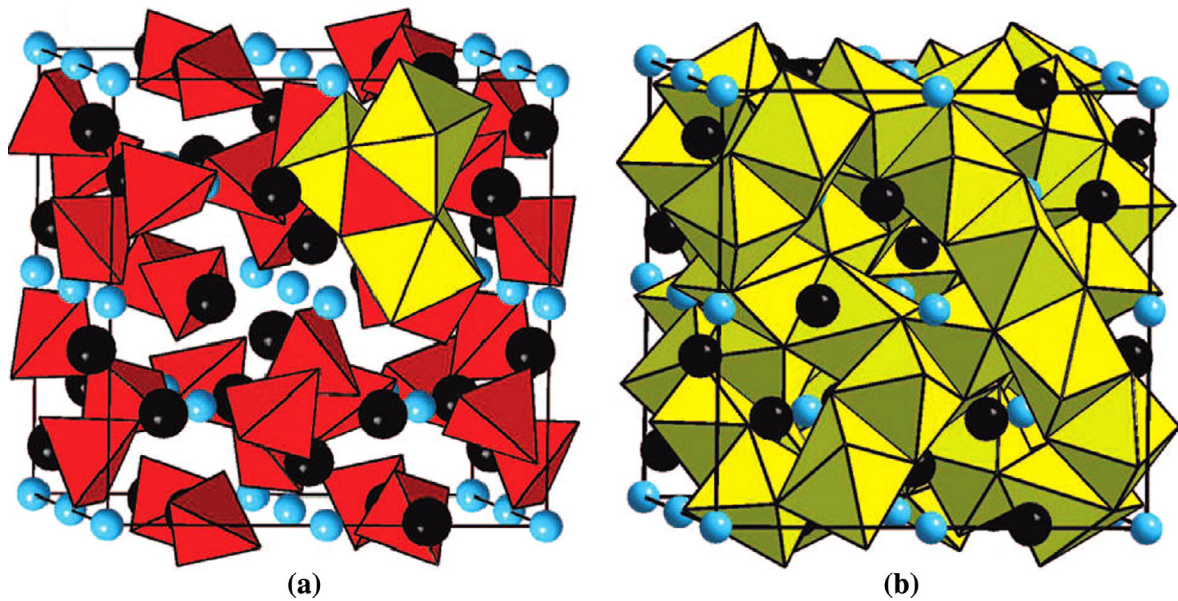


Fig. 1.11. Comparison of the structures (a) conventional lithium garnet $\text{Li}_3\text{Nd}_3\text{Te}_2\text{O}_{12}$ with lithium occupying tetrahedral sites (indicated in red units) and (b) stuffed lithium garnet $\text{Li}_5\text{La}_3\text{Ta}_2\text{O}_{12}$ with additional lithium occupying heavily distorted octahedral sites (indicated in yellow units). Black and blue spheres represent $\text{La}^{3+}/\text{Nd}^{3+}$ and $\text{Te}^{6+}/\text{Ta}^{5+}$, respectively [96].

2.1. Solid-state reaction

Solid-state reaction (SSR) is the most widely used method for the preparation of solid electrolyte materials. The method involves intimate grinding of solid precursors and then annealing/sintering at various temperatures.

Grinding by hand in an agate mortar remains a useful method. Ball mills, also known as centrifugal or planetary mills, are devices used to rapidly grind materials to colloidal fineness by developing high grinding energy via centrifugal and/or planetary action. Samples can be run wet or dry. Once the homogenous precursor powder is obtained, it is placed into a furnace and heated to a suitable temperature. Gases are generated and released followed by chemical interaction to form final product(s). Generally, this product may be again ground finely and then put into a furnace a second time. Finally powder materials are hydraulically pressed into a pellet shape to increase the interactivity between the powder grains and form a higher quality and/or higher density final product. Therefore solid-state synthesis normally requires intermittent grinding, high temperature and long duration of heating for the formation of final product. Hence, formation of product depends on thermodynamic and kinetic (rate of reaction) factors.

The first report of fast lithium ion conducting metal oxides with the nominal chemical composition of $\text{Li}_5\text{La}_3\text{M}_2\text{O}_{12}$ ($\text{M} = \text{Nb}, \text{Ta}$) was by Thangadurai et al. employing solid state reaction technique [90]. The starting precursor materials $\text{La}(\text{NO}_3)_3 \cdot 6\text{H}_2\text{O}$ or La_2O_3 (heated at 900°C for at least 24 h), $\text{LiOH} \cdot \text{H}_2\text{O}$ and M_2O_5 ($\text{M} = \text{Nb}, \text{Ta}$) were ball milled for 12 h in 2-propanol using zirconia balls. An additional 10 wt.% excess of $\text{LiOH} \cdot \text{H}_2\text{O}$ was added to compensate for the loss of lithium due to evaporation at elevated temperatures. The precursors were heated initially at 700°C for 6 h and once again ball milled for 12 h in 2-propanol and made into pellets and then finally sintered at 900°C for 24 h in air [90]. Following the successful synthesis of $\text{Li}_5\text{La}_3\text{M}_2\text{O}_{12}$ ($\text{M} = \text{Nb}, \text{Ta}$) fast lithium ion conductors through solid state reaction method, many research work had been initiated for further synthesis of lithium garnets.

However a breakthrough in the field of lithium garnets electrolytes came after the successful introduction of cubic phase ($Ia\bar{3}d$) $\text{Li}_7\text{La}_3\text{Zr}_2\text{O}_{12}$ with high Li^+ conductivity of $10^{-4} \text{ S cm}^{-1}$ by Murugan et al. [97,98]. $\text{Li}_7\text{La}_3\text{Zr}_2\text{O}_{12}$ was synthesized using solid-state reaction technique at high sintering temperature of 1230°C for 36 h [97,98]. The sintering conditions have greater influence on density, microstructure and Li^+ conductivity of the lithium garnets. The temperature required for the stabilization of cubic phase lithium garnet was found to be dependent on the Li^+ concentration [97–99].

Following the initial results of $\text{Li}_7\text{La}_3\text{Zr}_2\text{O}_{12}$, there have been a significant interest in the synthesis, structure and electrical properties of $\text{Li}_7\text{La}_3\text{Zr}_2\text{O}_{12}$ using various dopants through solid state reaction method. Among them Ta, Nb, Al, Ga, Ge, Si, Y, In, Sb, Te, W, Ce substituted LLZO [100–111] and related system $\text{Li}_7\text{La}_3\text{M}_2\text{O}_{12}$ ($\text{M} = \text{Sn}, \text{Hf}$) [112,113] prepared via solid-state reaction method have received notable attention.

The sintering temperature, space group, lattice parameter, bulk Li^+ conductivity (σ_{bulk}), total (bulk + grain-boundary) Li^+ conductivity (σ_{total}) and activation energy (E_a) of various lithium garnets prepared via solid state reaction method are provided in Table 2.1 [114–168].

Table 2.1

The sintering temperature, space group, lattice parameter, bulk Li⁺ conductivity (σ_{bulk}), total (bulk + grain-boundary) Li⁺ conductivity (σ_{total}) and activation energy (E_a) of various lithium garnets prepared by conventional solid state reaction method.

Composition	Final sintering temp., time	Space group	Lattice parameter (Å)	σ_{bulk} (S cm ⁻¹)	σ_{total} (S cm ⁻¹)	^a Activation energy, E_a (eV)	Ref.
Li ₃ Nd ₃ Te ₂ O ₁₂	850 °C, 10 h	<i>la</i> $\bar{3}$ d	12.56253 (9)	–	1 × 10 ⁻⁵ at 600 °C	1.22 (15) (25–600 °C)	[114]
Li ₃ Nd ₃ W ₂ O ₁₂	880 °C, 5 days	<i>la</i> $\bar{3}$ d	12.46869 (9)	–	–	–	[92]
Li _{3,05} Nd ₃ Te _{1,95} Sb _{0,05} O ₁₂	960 °C, 60 h	<i>la</i> $\bar{3}$ d	12.55576 (12)	–	~3 × 10 ⁻⁵ at 400 °C	~0.672 (6)	[96]
Li _{3,1} Nd ₃ Te _{1,9} Sb _{0,10} O ₁₂	960 °C, 60 h	<i>la</i> $\bar{3}$ d	12.5597 (9)	–	~2 × 10 ⁻⁴ at 400 °C	~0.56	[96]
Li _{3,2} Nd ₃ Te _{1,8} Sb _{0,20} O ₁₂	960 °C, 60 h	<i>la</i> $\bar{3}$ d	12.5602 (2)	–	~3 × 10 ⁻⁴ at 400 °C	~0.50	[96]
Li _{3,5} Nd ₃ Te _{1,5} Sb _{0,50} O ₁₂	960 °C, 60 h	<i>la</i> $\bar{3}$ d	12.59413 (12)	–	~1 × 10 ⁻² at 400 °C	~0.56	[96]
Li ₄ Nd ₃ TeSbO ₁₂	960 °C, 60 h	<i>la</i> $\bar{3}$ d	12.62138 (12)	–	~4 × 10 ⁻³ at 400 °C	~0.63	[96]
Li _{4,5} Nd ₃ Te _{0,5} Sb _{1,5} O ₁₂	960 °C, 60 h	<i>la</i> $\bar{3}$ d	12.6253 (2)	–	~3 × 10 ⁻³ at 400 °C	~0.59	[96]
Li ₃ Gd ₃ Te ₂ O ₁₂	900 °C, 24 h	<i>la</i> $\bar{3}$ d	12.37921 (1)	–	8.8 × 10 ⁻⁷ at 450 °C	0.88 (3)	[115]
Li ₃ Tb ₃ Te ₂ O ₁₂	900 °C, 24 h	<i>la</i> $\bar{3}$ d	12.35578 (9)	–	4.4 × 10 ⁻⁶ at 450 °C	0.77 (4)	[115]
Li ₃ Er ₃ Te ₂ O ₁₂	900 °C, 24 h	<i>la</i> $\bar{3}$ d	12.22712 (9)	–	2.8 × 10 ⁻⁸ at 450 °C	1.21 (3)	[115]
Li ₃ Lu ₃ Te ₂ O ₁₂	900 °C, 24 h	<i>la</i> $\bar{3}$ d	12.15970 (14)	–	8.1 × 10 ⁻⁸ at 450 °C	1.199 (7)	[115]
Li ₃ Y ₃ Te ₂ O ₁₂	825 °C, 12 h	<i>la</i> $\bar{3}$ d	12.2834	3.94 × 10 ⁻⁶ at 300 °C	1.48 × 10 ⁻⁶ at 300 °C	0.83 (33–300 °C)	[116]
Li _{4,22} Al _{0,26} La ₃ Zr ₂ WO ₁₂	1175 °C, 36 h	<i>la</i> $\bar{3}$ d	–	–	2.14 × 10 ⁻⁵ at 25 °C	0.46 (HT) 0.49 (LT)	[129]
Li ₅ La ₃ Nb ₂ O ₁₂	950 °C, 24 h	<i>la</i> $\bar{3}$ d	12.762 (3)	~10 ⁻⁶ at 25 °C	–	0.43	[90]
Li ₅ La ₃ Ta ₂ O ₁₂	950 °C, 24 h	<i>la</i> $\bar{3}$ d	12.766 (3)	1.2 × 10 ⁻⁶ at 25 °C (using rev. LiCoO ₂)	3.4 × 10 ⁻⁶ at 25 °C (using rev. LiCoO ₂)	0.56	[90]
Li ₅ La ₃ Nb ₂ O ₁₂	950 °C, 24 h	<i>la</i> $\bar{3}$ d	12.8189 (9)	2.3 × 10 ⁻⁵ at 50 °C	–	0.55	[117]
	1000 °C, 24 h		12.8005 (9)	4.4 × 10 ⁻⁵ at 50 °C	–	–	
Li _{5,5} La ₃ Nb _{1,75} In _{0,25} O ₁₂	950 °C, 24 h	<i>la</i> $\bar{3}$ d	12.821 (2)	1.8 × 10 ⁻⁴ at 50 °C	–	0.51	[117]
Li _{5,5} La _{2,75} Nb ₂ K _{0,25} O ₁₂	950 °C, 24 h	<i>la</i> $\bar{3}$ d	12.7937 (8)	6 × 10 ⁻⁵ at 50 °C	–	0.49	[117]
Li ₅ La ₃ Bi ₂ O ₁₂	775 °C, 48 h	<i>la</i> $\bar{3}$ d	13.0652 (4)	4 × 10 ⁻⁵ at 22 °C (Ar)	1.9 × 10 ⁻⁵ at 22 °C (Ar)	0.47 (22–300 °C)	[118]
Li ₅ La ₃ Sb ₂ O ₁₂	950 °C, 48 h	<i>la</i> $\bar{3}$ d	12.8566 (18)	8.2 × 10 ⁻⁶ at 24 °C (Ar)	7.8 × 10 ⁻⁶ at 24 °C (Ar)	~0.51 (24–300 °C)	[119]
Li ₅ BaLa ₂ Ta ₂ O _{11,5}	900 °C, 24 h	<i>la</i> $\bar{3}$ d	~12.89	7.14 × 10 ⁻⁶ at 50 °C	4.90 × 10 ⁻⁶ at 50 °C	~0.51 (17–350 °C)	[120]
Li _{5,75} BaLa ₂ Ta ₂ O _{11,75}	900 °C, 24 h	<i>la</i> $\bar{3}$ d	~12.938	3.55 × 10 ⁻⁵ at 50 °C	3.11 × 10 ⁻⁵ at 50 °C	~0.47 (17–350 °C)	[120]
Li _{5,75} BaLa ₂ Ta ₂ O _{11,875}	900 °C, 24 h	<i>la</i> $\bar{3}$ d	~12.96	9.48 × 10 ⁻⁵ at 50 °C	8.99 × 10 ⁻⁵ at 50 °C	~0.44 (17–350 °C)	[120]
Li ₅ Nd ₃ Sb ₂ O ₁₂	925 °C, 14 h	<i>la</i> $\bar{3}$ d	12.66238 (3)	1.3 × 10 ⁻⁷ at 25 °C	–	0.67 (<300 °C), 0.35 (>300 °C)	[121]
Li ₅ La ₃ Nb ₂ O ₁₂	1100 °C, 6 h	<i>la</i> $\bar{3}$ d	12.718 (2)	–	5.08 × 10 ⁻⁶ at 23 °C	0.60	[122]
Li ₅ La ₃ Nb _{1,95} Y _{0,05} O ₁₂	1100 °C, 6 h	<i>la</i> $\bar{3}$ d	12.717 (2)	–	1.34 × 10 ⁻⁵ at 23 °C	0.45	[122]
Li ₅ La ₃ Nb _{1,9} Y _{0,10} O ₁₂	1100 °C, 6 h	<i>la</i> $\bar{3}$ d	12.717 (3)	–	1.44 × 10 ⁻⁵ at 23 °C	0.51	[122]
Li ₅ La ₃ Nb _{1,85} Y _{0,15} O ₁₂	1100 °C, 6 h	<i>la</i> $\bar{3}$ d	12.732 (9)	–	5.71 × 10 ⁻⁶ at 23 °C	0.43	[122]
Li ₅ La ₃ Nb _{1,8} Y _{0,20} O ₁₂	1100 °C, 6 h	<i>la</i> $\bar{3}$ d	12.743 (8)	–	9.13 × 10 ⁻⁶ at 23 °C	0.43	[122]
Li ₅ La ₃ Nb _{1,75} Y _{0,25} O ₁₂	1100 °C, 6 h	<i>la</i> $\bar{3}$ d	12.717 (5)	–	9.68 × 10 ⁻⁶ at 23 °C	0.43	[122]
Li _{5,5} La ₃ Zr ₂ Ga _{0,5} O ₁₂	1150 °C, 3 h	<i>la</i> $\bar{3}$ d	12.9697 (1)	1 × 10 ⁻⁴ at RT	–	–	[111]
Li ₅ La ₃ Ta ₂ O ₁₂	900 °C, 10 h	<i>la</i> $\bar{3}$ d	12.8311	–	0.34 × 10 ⁻⁴ at RT	–	[102]
Li _{5,5} La ₃ Zr _{0,5} Ta _{1,5} O ₁₂	1000 °C, 20 h	<i>la</i> $\bar{3}$ d	12.861	–	9.3 × 10 ⁻⁵ at 25 °C	0.49	[103]
Li ₅ La ₃ Ta ₂ O ₁₂	950 °C, 24 h	<i>la</i> $\bar{3}$ d	12.708 (3)	–	–	0.60	[123]
Li _{5,5} Ba _{0,5} La _{2,5} Ta ₂ O ₁₂	950 °C, 24 h	<i>la</i> $\bar{3}$ d	12.823 (8)	–	–	0.44	[123]
Li ₅ La ₃ Nb ₂ O ₁₂	1150 °C, 12 h	<i>la</i> $\bar{3}$ d	12.786 (4)	1.73 × 10 ⁻⁴ at 25 °C	0.22 × 10 ⁻⁴ at 25 °C	0.45 (25–200 °C)	[124]
Li _{5,5} La ₃ Nb _{1,75} Sc _{0,25} O ₁₂	1150 °C, 12 h	<i>la</i> $\bar{3}$ d	~12.808	3.14 × 10 ⁻⁴ at 25 °C	0.52 × 10 ⁻⁴ at 25 °C	0.40 (25–200 °C)	[124]
Li ₅ La ₃ Nb ₂ O ₁₂	1100 °C, 6 h	<i>la</i> $\bar{3}$ d	12.774 (2)	–	–	–	[125]
Li _{5,1} La ₃ Nb _{1,95} Sm _{0,05} O ₁₂	1100 °C, 6 h	<i>la</i> $\bar{3}$ d	~12.799	–	1.80 × 10 ⁻⁵ at 25 °C	0.45 (25–225 °C)	[125]

(continued on next page)

Table 2.1 (continued)

Composition	Final sintering temp., time	Space group	Lattice parameter (Å)	σ_{bulk} (S cm ⁻¹)	σ_{total} (S cm ⁻¹)	^a Activation energy, E _a (eV)	Ref.
Li _{5.2} La ₃ Nb _{1.9} Sm _{0.10} O ₁₂	1100 °C, 6 h	<i>la</i> $\bar{3}$ <i>d</i>	12.806 (1)	–	2.32 × 10 ⁻⁵ at 25 °C	0.42 (25–225 °C)	[125]
Li _{5.3} La ₃ Nb _{1.85} Sm _{0.15} O ₁₂	1100 °C, 6 h	<i>la</i> $\bar{3}$ <i>d</i>	12.814 (1)	–	2.57 × 10 ⁻⁵ at 25 °C	0.41 (25–225 °C)	[125]
Li _{5.4} La ₃ Nb _{1.8} Sm _{0.20} O ₁₂	1100 °C, 6 h	<i>la</i> $\bar{3}$ <i>d</i>	12.838 (1)	–	3.71 × 10 ⁻⁵ at 25 °C	0.40 (25–225 °C)	[125]
Li _{5.5} La ₃ Nb _{1.75} Sm _{0.25} O ₁₂	1100 °C, 6 h	<i>la</i> $\bar{3}$ <i>d</i>	12.845 (2)	–	3.86 × 10 ⁻⁵ at 25 °C	0.39 (25–225 °C)	[125]
Li _{5.6} La ₃ Nb _{1.7} Sm _{0.30} O ₁₂	1100 °C, 6 h	<i>la</i> $\bar{3}$ <i>d</i>	12.851 (2)	–	5.84 × 10 ⁻⁵ at 25 °C	0.38 (25–225 °C)	[125]
Li _{5.5} La ₃ Ta _{1.75} Y _{0.25} O ₁₂	1100 °C, 6 h	<i>la</i> $\bar{3}$ <i>d</i>	12.8977 (4)	–	2.82 × 10 ⁻⁵ at 23 °C	0.65 (–50 to 50 °C)	[126]
Li _{5.5} La ₃ Zr _{1.25} Te _{0.75} O ₁₂	1150 °C, 12 h	–	–	–	9.47 × 10 ⁻⁵ at RT for Al ₂ O ₃ crucible	0.45 (150 °C to RT) 0.49 (RT to –50 °C) for Al ₂ O ₃ crucible	[127]
Li ₅ La ₃ ZrTeO ₁₂	1150 °C, 12 h	–	–	–	8.2 × 10 ⁻⁵ at RT for ZrO ₂ crucible	0.44 (150 °C to RT) 0.48 (RT to –50 °C) for ZrO ₂ crucible	[127]
Li ₅ La ₃ Nb ₂ O ₁₂	1150 °C, 12 h	<i>la</i> $\bar{3}$ <i>d</i>	1.27964 (1) as prepared	–	4.6 × 10 ⁻⁵ at RT for Al ₂ O ₃ crucible	0.43 (150 °C to RT) 0.48 (RT to –50 °C) for Al ₂ O ₃ crucible	[127]
Li _{5.9} Al _{0.2} La ₃ Zr _{1.75} W _{0.25} O ₁₂	1150 °C, 12 h	<i>la</i> $\bar{3}$ <i>d</i>	12.954 (1)	–	6.3 × 10 ⁻⁵ at RT for ZrO ₂ crucible	0.42 (150 °C to RT), 0.49 (RT to –50 °C) for ZrO ₂ crucible	[128]
Li _{5.4} Al _{0.2} La ₃ Zr _{1.5} W _{0.5} O ₁₂	1150 °C, 12 h	<i>la</i> $\bar{3}$ <i>d</i>	12.924 (1)	–	0.22 × 10 ⁻⁴ at 25 °C as prepared	0.552 (–20 to 150 °C) as prepared	[128]
Li _{5.5} La ₃ Zr _{1.25} W _{0.75} O ₁₂	1150 °C, 12 h	<i>la</i> $\bar{3}$ <i>d</i>	12.900 (1)	–	4.9 × 10 ⁻⁴ at 25 °C	0.35 (HT) 0.43 (LT)	[129]
Li _{5.1} La ₃ Ta _{1.95} Y _{0.05} O ₁₂	1100 °C, 6 h	<i>la</i> $\bar{3}$ <i>d</i>	12.8160 (3)	–	1.5 × 10 ⁻⁴ at 25 °C	0.40 (HT) 0.46 (LT)	[129]
Li _{5.2} La ₃ Ta _{1.9} Y _{0.10} O ₁₂	1100 °C, 6 h	<i>la</i> $\bar{3}$ <i>d</i>	12.8268 (4)	–	5.33 × 10 ⁻⁵ at 25 °C	0.43 (HT), 0.46 (LT)	[129]
Li _{5.4} La ₃ Ta _{1.8} Y _{0.20} O ₁₂	1100 °C, 6 h	<i>la</i> $\bar{3}$ <i>d</i>	12.8642 (3)	–	9.56 × 10 ⁻⁶ at 23 °C	0.43 (23–325 °C)	[130]
Li _{5.5} La ₃ Ta _{1.75} Y _{0.25} O ₁₂	1100 °C, 6 h	<i>la</i> $\bar{3}$ <i>d</i>	–	–	1.04 × 10 ⁻⁵ at 23 °C	0.40 (23–325 °C)	[130]
Li ₅ La ₃ Ta ₂ O ₁₂	1150 °C, 12 h	<i>la</i> $\bar{3}$ <i>d</i>	1.28214 (1) as prepared	–	1.07 × 10 ⁻⁵ at 23 °C	0.44 (23–325 °C)	[130]
Li _{5.9} La ₃ Zr _{1.45} W _{0.55} O ₁₂	1200 °C, 12 h	<i>la</i> $\bar{3}$ <i>d</i>	–	–	2.82 × 10 ⁻⁵ at 23 °C	0.43 (23–325 °C)	[130]
Li ₆ CaLa ₂ Nb ₂ O ₁₂	900 °C, 24 h	<i>la</i> $\bar{3}$ <i>d</i>	12.697 (2)	1.6 × 10 ⁻⁶ at 22 °C	0.13 × 10 ⁻⁴ at 25 °C as prepared	0.491 as prepared (–20 to 150 °C)	[128]
Li ₆ SrLa ₂ Nb ₂ O ₁₂	900 °C, 24 h	<i>la</i> $\bar{3}$ <i>d</i>	12.811 (1)	4.2 × 10 ⁻⁶ at 22 °C	4.4 × 10 ⁻⁴ at 25 °C	0.43 (25–70 °C)	[131]
Li ₆ BaLa ₂ Nb ₂ O ₁₂	900 °C, 24 h	<i>la</i> $\bar{3}$ <i>d</i>	12.868 (1)	6.0 × 10 ⁻⁶ at 22 °C	–	0.55 (25–300 °C)	[132]
Li ₆ SrLa ₂ Ta ₂ O ₁₂	900 °C, 24 h	I2 ₃	12.808 (2)	8.84 × 10 ⁻⁶ at 22 °C	–	0.50 (20–200 °C)	[132]
Li ₆ BaLa ₂ Ta ₂ O ₁₂	900 °C, 24 h	I2 ₃	12.946 (3)	5.38 × 10 ⁻⁵ at 22 °C	–	0.44 (20–200 °C)	[132]
Li ₆ BaLa ₂ Ta ₂ O ₁₂	900 °C, 24 h	<i>la</i> $\bar{3}$ <i>d</i>	–	–	7 × 10 ⁻⁶ at 22 °C	0.50	[133]
Li ₆ SrLa ₂ Nb ₂ O ₁₂	900 °C, 14 h	<i>la</i> $\bar{3}$ <i>d</i>	–	–	4 × 10 ⁻⁵ at 22 °C	0.40	[133]
Li ₆ SrLa ₂ Bi ₂ O ₁₂	750 °C, 48 h	<i>la</i> $\bar{3}$ <i>d</i>	13.0893 (9)	5.2 × 10 ⁻⁵ at 22 °C	–	0.40 (30–370 °C)	[134]
Li ₆ SrLa ₂ Sb ₂ O ₁₂	950 °C, 48 h	<i>la</i> $\bar{3}$ <i>d</i>	12.8933 (3)	6.6 × 10 ⁻⁶ at 24 °C (Ar)	–	–	[135]
Li ₆ BaLa ₂ Ta ₂ O ₁₂	900 °C, 24 h	<i>la</i> $\bar{3}$ <i>d</i>	12.9755 (4)	1.81 × 10 ⁻⁴ at 50 °C	2.0 × 10 ⁻⁵ at 22 °C	E _a (b) = 0.43 (22–100 °C) E _a (t) = 0.42 (22–300 °C)	[118]
Li _{6.25} BaLa ₂ Ta ₂ O _{12.125}	900 °C, 24 h	<i>la</i> $\bar{3}$ <i>d</i>	~12.96	1.57 × 10 ⁻⁴ at 50 °C	6.3 × 10 ⁻⁶ at 24 °C (Ar)	0.54 (24–300 °C)	[119]
Li _{6.50} BaLa ₂ Ta ₂ O _{12.25}	900 °C, 24 h	<i>la</i> $\bar{3}$ <i>d</i>	~12.958	1.07 × 10 ⁻⁴ at 50 °C	1.51 × 10 ⁻⁴ at 50 °C	~0.42 (17–350 °C)	[120]
Li _{6.75} BaLa ₂ Ta ₂ O _{12.375}	900 °C, 24 h	<i>la</i> $\bar{3}$ <i>d</i>	~12.948	1.09 × 10 ⁻⁴ at 50 °C	1.46 × 10 ⁻⁴ at 50 °C	~0.42 (17–350 °C)	[120]
Li ₆ CaLa ₂ Ta ₂ O ₁₂	950 °C, 24 h	<i>la</i> $\bar{3}$ <i>d</i>	12.734 (3)	3.59 × 10 ⁻⁶ at 50 °C	3.53 × 10 ⁻⁶ at 50 °C	0.53 (17–350 °C)	[120]

Table 2.1 (continued)

Composition	Final sintering temp., time	Space group	Lattice parameter (Å)	σ_{bulk} (S cm ⁻¹)	σ_{total} (S cm ⁻¹)	^a Activation energy, E _a (eV)	Ref.
Li ₆ SrLa ₂ Ta ₂ O ₁₂	900 °C, 24 h	<i>la</i> $\bar{3}$ <i>d</i>	12.826	2.61 × 10 ⁻⁵ at 50 °C	2.26 × 10 ⁻⁵ at 50 °C	–	[120]
Li ₆ SrLa ₂ Ta ₂ O ₁₂	950 °C, 24 h	<i>la</i> $\bar{3}$ <i>d</i>	12.835	3.66 × 10 ⁻⁵ at 50 °C	3.05 × 10 ⁻⁵ at 50 °C	0.45 (17–350 °C)	[120]
Li ₆ Sr _{0.5} Ba _{0.5} La ₂ Ta ₂ O ₁₂	900 °C, 24 h	<i>la</i> $\bar{3}$ <i>d</i>	12.879	4.64 × 10 ⁻⁵ at 50 °C	3.93 × 10 ⁻⁵ at 50 °C	–	[120]
Li ₆ Sr _{0.5} Ba _{0.5} La ₂ Ta ₂ O ₁₂	950 °C, 24 h	<i>la</i> $\bar{3}$ <i>d</i>	12.862	4.96 × 10 ⁻⁵ at 50 °C	4.46 × 10 ⁻⁵ at 50 °C	0.44 (17–350 °C)	[120]
Li ₆ BaLa ₂ Ta ₂ O ₁₂	900 °C, 24 h	<i>la</i> $\bar{3}$ <i>d</i>	12.973	1.30 × 10 ⁻⁴ at 50 °C	1.13 × 10 ⁻⁴ at 50 °C	–	[120]
Li ₆ BaLa ₂ Ta ₂ O ₁₂	950 °C, 24 h	<i>la</i> $\bar{3}$ <i>d</i>	12.975	1.01 × 10 ⁻⁴ at 50 °C	9.28 × 10 ⁻⁵ at 50 °C	0.42 (17–350 °C)	[120]
Li ₆ CaLa ₂ Ta ₂ O ₁₂	1000 °C, 4 h	<i>la</i> $\bar{3}$ <i>d</i>	12.725 (2)	–	2.2 × 10 ⁻⁶ at 27 °C	0.50 (25–350 °C)	[136]
Li ₆ BaLa ₂ Ta ₂ O ₁₂	1000 °C, 4 h	<i>la</i> $\bar{3}$ <i>d</i>	13.001 (4)	–	1.3 × 10 ⁻⁵ at 25 °C	0.44 (25–350 °C)	[136]
Li ₆ CaLa ₂ Sb ₂ O ₁₂	900 °C, 24 h	<i>la</i> $\bar{3}$ <i>d</i>	12.78594 (12)	–	1 × 10 ⁻⁷ at 95 °C	0.82 (3)	[115]
Li _{6,4} Ca _{1,4} La _{1,6} Sb ₂ O ₁₂	900 °C, 24 h	<i>la</i> $\bar{3}$ <i>d</i>	12.7730 (2)	–	–	–	[115]
Li ₆ La ₃ ZrTaO ₁₂	1120 °C, 8 h	<i>la</i> $\bar{3}$ <i>d</i>	12.8873	2.5 × 10 ⁻⁴ at 25 °C	1.8 × 10 ⁻⁴ at 25 °C	0.42 (25–177 °C)	[137]
Li _{6,75} La ₃ Zr _{1,75} Nb _{0,25} O ₁₂	1200 °C, 36 h	<i>la</i> $\bar{3}$ <i>d</i>	~12.95	–	0.8 × 10 ⁻³ at 25 °C	0.31	[101]
Li _{6,5} La ₃ Nb _{1,25} Y _{0,75} O ₁₂	1100 °C, 6 h	<i>la</i> $\bar{3}$ <i>d</i>	12.9488 (11)	2.7 × 10 ⁻⁴ at 25 °C	–	0.36	[138]
Li ₆ La ₃ SnTaO ₁₂	1130 °C, 12 h	<i>la</i> $\bar{3}$ <i>d</i>	12.8693	–	4.2 × 10 ⁻⁵ at 20 °C	0.498 (–50 to 90 °C)	[139]
Li ₆ La ₃ SnNbO ₁₂	1130 °C, 12 h	<i>la</i> $\bar{3}$ <i>d</i>	12.8682	–	3.5 × 10 ⁻⁵ at 20 °C	0.503 (–50 to 90 °C)	[139]
Li ₆ La ₃ SnSbO ₁₂	1130 °C, 12 h	<i>la</i> $\bar{3}$ <i>d</i>	12.8991	–	2.2 × 10 ⁻⁵ at 20 °C	0.504 (–50 to 90 °C)	[139]
Li _{6,5} La _{2,5} Ba _{0,5} ZrTaO ₁₂	1100 °C, 6 h	<i>la</i> $\bar{3}$ <i>d</i>	12.764 (3)	–	9.0 × 10 ⁻⁵ at 24 °C	0.57 (–53 to 17 °C)	[140]
Li ₆ La ₃ ZrTaO ₁₂	1000 °C, 20 h	<i>la</i> $\bar{3}$ <i>d</i>	~12.921	–	2.6 × 10 ⁻⁴ at 25 °C	0.46 (–40 to 100 °C)	[103]
Li _{6,5} La ₃ Zr _{1,5} Ta _{0,5} O ₁₂	1000 °C, 20 h	<i>la</i> $\bar{3}$ <i>d</i>	~12.958	–	2 × 10 ⁻⁶ at 25 °C	0.49 (–40 to 100 °C)	[103]
Li _{6,625} La ₃ Zr _{1,625} Ta _{0,375} O ₁₂ (29 mol.% Al)	1000 °C, 20 h	<i>la</i> $\bar{3}$ <i>d</i>	~12.9438	–	5.2 × 10 ⁻⁴ at 25 °C	0.41 (–40 to 100 °C)	[103]
Li _{6,8} La ₃ Hf _{1,8} Ta _{0,2} O ₁₂	1130 °C, 48 h	<i>la</i> $\bar{3}$ <i>d</i>	12.9439 (7)	–	1.58 × 10 ⁻⁴ at 22 °C	–	[141]
Li _{6,7} La ₃ Hf _{1,7} Ta _{0,3} O ₁₂	1130 °C, 48 h	<i>la</i> $\bar{3}$ <i>d</i>	12.9399 (8)	–	1.83 × 10 ⁻⁴ at 22 °C	0.448 (–50 to 100 °C)	[141]
Li _{6,6} La ₃ Hf _{1,6} Ta _{0,4} O ₁₂	1130 °C, 48 h	<i>la</i> $\bar{3}$ <i>d</i>	12.9362 (4)	–	2.99 × 10 ⁻⁴ at 22 °C	0.440 (–50 to 100 °C)	[141]
Li _{6,55} La ₃ Hf _{1,55} Ta _{0,45} O ₁₂	1130 °C, 48 h	<i>la</i> $\bar{3}$ <i>d</i>	12.9330 (2)	–	3.45 × 10 ⁻⁴ at 22 °C	0.438 (–50 to 100 °C)	[141]
Li _{6,5} La ₃ Hf _{1,5} Ta _{0,5} O ₁₂	1130 °C, 48 h	<i>la</i> $\bar{3}$ <i>d</i>	12.9298 (2)	–	2.61 × 10 ⁻⁴ at 22 °C	0.465 (–50 to 100 °C)	[141]
Li _{6,45} La ₃ Hf _{1,45} Ta _{0,55} O ₁₂	1130 °C, 48 h	<i>la</i> $\bar{3}$ <i>d</i>	12.9257 (2)	–	2.21 × 10 ⁻⁴ at 22 °C	–	[141]
Li _{6,4} La ₃ Hf _{1,4} Ta _{0,6} O ₁₂	1130 °C, 48 h	<i>la</i> $\bar{3}$ <i>d</i>	12.9275 (3)	–	2.20 × 10 ⁻⁴ at 22 °C	0.471 (–50 to 100 °C)	[141]
Li _{6,8} La ₃ Zr _{1,8} Ta _{0,2} O ₁₂	1140 °C, 16 h	<i>la</i> $\bar{3}$ <i>d</i>	~12.96	–	2.8 × 10 ⁻⁴ at 25 °C	–	[104]
Li _{6,6} La ₃ Zr _{1,6} Ta _{0,4} O ₁₂	1140 °C, 16 h	<i>la</i> $\bar{3}$ <i>d</i>	~12.94	–	7.3 × 10 ⁻⁴ at 25 °C	–	[104]
Li _{6,5} La ₃ Zr _{1,5} Ta _{0,5} O ₁₂	1140 °C, 16 h	<i>la</i> $\bar{3}$ <i>d</i>	–	–	9.2 × 10 ⁻⁴ at 25 °C	–	[104]
Li _{6,4} La ₃ Zr _{1,4} Ta _{0,6} O ₁₂	1140 °C, 16 h	<i>la</i> $\bar{3}$ <i>d</i>	~12.92	–	1.0 × 10 ⁻³ at 25 °C	0.35 (25–157 °C)	[104]
Li _{6,2} La ₃ Zr _{1,2} Ta _{0,8} O ₁₂	1120 °C, 8 h	<i>la</i> $\bar{3}$ <i>d</i>	~12.90	–	3.2 × 10 ⁻⁴ at 25 °C	–	[104]
Li ₆ La ₃ ZrTaO ₁₂	1120 °C, 8 h	<i>la</i> $\bar{3}$ <i>d</i>	~12.89	–	1.6 × 10 ⁻⁴ at 25 °C	–	[104]
Li _{6,8} La ₃ Zr _{1,8} Sb _{0,2} O ₁₂	1100 °C, 24 h	<i>la</i> $\bar{3}$ <i>d</i>	12.97545	–	5.9 × 10 ⁻⁵ at 30 °C	0.39 (–120 to 200 °C)	[106]
Li _{6,6} La ₃ Zr _{1,6} Sb _{0,4} O ₁₂	1100 °C, 24 h	<i>la</i> $\bar{3}$ <i>d</i>	12.95955	–	7.7 × 10 ⁻⁴ at 30 °C	0.34 (–120 to 200 °C)	[106]
Li _{6,4} La ₃ Zr _{1,4} Sb _{0,6} O ₁₂	1100 °C, 24 h	<i>la</i> $\bar{3}$ <i>d</i>	12.95179	–	6.6 × 10 ⁻⁴ at 30 °C	0.36 (–120 to 200 °C)	[106]
Li _{6,2} La ₃ Zr _{1,2} Sb _{0,8} O ₁₂	1100 °C, 24 h	<i>la</i> $\bar{3}$ <i>d</i>	12.92484	–	4.5 × 10 ⁻⁴ at 30 °C	0.37 (–120 to 200 °C)	[106]
Li ₆ La ₃ Zr _{1,0} Sb _{1,0} O ₁₂	1100 °C, 24 h	<i>la</i> $\bar{3}$ <i>d</i>	12.9237	–	2.6 × 10 ⁻⁴ at 30 °C	0.38 (–120 to 200 °C)	[106]
Li _{6,8} La ₃ Zr _{1,8} Ta _{0,2} O ₁₂	1130 °C	<i>la</i> $\bar{3}$ <i>d</i>	12.9780	–	7.3 × 10 ⁻⁴ at RT	–	[102]
Li _{6,75} La ₃ Zr _{1,75} Ta _{0,25} O ₁₂	1130 °C	<i>la</i> $\bar{3}$ <i>d</i>	12.9801	–	6.3 × 10 ⁻⁴ at RT	–	[102]
Li _{6,7} La ₃ Zr _{1,7} Ta _{0,3} O ₁₂	1100 °C	<i>la</i> $\bar{3}$ <i>d</i>	12.9721	9.6 × 10 ⁻⁴ at RT	6.9 × 10 ⁻⁴ at RT	E _{a(b)} = 0.37, E _{a(t)} = 0.36	[102]
Li _{6,65} La ₃ Zr _{1,65} Ta _{0,35} O ₁₂	1130 °C	<i>la</i> $\bar{3}$ <i>d</i>	12.9591	–	4.6 × 10 ⁻⁴ at RT	–	[102]
Li _{6,6} La ₃ Zr _{1,6} Ta _{0,4} O ₁₂	1130 °C	<i>la</i> $\bar{3}$ <i>d</i>	12.9470	–	4.7 × 10 ⁻⁴ at RT	–	[102]

(continued on next page)

Table 2.1 (continued)

Composition	Final sintering temp., time	Space group	Lattice parameter (Å)	σ_{bulk} (S cm ⁻¹)	σ_{total} (S cm ⁻¹)	^a Activation energy, E _a (eV)	Ref.
Li _{6.55} La ₃ Zr _{1.55} Ta _{0.45} O ₁₂	1130 °C	<i>la</i> $\bar{3}$ <i>d</i>	12.9489	–	4.0 × 10 ⁻⁴ at RT	–	[102]
Li _{6.5} La ₃ Zr _{1.5} Ta _{0.5} O ₁₂	1130 °C	<i>la</i> $\bar{3}$ <i>d</i>	12.9187	–	2.8 × 10 ⁻⁴ at RT	–	[102]
Li ₆ La ₃ ZrTaO ₁₂	1100 °C	<i>la</i> $\bar{3}$ <i>d</i>	12.8900	–	3.5 × 10 ⁻⁴ at RT	–	[102]
Li _{6.4} La ₃ Zr _{1.6} W _{0.3} O ₁₂	1100 °C, 36 h	<i>la</i> $\bar{3}$ <i>d</i>	12.96507	–	7.89 × 10 ⁻⁴ at 30 °C	0.45 (–100 to 100 °C)	[107]
Li ₆ La ₃ Zr _{1.5} W _{0.5} O ₁₂	1100 °C, 36 h	<i>la</i> $\bar{3}$ <i>d</i>	12.94385	–	2.08 × 10 ⁻⁴ at 30 °C	0.46 (–100 to 100 °C)	[107]
Li _{6.75} La ₃ Zr _{1.875} Te _{0.125} O ₁₂	1100 °C, 15 h	<i>la</i> $\bar{3}$ <i>d</i>	12.9469	–	3.30 × 10 ⁻⁴ at 30 °C	0.41 (–100 to 100 °C)	[108]
Li _{6.5} La ₃ Zr _{1.75} Te _{0.25} O ₁₂	1100 °C, 15 h	<i>la</i> $\bar{3}$ <i>d</i>	12.9134	–	1.02 × 10 ⁻⁴ at 30 °C	0.38 (–100 to 100 °C)	[108]
Li _{6.75} La ₃ Zr _{1.75} Ta _{0.25} O ₁₂ 0 wt.% Li ₂ O	1230 °C, 6 h	–	–	–	2.2 × 10 ⁻⁴ at 28 °C	0.41	[143]
Li _{6.75} La ₃ Zr _{1.75} Ta _{0.25} O ₁₂ 2 wt.% Li ₂ O	1200 °C, 6 h	–	–	–	3.3 × 10 ⁻⁴ at 28 °C	0.38	[143]
Li _{6.75} La ₃ Zr _{1.75} Ta _{0.25} O ₁₂ 4 wt.% Li ₂ O	1200 °C, 6 h	–	–	–	4.4 × 10 ⁻⁴ at 28 °C	0.33	[143]
Li _{6.75} La ₃ Zr _{1.75} Ta _{0.25} O ₁₂ 6 wt.% Li ₂ O	1170 °C, 6 h	–	–	–	6.4 × 10 ⁻⁴ at 28 °C	0.30	[143]
Li _{6.75} La ₃ Zr _{1.75} Ta _{0.25} O ₁₂ 8 wt.% Li ₂ O	1170 °C, 6 h	–	–	–	2.7 × 10 ⁻⁴ at 28 °C	0.39	[143]
Li _{6.75} La ₃ Zr _{1.75} Ta _{0.25} O ₁₂ + 0 wt.% Li ₃ PO ₄	1175 °C, 36 h	<i>la</i> $\bar{3}$ <i>d</i>	–	–	2.9 × 10 ⁻⁴ at 25 °C	0.42	[144]
Li _{6.75} La ₃ Zr _{1.75} Ta _{0.25} O ₁₂ + 1 wt.% Li ₃ PO ₄	1175 °C, 6 h	<i>la</i> $\bar{3}$ <i>d</i>	–	–	7.2 × 10 ⁻⁴ at 25 °C	0.42	[144]
Li _{6.75} La ₃ Zr _{1.75} Ta _{0.25} O ₁₂ + 2 wt.% Li ₃ PO ₄	1175 °C, 6 h	<i>la</i> $\bar{3}$ <i>d</i>	–	–	4.7 × 10 ⁻⁴ at 25 °C	0.48	[144]
Li _{6.75} La ₃ Zr _{1.75} Ta _{0.25} O ₁₂ + 4 wt.% Li ₃ PO ₄	1150 °C, 6 h	<i>la</i> $\bar{3}$ <i>d</i>	–	–	3.1 × 10 ⁻⁴ at 25 °C	0.46	[144]
Li _{6.75} La ₃ Zr _{1.75} Ta _{0.25} O ₁₂ + 6 wt.% Li ₃ PO ₄	1150 °C, 6 h	<i>la</i> $\bar{3}$ <i>d</i>	–	–	1.6 × 10 ⁻⁴ at 25 °C	0.46	[144]
Li _{6.6} La _{2.6} Ce _{0.4} Zr ₂ O ₁₂	1050 °C, 1 h	<i>la</i> $\bar{3}$ <i>d</i>	13.020	–	1.44 × 10 ⁻⁵ at RT	0.48	[109]
Li _{6.4} La _{2.4} Ce _{0.6} Zr ₂ O ₁₂	–	<i>la</i> $\bar{3}$ <i>d</i>	13.014	–	1.26 × 10 ⁻⁵ at RT	0.50	[109]
Li ₆ La ₂ BaTa ₂ O ₁₂	900 °C, 24 h	<i>la</i> $\bar{3}$ <i>d</i>	12.9958 (9)	–	8.77 × 10 ⁻⁶ at RT	0.41 (20–255 °C)	[145]
Li ₆ La ₂ BaNb _{0.5} Ta _{1.5} O ₁₂	900 °C, 24 h	<i>la</i> $\bar{3}$ <i>d</i>	12.87876 (6)	–	4.21 × 10 ⁻⁶ at RT	0.47 (20–255 °C)	[145]
Li ₆ La ₂ BaNbTaO ₁₂	900 °C, 24 h	<i>la</i> $\bar{3}$ <i>d</i>	12.9897 (5)	–	3.09 × 10 ⁻⁶ at RT	0.47 (20–255 °C)	[145]
Li ₆ La ₂ BaNb _{1.5} Ta _{0.5} O ₁₂	900 °C, 24 h	<i>la</i> $\bar{3}$ <i>d</i>	13.0681 (12)	–	1.01 × 10 ⁻⁶ at RT	0.50 (20–255 °C)	[145]
Li ₆ La ₂ BaNb ₂ O ₁₂	900 °C, 24 h	<i>la</i> $\bar{3}$ <i>d</i>	12.8893 (2)	–	6.69 × 10 ⁻⁶ at RT	0.42 (20–255 °C)	[145]
Li ₆ BaLa ₂ Ta ₂ O ₁₂	950 °C, 24 h	<i>la</i> $\bar{3}$ <i>d</i>	12.861 (2)	–	10 ⁻⁴ at 25 °C	0.39 (25–125 °C)	[123]
Li ₆ BaLa ₂ Ta ₂ O ₁₂	900 °C, 12 h	<i>la</i> $\bar{3}$ <i>d</i>	12.99726 (7)	–	1.5 × 10 ⁻⁵ at 18 °C	0.47	[146]
Li ₆ Ba _{0.5} Sr _{0.5} La ₂ Ta ₂ O ₁₂	900 °C, 12 h	<i>la</i> $\bar{3}$ <i>d</i>	12.91529 (4)	–	7.1 × 10 ⁻⁶ at 18 °C	0.45	[146]
Li ₆ SrLa ₂ Ta ₂ O ₁₂	900 °C, 12 h	<i>la</i> $\bar{3}$ <i>d</i>	12.83013 (12)	–	5.4 × 10 ⁻⁶ at 18 °C	0.45	[146]
Li ₆ Sr _{0.5} Ca _{0.5} La ₂ Ta ₂ O ₁₂	900 °C, 12 h	<i>la</i> $\bar{3}$ <i>d</i>	12.77584 (4)	–	3.2 × 10 ⁻⁶ at 18 °C	0.50	[146]
Li ₆ CaLa ₂ Ta ₂ O ₁₂	900 °C, 12 h	<i>la</i> $\bar{3}$ <i>d</i>	12.70877 (8)	–	2.2 × 10 ⁻⁶ at 18 °C	0.47	[146]
Li _{6.5} La ₃ Zr _{1.75} Te _{0.25} O ₁₂	1150 °C, 12 h	<i>la</i> $\bar{3}$ <i>d</i> for Al ₂ O ₃ crucible	12.96183 (12)	–	4 × 10 ⁻⁶ at RT for Al ₂ O ₃ crucible	0.33 (150 °C to RT)/0.46 RT to –50 °C) for Al ₂ O ₃ crucible	[127]
		<i>la</i> $\bar{3}$ <i>d</i> for ZrO ₂ crucible	12.96251 (12)	–	3.69 × 10 ⁻⁶ at RT for ZrO ₂ crucible	0.37 (150 °C to RT)/0.47 RT to –50 °C) for ZrO ₂ crucible	
Li ₆ La ₃ Zr _{1.5} Te _{0.5} O ₁₂	1150 °C, 12 h	<i>la</i> $\bar{3}$ <i>d</i> with (La _{0.5} Zr _{0.5} O _{1.75}) Impurity phase	–	–	2.19 × 10 ⁻⁶ at RT for Al ₂ O ₃ crucible	0.37 (150 °C to RT)/0.48 (RT to –50 °C) for Al ₂ O ₃ crucible	[127]

Table 2.1 (continued)

Composition	Final sintering temp., time	Space group	Lattice parameter (Å)	σ_{bulk} (S cm ⁻¹)	σ_{total} (S cm ⁻¹)	^a Activation energy, E _a (eV)	Ref.
		<i>la3d</i>			2.30×10^{-6} at RT for ZrO ₂ crucible	0.39 (150 °C to RT)/0.47 (RT to -50 °C) for ZrO ₂ crucible	
Li _{6.925} La ₃ Zr _{1.925} Sb _{0.075} O ₁₂	1160 °C, 6 h	<i>la3d</i>	12.9538	3.83×10^{-4} at 30 °C	3.40×10^{-4} at 30 °C	0.37 (-60 to 60 °C)	[147]
Li _{6.6} La ₃ Zr _{1.6} Ta _{0.4} O ₁₂	1200 °C, 18 h	<i>la3d</i>	12.9484 (2)	3.13×10^{-4} at 27 °C	3.04×10^{-4} at 27 °C	0.38 (27–200 °C)	[148]
Li _{6.6} La _{2.875} Y _{0.125} Zr _{1.6} Ta _{0.4} O ₁₂	1200 °C, 18 h	<i>la3d</i>	12.9371 (2)	–	3.17×10^{-4} at 27 °C	0.35 (27–200 °C)	[148]
Li _{6.6} La _{2.75} Y _{0.25} Zr _{1.6} Ta _{0.4} O ₁₂	1200 °C, 18 h	<i>la3d</i>	12.9214 (1)	–	4.36×10^{-4} at 27 °C	0.34 (27–200 °C)	[148]
Li _{6.6} La _{2.5} Y _{0.5} Zr _{1.6} Ta _{0.4} O ₁₂	1200 °C, 18 h	<i>la3d</i>	12.9041 (3)	3×10^{-4} at 27 °C	2.26×10^{-4} at 27 °C	0.39 (27–200 °C)	[148]
Li _{6.4} La ₃ Zr _{1.4} Ta _{0.6} O ₁₂	1140 °C, 16 h	<i>la3d</i>	–	–	1.02×10^{-3} at RT	–	[149]
Li _{6.5} La ₃ Ta _{0.5} Zr _{1.5} O ₁₂ 0 mol.% excess Li	1140 °C, 16 h	<i>la3d</i>	–	–	2.48×10^{-6} at RT	–	[150]
Li _{6.5} La ₃ Ta _{0.5} Zr _{1.5} O ₁₂ 10 mol.% excess Li	1140 °C, 16 h	<i>la3d</i>	–	–	1.06×10^{-5} at RT	–	[150]
Li _{6.5} La ₃ Ta _{0.5} Zr _{1.5} O ₁₂ 20 mol.% excess Li	1140 °C, 16 h	<i>la3d</i>	–	–	1.81×10^{-4} at RT	–	[150]
Li _{6.5} La ₃ Ta _{0.5} Zr _{1.5} O ₁₂ 30 mol.% excess Li	1140 °C, 16 h	<i>la3d</i>	–	–	4.33×10^{-4} at RT	–	[150]
Li _{6.5} La ₃ Ta _{0.5} Zr _{1.5} O ₁₂ 40 mol.% excess Li	1140 °C, 16 h	<i>la3d</i>	–	–	3.72×10^{-4} at RT	–	[150]
Li _{6.5} La ₃ Ta _{0.5} Zr _{1.5} O ₁₂ 50 mol.% excess Li	1140 °C, 16 h	<i>la3d</i>	–	–	3.66×10^{-4} at RT	–	[150]
Li _{6.75} La ₃ Zr _{1.75} Ta _{0.25} O ₁₂	1100 °C, 15 h	<i>la3d</i>	–	–	4.1×10^{-4} at 27 °C	0.42 (27–130 °C)	[151]
Li _{6.5} La ₃ Zr _{1.5} Ta _{0.5} O ₁₂	1100 °C, 15 h	<i>la3d</i>	–	–	6.1×10^{-4} at 27 °C	0.40 (27–130 °C)	[151]
Li ₆ La ₃ ZrTaO ₁₂	1100 °C, 15 h	<i>la3d</i>	–	–	2.1×10^{-4} at 27 °C	0.42 (27–130 °C)	[151]
Li _{6.75} La ₃ Zr _{1.75} Ta _{0.25} O ₁₂ (in Oxygen)	1140 °C, 9 h	<i>la3d</i>	12.964	–	7.4×10^{-4} at 25 °C	0.33	[152]
Li _{6.75} La ₃ Zr _{1.75} Ta _{0.25} O ₁₂ (in Air)	1140 °C, 9 h	<i>la3d</i>	12.963	–	2.4×10^{-4} at 25 °C	0.39	[152]
Li _{6.75} La ₃ Zr _{1.75} Ta _{0.25} O ₁₂ (in Nitrogen)	1140 °C, 9 h	<i>la3d</i>	12.963	–	2.1×10^{-4} at 25 °C	0.43	[152]
Li _{6.75} La ₃ Zr _{1.75} Ta _{0.25} O ₁₂ (in argon)	1140 °C, 9 h	<i>la3d</i>	12.962	–	1.8×10^{-4} at 25 °C	0.44	[152]
Li ₆ La ₃ Nb _{1.5} Sc _{0.5} O ₁₂	1150 °C, 12 h	<i>la3d</i>	~12.827	3.55×10^{-4} at 25 °C	1.02×10^{-4} at 25 °C	0.40 (25–200 °C)	[124]
Li _{6.25} La ₃ Nb _{1.375} Sc _{0.625} O ₁₂	1150 °C, 12 h	<i>la3d</i>	~12.832	3.70×10^{-4} at 25 °C	1.38×10^{-4} at 25 °C	0.36 (25–200 °C)	[124]
Li _{6.5} La ₃ Nb _{1.25} Sc _{0.75} O ₁₂	1150 °C, 12 h	<i>la3d</i>	12.844 (6)	3.19×10^{-4} at 25 °C	1.26×10^{-4} at 25 °C	0.39 (25–200 °C)	[124]
Li ₆ La ₃ Ta _{1.5} Y _{0.5} O ₁₂	1100 °C, 6 h	<i>la3d</i>	12.937 (1)	–	1.26×10^{-4} at 23 °C	0.55 (-50 to 50 °C)	[126]
Li _{6.5} La ₃ Ta _{1.25} Y _{0.75} O ₁₂	1100 °C, 6 h	<i>la3d</i>	12.964 (2)	–	1.83×10^{-4} at 23 °C	0.36 (-50 to 50 °C)	[126]
Li _{6.8} La ₃ Zr _{1.8} Ta _{0.2} O ₁₂	1200 °C, 24 h	<i>la3d</i>	–	2.2×10^{-6} at 33 °C	1.1×10^{-6} at 33 °C	E _{a(t)} = 0.55 (33–240 °C)	[153]
Li _{6.6} La ₃ Zr _{1.6} Ta _{0.4} O ₁₂	1200 °C, 24 h	<i>la3d</i>	–	1.5×10^{-4} at 33 °C	1.1×10^{-4} at 33 °C	E _{a(t)} = 0.41 (33–240 °C)	[153]
Li _{6.4} La ₃ Zr _{1.4} Ta _{0.6} O ₁₂	1200 °C, 24 h	<i>la3d</i>	–	2.3×10^{-4} at 33 °C	1.5×10^{-4} at 33 °C	E _{a(t)} = 0.40 (33–240 °C)	[153]
Li _{6.2} La ₃ Zr _{1.2} Ta _{0.8} O ₁₂	1200 °C, 24 h	<i>la3d</i>	–	4.9×10^{-6} at 33 °C	2.3×10^{-6} at 33 °C	E _{a(t)} = 0.53 (33–240 °C)	[153]
Li _{6.4} La ₃ Zr _{1.4} Ta _{0.6} O ₁₂ + 0.5 wt.% Li ₄ SiO ₄	1200 °C, 24 h	<i>la3d</i>	–	4.0×10^{-4} at 33 °C	2.5×10^{-4} at 33 °C	E _{a(t)} = 0.37 (33–240 °C)	[153]
Li _{6.4} La ₃ Zr _{1.4} Ta _{0.6} O ₁₂ + 1.0 wt.% Li ₄ SiO ₄	1200 °C, 24 h	<i>la3d</i>	–	4.3×10^{-4} at 33 °C	3.7×10^{-4} at 33 °C	E _{a(t)} = 0.35 (33–240 °C)	[153]
Li _{6.4} La ₃ Zr _{1.4} Ta _{0.6} O ₁₂ + 1.5 wt.% Li ₄ SiO ₄	1200 °C, 24 h	<i>la3d</i>	–	3.5×10^{-4} at 33 °C	2.4×10^{-4} at 33 °C	E _{a(t)} = 0.38 (33–240 °C)	[153]
Li _{6.28} Al _{0.24} La ₃ Zr ₂ O ₁₂	1200 °C, 12 h	<i>la3d</i>	12.9731	–	4.43×10^{-4} at 30 °C	0.37 (30–200 °C)	[154]

(continued on next page)

Table 2.1 (continued)

Composition	Final sintering temp., time	Space group	Lattice parameter (Å)	σ_{bulk} (S cm ⁻¹)	σ_{total} (S cm ⁻¹)	^a Activation energy, E _a (eV)	Ref.
Li _{6.5} La ₃ Zr _{1.5} Ta _{0.5} O ₁₂	1140 °C, 16 h	<i>la</i> $\bar{3}$ <i>d</i>	12.9773	–	–	–	[155]
Li ₆ La ₂ BaTa ₂ O ₁₂	900 °C, 24 h	<i>la</i> $\bar{3}$ <i>d</i>	12.9826	6.2 × 10 ⁻⁵ at 33 °C	5.82 × 10 ⁻⁵ at 33 °C	0.41	[116]
Li _{6.5} La _{1.5} Ba _{1.5} Ta ₂ O ₁₂	900 °C, 24 h	<i>la</i> $\bar{3}$ <i>d</i>	13.0458	6.37 × 10 ⁻⁵ at 33 °C	6.17 × 10 ⁻⁵ at 33 °C	0.40 (33–300 °C)	[116]
Li _{6.25} La ₃ Nb _{1.375} Sc _{0.625} O ₁₂	1150 °C, 12 h	<i>la</i> $\bar{3}$ <i>d</i>	1.28466 (1) as prepared	–	1.02 × 10 ⁻⁴ at 25 °C as prepared	0.428 (–20 to 150 °C) as prepared	[128]
Li _{6.25} La ₃ Nb _{0.75} Zr _{1.25} O ₁₂	1150 °C, 12 h	<i>la</i> $\bar{3}$ <i>d</i>	1.29091 (1) as prepared	–	2.03 × 10 ⁻⁴ at 25 °C as prepared	0.422 (–20 to 150 °C) as prepared	[128]
Li _{6.25} La ₃ Ta _{1.375} Sc _{0.625} O ₁₂	1150 °C, 12 h	<i>la</i> $\bar{3}$ <i>d</i>	1.28533 (1) as prepared	–	0.97 × 10 ⁻⁴ at 25 °C as prepared	0.432 (–20 to 150 °C) as prepared	[128]
Li _{6.25} La ₃ Ta _{0.75} Zr _{1.25} O ₁₂	1150 °C, 12 h	<i>la</i> $\bar{3}$ <i>d</i>	1.29122 (0) as prepared	–	2.72 × 10 ⁻⁴ at 25 °C as prepared	0.407 (–20 to 150 °C) as prepared	[128]
Li _{6.22} Al _{0.26} La ₃ Zr ₂ O ₁₂	1150 °C, 36 h	<i>la</i> $\bar{3}$ <i>d</i>	–	–	1.3 × 10 ⁻⁵ at 25 °C	0.40 (HT)	[129]
Li ₆ La ₃ Ta _{1.5} Y _{0.50} O ₁₂	1100 °C, 6 h	<i>la</i> $\bar{3}$ <i>d</i>	–	–	1.26 × 10 ⁻⁴ at 23 °C	0.37 (23–325 °C)	[130]
Li _{6.5} La ₃ Ta _{1.25} Y _{0.75} O ₁₂	1100 °C, 6 h	<i>la</i> $\bar{3}$ <i>d</i>	–	–	1.83 × 10 ⁻⁴ at 23 °C	0.33 (23–325 °C)	[130]
Li _{6.5} La ₃ Zr _{1.75} W _{0.25} O ₁₂	1200 °C, 12 h	<i>la</i> $\bar{3}$ <i>d</i>	–	–	4.9 × 10 ⁻⁴ at 25 °C	0.42 (25–70 °C)	[131]
Li _{6.3} La ₃ Zr _{1.65} W _{0.35} O ₁₂	1200 °C, 12 h	<i>la</i> $\bar{3}$ <i>d</i>	–	–	6.6 × 10 ⁻⁴ at 25 °C	0.42 (25–70 °C)	[131]
Li _{6.1} La ₃ Zr _{1.55} W _{0.45} O ₁₂	1200 °C, 12 h	<i>la</i> $\bar{3}$ <i>d</i>	–	–	6.4 × 10 ⁻⁴ at 25 °C	0.43 (25–70 °C)	[131]
Li _{6.65} La _{2.75} Ba _{0.25} Zr _{1.4} Ta _{0.5} Nb _{0.1} O ₁₂	1150 °C, 12 h	<i>la</i> $\bar{3}$ <i>d</i>	–	5.27 × 10 ⁻⁴ at 25 °C 1.62 × 10 ⁻³ at 53 °C	–	0.26 (20–300 °C)	[156]
Li _{6.4} La ₃ Zr _{1.4} Ta _{0.6} O ₁₂	1150 °C, 12 h	<i>la</i> $\bar{3}$ <i>d</i>	–	7.24 × 10 ⁻⁴ at 25 °C 1.96 × 10 ⁻³ at 53 °C	–	0.24 (20–300 °C)	[156]
Li _{6.4} La ₃ Zr _{1.4} Ta _{0.5} Nb _{0.1} O ₁₂	1150 °C, 12 h	<i>la</i> $\bar{3}$ <i>d</i>	–	4.44 × 10 ⁻⁴ at 25 °C 1.50 × 10 ⁻³ at 53 °C	–	0.27 (20–300 °C)	[156]
Li _{6.4} La ₃ Zr _{1.4} Ta _{0.4} Nb _{0.2} O ₁₂	1150 °C, 12 h	<i>la</i> $\bar{3}$ <i>d</i>	–	4.55 × 10 ⁻⁴ at 25 °C 1.37 × 10 ⁻³ at 53 °C	–	0.28 (20–300 °C)	[156]
Li _{6.4} La ₃ Zr _{1.4} Ta _{0.3} Nb _{0.3} O ₁₂	1150, 12 h	<i>la</i> $\bar{3}$ <i>d</i>	–	6.06 × 10 ⁻⁴ at 25 °C 1.69 × 10 ⁻³ at 53 °C	–	0.26 (20–300 °C)	[156]
Li _{6.75} La ₃ Nb _{0.25} Zr _{1.75} O ₁₂	1050 °C, 12 h	<i>la</i> $\bar{3}$ <i>d</i>	–	–	2.3 × 10 ⁻⁴	–	[99]
Li _{6.75} La _{2.8} Ga _{0.2} Nb _{0.25} Zr _{1.75} O ₁₂	1050 °C, 12 h	<i>la</i> $\bar{3}$ <i>d</i>	–	–	2.28 × 10 ⁻⁴	–	[99]
Li _{6.75} La ₃ Ta _{0.25} Zr _{1.75} O ₁₂	1050 °C, 12 h	<i>la</i> $\bar{3}$ <i>d</i>	–	–	1.97 × 10 ⁻⁴	–	[99]
Li _{6.75} La _{2.8} Ga _{0.2} Ta _{0.25} Zr _{1.75} O ₁₂	1050 °C, 12 h	<i>la</i> $\bar{3}$ <i>d</i>	–	–	1.64 × 10 ⁻⁴	–	[99]
Li ₅ La ₃ Ta ₂ O ₁₂	900 °C	<i>la</i> $\bar{3}$ <i>d</i>	–	–	0.34 × 10 ⁻⁴ at RT	–	[104]
Li ₇ La ₃ Zr ₂ O ₁₂	1230 °C, 36 h	<i>la</i> $\bar{3}$ <i>d</i>	12.9682 (6)	5.11 × 10 ⁻⁴ at 25 °C	7.74 × 10 ⁻⁴ at 25 °C	E _{a(b)} = 0.32 (18–50 °C) E _{a(t)} = 0.30 (18–300 °C)	[97,98]
Li ₇ BaLa ₂ Ta ₂ O _{12.5}	900 °C, 24 h	<i>la</i> $\bar{3}$ <i>d</i>	~12.946	1.01 × 10 ⁻⁴ at 50 °C	9.70 × 10 ⁻⁵ at 50 °C	~0.45 (17–350 °C)	[120]
Li ₇ La ₃ Sn ₂ O ₁₂	900 °C, 12 h	14 ₁ / <i>acd</i>	a = b = 13.1206 (1) c = 12.5467 (1)	–	–	0.79	[112]
Li ₇ La ₃ Zr ₂ O ₁₂	980 °C, 5 h	14 ₁ / <i>acd</i>	a = 13.134 (4) c = 12.663 (8)	1.63 × 10 ⁻⁶ at 27 °C	–	0.54 (27–287 °C)	[157]
Li ₇ La ₃ Ta ₂ O ₁₂	900 °C, 24 h	<i>la</i> $\bar{3}$ <i>d</i>	–	3.3 × 10 ⁻⁶ at 27 °C	2.2 × 10 ⁻⁶ at 27 °C	0.38	[158]
Li ₇ La ₃ Hf ₂ O ₁₂	980 °C, 5 h	14 ₁ / <i>acd</i>	a = 13.106 (2) c = 12.630 (2)	9.85 × 10 ⁻⁷ at 27 °C	–	0.53 (27–307 °C)	[159]
Li ₇ La ₃ Hf ₂ O ₁₂	1250 °C, 36 h	<i>la</i> $\bar{3}$ <i>d</i>	12.938 (1)	2.4 × 10 ⁻⁴ at 25 °C	–	0.29 (RT to 175 °C)	[113]
Li ₇ La ₃ Zr ₂ O ₁₂	1230 °C, 36 h	<i>la</i> $\bar{3}$ <i>d</i>	–	1.8 × 10 ⁻⁴ at 25 °C	–	–	[160]
Li _{7.06} La ₃ Y _{0.06} Zr _{1.94} O ₁₂	1200 °C, 16 h	<i>la</i> $\bar{3}$ <i>d</i>	12.9672	9.56 × 10 ⁻⁴ at 25 °C	8.10 × 10 ⁻⁴ at 25 °C	E _{a(b)} = 0.29, E _{a(t)} = 0.26	[105]
Li ₇ La ₃ Zr ₂ O ₁₂	1230 °C, 30 h	<i>la</i> $\bar{3}$ <i>d</i>	12.9727 (2)	–	4 × 10 ⁻⁴ at 25 °C	0.34	[161]

Table 2.1 (continued)

Composition	Final sintering temp., time	Space group	Lattice parameter (Å)	σ_{bulk} (S cm ⁻¹)	σ_{total} (S cm ⁻¹)	^a Activation energy, E_a (eV)	Ref.
		<i>la3d</i>					
Li ₇ La ₃ Zr ₂ O ₁₂	1130 °C, 12 h	<i>I4₁/acd</i>	–	–	2×10^{-6} at 25 °C	0.49	[161]
Ge-doped Li ₇ La ₃ Zr ₂ O ₁₂	1200 °C, 20 h	<i>la3d</i>	–	–	7.63×10^{-4} at 25 °C	–	[110]
Li ₇ La ₃ Zr ₂ O ₁₂	1230 °C, 8 h	<i>la3d</i>	12.8974	–	1.6×10^{-4} at RT	–	[162]
Li ₇ La ₃ Zr ₂ O ₁₂ 0.204 mol Al	1000 °C, 4 h	<i>la3d</i>	–	–	4×10^{-4} at RT	0.26	[100]
Li ₇ La ₃ Zr ₂ O ₁₂ (28 mol.% Al)	1230 °C, 36 h	<i>la3d</i>	12.9727	–	3.5×10^{-4} at 25 °C	0.36	[103]
Li ₇ La ₃ Zr ₂ O ₁₂	1250 °C, 8 h	<i>I4₁/acd</i>	–	2.09×10^{-6} at 20 °C	1.3×10^{-6} at 20 °C	~0.46	[163]
Li ₇ La ₃ Zr ₂ O ₁₂ (1.7 wt.% Sr)	1200 °C, 20–24 h	<i>la3d</i>	12.980	–	5×10^{-4} at 24 °C	0.31 (–10 to 60 °C)	[164]
Li ₇ La ₃ Ta ₂ O ₁₃	900 °C, 24 h	<i>la3d</i>	12.830 (4)	3.21×10^{-6} at 40 °C	–	0.55	[165]
Li ₇ Nd ₃ Zr ₂ O ₁₂	850 °C, 12 h	<i>I4₁/acd</i>	a = 12.9471 c = 12.5512	–	–	0.66 (100–400 °C)	[166]
Li _{7.06} La ₃ Zr _{1.94} Y _{0.06} O ₁₂	950 °C, 12 h	<i>la3d</i>	12.974 (3)	10^{-6} at 23 °C	–	0.47	[167]
Li _{7.16} La ₃ Zr _{1.84} Y _{0.16} O ₁₂	950 °C, 12 h	<i>la3d</i>	12.995 (2)	10^{-6} at 23 °C	–	0.47	[167]
Li ₇ La ₃ Zr ₂ O ₁₂	1000 °C, 4 h and hot pressed at 1050 °C 1 h	<i>I4₁/acd</i>	a = b = 13.0682, c = 12.70201	–	5.77×10^{-6}	0.40 (25–100 °C)	[109]
Li ₇ La ₃ Nb ₂ ScO ₁₂	1150 °C, 12 h	<i>la3d</i>	~12.846	1.42×10^{-4} at 25 °C	0.68×10^{-4} at 25 °C	0.40 (25–200 °C)	[124]
Li ₇ La ₃ Zr ₂ O ₁₂	1230 °C, 6 h	<i>la3d</i>	1.29544	1.81×10^{-4} at 30 °C	1.19×10^{-4} at 30 °C	0.41 (–60 to 60 °C)	[147]
Li ₇ La ₃ Zr ₂ O ₁₂	1200 °C, 24 h	<i>I4₁/acd</i>	–	–	9.9×10^{-6} at 27 °C	0.43 (27–130 °C)	[151]
Li ₇ La ₃ Zr ₂ O ₁₂	1200 °C, 12 h	<i>I4₁/acd</i>	–	–	1.7×10^{-5} at 25 °C	0.47 (25–70 °C)	[131]
Li ₇ La ₃ Zr ₂ O ₁₂ 1.0 wt.%. LiF	1230 °C, 36 h	<i>la3d</i>	–	–	5×10^{-4} at RT	0.26 (25–150 °C)	[168]
Li ₇ La ₃ Zr ₂ O ₁₂ 1.5 wt.%. CaF ₂	1230 °C, 36 h	<i>la3d</i>	–	–	5×10^{-5} at RT	–	[168]
Li ₇ La ₃ Zr ₂ O ₁₂ 2 wt.%. Al ₂ O ₃	1230 °C, 36 h	<i>la3d</i>	–	–	2×10^{-4} at RT	–	[168]
Li ₇ La ₃ Zr ₂ O ₁₂	1175 °C, 12 h	<i>la3d</i>	–	1.74×10^{-4} at 25 °C 0.41×10^{-3} at 53 °C	–	0.26 (20–300 °C)	[156]

$E_{a(b)}$ -activation energy for bulk Li⁺ conductivity.

$E_{a(t)}$ -activation energy for total (bulk + grain-boundary) Li⁺ conductivity.

HT-High temperature.

LT-Low temperature.

^a Activation energy for total (bulk + grain-boundary) Li⁺ conductivity unless specified.

Though solid-state reaction method is a simple synthesis technique, it has a lot of disadvantages too. The high sintering temperature and long exposure of heating result in possible evaporation of lithium from the product structure. Moreover, it is also difficult to control the chemical stoichiometry of the lithium garnets through solid-state synthesis due to the volatile nature of lithium at high temperature sintering. Another major issue of solid-state reaction method is the inhomogeneity in the end product and formation of impure phases. Hence, various efforts had been made to prepare the lithium garnets at lower sintering temperature by simple wet chemical synthesis techniques.

The composition and microstructure of the pellets play an important role in influencing the ionic conductivity, relative density, and air stability of lithium garnets. Jin et al. showed that the grain-boundaries are high interfacial energy regions for the reactions between LLZO and moisture, thereby decreases the total conductivity of LLZO after one-week air exposure [169]. Cheng et al. pointed that Al-LLZO in contact with air forms Li_2CO_3 layer on the LLZO surface resulting in a drastic increase of the interfacial resistance. One possible approach to overcome this issue is surface polishing on LLZO that removes Li_2CO_3 and substantially decrease the interfacial impedance [170].

Xia et al., reported that the 0.25Al-LLZO pellets sintered in Pt crucibles exhibit high relative density ($\sim 96\%$), high ionic conductivity ($4.48 \times 10^{-4} \text{ S cm}^{-1}$), and good stability in ambient air [171]. In contrast, the pellets prepared using Al_2O_3 crucibles exhibit relatively lesser conductivity and poor stability in ambient air. The increased ionic conductivity is associated with the controlled amount of Al dopant and the desirable amount of Li content in the LLZO samples. The pellets sintered in Pt crucibles have higher relative density, larger grains and less grain boundaries than in alumina crucibles, which provide less high interfacial energy regions for the reactions between LLZO and water, CO_2 in the air to form Li_2CO_3 [171]. Hence preparation of phase pure (optimized composition), dense, larger grains and less grain boundaries LLZO is essential, which is possible through careful control of the processing variables. The schematic representation of LLZO pellet sintered using Pt and Al crucibles and the effect of ionic conductivity with respect to time are shown as Fig. 2.1(a) and (b). Moreover, the XPS spectra as shown in Fig. 2.1(c) of the pellets sintered using Pt and Al crucibles indicates that area ratio of Li_2CO_3 to Li-O is much less, suggesting less Li_2CO_3 formation in case of Pt crucible [171].

Recently, Cheng et al., reported the effects of grain size and surface composition on the air-stability of LLZO pellets by soft X-ray absorption and Raman spectroscopy, and suggested that LLZO with small grains and large amount of grain boundaries was more air stable [172,173].

2.2. Wet chemical techniques

The wet chemical process begins with liquid precursors, so provides molecular level mixing of the components [174,175]. Hence, the precursors can react relatively at lower temperatures and in shorter times, without the need for intermittent grinding, and this synthesis route typically yields finer powders with a more uniform size distribution [176]. The powder obtained from the wet chemical method generally expected to show better performance due to their higher homogeneity in composition, finer crystal size, higher purity and surface area.

2.2.1. Sol-gel method

Sol-gel technique follows the route line of hydrolysis and polymerization to form amorphous or crystalline material at low temperature processing in solution state. Preparation of various garnet structured electrolyte materials have been reported using sol gel synthesis technique.

Preparation of nanocrystalline cubic phase lithium garnets $\text{Li}_5\text{La}_3\text{Ta}_2\text{O}_{12}$ and $\text{Li}_5\text{La}_3\text{Bi}_2\text{O}_{12}$ through sol-gel method by sintering the gels at 700°C and 650°C , respectively, were first reported by Gao et al. [177,178]. Shimonishi et al. reported the preparation of $\text{Li}_6\text{La}_3\text{Zr}_2\text{O}_{11.5}$ in cubic phase and $\text{Li}_7\text{La}_3\text{Zr}_2\text{O}_{12}$ in tetragonal phase by sintering the gels at 1180°C and 800°C , respectively [175]. Kokal et al. reported the preparation of LLZO in cubic phase at 700°C by sol-gel method and also they reported the cubic to tetragonal modification at 724°C [174]. Janani et al. synthesized polycrystalline cubic phase $\text{Li}_7\text{La}_3\text{Zr}_2\text{O}_{12}$ (LLZO) at 700°C by modified sol-gel processes using citric acid as organic complexing agent and butan-1-ol or propan-2-ol as surface active agent [179]. Janani et al. also reported the preparation of LLZO and high Li^+ conductive 0.9 wt.% of Al doped LLZO i.e., $\text{Li}_{6.16}\text{Al}_{0.28}\text{La}_3\text{Zr}_2\text{O}_{12}$ (Al-LLZO) in cubic phase by modified sol-gel technique [176]. The flow chart utilized for the preparation of LLZO and high Li^+ conductive 0.9 wt.% of Al doped LLZO i.e., $\text{Li}_{6.16}\text{Al}_{0.28}\text{La}_3\text{Zr}_2\text{O}_{12}$ (Al-LLZO) in cubic phase using modified sol-gel technique by Janani et al. [176] is shown in Fig. 2.2.

2.2.2. Pechini method

Pechini process is based on the ability of carboxylic acids (citric acid, tartaric acid, polyacrylic acid, etc.) to chelate the various metal ions. These metal carboxylates can undergo polyesterification when, heated with polyhydroxy alcohol (ethylene glycol, glycerol, polyvinyl alcohol, etc.) and lead to the formation of polymeric resin, with three dimensional network. The cations are uniformly distributed throughout polymeric resin, which inhibits the precipitation. Further, the calcination of dried resin yields ultra fine oxide powders at very low temperature. The product formed is highly homogeneous with reduced particle size. Jin et al. reported the stabilization of cubic phase LLZO by the incorporation of different amounts of Al (0, 0.2, 0.7, 1.2, and 2.5 wt.%) through a polymerized complex (Pechini) method [180]. Moreover, even small amounts of Al (e.g., 0.2 wt.%) greatly increased the density of LLZO pellets after sintering. SEM observations of Al-doped pellets verified the existence of a liquid phase. Dilatometry showed pellet densification accelerated around 1055°C suggested the formation

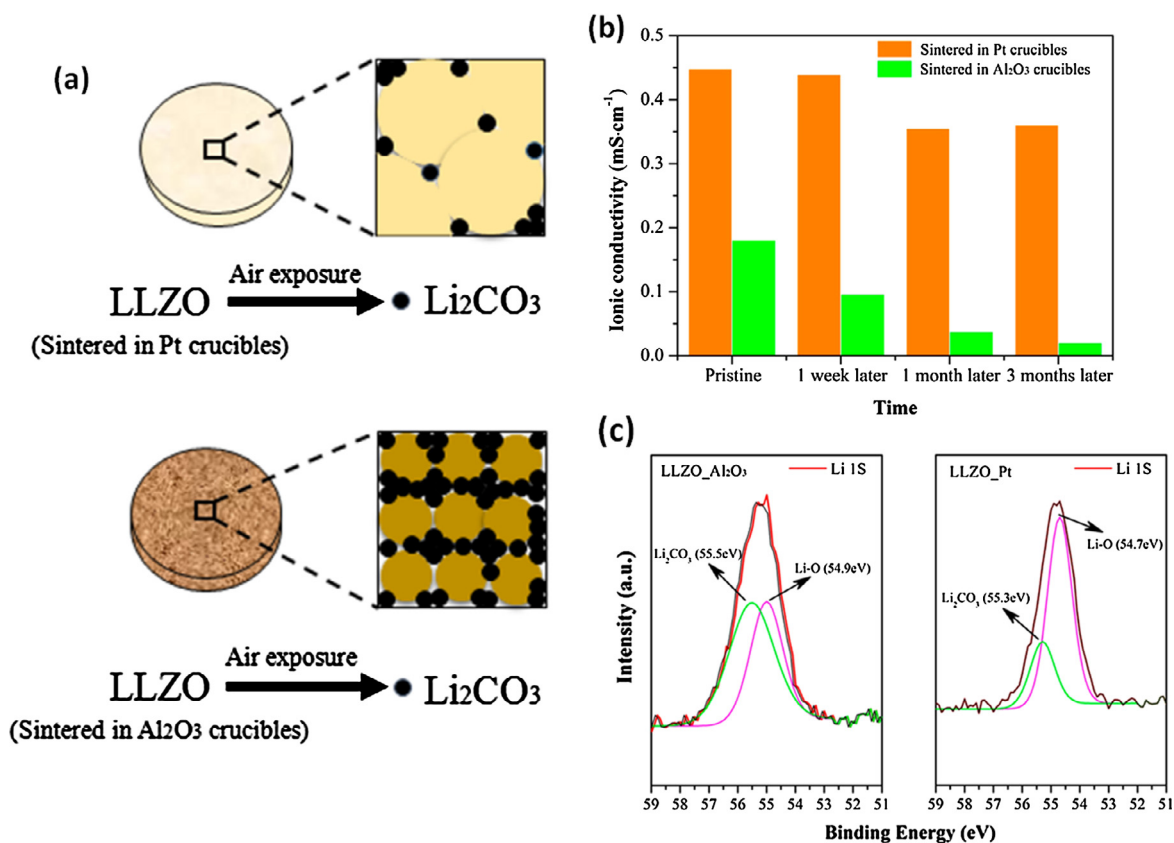


Fig. 2.1. (a) A schematic depicting LLZO pellets sintered using Pt and Alumina crucibles (b) shows the variation of ionic conductivity of the pellets as a function of time. (c) The XPS spectra of the pellets sintered using Alumina/Pt crucibles [171].

of a Li₂O–Al₂O₃ eutectic. With optimal additions of Al (e.g., 1.2 wt.%), LLZO electrolyte sintered at 1200 °C for only 6 h showed Li⁺ conductivity of 2.0×10^{-4} S cm⁻¹ at room temperature [180].

2.2.3. Combustion method

Solution combustion is a novel technique based on the gelling and subsequent combustion of an aqueous solution containing salts of the desired metals and organic fuel giving a voluminous and fluffy product with large surface area. Li₇La₃Zr₂O₁₂ (LLZO) and Li_{6.28}Al_{0.24}La₃Zr₂O₁₂ (Al-LLZO) lithium garnets were successfully prepared in shorter duration of time by simple combustion technique [181]. Three factors were considered by Dhivya et al. to find the optimal condition to derive the high Li⁺ conductive cubic phase LLZO and Al-LLZO: amount of excess lithium source, the synthesis temperature and the sintering time [181]. Fig. 2.3 shows the schematic representation for the synthesis of high Li⁺ conductive cubic phase (*Ia* $\bar{3}$ d) Al-LLZO by simple combustion technique. High Li⁺ conductive cubic phase (*Ia* $\bar{3}$ d) was derived for the Al-LLZO prepared with 10 wt.% excess lithium source (Al-LLZO-10), relatively at lower sintering temperature of 950 °C. Al-LLZO-10 sintered at 1200 °C for just 6 h exhibited maximized relative density of 95% and total (bulk + grain-boundary) Li⁺ conductivity of 5.1×10^{-4} S cm⁻¹ at 30 °C with particle size of around 613 nm [181].

Afyon et al. reported a novel low temperature synthesis processing route for cubic phase Li_{6.4}Ga_{0.2}La₃Zr₂O₁₂ through which the synthesis-sintering temperature is decreased by ~200 °C [182]. The tetragonal phase of Li₇La₃Zr₂O₁₂ was synthesized by a modified sol-gel – combustion method at a temperature of ~600 °C, one of the lowest reported for Li₇La₃Zr₂O₁₂ garnet-type fast Li-ion conductor [182]. Post-synthetic Ga-doping was shown to induce a phase transformation to the cubic phase at a very low temperature of ~100 °C. AC impedance measurements revealed high bulk Li-ionic conductivities in the range of $\sim 4.0 \times 10^{-4}$ S cm⁻¹ at 20 °C for the cubic phase Li_{6.4}Ga_{0.2}La₃Zr₂O₁₂ pellets processed at a rather low temperature of 950 °C for 6 h. Higher processing temperatures (~1100 °C) lead to Li-loss, substantial decrease in Li⁺ conduction and relative density [182].

2.2.4. Chemical co-precipitation method

Chemical co-precipitation method has many advantages, such as being a simple process, molecular level mixing and creating fine precursor powder. Shao et al. synthesized LLZO solid electrolyte powder by chemical co-precipitation method [183]. The LLZO powder calcined at 850 °C was in tetragonal phase confirmed by X-ray diffraction (XRD). Scanning electron

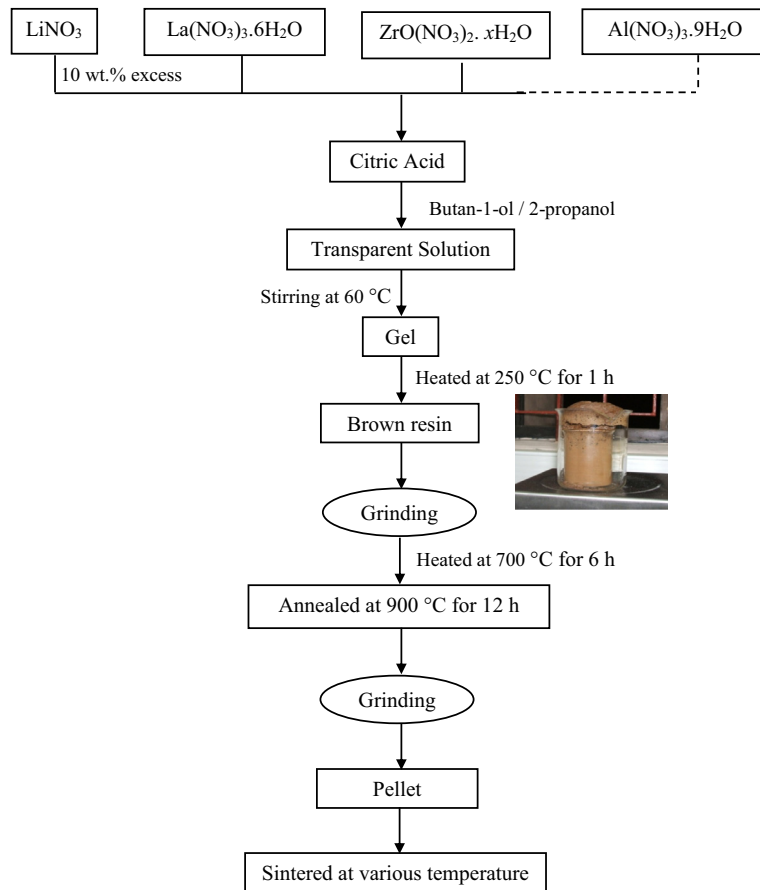


Fig. 2.2. Flow diagram for the preparation of LLZO and Al-LLZO using modified sol-gel technique [176].

microscopy (SEM) showed that the particles sizes of LLZO precursor powder were in the range of 0.5–1 μm . Tetragonal LLZO completely transformed into cubic phase at the temperature above 1150 $^{\circ}\text{C}$. The total ionic conductivity of LLZO pellet sintered at 1180 $^{\circ}\text{C}$ was $2.0 \times 10^{-4} \text{ S cm}^{-1}$ at 30 $^{\circ}\text{C}$, and the activation energy was 0.25 eV [183].

The sintering temperature, space group, lattice parameter, bulk Li^+ conductivity (σ_{bulk}), total (bulk + grain-boundary) Li^+ conductivity (σ_{total}) and activation energy (E_a) of various lithium garnets prepared via., sol-gel, pechni and combustion techniques are provided as Table 2.2 [174–183].

The composition and microstructure play an important role in influencing the ionic conductivity, relative density, and air stability of lithium garnets. The pellets with higher relative density, larger grains and less grain-boundary provide less high interfacial energy regions for the reactions between lithium garnet phase and water, CO_2 in the air to form Li_2CO_3 . Hence preparation of phase pure (optimized composition), dense, larger grains and less grain boundaries lithium garnets is essential, which is possible through careful control of the processing variables.

2.3. Growth of single crystal

The first attempt to investigate the crystal structure of $\text{Li}_5\text{La}_3\text{M}_2\text{O}_{12}$ ($\text{M} = \text{Nb}, \text{Ta}$) using transparent single crystal with approximate dimension of $0.2 \times 0.2 \times 0.2 \text{ mm}^3$ was put forward by Hyooma et al. [95]. In 2009, Roof et al. [184] reported the single crystals of a series of garnet like structure lanthanum containing tantalates with nominal formula $\text{Ln}_3\text{Li}_5\text{Ta}_2\text{O}_{12}$ ($\text{Ln} = \text{La}, \text{Pr}, \text{Nd}$) using molten alkali metal hydroxides fluxes. They used the technique of loading the starting materials Ta_2O_5 , Ln_2O_3 , $\text{LiOH}\cdot x\text{H}_2\text{O}$, lanthanide sesquioxides on a silver tube. Sintering was done at 600 $^{\circ}\text{C}$ for 24 h followed by subsequent natural cooling of the furnace. Colorless, yellow and blue single crystals of $\text{La}_3\text{Li}_5\text{Ta}_2\text{O}_{12}$, $\text{Pr}_3\text{Li}_5\text{Ta}_2\text{O}_{12}$ and $\text{Nd}_3\text{Li}_5\text{Ta}_2\text{O}_{12}$, respectively, were isolated by vacuum filtration. It was suggested that hydroxide fluxes are an excellent medium for the dissolution of lanthanide oxides, late transition metals such as iridium, ruthenium and transition metal oxides such as niobium and tantalum oxide. An interesting phenomenon observed in $\text{Li}_5\text{Nd}_3\text{Ta}_2\text{O}_{12}$ is the Alexandrite effect, where the specimen changes color as a function of the light source used for illumination [185].

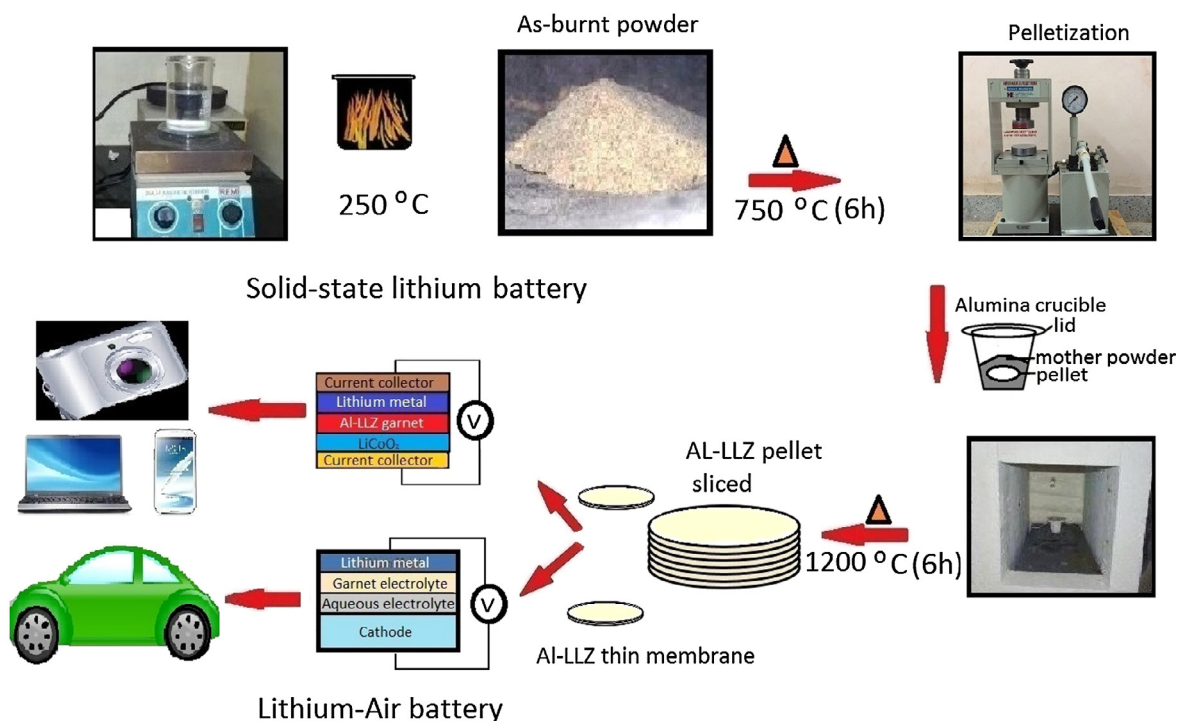


Fig. 2.3. Schematic representation for the synthesis of high Li^+ conductive cubic phase ($Ia\bar{3}d$) Al-LLZO through simple combustion technique [181].

Table 2.2

The sintering temperature, space group, lattice parameter, bulk Li^+ conductivity (σ_{bulk}), total (bulk + grain-boundary) Li^+ conductivity (σ_{total}) and activation energy (E_a) of various lithium garnets prepared via, sol-gel, pechni and combustion techniques.

Composition	Synthesis method	Final sintering temp. & time	Space group	Lattice parameter (Å)	σ_{bulk} (S cm^{-1})	σ_{total} (S cm^{-1})	^a Activation energy, E_a (eV)	Ref.
$\text{Li}_7\text{La}_3\text{Zr}_2\text{O}_{12}$	Sol-gel Pechni	700 °C, 5 h	$Ia\bar{3}d$	13.002 (1)	–	–	–	[174]
$\text{Li}_7\text{La}_3\text{Zr}_2\text{O}_{12}$	Sol-gel Pechni	800 °C, 5 h	$I4_1/acd$	13.122 (3) 12.672 (3)	–	3.12×10^{-7} at 25 °C	0.67 (17–80 °C)	[174]
$\text{Li}_6\text{La}_3\text{Zr}_2\text{O}_{11.5}$	Sol-gel	1180 °C, 36 h	$Ia\bar{3}d$	–	5.69×10^{-4} at 25 °C	1.39×10^{-4} at 25 °C	–	[175]
$\text{Li}_{6.16}\text{Al}_{0.28}\text{La}_3\text{Zr}_2\text{O}_{12}$ (Al-LLZO)	Sol-gel	900 °C, 36 h	$I4_1/acd$	–	–	3×10^{-7} at 33 °C	–	[176]
$\text{Li}_{6.16}\text{Al}_{0.28}\text{La}_3\text{Zr}_2\text{O}_{12}$ (Al-LLZO)	Sol-gel	1200 °C, 12 h	$Ia\bar{3}d$	–	2.1×10^{-4} at 33 °C	1.1×10^{-4} at 33 °C	0.38 (33–240 °C)	[176]
$\text{Li}_5\text{La}_3\text{Ta}_2\text{O}_{12}$	Sol-gel	900 °C, 5 h	$Ia\bar{3}d$	–	–	1.54×10^{-6} at 25 °C	0.57	[177]
$\text{Li}_5\text{La}_3\text{Bi}_2\text{O}_{12}$	Pechni	650 °C, 5 h	$Ia\bar{3}d$	13.06 (6)	–	2.4×10^{-5} at 26 °C	0.40	[178]
$\text{Li}_7\text{La}_3\text{Zr}_2\text{O}_{12}$	Sol-gel	700 °C, 12 h	$Ia\bar{3}d$	–	–	–	–	[179]
1.2 wt.% Al doped $\text{Li}_7\text{La}_3\text{Zr}_2\text{O}_{12}$	Pechni	1200 °C, 6 h	$Ia\bar{3}d$	–	–	2.0×10^{-4} at 25 °C	–	[180]
$\text{Li}_{6.28}\text{Al}_{0.24}\text{La}_3\text{Zr}_2\text{O}_{12}$ (Al-LLZO) with 10 wt.% excess Li	Combustion	1200 °C, 6 h	$Ia\bar{3}d$	12.9767 (1)	–	5.1×10^{-4} at 30 °C	0.29 (30–200 °C)	[181]
$\text{Li}_{6.4}\text{Ga}_{0.2}\text{La}_3\text{Zr}_2\text{O}_{12}$	Modified sol-gel combustion	950 °C, 6 h	–	–	4.0×10^{-4} at 20 °C	0.24×10^{-4}	0.32	[182]
$\text{Li}_7\text{La}_3\text{Zr}_2\text{O}_{12}$	Chemical co-precipitation method	1180 °C, 20 h	$Ia\bar{3}d$	–	–	2.0×10^{-4} at 30 °C	0.25 (15–90 °C)	[183]

^a Activation energy for total (bulk + grain-boundary) Li^+ conductivity.

Recently, Xiao et al. [186] developed a unique simple low temperature growth mode for the growth of $\text{Li}_5\text{La}_3\text{Ta}_2\text{O}_{12}$ crystals from lithium hydroxide flux. The growth of $\text{Li}_5\text{La}_3\text{Ta}_2\text{O}_{12}$ single crystals was independent of the cooling rate, but was affected by kind of flux and solute concentration. It was observed that a low solute concentration (1 or 5 mol.%) was the

key to obtain well-dispersed and idiomorphic single crystals. The optimum growth conditions involved a holding temperature of 500 °C, a solute concentration of 1 or 5 mol.%, and a holding time of 10 h, for the formation and growth of $\text{Li}_5\text{La}_3\text{Ta}_2\text{O}_{12}$ single crystals as shown in Fig. 2.4.

Awaka et al. [157] in 2009 succeeded in synthesizing tetragonal phase transparent $\text{Li}_7\text{La}_3\text{Zr}_2\text{O}_{12}$ single crystals by a flux method. Li_2CO_3 was chosen as the flux in the synthesis. As prepared $\text{Li}_7\text{La}_3\text{Zr}_2\text{O}_{12}$ and Li_2CO_3 well-mixed in the nominal weight ratio 1:1, transferred into a gold crucible was sintered at temperatures elevating to 1040 °C at the rate of 200 °C/h, fixing hold time as 48 h. Finally the gold crucible was immersed in hot water so as to separate the crystals from the solidified melts. Fig. 2.5. shows the typical SEM image of grown transparent single-crystal tetragonal phase $\text{Li}_7\text{La}_3\text{Zr}_2\text{O}_{12}$.

Another attempt was made in 2010 by Awaka et al. [187] to prepare cubic phase $\text{Li}_7\text{La}_3\text{Zr}_2\text{O}_{12}$ single crystals. The starting materials Li_2CO_3 : La_2O_3 : ZrO_2 were mixed in a molar ratio of 3.85:1.5:2.0, respectively. Upon sintering the mixture at 1250 °C, spherical shaped transparent and colorless crystals approximately with 0.05 mm diameter were obtained.

Later in 2011, Geiger et al. [188] put forth an effort to obtain $\text{Li}_7\text{La}_3\text{Zr}_2\text{O}_{12}$ single crystals by solid-state sintering, flux-based (molten Li-borates) and hydrothermal experiments at elevated pressures [188]. The ZrO_2 (99% Aldrich), La_2O_3 (99.99% Chempur), and Li_2CO_3 (99% Alfa) were mixed in stoichiometric proportions to give $\text{Li}_7\text{La}_3\text{Zr}_2\text{O}_{12}$ with 5 wt.% extra Li_2CO_3 and were pressed to pellets, which was then sintered at 800 °C. The obtained reaction product was ground and seeded with small amounts of already prepared fine-grained $\text{Li}_7\text{La}_3\text{Zr}_2\text{O}_{12}$. The dense pressed pellets were welded into Pt(Pd)/Au capsule then sintered at temperatures of 900–1100 °C. A number of crystals were analyzed by X-ray methods to investigate the nature of the crystals. Most were found to be single and some polycrystalline. The microprobe analysis revealed the presence of measurable amounts of Al_2O_3 (ca. 1.3 wt.%) that had emanated from the Al_2O_3 in the ceramic crucibles used for the preparation and synthesis of LLZO single crystal [188]. The backscattered X-ray images also showed the presence of small amount of Al in the form of LaAlO_3 as well as La_3O_6 , which was found as very tiny grains between the garnet crystals. The heterovalent substitution of 3Li^+ by Al^{3+} in LLZO garnet could stabilize the cubic phase of LLZO relative to the tetragonal structure. Moreover, Al substitution aided in reducing the Li site occupancies, thereby increasing the number of empty structural sites which enhanced the Li^+ mobility and thus conductivity [188].

2.4. Thin film processing techniques

In parallel to the synthesis of bulk ceramic electrolytes, effort has also been made for the preparation of thin film electrolytes, which is critical for the thin film lithium batteries used in the microelectronic devices. Thin film fabrication of garnet-type oxides have been explored by radio-frequency (RF) sputtering, pulsed laser deposition (PLD), metal-organic chemical vapor deposition (MOCVD) and sol-gel techniques.

2.4.1. Radio-frequency (RF) magnetron sputtering

As compared with other fabrication methods, radio-frequency (RF) magnetron sputtering is considered to be an easy, established process of deposition which can be easily controlled. Kalita et al. reported the lithium–lanthanum–zirconium–oxide (Li–La–Zr–O) thin films deposited using radio-frequency (RF) magnetron sputtering by varying the RF power [189]. The X-ray diffraction (XRD) studies on the films deposited at room temperature indicated the amorphous nature

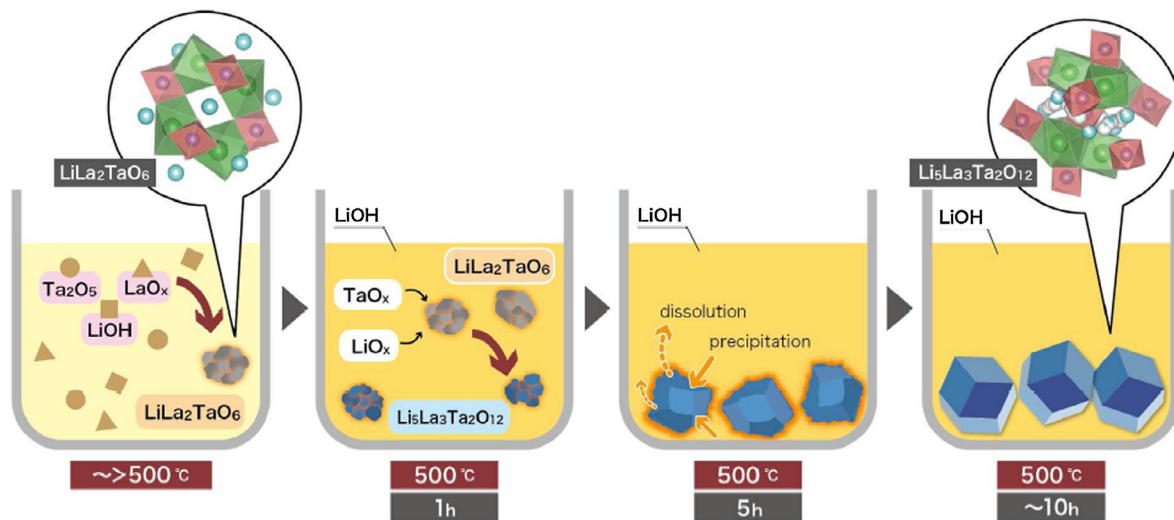


Fig. 2.4. Schematic representation of the formation manner of idiomorphic $\text{Li}_5\text{La}_3\text{Ta}_2\text{O}_{12}$ single crystal from LiOH flux. Temperature: 500 °C, solute conc.: 5 mol.% [186].

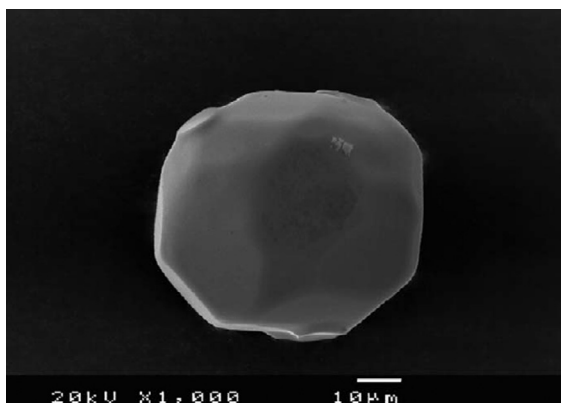


Fig. 2.5. SEM micrograph of a single-crystal tetragonal phase $\text{Li}_7\text{La}_3\text{Zr}_2\text{O}_{12}$ [157].

and they also reported that the Li–La–Zr–O thin film deposited at 40 W, exhibited the ionic conductivity of $4 \times 10^{-7} \text{ S cm}^{-1}$ [189].

Lobe et al. deposited Ta and Al-substituted LLZO thin films on Aluchrom YHf substrates by RF magnetron sputtering [190]. The substrate temperature was identified to be an important parameter for the formation of cubic garnet-structured LLZO thin films. The XRD studies indicated that the formation of LLZO phase starts at around 650 °C, whereas the single phase cubic thin films of LLZO were obtained at substrate temperatures of 700 °C and higher. However, scanning electron microscopy (SEM), time-of-flight-secondary ion mass spectrometry (ToF-SIMS) studies indicated the formation of an interlayer $\gamma\text{-LiAlO}_2$ between LLZO thin film and the substrate, at the higher substrate temperature. The thickness of the interlayer increased with the increasing temperature. The cross sectional backscattered electron (BSE) image of thin films deposited at 700 °C and 800 °C as shown in Fig. 2.6 revealed an interlayer between the thin film and the substrate (Fig. 2.6b). The impedance measurements were carried out using two different set-ups viz., perpendicular to the thin film and parallel to the thin film [190]. The combined total ionic conductivity of the $\gamma\text{-LiAlO}_2$ interlayer and the LLZO thin film (perpendicular to the plane) was determined to be $2.0 \times 10^{-9} \text{ S cm}^{-1}$ for the sample deposited at 700 °C. On the other hand, the impedance measured parallel to the thin film deposited at 700 °C exhibited a room temperature conductivity of $1.2 \times 10^{-4} \text{ S cm}^{-1}$ with activation energy of 0.47 eV [190].

2.4.2. Pulsed laser deposition (PLD)

The growth of Li^+ conducting $\text{Li}_6\text{BaLa}_2\text{Ta}_2\text{O}_{12}$ garnet-type thin films by pulsed laser deposition (PLD) was reported by Reinacher et al. [191]. Thin films were grown on MgO (100) by ablation of the bulk target material consisting of $\text{Li}_6\text{BaLa}_2\text{Ta}_2\text{O}_{12}$ with 5 mol.% excess of Li_2O to compensate lithium loss during thin film growth. The bulk material showed electrical conductivity of up to $5.0 \times 10^{-5} \text{ S cm}^{-1}$ at 25 °C, whereas the deposited $\text{Li}_6\text{BaLa}_2\text{Ta}_2\text{O}_{12}$ films exhibited a lower conductivity of $2 \times 10^{-6} \text{ S cm}^{-1}$ at 25 °C [191]. The $\text{Li}_6\text{BaLa}_2\text{Ta}_2\text{O}_{12}$ thin film was found to be stable versus metallic lithium and appeared to be well suited as a protective coating for electrodes, separators or even other electrolytes that are unstable against lithium as shown in Fig. 2.7(a) and (b).

There are only few reports regarding the fabrication of LLZO thin films. Tan et al. prepared LLZO thin film on SrTiO_3 (100) and sapphire (0001) substrates by pulsed laser deposition (PLD) with subsequent post-annealing [192]. As-deposited LLZO films were amorphous and then were crystallized on annealing. The as-deposited LLZO films exhibited a Li^+ conductivity of $3.35 \times 10^{-7} \text{ S cm}^{-1}$ and pulsed laser annealed LLZO films were found to have a Li^+ conductivity of $7.36 \times 10^{-7} \text{ S cm}^{-1}$ [192]. Moreover, LLZO films were found to be electrochemically stable against lithium metal. Kim et al. reported the epitaxial growth of LLZO films on garnet $\text{Gd}_3\text{Ga}_5\text{O}_{12}$ substrate prepared by PLD [193]. Two orientations of the films were obtained depending on the $\text{Gd}_3\text{Ga}_5\text{O}_{12}$ (GGG) substrate orientation, LLZO (001)/GGG (001) and LLZO (111)/GGG (111). The ionic conductivities in the grains of the (001) and (111) films were $2.5 \times 10^{-6} \text{ S cm}^{-1}$ and $1.0 \times 10^{-5} \text{ S cm}^{-1}$ at 25 °C, respectively [193].

The effect of deposition temperature and substrate type on the structural, physical and electrochemical properties of Li–La–Zr–O thin films made by PLD were investigated by Park et al. [194]. Thin films deposited at 600 °C on MgO (100) substrate contained both cubic and tetragonal polymorphs of LLZO at the surface and had the conductivity of $1.61 \times 10^{-6} \text{ S cm}^{-1}$ at room temperature [194]. Increasing the PLD deposition temperature to 750 °C led to the formation of $\text{La}_2\text{Zr}_2\text{O}_7$, resulting in higher activation energy of 0.67 eV and a decrease in the conductivity of two to three orders of magnitude. Park et al. reported that aluminum can react with the films when deposited on Al_2O_3 containing substrates such as sapphire or anodized aluminum oxide (AAO) [194]. Fig. 2.8 shows an SEM image of the polished cross section of a film deposited at 700 °C on an AAO substrate. The film was divided into two distinct regions with different contrasts, indicating that the composition is non-uniform. An energy dispersive X-ray spectroscopy (EDX) scan along the dotted line in Fig. 2.8 revealed that the upper region of the film was rich in aluminum and oxygen.

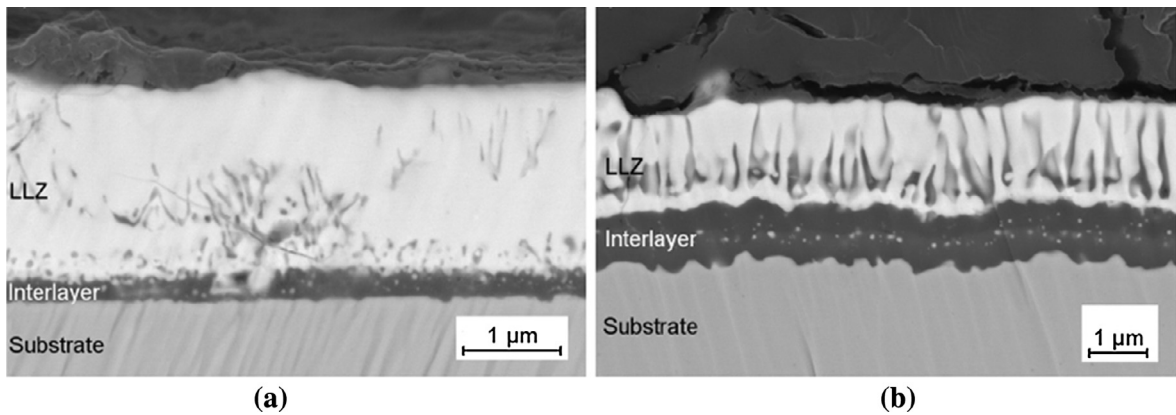


Fig. 2.6. Microstructure of the thin films deposited at 700 °C and 800 °C by RF magnetron sputtering technique (a) cross-section, BSE-image at 700 °C, (b) cross-section, BSE-image at 800 °C [190].

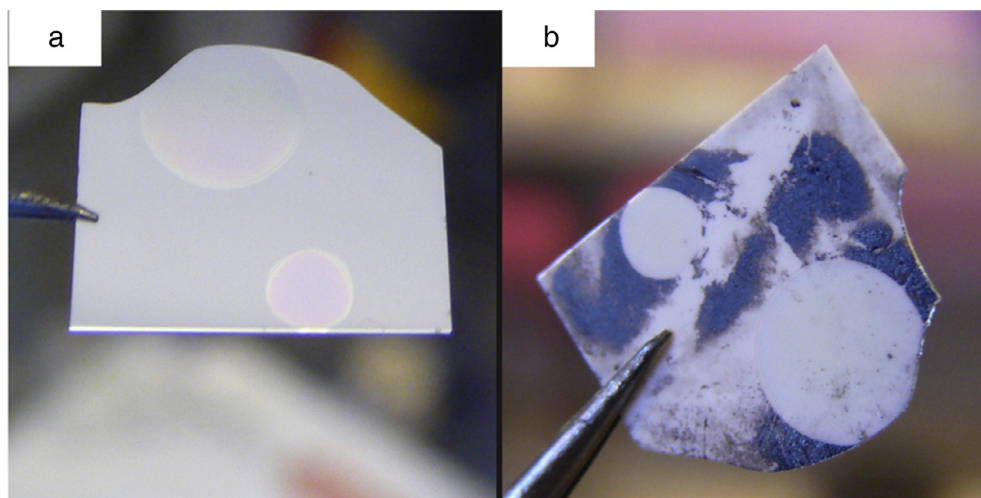


Fig. 2.7. (a) Image of the circular $\text{Li}_6\text{BaLa}_2\text{Ta}_2\text{O}_{12}$ thin films (thickness approx. 200 nm), deposited using a mask during the PLD process on a Li^+ conductive Ohara glass-ceramic (Ohara Inc., Kanagawa Japan), before its exposure to metallic Li [191]. (b) Ohara glass-ceramic protected with the $\text{Li}_6\text{BaLa}_2\text{Ta}_2\text{O}_{12}$ thin film after removal of metallic Li being applied on the sample for 12 h [191].

2.4.3. Metal-organic chemical vapor deposition (MOCVD)

Metal-organic chemical vapor deposition (MOCVD) is a versatile technique for the preparation of thin films at high deposition rates and moderate vacuum conditions. Moreover, the morphology and phase formation of the thin films can be controlled by this technique to design all-solid-state thin-film batteries.

Katsui et al. prepared cubic and tetragonal LLZO films on polycrystalline Al_2O_3 by MOCVD and investigated the effect of deposition temperature (T_{sub}) on the formation of phase, morphology and deposition rates [195]. The morphology of tetragonal and cubic LLZO film prepared by MOCVD varied depending upon the deposition temperature [195]. At $T_{\text{sub}} = 973$ K, a pyrochlore type $\text{La}_2\text{Zr}_2\text{O}_7$ film having the (111) orientation was deposited. At $T_{\text{sub}} = 1023$ – 1173 K, tetragonal LLZO films were grown. Cubic LLZO films with fine granular surface were obtained at $T_{\text{sub}} = 1173$ – 1223 K. The deposition rates of the cubic and tetragonal LLZO films were approximately $20 \mu\text{m h}^{-1}$, which were one to two orders of magnitude greater than those of LLZO films by pulsed laser deposition [195].

2.4.4. Sol-gel spin coating method

The sol-gel process coupled with dip-coating [196] or spin-coating [197] to produce thin films has many advantages over vacuum-based processes such as flexible synthesis conditions, easy control of chemical components, simplicity of the process, low cost, and high yield. Chen et al. reported the preparation of amorphous LLZO thin films via the sol-gel process and the impact of film thickness and the temperature of the heat treatment on the conductivity of the thin film [198].

The ionic conductivity of the films decreased with increasing annealing temperature, from $1.67 \times 10^{-6} \text{ S cm}^{-1}$ for 600 °C annealed film to $8.53 \times 10^{-7} \text{ S cm}^{-1}$ for 800 °C annealed film. Also, the influence of the thickness of the films on the conduc-

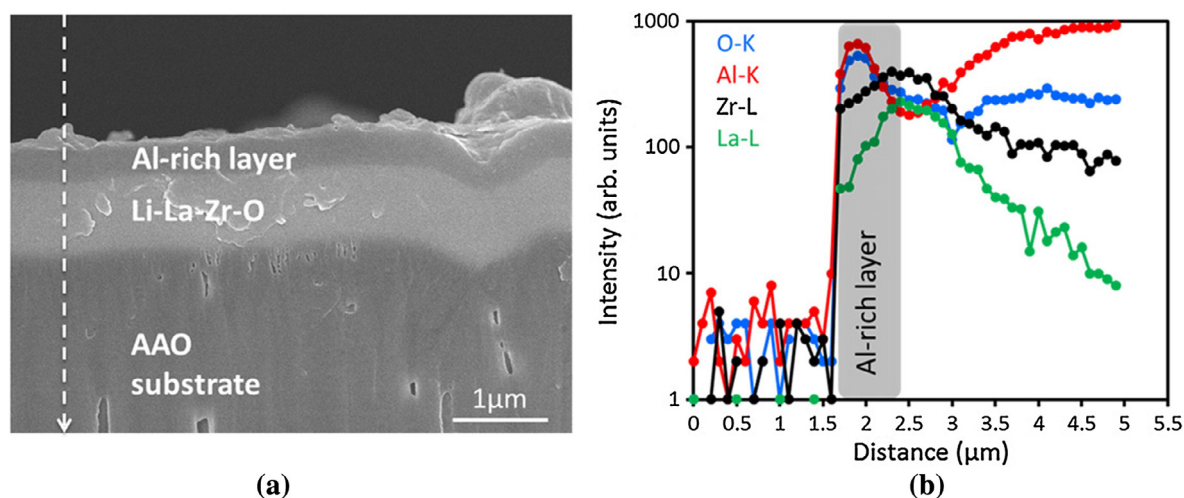


Fig. 2.8. (a) SEM image of a polished cross section of the Li-La-Zr-O film deposited on an anodized aluminum oxide (AAO) substrate at 700 °C [194] and (b) the corresponding EDX profile along the indicated dashed line [194].

Table 2.3

Lithium garnets prepared as thin films, their deposition technique, Li⁺ conductivity measured at room temperature (σ_{RT}) and activation energy (E_a).

Composition	Deposition technique	σ_{RT} (S cm ⁻¹)	^a Activation energy, E_a (eV)	Ref.
Li ₇ La ₃ Zr ₂ O ₁₂	RF-MS	4.0×10^{-7}	0.70	[189]
Ta- and Al-substituted LLZO	RF-MS	1.2×10^{-4}	0.47	[190]
Li ₆ BaLa ₂ Ta ₂ O ₁₂	PLD	2.0×10^{-6}	0.42	[191]
Li ₇ La ₃ Zr ₂ O ₁₂	PLD	7.19×10^{-8}	0.45	[192]
Li ₇ La ₃ Zr ₂ O ₁₂ (001)	PLD	2.5×10^{-6}	0.52	[193]
Li ₇ La ₃ Zr ₂ O ₁₂ (111)	PLD	1.0×10^{-5}	0.55	[193]

^a Activation energy for total (bulk + grain-boundary) Li⁺ conductivity.

tivity was investigated and the conductivity of the films first increased with increasing thickness and then decreased with further increase of thickness [198].

Some of the well known Li⁺ conducting materials which were prepared as thin films, their deposition method, Li⁺ conductivity at room temperature (σ_{RT}) and activation energy (E_a) are summarized as Table 2.3 [189–193].

2.5. Nebulized spray pyrolysis (NSP) technique

Organic components used as a complexing agent in the solution-based techniques leaves a large quantity of organic residue after synthesis. As a result post-annealing and grinding are necessary in case of solution-based techniques [174]. Nebulized spray pyrolysis (NSP) is a solution-based aerosol technique in which, the use of organic solvents can be excluded due to the readily available nitrate based precursors. It is possible to synthesise nanocrystalline powders using NSP owing to the simultaneous thermolysis of precursors and annealing treatment. Moreover, NSP offers less synthesis time compared to other techniques. The dense films with controlled thickness can be deposited on appropriate substrate using this NSP technique.

Djenadic et al. reported that Al-doped Li_{7-3x}La₃Zr₂Al_xO₁₂ ($x = 0-0.25$) (LLZO) with ultra-fine grained ceramics prepared using NSP exhibited a room temperature ionic conductivity of 1.2×10^{-6} S cm⁻¹ and 4.4×10^{-6} S cm⁻¹ for tetragonal ($x = 0$) and cubic ($x = 0.15$) phase, respectively [199]. Further increase in Al-content led to the formation of secondary phase. The experimental setup used by Djenadic et al. for the preparation of nanoparticles with the composition Li_{7-3x}La₃Zr₂Al_xO₁₂ ($x = 0-0.25$) using the Nebulized spray pyrolysis (NSP) method is shown in Fig. 2.9 [199].

Recently, Yi et al. reported a thin flexible films <30 μm by adopting the liquid feed-flame spray pyrolysis (LF-FSP) and conventional casting-sintering process [200]. Nano powders of Li_{6.25}Al_{0.25}La₃Zr₂O₁₂ with 50 wt.% excess lithium were produced using LF-FSP. The spherical nano powders were ball milled and further processed to green films by casting on Mylar sheet. A single phase cubic LLZO was able to achieve by sintering the green film at 1080 °C for 1 h. Further increase in sintering temperature leads the formation of minor impurity phase of La₂Zr₂O₇ and La₂O₃ phases. Flexible thick translucent films (<30 μm) with 2 × 2 cm² lateral dimensions as shown in Fig. 2.10(a) were produced with a relative density of 94 ± 1%. The film exhibited a room temperature Li⁺ conductivity of 0.2 ± 0.03 mS cm⁻¹ (Fig. 2.10(b)) with an activation energy of 0.35 ± 0.01 eV [200].

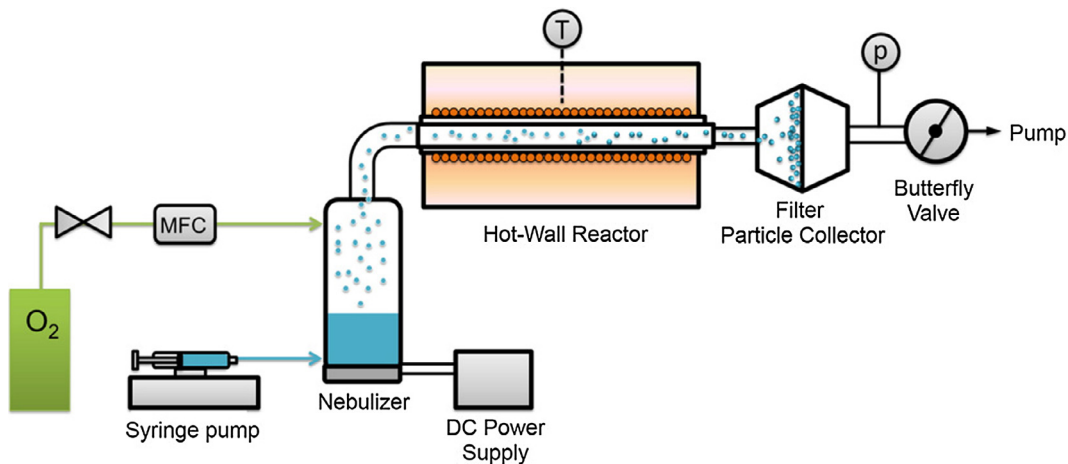


Fig. 2.9. Nebulized spray pyrolysis experimental setup [199].

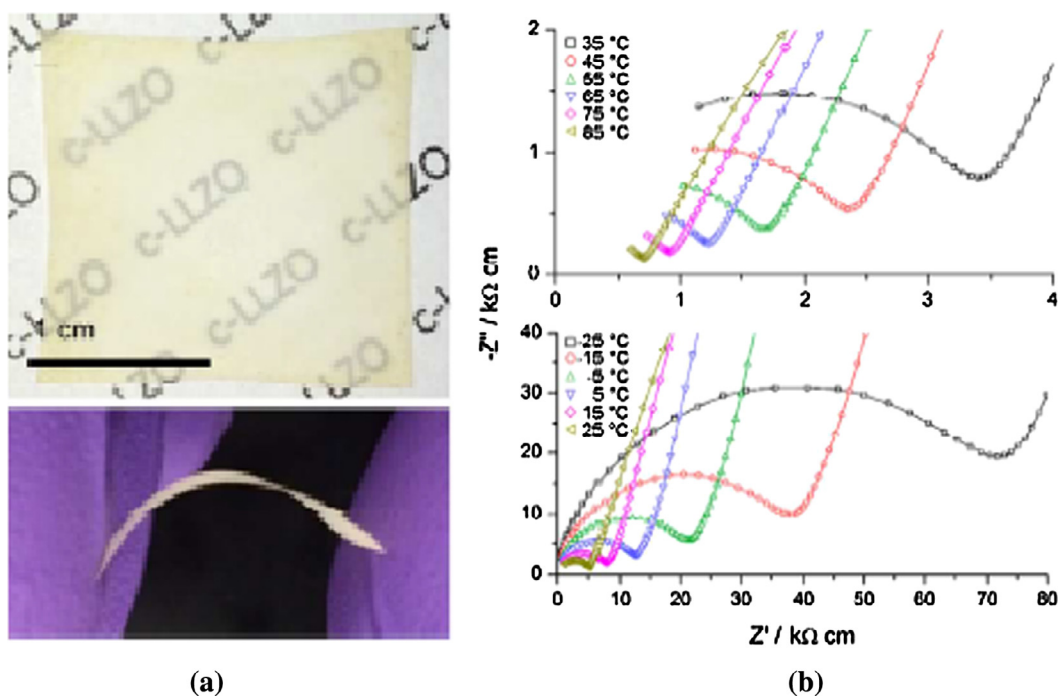


Fig. 2.10. (a) Photographic image of translucent freestanding cubic LLZO film and (b) temperature dependent impedance plots of the sintered LLZO films [200]

2.6. Electrospinning technique

In order to obtain nanostructured LLZO and to investigate its phase transformations, the electrospinning technique was selected, as it has been a versatile method for preparing ceramic nanofibers or nanowires from sol-gel precursors. Yang et al. synthesized LLZO nanowires with electrospinning for the first time and also studied the particle size- dependent phase transformation [201]. A photograph of an as-spun flexible nanowire mat and the SEM image of (a) as-spun LLZO nanowires and the nanowires after calcination at 700 °C for (b) 1.5, (c) 2, (d) 2.5, (e) 3, and (f, g) 5 h is shown in Fig. 2.11. SEM images revealed that, as the heating time increased, the nanowires became thicker and underwent coalescence to form larger ligaments. Yang et al. showed that, the cubic LLZO can be stabilized at room temperature in nanostructured particles without the use of extrinsic dopants and the heating promoted coalescence and grain growth which led into a transformation to tetragonal LLZO [201].

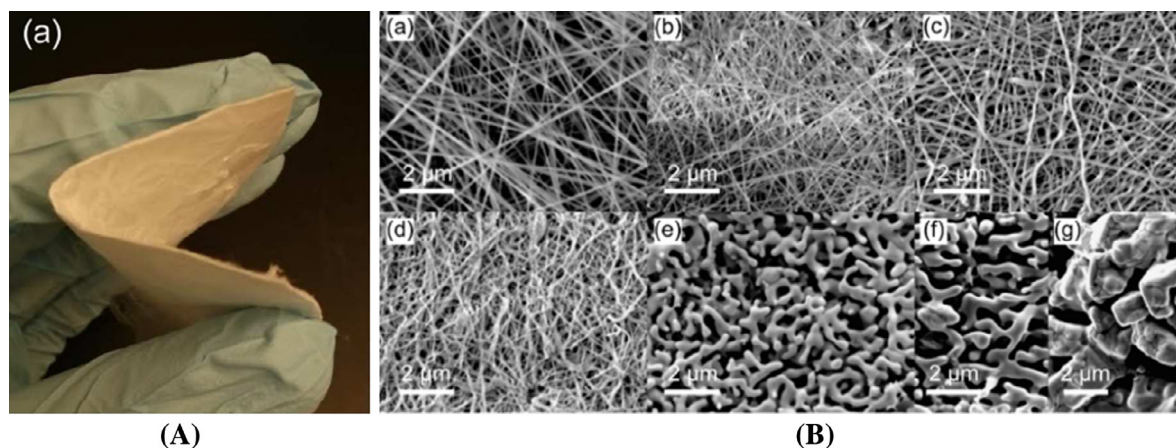


Fig. 2.11. (A) Photograph showing appreciably flexible as-spun LLZO fiber mat [201] and (B) SEM image of (a) as-spun LLZO nanowires and the nanowires after calcination for (b) 1.5 h, (c) 2 h, (d) 2.5 h, (e) 3 h, and (f, g) 5 h at 700 °C [201].

Yang et al. also reported that the transformation between the tetragonal and cubic phases in the LLZO system can be induced by a change in dimensions, with cubic LLZO stabilized in nanostructures and tetragonal LLZO preferred for larger particle [201]. The mechanism is likely related to the difference in surface energy between the high-temperature cubic phase and the low temperature tetragonal phase. Since nanocrystallites connect to each other and form larger structures (nanowires) at the crystallization stage, the agglomeration in nanopowders derived from electrospinning can be greatly prevented.

In general, the best synthesis method for lithium garnets is expected to meet the following criteria,

- The synthetic method has to be of low cost.
- Product formed should be phase pure and homogeneous.
- Materials with proper physical and chemical characteristics suitable for battery application.

Thus, the exploration of new novel synthetic method and processing technology plays a vital role for the development of high performance lithium batteries based on garnet structured electrolyte.

2.7. Sintering of lithium garnets

In addition to the stabilization of high Li^+ conductive cubic phase, the dense microstructure related to grains and grain-boundaries is also a critical issue for the successful application of LLZO as solid electrolyte membrane in all-solid-state lithium and lithium-air battery technologies. The dense microstructure is expected to enhance the total (bulk + grain-boundary) Li^+ conductivity by reducing the grain-boundary resistance and also expected to barricade the dendritic growth during lithium deposition in an electrochemical cell. Ceramics are usually sintered at elevated temperatures for longer duration to yield high dense pellets.

High porosity in solid electrolytes may cause a high grain-boundary resistance as well as mechanical failure. Owing to the volatilization of Li components or gas filling in pores during sintering, the LLZO solid electrolytes obtained via conventional solid state method usually show a limited density as well as relatively poor total Li^+ conductivity.

2.7.1. Densification by sintering agent

Usually, in most of the polycrystalline ceramic lithium ion conductors, the total (bulk + grain-boundary) Li^+ conductivity at room temperature is only half of the σ_{bulk} because of the grain-boundary resistance (GBR). The GBR needs to be reduced to improve the σ_{total} of solid electrolytes. Densification of the solid electrolyte can reduce the GBR. The presence of a glassy phase at the grain-boundary region has improved the total (bulk + grain-boundary) Li^+ conductivity in various solid electrolytes. Kumazaki et al. reported the preparation of high Li^+ conductive LLZO solid electrolyte by the inclusion of appropriate amounts of both aluminum (Al) and silicon (Si) [202].

Microanalyses by transmission electron microscopy (TEM), coupled with energy-dispersive X-ray microanalysis and electron energy-loss spectroscopy revealed the presence of amorphous Li–Al–Si–O with nano crystalline LiAlSiO_4 at grain boundaries. Amorphous Li–Al–Si–O with nano-crystalline LiAlSiO_4 presented at the grain boundaries facilitated the Li^+ transfer between the LLZO particles, resulting in the reduction of the GBR and then increasing the total Li^+ conductivity of LLZO [202]. Total Li^+ conductivity at 298 K of pelletized LLZO was improved to $6.8 \times 10^{-4} \text{ S cm}^{-1}$ by including appropriate amounts of Al and Si.

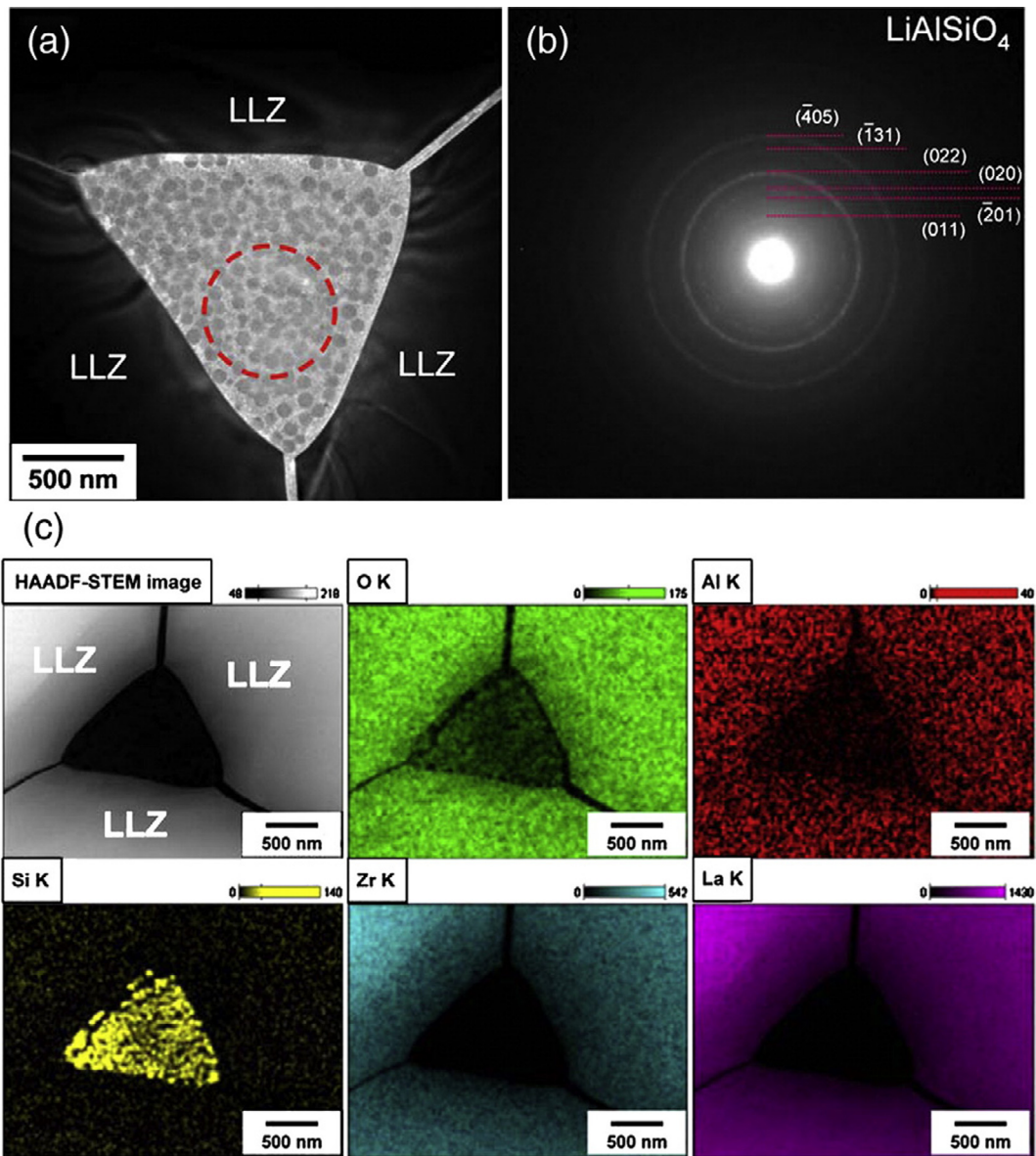


Fig. 2.12. (a) TEM image of LLZO around a triple-point grain-boundary. (b) Selected area electron diffraction (SAED) pattern measured at the dotted circle in (a). (c) High-angle annular dark-field-scanning tunneling microscopy (HAADF-STEM) image and energy dispersive X-ray (EDX) mapping of O, Al, Si, Zr, and La measured in (a) [202].

Fig. 2.12(a) shows a TEM image at a triple-point grain-boundary in LLZO. The triple-point grain-boundary is comprised of polygonal crystalline particles and an amorphous substance [202]. The selected area electron diffraction (SAED) pattern shown in Fig. 2.12(b) measured at the triple-point detected crystalline monoclinic phase LiAlSiO_4 [202]. EDX analysis revealed the presence of Si, Al, and O as major elements in the boundary (Fig. 2.12(c)).

The sintering temperature of ceramics can be reduced by utilizing suitable sintering aids with a low melting temperature. Even if the melting point of sintering aid is slightly higher than the sintering temperature, it may help to sinter the ceramics through the formation of eutectic. The liquid-phase sintering could be a useful way to improve the ceramic density, since the liquid phases formed in between the grains could expel the residual pores. Improvement of lithium garnet ceramic ionic conductivity is hindered by the high porosity related to the severe volatilization of lithium components during sintering.

An attempt has been made to enhance the density of Ta doped LLZO by the addition of Li_3PO_4 and Li_2O [143,144,152] and LLZO by the addition of Li_3BO_3 [203,204]. Li et al. introduced Li_2O additives in concentration of 2–8 wt.% into the cubic phase $\text{Li}_{6.75}\text{La}_3\text{Zr}_{1.75}\text{Ta}_{0.25}\text{O}_{12}$ (LLZOTO) during the solid-state reaction processes [143]. It was found that, the Li_2O additives led to the formation of glassy-like phases at the grain boundaries related to the liquid-phase sintering behavior, which eliminated

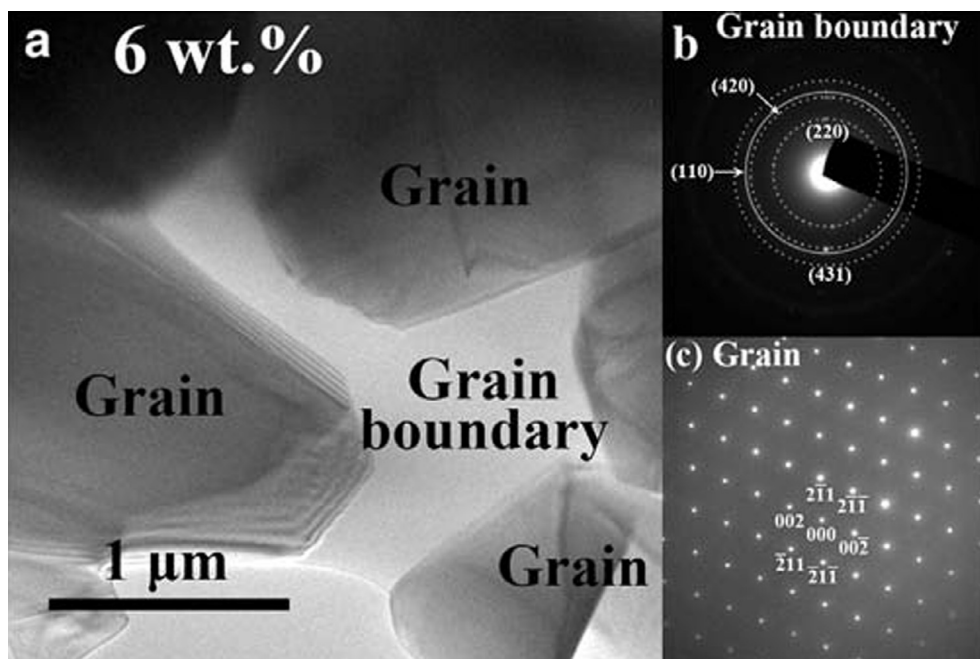


Fig. 2.13. (a) A typical image for the ion-beam-cut cross section of the 94% LLZOTO–6% Li₂O sample, (b) selected area electron diffraction (SAED) pattern for the materials at the grain boundaries, and (c) SAED pattern for the materials at the grains [143].

the residual pores therein and increased the relative density from 91.5% to 97.3%. Measurement of conductivity indicated that, the optimum concentration of Li₂O (6 wt.%) led to a Li⁺ conductivity of $6.4 \times 10^{-4} \text{ S cm}^{-1}$ at room temperature, along with the relative density of 97.2% [143].

TEM in combination with SAED carried out for the ion beam-cut cross section of the sample of 94% LLZOTO–6%Li₂O is shown in Fig. 2.13(a) [143]. SAED revealed that, the materials at the grain boundaries consisted of two sets of diffused diffraction rings, which can be attributed to weakly crystallized LLZOTO and Li_{0.5}La₂Al_{0.5}O₄, as shown in Fig. 2.13(b) [143]. In the grains, only one set of ordered sharp diffraction spots can be observed, clearly indicating the high-quality crystallized LLZOTO, as shown in Fig. 2.13(c) [143]. Therefore, the above results demonstrate that the grains are composed of crystalline LLZOTO while the grain boundaries consisted of glassy-like materials of the LLZOTO, mixed with the Li_{0.5}La₂Al_{0.5}O₄ [143].

The effects Li₃PO₄ as sintering aid in different concentrations (0 wt.%, 1 wt.%, 2 wt.%, 4 wt.% and 6 wt.%) on density and conduction properties of Li_{7-x}La₃Zr_{2-x}Ta_xO₁₂ (LLZOTO, $x = 0.25$) electrolytes have been studied by Yang et al. [144]. Li₃PO₄ can be used as a sintering aid because of its low melting point of 837 °C as well as ionically conducting property. It acted as a binder between the grains to improve the ceramic density. Through Li₃PO₄ addition, the sintering time was greatly reduced from 36 h to 6 h. The sintering temperature of 1175 °C was found to be the optimum sintering temperature for the pellets with 1 wt.% and 2 wt.% Li₃PO₄, while that of 1150 °C for the pellets with 4 wt.% and 6 wt.% Li₃PO₄ [144]. The sample incorporated with 1 wt.% Li₃PO₄ exhibited a maximized total Li⁺ conductivity of $7.2 \times 10^{-4} \text{ S cm}^{-1}$ with an optimum relative density value of 92.7% [144].

Flowing oxygen during sintering was found to be a powerful and economical alternative method to prepare high density ceramics. Flowing oxygen during sintering can facilitate sintering by filling pores with pure oxygen, aiding densification compared with other molecules in air or inert atmospheres. In view of the good solubility and diffusivity of oxygen, the pores filled with oxygen could disappear easily by oxygen migration via lattice diffusion or vacancy transport. Pure oxygen sintering can significantly enhance both the density and ionic conductivity of solid electrolytes. Li et al. reported that the garnet-type Al-contained Li_{6.75}La₃Zr_{1.75}Ta_{0.25}O₁₂ (LLZOTO-Al) solid electrolytes prepared by conventional solid-state reaction followed by flowing oxygen sintering process exhibited high density (96%) with an overall ionic conductivity as high as $7.4 \times 10^{-4} \text{ S cm}^{-1}$ at 25 °C, remarkably higher than that obtained by sintering in other atmospheres [152].

Takano et al. reported the preparation of Al-doped Li₇La₃Zr₂O₁₂ (LLZO) by sol-gel process [203]. Single phase cubic LLZO was obtained by a heat treatment at 700 °C. For the sintering at lower temperatures and formation of the composite electrolytes, LiBO₂ or Li₃BO₃ was added as sintering additives. The LLZO powders were sintered at 900 °C using LiBO₂ or Li₃BO₃ to form composite solid electrolyte. The composite sintered with LiBO₂ contained La₂Zr₂O₇ as an impurity phase. On the other hand, the composite sintered with Li₃BO₃ exhibited single phase cubic LLZO. The composite of Al-doped LLZO and Li₃BO₃ sintered at 900 °C showed the total electrical conductivity of $1.9 \times 10^{-5} \text{ S cm}^{-1}$, while Al-doped LLZO pellet without additives showed $1.6 \times 10^{-6} \text{ S cm}^{-1}$ [202].

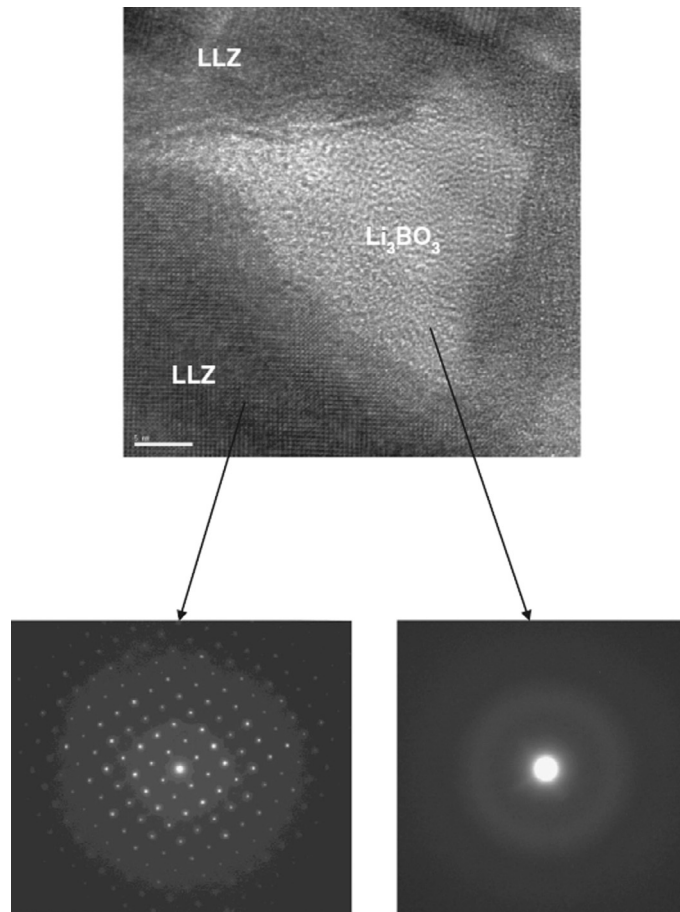


Fig. 2.14. TEM and electron diffraction images of the pellet sintered with Li_3BO_3 [204].

Tadanaga et al. synthesized highly lithium ion conductive composites with Al-doped $\text{Li}_7\text{La}_3\text{Zr}_2\text{O}_{12}$ (LLZO) and amorphous Li_3BO_3 from sol-gel derived precursor powders of LLZO and Li_3BO_3 [204]. Precursor LLZO powders with cubic phase were obtained by a heat treatment of the dried gel precursor at 600 °C. Pellets of the mixture of the obtained LLZO and Li_3BO_3 were first held at 700 °C and then successively sintered at 900 °C. In the heat-treatment at 900 °C, the lithium loss during heat-treatment was assumed to be suppressed. During sintering of precursor powders of LLZO and lithium borate, the liquid phase of lithium borate acts as an accelerator for inter-reaction of grains at grain boundaries and the grain growth. In the obtained composite, amorphous lithium borate would be formed as a thin layer at the grain boundaries. This glassy phases would reduce the grain-boundary resistance, and thus the composite exhibited high total Li^+ conductivity of $1 \times 10^{-4} \text{ S cm}^{-1}$ at 30 °C. Density of the sintered pellet with Li_3BO_3 was higher (92%) than that of the pellet without Li_3BO_3 (58%). Fig. 2.14 shows the TEM and electron diffraction images of the sintered pellet with Li_3BO_3 [204]. As indicated from TEM observation, LLZO particles are basically the continuous phase in the composite, and Li_3BO_3 exists at the triple grain-boundary as amorphous phase or at the grain boundaries as a thin layer between LLZO particles. Li_3BO_3 should form a liquid phase during heat treatment at 700 °C, and promoted the rearrangement of LLZO particles. In the sintering at 900 °C, the grain growth of LLZO particles must be promoted with the liquid phase, and the lithium loss must be also suppressed by the liquid phase. After sintering and cooling, Li_3BO_3 exists at grain boundaries as amorphous phase to form the composite [204].

Janani et al. has carried out a systematic investigations on the preparation of high Li^+ conductive 0.9 wt.% of Al doped LLZO i.e., $\text{Li}_{6.16}\text{Al}_{0.28}\text{La}_3\text{Zr}_2\text{O}_{12}$ (Al-LLZO) in cubic phase by modified sol-gel technique and also investigated the influence of various sintering additives Li_3BO_3 , Li_3PO_4 and Li_4SiO_4 on the density and total (bulk + grain-boundary) Li^+ conductivity of Al-LLZO [176]. As revealed by SEM investigations (Fig. 2.15), although the addition of Li_3PO_4 helped to increase the growth of large grains, the total (bulk + grain-boundary) Li^+ conductivity was found to be reduced by the segregation of possible secondary phase AlPO_4 at the grain-boundary. On the other hand, the addition of Li_4SiO_4 helped to enhance the density, reduce the grain-boundary resistance and thereby enhance the total (bulk + grain-boundary) Li^+ conductivity. The Si^{4+} from Li_4SiO_4 might replace some of the $\text{Al}^{3+}/\text{Li}^+$ in Al-LLZO, which may lead to $\text{Al}^{3+}/\text{Li}^+$ extraction from the bulk into the grain-boundary region for the formation of favorable Li^+ conducting thin layer with the possible combination of Li–Al–Si–O in the

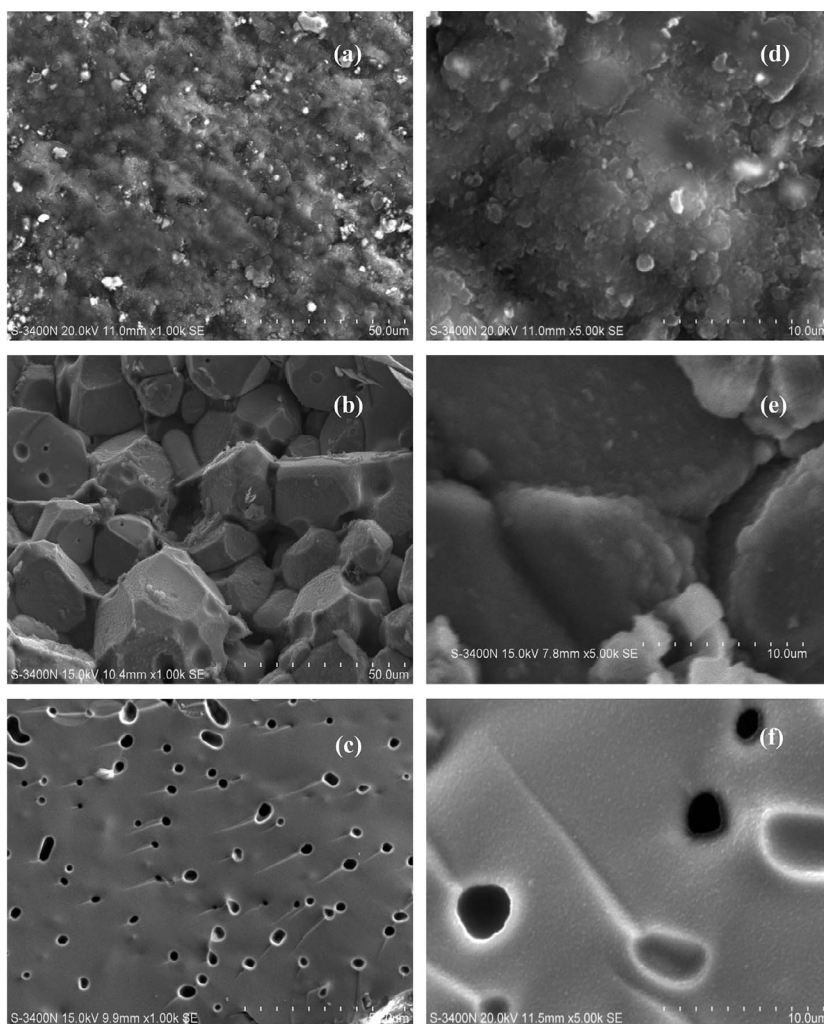


Fig. 2.15. SEM images of the fractured surfaces of (a) Al-LLZO, (b) Al-LLZO added with 1 wt.% of Li_3PO_4 , (c) Al-LLZO added with 1 wt.% of Li_4SiO_4 sintered at 1200°C and (d–f) represent corresponding magnified SEM images, respectively [176].

grain-boundary. Hence, the increased numbers of empty structural sites in Al-LLZO lattice could permit increased Li^+ mobility and thus result into an increase in bulk conductivity and simultaneous enhancement in the grain-boundary conductivity through the favorable Li^+ conducting Li–Al–Si–O phase at the grain-boundary [176]. On the other hand, the segregation of unfavorable AlPO_4 at the grain-boundaries in the case of Al-LLZO added with 1 wt.% of Li_3PO_4 might result into low total (bulk + grain-boundary) Li^+ conductivity.

Among the three chosen sintering additives, Li_3BO_3 , Li_3PO_4 and Li_4SiO_4 , Li_4SiO_4 appeared to be a better sintering additive for the enhancement of the total (bulk + grain-boundary) Li^+ conductivity and density of Al-LLZO [176]. The Al-LLZO added with 1 wt.% of Li_4SiO_4 sintered at 1200°C exhibited the maximized room temperature (33°C) total (bulk + grain-boundary) Li^+ conductivity of $6.1 \times 10^{-4} \text{ S cm}^{-1}$ and maximized density of 4.86 g cm^{-3} (relative density 96%) [176].

The influence of 0.5, 1 and 1.5 wt.% Li_4SiO_4 sintering additive on the Li^+ conductivity and density of $\text{Li}_{6.4}\text{La}_3\text{Zr}_{1.4}\text{Ta}_{0.6}\text{O}_{12}$ was also investigated by Janani et al. [153]. Maximized room temperature (33°C) total (bulk + grain-boundary) Li^+ conductivity of $3.7 \times 10^{-4} \text{ S cm}^{-1}$ and maximized density of 5.30 g cm^{-3} was observed for $\text{Li}_{6.4}\text{La}_3\text{Zr}_{1.4}\text{Ta}_{0.6}\text{O}_{12}$ added with 1 wt.% of Li_4SiO_4 [153].

2.7.2. Hot press technique

High sintering temperature and a long sintering period are required to prepare grain-boundary-free high-density LLZO using conventional solid state reactions. Hot pressing (HP) is a useful technique to obtain a dense pellet, which involves the simultaneous application of heat and pressure.

Rangasamy et al. investigated the effect of Al and Li concentration on the formation of cubic garnet of nominal composition $\text{Li}_7\text{La}_3\text{Zr}_2\text{O}_{12}$ using uniaxial hot-pressing [100]. A thick pellet of cubic LLZO pellet with the composition $\text{Li}_{6.24}\text{La}_3\text{Zr}_2\text{Al}_{0.24}\text{O}_{11.98}$

was prepared by loading single phase powder into a graphite die and heating at 1000 °C under 40 MPa pressure for 1 h under flowing argon. The resulting pellet was removed from the hot press and heated in air at 1000 °C for 4 h to burn of residual graphite from the hot pressing die. After burning off the graphite residue, the pellet appeared bright. The hot-pressed material had a relative density of 98%. An SEM micrograph of the hot-pressed $\text{Li}_{6.24}\text{La}_3\text{Zr}_2\text{Al}_{0.24}\text{O}_{11.98}$ fracture surface is shown in Fig. 2.16. As shown in Fig. 2.16, the sample was very dense in agreement with the high relative density, very few voids were observed. Secondly, the fracture is mainly transgranular, indicating high grain-boundary strength. The room temperature total ionic conductivity of the hot-pressed material was $4.0 \times 10^{-4} \text{ S cm}^{-1}$ and the electronic conductivity was $2 \times 10^{-8} \text{ S cm}^{-1}$ [100].

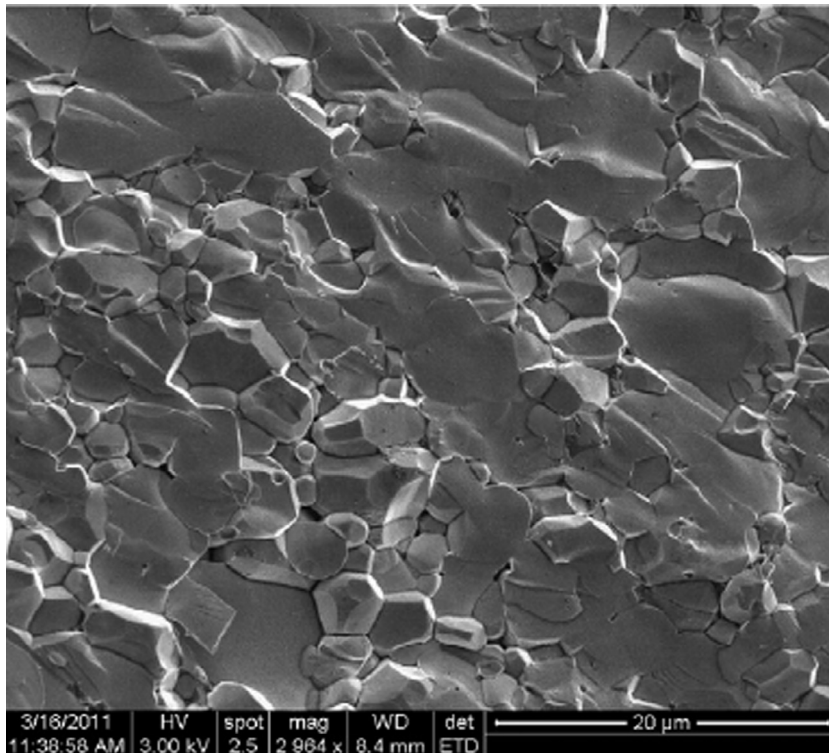


Fig. 2.16. SEM image of a fractured surface of hot-pressed $\text{Li}_{6.24}\text{La}_3\text{Zr}_2\text{Al}_{0.24}\text{O}_{11.98}$ [100].

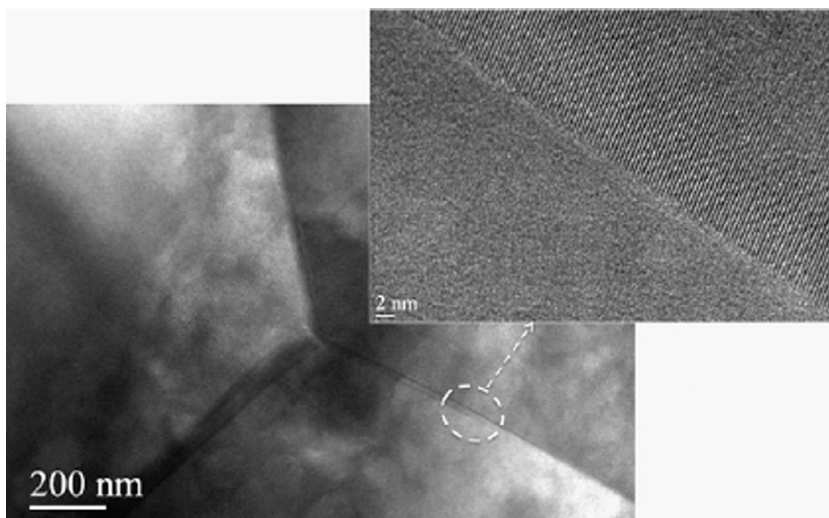


Fig. 2.17. TEM micrograph of a typical triple junction in the hot-pressed $\text{Li}_{6.24}\text{La}_3\text{Zr}_2\text{Al}_{0.24}\text{O}_{11.98}$ material [100].

Hot-pressing technique was used by Wolfenstine et al. to prepare a dense (97% relative density) cubic Al substituted LLZO material at 1000 °C [205]. Electron microscopy analysis revealed equiaxed grains, grain boundaries, and triple junctions free of amorphous and second phases and no Al segregation at grain boundaries [205]. The TEM micrograph of a typical triple junction in the hot-pressed $\text{Li}_{6.24}\text{La}_3\text{Zr}_2\text{Al}_{0.24}\text{O}_{11.98}$ material is shown in Fig. 2.17.

Recently, a transparent garnet-type lithium-ion conducting solid electrolyte of 1.0 wt.% Al_2O_3 -doped $\text{Li}_7\text{La}_3\text{Zr}_2\text{O}_{12}$ (A-LLZO) was prepared using hot isostatic pressing (HIP) by Suzuki et al. [206]. The relative density of the LLZO pellet was increased from 91.5% to 99.1% by HIP treatment. The bulk conductivity of the HIP treated A-LLZO was $9.9 \times 10^{-4} \text{ S cm}^{-1}$ at 25 °C.

2.7.3. Fast microwave-assisted synthesis

Most of the reported lithium-containing garnets have been synthesized by conventional solid-state routes employing long reaction times at high temperatures and by sol-gel technique. Nowadays, the implementation of microwave irradiation during solid-state synthesis is emerging as an alternative preparative approach, enabling reductions in reaction times and heating temperatures, due to the strong absorption of microwave radiation by the starting materials.

Amores et al. presented a fast, reliable microwave assisted approach for the synthesis of Al-doped LLZO garnet with a nominal composition of $\text{Li}_{6.5}\text{Al}_{0.25}\text{La}_{2.92}\text{Zr}_2\text{O}_{12}$ [207]. The highly crystalline cubic phase was obtained at much shorter reaction time (1000 °C for 1 h) compared with conventional solid state methods. The lithium ion diffusion behavior has been examined by both electrochemical impedance spectroscopy (EIS) and muon spin relaxation (μSR) spectroscopy, displaying activation energies of $0.55 \pm 0.03 \text{ eV}$ and $0.19 \pm 0.01 \text{ eV}$ respectively [207]. This synthetic method was found to be a viable, significantly faster, alternative route to derive cubic phase Li-stuffed garnets.

2.7.4. Spark plasma sintering (SPS) process

Spark plasma sintering (SPS) is an advanced sintering technique, which utilizes simultaneous applications of uniaxial pressure and pulsed direct electrical current (pulsed DC) to densify powder compacts [208–212]. The heating rates (up to 600 °C min^{-1}) achieved in SPS are more than an order of magnitude greater than that achieved with the more conventional sintering techniques.

Spark plasma sintering (SPS) offers advantages that include faster densification, activated materials synthesis, formation of atomically clean grain boundaries, good grain-to-grain bonding, and minimization of particle coarsening that allows the retention of nanosized grains/particles during synthesis or sintering.

SPS uses high ampere DC pulse current to generate spark plasma between the particles, as shown in Fig. 2.18(a) [213]. Uniaxial compression is applied and the process is carried out under vacuum or inert gas atmosphere. Discharge is generated at the particle contact point during the SPS process. Heat and high pressure are concentrated in this small contact area, and joule heating is generated by the electrical current (Fig. 2.18(b)). Necking of the particles begins and sintering and densification proceed to occur [213].

Baek et al. reported the compatibility of Li-La-(Zr-Ta)-O garnet related lithium ion conductors with all solid state battery (ASSB) systems processed by spark plasma sintering (SPS) [214]. $\text{Li}_{7-x}\text{La}_3\text{Zr}_{1.5}\text{Ta}_{0.5}\text{O}_{12-d}$ processed by SPS shows a high ionic

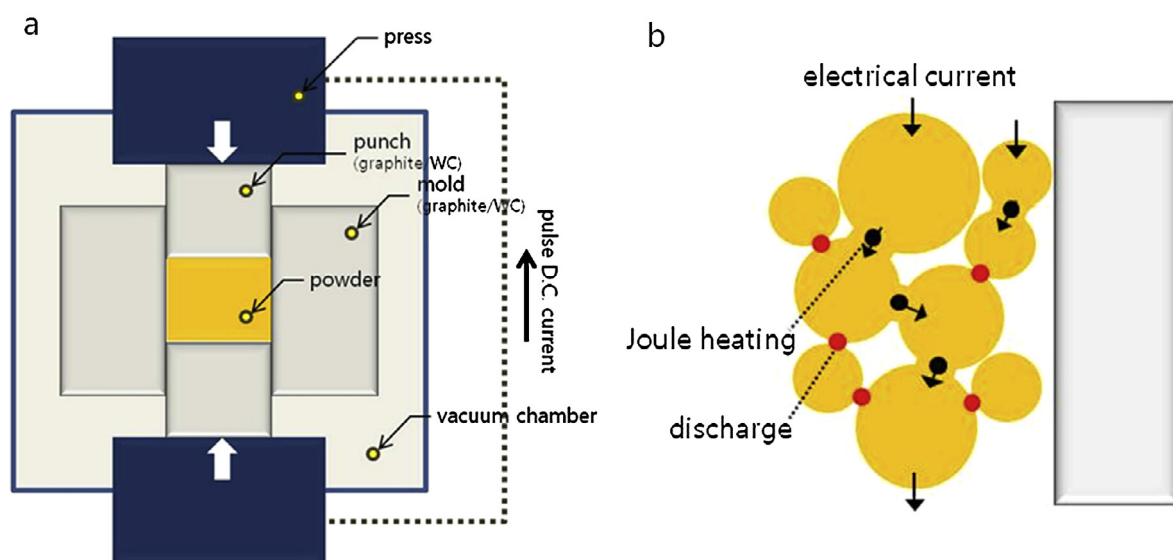


Fig. 2.18. (a) Schematic diagram of the components of the SPS apparatus and (b) illustrations of the mechanism of the SPS technique [213].

conductivity of $1.35 \times 10^{-3} \text{ S cm}^{-1}$ and $1.23 \times 10^{-2} \text{ S cm}^{-1}$ at 25°C and 80°C , respectively [214]. In addition, the material also showed good structural stability, which is a critical challenge encountered in garnet structured materials treated under severe SPS process conditions. An ASSB assembled by SPS using the $\text{Li}_4\text{Ti}_5\text{O}_{12}$ – $\text{Li}_{7-x}\text{La}_3\text{Zr}_{1.5}\text{Ta}_{0.5}\text{O}_{12-d}$ composite electrode showed a surface capacity of 0.2 mAh cm^{-2} at 80°C . The battery showed a well-organized structure with a good lithium diffusion percolation path and the low solid contact resistance without any defects and undesirable reactions arising from the sintering method [214].

2.7.5. Field assisted sintering technology (FAST)

Field assisted sintering technology (FAST) is a combination of a uniaxial pressing process and a direct passing of electric DC current through the graphite tool to sinter the material, if the powder is not electrically conductive. The production of Joule heat within tool enables the densification of various materials with higher heating rates and shorter dwell times [215].

Zhang et al. prepared a high performance lithium ion conducting $\text{Li}_7\text{La}_3\text{Zr}_2\text{O}_{12}$ solid electrolytes with cubic phase by a one-step FAST method in the temperature range of 1100 – 1180°C with very short sintering time of not $>10 \text{ min}$ [216]. The loss of Li during the FAST process is very limited. The limited loss of Li is mainly because the total sintering time by FAST is comparatively very short. The sample sintered at 1150°C exhibited a maximum relative density of 99.8% and the maximized ionic conductivity value of about $5.7 \times 10^{-4} \text{ S cm}^{-1}$ with activation energy of 0.3 eV in the temperature range of 50 – 300°C [216]. Fig. 2.19 shows the SEM micrographs of the cross sections of the samples sintered at (a) 1150°C and (b) 1200°C . The particles sintered at these temperatures (Fig. 2.19(a) and (b)) had tight contact with each other with no voids; the fracture was almost transgranular, indicating a good interfacial bonding in the sintered pellets [216].

It is expected that, the high sintering rates of FAST for preparation of LLZO can extremely reduce the loss of Li. Moreover, the chemical reaction between the raw materials to synthesis LLZO and the sintering densification of the pellets are both accomplished in one step during the field assisted sintering technology without any other heat treatment and intermittent grinding. FAST shows great advantages for synthesizing this material including very short sintering time, relative lower sintering temperature, one step heat treatment process and higher performance of sintered LLZO ceramics over other reported methods. This sintering technology is a particularly efficient method for preparing high Li ionic conductivity cubic phase LLZO solid electrolytes.

2.8. 3D Li^+ conducting ceramic nanofibre network

The success of high energy density solid state lithium battery will strongly rely on lithium metal anode designs with good stability to achieve high energy density and long cycle life. Kun Fu et al. recently reported a 3D lithium-ion-conducting ceramic network using polyethylene oxide (PEO)-based composite containing Al doped LLZO, $\text{Li}_{6.4}\text{La}_3\text{Zr}_2\text{Al}_{0.2}\text{O}_{12}$ [217].

The procedure reported by Kun Fu et al. for the preparation of flexible solid-state garnet LLZO nanofiber-reinforced polymer composite electrolytes shown in Fig. 2.20(a), depicts the electrospinning of polyvinylpyrrolidone (PVP) polymer mixed with $\text{Li}_{6.4}\text{La}_3\text{Zr}_2\text{Al}_{0.2}\text{O}_{12}$ followed by the calcination of the as-prepared nanofibers at 800°C in air for 2 h [217]. The fabrication of fiber-reinforced polymer composite (FRPC) membrane using the 3D porous garnet nanofiber network is shown schematically as Fig. 2.20(b). PEO polymer mixed with Li salt then, the Li salt–PEO polymer is reinforced by the 3D nanofibers to form a composite (FRPC) electrolyte membrane. Photographic image of the prepared flexible FRPC membrane is shown as Fig. 2.20(c). The flexible FRPC solid-state electrolyte composite membrane exhibited an ionic conductivity of $2.5 \times 10^{-4} \text{ S cm}^{-1}$ at room temperature. The linear sweep voltammetry (LSV) profile of the prepared FRPC electrolyte using lithium metal as the counter and reference electrode and stainless steel as the working electrode shown as Fig. 2.20(d) exhibits a stable voltage window up to 6.0 V vs. Li/Li^+ .

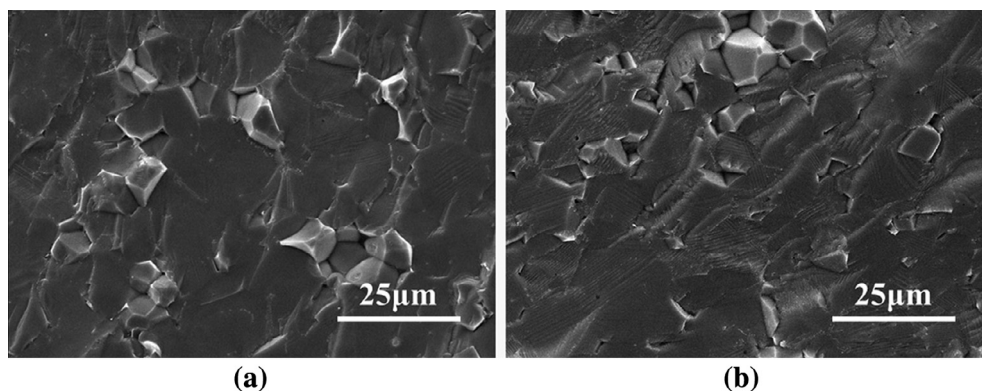


Fig. 2.19. SEM micrographs of the cross sections of the LLZO samples sintered by FAST at (a) 1150°C and (b) 1200°C [216].

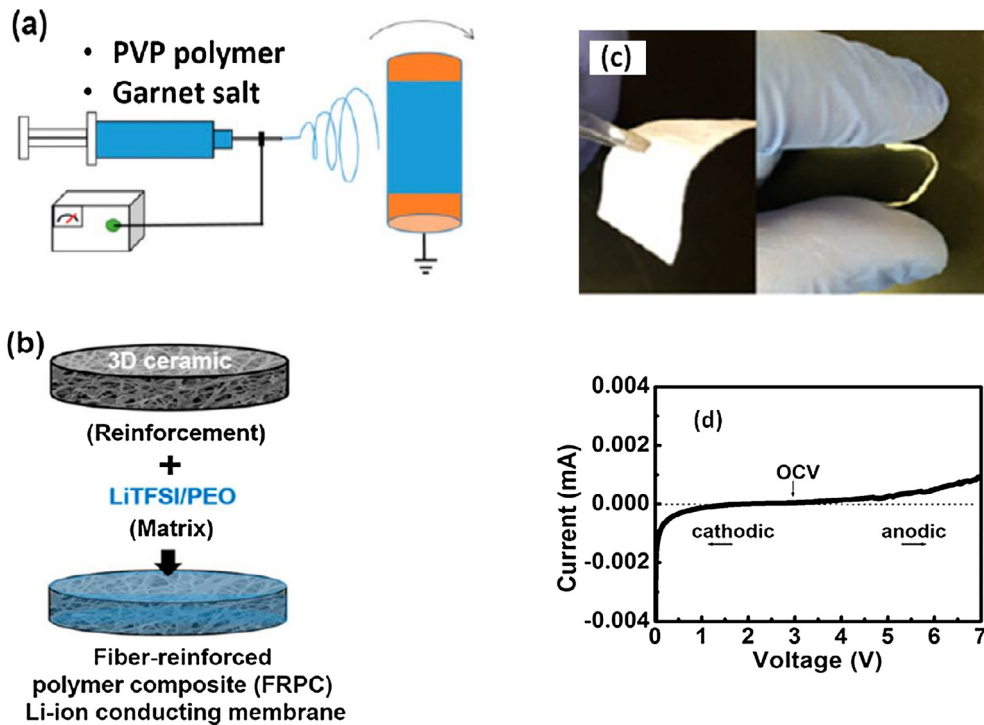


Fig. 2.20. (a) Schematic of the electrospinning equipment, (b) flowchart for the fabrication of fiber-reinforced polymer composite lithium ion conducting membrane, (c) photographic image/Picture of flexible FRPC membrane and (d) cyclic voltammogram of FRPC membrane [217].

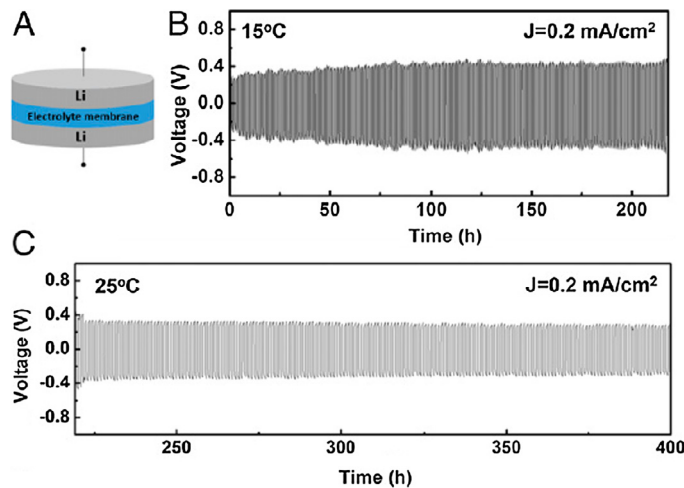


Fig. 2.21. (a) Depicts the schematic of a symmetric cell containing FRPC electrolyte membrane sandwiched between lithium, (b) and (c) voltage vs. time profile of lithium plating/stripping at a current density of 0.2 mA/cm^2 at 15 °C and at 25 °C respectively [217].

The mechanical stability of the prepared FRPC electrolyte membrane against Li dendrites was evaluated by using a symmetric Li|FRPC electrolyte|Li cell [217]. The membrane effectively blocked dendrites during repeated lithium stripping/plating at room temperature, with a current density of 0.2 mA/cm^2 for around 500 h and a current density of 0.5 mA/cm^2 for over 300 h as depicted in Fig. 2.21. The FRPC membrane shown superior electrochemical stability to high voltage and high mechanical stability to effectively block lithium dendrites and it can be used in electrochemical energy storage systems [217].

3. Structural analysis of lithium garnets

3.1. X-ray and neutron diffraction analysis

In order to understand the Li^+ transport properties in lithium garnets, knowledge of an accurate distribution of lithium in lithium garnets is necessary. Number of studies have been employed using both X-ray and neutron diffraction to determine the crystal structure of lithium garnets. Owing to the limitations of X-ray diffraction towards lithium, there exists an uncertainty in the determination of occupancy of lithium in stuffed lithium garnets through X-ray diffraction. Neutron powder diffraction measurement is relatively more sensitive in detecting the lithium atoms in stuffed lithium garnets.

Examination on the diffraction data (both X-ray and neutron diffraction) of conventional lithium garnet (stoichiometric) $\text{Li}_3\text{Ln}_3\text{Te}_2\text{O}_{12}$ ($\text{Ln} = \text{Y}, \text{Pr}, \text{Nd}, \text{Sm-Lu}$) by O'Callaghan et al. showed an unambiguous distributions of Ln^{3+} cations across 8-fold coordination site and Te^{6+} cation across 6-fold coordination site [114]. Neutron diffraction data collected from all the compounds in the series $\text{Li}_3\text{Ln}_3\text{Te}_2\text{O}_{12}$ ($\text{Ln} = \text{Y}, \text{Pr}, \text{Nd}, \text{Sm-Lu}$) indicated the presence of a cubic unit cell with a higher symmetry space group $la3d$ [114]. Analysis of neutron diffraction data on $\text{Li}_3\text{Ln}_3\text{Te}_2\text{O}_{12}$ indicated that the lithium precisely fill the tetrahedrally coordinated site (24d) leaving the octahedrally coordinated site vacant [114]. Investigations also indicated that the conventional lithium garnet structure can hold varying sizes of cations without any change in the symmetry [114]. Results on the neutron diffraction confirmed that $\text{Li}_3\text{Nd}_3\text{W}_2\text{O}_{12}$ [92] is isostructural with that of $\text{Li}_3\text{Ln}_3\text{Te}_2\text{O}_{12}$ and adopts the conventional garnet structure with Li^+ fully occupying the tetrahedrally coordinated site (24d) in the $[\text{Nd}_3\text{W}_2\text{O}_{12}]^{3-}$ framework as shown in Fig. 3.1 [92].

It is possible to change the lithium content in $\text{Li}_x\text{A}_3\text{B}_2\text{O}_{12}$ by the partial replacement of higher or lower oxidation state of either A or B cations. In conventional garnet structure, there exist interstices within the oxygen framework such as six fold coordinated 16b positions with the point symmetry 32, six fold coordinated 48g positions with point symmetry 2, and four fold coordinated 96h position with point symmetry 1 which can be filled by excess cations such as Li^+/H^+ [218].

Neutron diffraction studies on $\text{Li}_{3+x}\text{Nd}_3\text{Te}_{2-x}\text{Sb}_x\text{O}_{12}$ (partial replacement of hexavalent tellurium by pentavalent antimony) showed that, the Li^+ is distributed over a mixture of oxide tetrahedral and heavily distorted octahedral [96]. As the lithium content in $\text{Li}_{3+x}\text{Nd}_3\text{Te}_{2-x}\text{Sb}_x\text{O}_{12}$ was increased, the occupancy of the oxide octahedra increased continuously along with an increase in the vacancy concentration of the tetrahedral site [96].

The crystal structure of higher lithium content $\text{Li}_5\text{La}_3\text{M}_2\text{O}_{12}$ ($\text{M} = \text{Nb}, \text{Ta}$) was first proposed by Mazza [219] in 1988 by using PXRD (Powder X-ray Diffraction) data. Mazza predicted that the occupancy of La^{3+} on the A^{II} site, Nb^{5+} or Ta^{5+} on the B^{III} site, three Li^+ on the tetrahedrally coordinated Si^{IV} site and two additional Li^+ occupied the distorted octahedral coordinated site of the orthosilicates with chemical formula $\text{A}_3^{\text{II}}\text{B}_2^{\text{III}}(\text{SiO}_4)_3$ [219]. Later Hyooma and Hayashi predicted that $\text{Li}_5\text{Ln}_3\text{M}_2\text{O}_{12}$ ($\text{M} = \text{Nb}, \text{Ta}$) consist of a 3 dimensional network of $\text{La}, \text{Nb}(\text{Ta}), \text{O}$ that belonged to cubic unit cell with lower symmetry non-centrosymmetric space group of $I2_13$ (No. 199) [95]. They also predicted that the lithium atoms in $\text{Li}_5\text{Ln}_3\text{M}_2\text{O}_{12}$ ($\text{M} = \text{Nb}, \text{Ta}$) garnets may occupy two types of interstices i.e., undistorted Li (1) and distorted Li (2) octahedral sites [95].

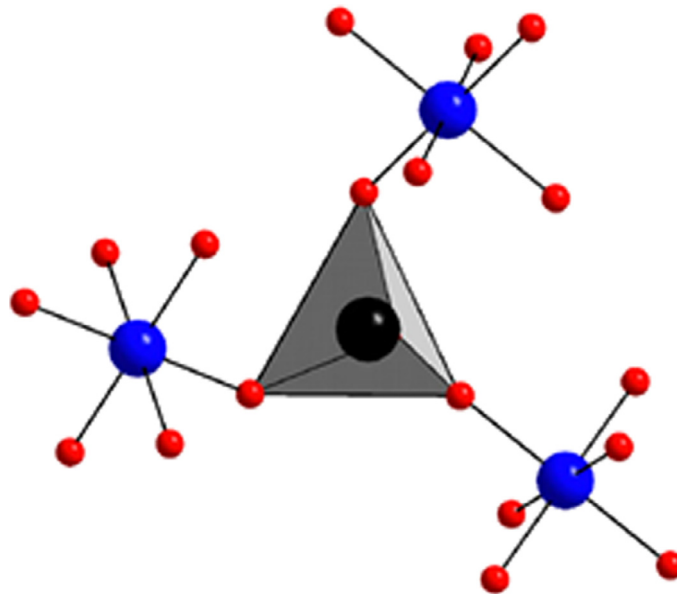


Fig. 3.1. The lithium cations in $\text{Li}_3\text{Nd}_3\text{W}_2\text{O}_{12}$ are in LiO_4 tetrahedron (gray) linked through shared apices with W (dark blue) which is octahedrally coordinated by oxide anions (red) [92].

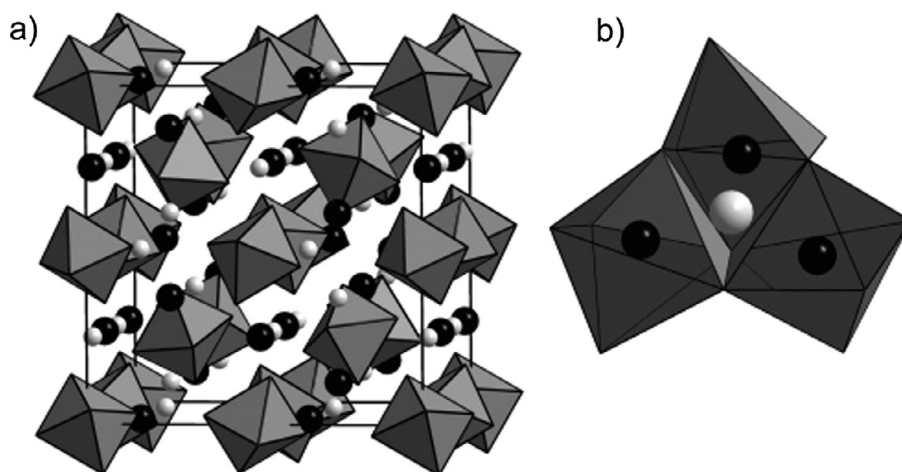


Fig. 3.2. (a) Crystal structure of $\text{Li}_5\text{La}_3\text{Ta}_2\text{O}_{12}$. The octahedra represent TaO_6 units whereas the dark and light spheres represent lanthanum and the tetrahedrally coordinated lithium, respectively [114] and (b) the oxide tetrahedron enclosing Li^+ on the 24d site (light gray) shares each face with an oxide octahedron, accommodating additional Li^+ on the 48g site (dark gray) [114].

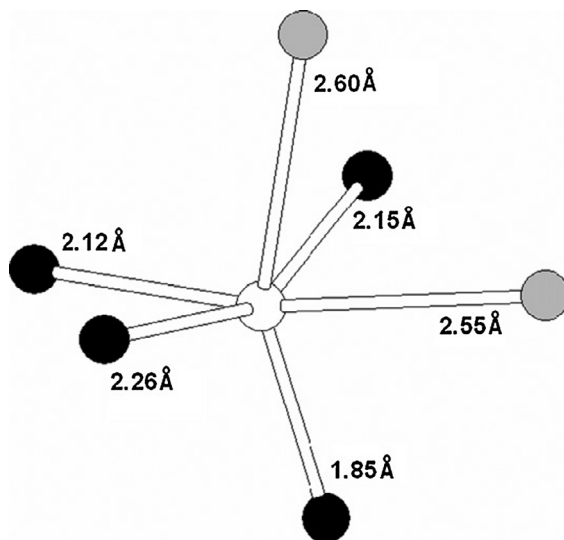


Fig. 3.3. Geometry of the Li2 site in $\text{Li}_5\text{La}_3\text{Sb}_2\text{O}_{12}$; white sphere represents Li whereas the black and the gray spheres represents four closest oxygen atoms in a distorted tetrahedral arrangement and the two most distant oxygen atoms, respectively [121].

Neutron diffraction investigations on the lithium distribution in $\text{Li}_5\text{La}_3\text{M}_2\text{O}_{12}$ ($M = \text{Nb}, \text{Ta}$) by Cussen et al. revealed that, the Li^+ occupies both tetrahedral site (24d) and distorted octahedral site (away from 48g towards 96h position) that which is normally vacant in the ideal garnet structure [220]. The crystal structure of $\text{Li}_5\text{La}_3\text{Ta}_2\text{O}_{12}$ predicted by O' Callaghan et al. is shown as Fig. 3.2 [114]. The structure of Sb containing lithium garnets $\text{Li}_5\text{Ln}_3\text{Sb}_2\text{O}_{12}$ ($\text{Ln} = \text{La}, \text{Pr}, \text{Nd}, \text{Sm}$) has been reported by Percival et al. [221]. The structural refinement of $\text{Li}_5\text{Nd}_3\text{Sb}_2\text{O}_{12}$ by Percival et al. using neutron diffraction also suggested that the Li is located both in the tetrahedral site (24d), as well as a more distorted octahedral site (96h) [121]. Moreover, a close inspection of the distorted octahedral site (96h) suggested that the coordination is approaching tetrahedral with a further two longer (2.6 Å) bonds as shown in Fig. 3.3.

Efforts have been made to identify the position occupied by lithium in the $\text{Li}_6\text{BaLa}_2\text{Ta}_2\text{O}_{12}$ garnet structure by using PXRD and neutron diffraction studies [222]. The lithium in $\text{Li}_6\text{BaLa}_2\text{Ta}_2\text{O}_{12}$ occupy partially at the tetrahedral 24d site (Li(1)) and at the distorted octahedral 96h site (Li(2)), whereas in ideal lithium garnet system Li^+ occupy exclusively in tetrahedral sites [222]. The increase in lithium content in $\text{Li}_6\text{BaLa}_2\text{Ta}_2\text{O}_{12}$ result into increase in the occupancy of Li (2) sites and simultaneous decrease in the occupancy in Li (1) sites which therefore increases the vacancies in tetrahedral (24d) sites.

Single-crystal X-ray structure analysis of tetragonal phase $\text{Li}_7\text{La}_3\text{Zr}_2\text{O}_{12}$ by Awaka et al. [157] predicted a space group $I4_1/acd$. The Li atom of tetragonal phase $\text{Li}_7\text{La}_3\text{Zr}_2\text{O}_{12}$ occupies three different sites i.e., Li(1) atoms occupy tetrahedral 8a

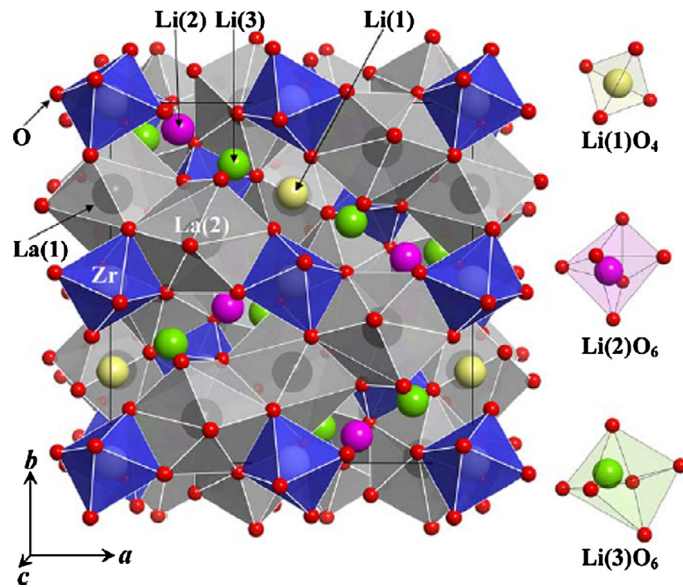


Fig. 3.4. Structure of tetragonal $\text{Li}_7\text{La}_3\text{Zr}_2\text{O}_{12}$ [157].

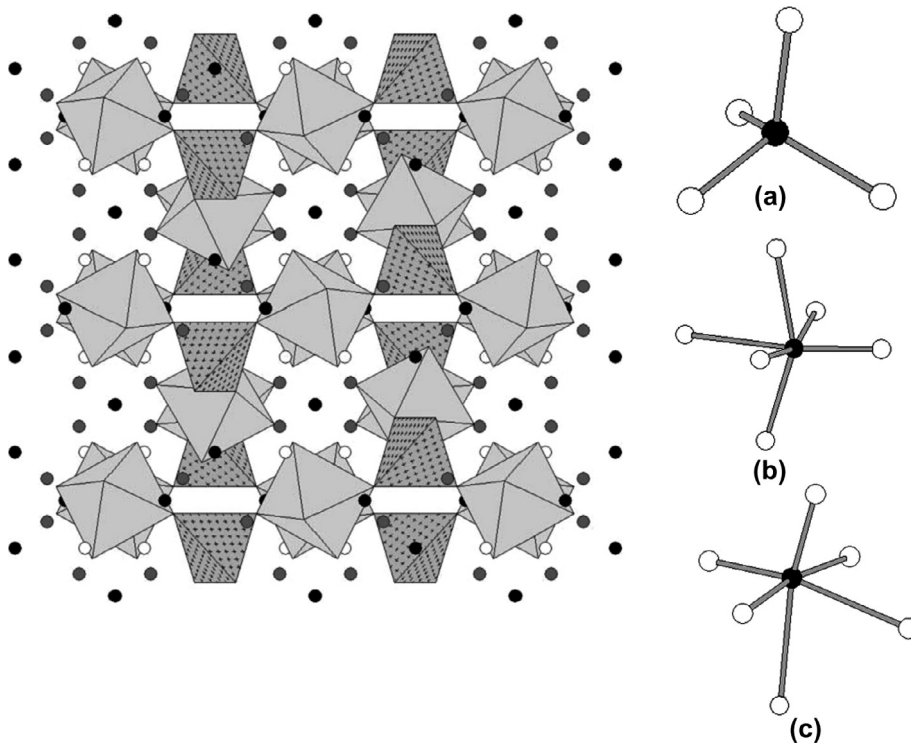


Fig. 3.5. Crystal Structure of $\text{Li}_7\text{La}_3\text{Sn}_2\text{O}_{12}$ (black spheres = La, light gray octahedra = SnO_6 , patterned gray tetrahedra = LiO_4 , gray spheres = Li2, white spheres = Li3) along with the local coordination in the three Li sites in (a) Li1, (b) Li2, (c) Li3 [112].

sites, Li(2) and Li(3) atoms occupy octahedral 16f and 32g sites, respectively [157] as shown in Fig. 3.4. Neutron diffraction studies on Sn containing lithium garnet $\text{Li}_7\text{La}_3\text{Sn}_2\text{O}_{12}$ (LLS) by Percival et al. indicated that $\text{Li}_7\text{La}_3\text{Sn}_2\text{O}_{12}$ takes tetragonal structure with space group $I4_1/acd$ [112]. The occupancy of lithium was found to be ordered in three fully occupied sites (Viz., Li(1), Li(2) and Li(3)) [112]. Also the neutron diffraction investigation indicated that unlike other cubic lithium garnets, tetragonal $\text{Li}_7\text{La}_3\text{Sn}_2\text{O}_{12}$ does not exhibit short Li-Li distance. Moreover, the *in situ* high temperature X-ray diffraction data on

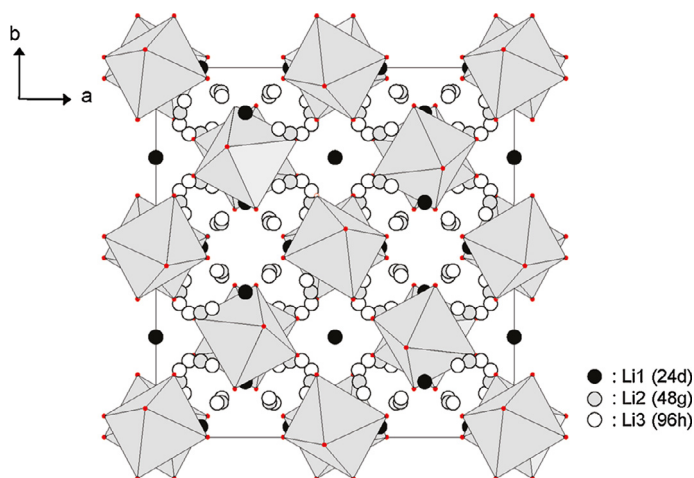


Fig. 3.6. Partial projection of $\text{Li}_{7-x}\text{H}_x\text{La}_3\text{Sn}_2\text{O}_{12}$ structure showing the three Li^+ sites [223].

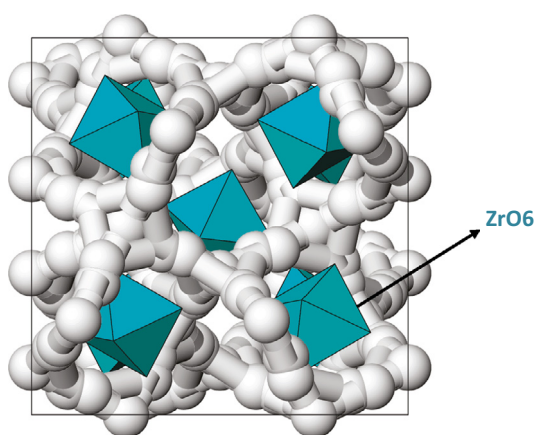


Fig. 3.7. Structure of cubic phase ($Ia\bar{3}d$) $\text{Li}_7\text{La}_3\text{Zr}_2\text{O}_{12}$. Lithium sites are represented by white spheres and ZrO_6 octahedra are represented by blue spheres [188].

$\text{Li}_7\text{La}_3\text{Sn}_2\text{O}_{12}$ indicated a reversible phase transition from tetragonal to cubic at around 750°C . The crystal structure of $\text{Li}_7\text{La}_3\text{Sn}_2\text{O}_{12}$ along with different geometries is illustrated in Fig. 3.5 [112].

Later, Galven et al. reported the transformation of tetragonal $\text{Li}_7\text{La}_3\text{Sn}_2\text{O}_{12}$ into cubic garnet phase with nominal composition $\text{Li}_{7-x}\text{H}_x\text{La}_3\text{Sn}_2\text{O}_{12}$ (Fig. 3.6) by means of Li^+/H^+ exchange [223]. Comparison of Li^+ distribution in $\text{Li}_7\text{La}_3\text{Sn}_2\text{O}_{12}$ and $\text{Li}_{7-x}\text{H}_x\text{La}_3\text{Sn}_2\text{O}_{12}$ revealed that, the Li1 site (24d) of the $\text{Li}_{7-x}\text{H}_x\text{La}_3\text{Sn}_2\text{O}_{12}$ cubic garnet corresponds to the two sites 8a and 16e in the tetragonal $\text{Li}_7\text{La}_3\text{Sn}_2\text{O}_{12}$. Similarly the Li2 site (48g) of $\text{Li}_{7-x}\text{H}_x\text{La}_3\text{Sn}_2\text{O}_{12}$ corresponds to the two sites Li2 (32g) and Li3 (16f). The Li3 (96h) site is empty in tetragonal $\text{Li}_7\text{La}_3\text{Sn}_2\text{O}_{12}$ [223].

Single-crystal X-ray structure analysis by Awaka et al. predicted cubic phase $\text{Li}_7\text{La}_3\text{Zr}_2\text{O}_{12}$ with a space group $Ia\bar{3}d$ [187]. In the cubic phase LLZO the Zr occupies 6-fold coordinated octahedral site and La occupy the 8-fold coordinated dodecahedral site [187]. Lithium occupy two sites i.e., tetrahedral 24d site and distorted octahedral 96h site which is vacant in ideal garnet structure [187]. Kotobuki et al. was the first to study the effect of Al_2O_3 on $\text{Li}_7\text{La}_3\text{Zr}_2\text{O}_{12}$ [224]. The significant factor in the phase formation of $\text{Li}_7\text{La}_3\text{Zr}_2\text{O}_{12}$ was resolved when Geiger et al. prepared cubic and tetragonal phase $\text{Li}_7\text{La}_3\text{Zr}_2\text{O}_{12}$ by means of two different sintering methods using alumina and platinum crucibles [188]. The samples prepared using alumina crucible crystallized in cubic phase on the other hand synthesized using platinum crucibles yielded purely tetragonal phase. The existence of cubic structure $\text{Li}_7\text{La}_3\text{Zr}_2\text{O}_{12}$ was due to the Al^{3+} contamination that might have resulted from high temperature sintering using alumina crucibles [188]. The crystal structure of cubic LLZO ($Ia\bar{3}d$) is shown in Fig. 3.7. The Al^{3+} replaces some of the Li^+ and increases the number of empty structural sites thereby increase the Li^+ mobility compared to the one prepared using platinum crucible. Consequently, doping Al^{3+} into LLZO has become a key way to stabilize the high Li^+ conducting cubic phase ($Ia\bar{3}d$).

Neutron diffraction studies on Ga doped $\text{Li}_{5.5}\text{La}_3\text{Zr}_2\text{Ga}_{0.5}\text{O}_{12}$ indicated the 0.5 Ga and 0.79 (3) Li on the tetrahedral Li1 site and the remaining 4.71 (3) Li on the distorted octahedral Li2 site [225]. Recent neutron diffraction refinements on Mo^{6+} substituted $\text{Li}_{7-2x}\text{La}_3\text{Zr}_{2-x}\text{Mo}_x\text{O}_{12}$ indicated that refinement considering Mo^{6+} in tetrahedra 24d site fails due to unrealistically high Mo^{6+} of 0.7 pfu. Further refinement indicated that Mo^{6+} located at the octahedrally coordinated 16a site of the cubic garnet structure with 0.256 per formula unit [226].

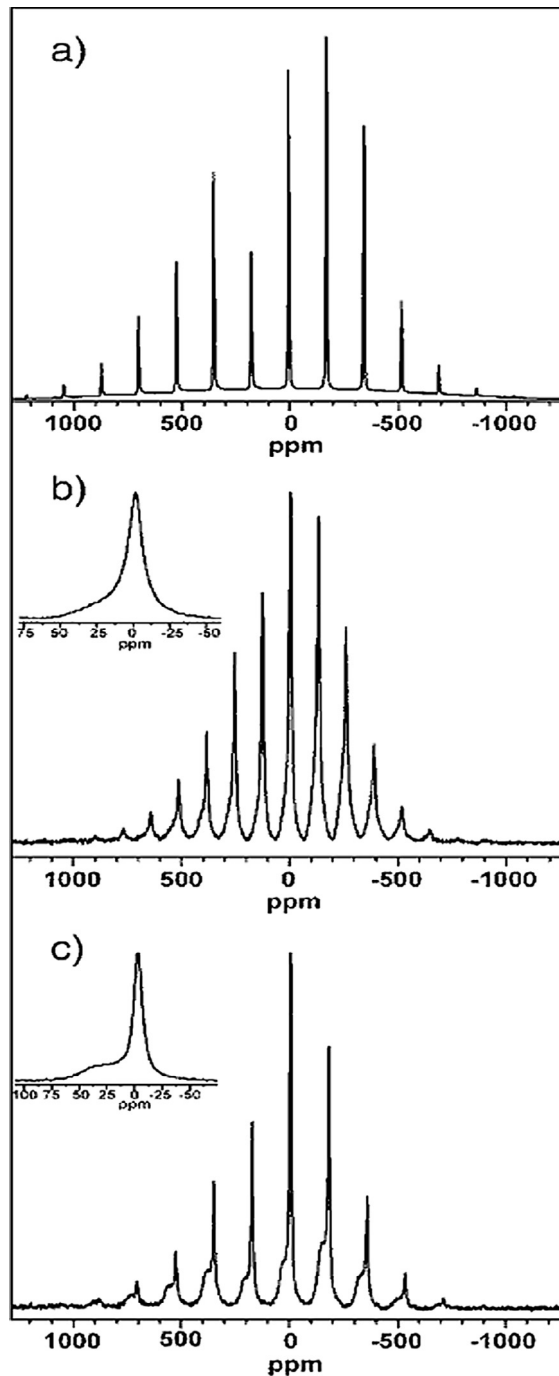


Fig. 3.8. ^7Li MAS spectrum of (a) $\text{Li}_3\text{Nd}_3\text{Te}_2\text{O}_{12}$ with lithium occupying tetrahedral site and (b) $\text{Li}_{4,0}\text{Nd}_3\text{SbTeO}_{12}$ and (c) $\text{Li}_{4,5}\text{Nd}_3\text{Sb}_{1,5}\text{Te}_{0,5}\text{O}_{12}$ with the occupancy of lithium in a mixture of tetrahedral and octahedral sites. The expansion of the centre band is shown in the insets (b) and (c) [96].

3.2. Nuclear magnetic resonance spectroscopy (NMR)

Nuclear Magnetic Resonance Spectroscopy (NMR) is an ideal method for probing the lithium local structures in lithium oxides. It is quite helpful to deliver further insights on Li^+ self diffusion from a microscopic point of view by taking advantage of methods that are sensitive to ion hopping on the Angstrom scale. In the most cases of the investigation of lithium garnets by solid state NMR spectroscopy, ^7Li isotopes were studied, this is because ^7Li nuclei have significantly higher natural abundance in comparison with ^6Li nuclei (^6Li :7.42%; ^7Li :92.58%). The foremost difference between ^7Li and ^6Li NMR spectra is that the observation of broadened peak in case of ^7Li NMR. This is because ^7Li NMR spectra are dominated by the quadrupolar interaction and the homonuclear dipolar coupling. Some residual broadening often remains, even under fast magic angle spinning (MAS) conditions. In contrast to ^7Li , the ^6Li offers much smaller quadrupolar moment and weaker homonuclear dipolar coupling hence allows higher resolution spectra with smaller number of spinning sidebands.

^7Li MAS NMR spectrum of conventional lithium garnet with composition $\text{Li}_3\text{Nd}_3\text{Te}_2\text{O}_{12}$ exhibited single narrow spinning side band at +10 ppm indicating the occupancy of Li on tetrahedrally coordinated site [96] as shown in Fig. 3.8. On the other hand, increase in the concentration of Li i.e., for $\text{Li}_{4.5}\text{Nd}_3\text{Te}_{0.5}\text{Sb}_{1.5}\text{O}_{12}$, two sideband manifolds were observed at –3 and 25 ppm, respectively. Comparison of the NMR spectrum of $\text{Li}_3\text{Nd}_3\text{Te}_2\text{O}_{12}$ with that of $\text{Li}_{4.5}\text{Nd}_3\text{Te}_{0.5}\text{Sb}_{1.5}\text{O}_{12}$ envisage that the narrower line observed at –3 ppm was due to the occupancy of lithium in tetrahedral sites, while the broader line at 25 ppm are due to the occupancy of lithium in octahedral sites [96].

In order to understand the location and Li^+ dynamics of stuffed lithium garnets with composition $\text{Li}_5\text{La}_3\text{Nb}_2\text{O}_{12}$ sintered at two different temperatures 850 and 900 °C Wullen et al. carried out ^7Li NMR, ^6Li NMR, ^6Li - $\{^7\text{Li}\}$ - Cross Polarization Magic angle spinning (CPMAS) NMR, ^6Li - $\{^7\text{Li}\}$ - Cross Polarization Magic angle spinning Rotational Echo Double Resonance (CPMS REDOR)-NMR and 2D- ^6Li - $\{^7\text{Li}\}$ -CPMAS Exchange NMR measurements [227]. Their investigation indicated the presence of two Li sites with different mobilities with 60% of Li occupied in tetrahedral coordinated site (full occupancy of the site) and the remaining lithium in octahedral site (1/3 of occupancy) for the sample sintered at 850 °C. In contrast, 2/3 of octahedral site and 1/3 of tetrahedral site are occupied for the sample sintered at 900 °C. Moreover, the temperature dependent NMR studies indicated that there was no exchange of Li between the two sites, in specific, the octahedrally coordinate Li cations are mobile species whereas tetrahedrally coordinated Li does not involved in Li^+ dynamics [227].

The earlier study on room temperature ^6Li MAS NMR spectra of tetragonal $\text{Li}_7\text{La}_3\text{Zr}_2\text{O}_{12}$ [228], revealed the occupancy of lithium in different sites (distorted octahedral interstices 16f, 32g and tetrahedral 8a site) [228]. In order to find the incorporation of Al into garnet ^{27}Al NMR has been studied extensively. The structure and ion dynamics studies of Al doped $\text{Li}_7\text{La}_3\text{Zr}_2\text{O}_{12}$ using ^{27}Al NMR revealed that Al^{3+} are located in 24d site that are responsible for the stabilization of cubic garnet structure ($Ia\bar{3}d$). A comparison of ^6Li MAS NMR spectra of Al doped $\text{Li}_7\text{La}_3\text{Zr}_2\text{O}_{12}$ with that of tetragonal Al free $\text{Li}_7\text{La}_3\text{Zr}_2\text{O}_{12}$ reported by Buschmann et al. as shown in Fig. 3.9 indicated that the former has a broad line width of 1.1 ppm even under MAS condition [161]. The signal with low intensity in case of tetragonal LLZO indicates the occupancy of Li^+ in tetrahedral 8a site. On the other hand, the absence of low intensity signals at tetrahedral 8a site in case of Al doped $\text{Li}_7\text{La}_3\text{Zr}_2\text{O}_{12}$ is the signature for the cubic nature of the sample [161].

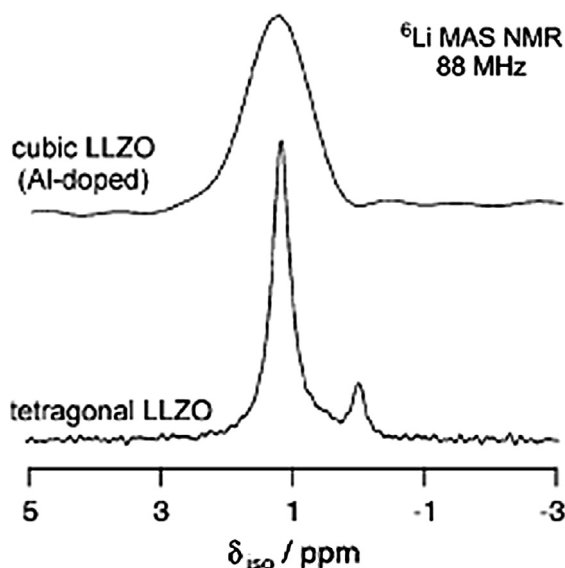


Fig. 3.9. ^6Li MAS NMR spectra of cubic and tetragonal LLZO [161].

Duvel et al. indicated that Al^{3+} replaces three Li^+ at lower doping concentration, whereas increase in Al concentration replaces both La^{3+} and Zr^{4+} sites, respectively in LLZO [229]. The results indicates that Al doping in the LLZO is not only restricted to Li sublattice but have an impact on the garnet framework itself [229].

The examination of disposition of Al cations during the formation of low temperature (850 °C) cubic LLZO using ^{27}Al NMR revealed that the Al slowly diffuse into the garnet structure and initially forms Li_5AlO_4 which then later reacts with tetragonal phase and transforms into cubic phase LLZO [230]. Moreover, ^{27}Al NMR exhibits overlap resonances suggesting multiple Al environments that arise due to the disorder created by the 24d Li site that which results in the formation of the low temperature cubic phase [230].

^{71}Ga NMR study on $\text{Li}_{5.5}\text{La}_3\text{Zr}_2\text{Ga}_{0.5}\text{O}_{12}$ exhibited a single broad peak with a chemical shift of ≈ 221 ppm which gave a clear insight that Ga is located on the tetrahedra 24d site [225]. Bottke et al. studied the NMR relaxometry and stimulated echo NMR of Mo^{6+} doped $\text{Li}_{6.5}\text{La}_3\text{Zr}_{1.75}\text{Mo}_{0.25}\text{O}_{12}$ [231]. The NMR results obtained using ^7Li NMR spin-alignment echo correlation spectroscopy forecasted that both 24d and 96h sites involving in the Li^+ diffusion. Moreover, the results indicated that unlike LLZO-based garnets the Li sublattice of $\text{Li}_{6.5}\text{La}_3\text{Zr}_{1.75}\text{Mo}_{0.25}\text{O}_{12}$ remains intact offering the possibility to get into a depth of Li^+ dynamics [231].

In order to the find the relation between local structures and dynamic properties of Al and Ga substituted LLZO a systematic investigation has been carried out in cubic mixed-doped $\text{Li}_{7-3(x+y)}\text{Ga}_x\text{Al}_y\text{La}_3\text{Zr}_2\text{O}_{12}$ using ^{27}Al and ^{71}Ga NMR by Rettenwander et al. [232]. Two resonances corresponding to the occupancy of 24d (243 ppm) and 96h sites (193 ppm) had been observed using ^{71}Ga MAS NMR spectra recorded at 21.1 T. This behavior of Ga indicates that it is similar to that of Al. Earlier ^{71}Ga NMR studies by Howard et al. [225] and Rettenwander et al. [232] of doped LLZO revealed the occupancy of only one of the two sites (96h) at an applied field of 9.4 T with relatively slow sample spinning. On the other hand, investigation on ^{71}Ga NMR by Bernuy-Lopez et al. [233] indicated the occupancy of 24d signal at 11.75 T with fast sample spinning. It has been suggested that the lower spinning rate might be the reason for the absence of 96h signal in case of first two studies. The observation of both 24d and 96h sites in the Ga doped LLZO indicated that Ga can populate both the 96h and 24d sites in the Ga doped LLZO [234].

3.3. Raman spectroscopy

Raman scattering is a very powerful and useful technique for acquiring structural information on the Li^+ conductive oxides. Raman spectroscopy provides additional structural information on lithium garnets compared to that of powder X-ray diffractions. For a deeper understanding of the Raman spectra of lithium garnets, detailed Raman spectroscopic studies on single crystals along with a factor group analysis of vibrational modes are essential. Unfortunately attempt to grow single

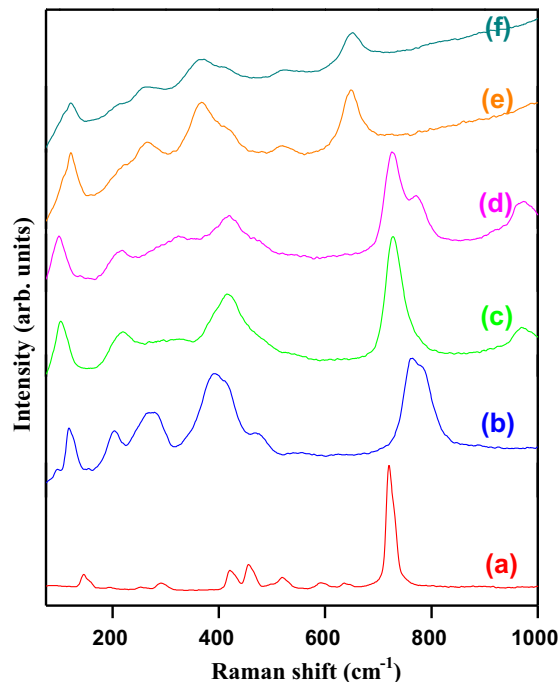


Fig. 3.10. Raman spectra of (a) $\text{Li}_3\text{Y}_3\text{Te}_2\text{O}_{12}$, (b) $\text{Li}_5\text{La}_3\text{Ta}_2\text{O}_{12}$, (c) $\text{Li}_6\text{La}_2\text{BaTa}_2\text{O}_{12}$, (d) $\text{Li}_{6.5}\text{La}_{1.5}\text{Ba}_{1.5}\text{Ta}_2\text{O}_{12}$, (e) $\text{Li}_7\text{La}_3\text{Zr}_2\text{O}_{12}$ and (f) $\text{Li}_{7.5}\text{La}_{2.5}\text{Sr}_{0.5}\text{Zr}_2\text{O}_{12}$ sintered at different elevated temperatures measured in the range 75–1000 cm^{-1} [116].

crystals of lithium garnets with appreciable size for polarized Raman studies were unsuccessful. For several lithium metal oxide materials and lithium garnets it has been demonstrated that the internal modes of LiO_6 appear in the range $200\text{--}300\text{ cm}^{-1}$, whereas the internal modes of LiO_4 occur in the range $350\text{--}500\text{ cm}^{-1}$ [235,236]. Because of the complex nature of the structure of lithium garnets, considerable mixing between internal modes of LiO_4 , LiO_6 and the other coordinated groups present in the structure is expected, and thus the interpretation of Raman spectra of lithium garnets becomes much more complicated.

The Raman spectra of $\text{Li}_x\text{A}_3\text{B}_2\text{O}_{12}$ with $3 \leq x \leq 7.5$ sintered at elevated temperatures measured in the range $75\text{--}1000\text{ cm}^{-1}$ shown in Fig. 3.10 [116] indicated appreciable variation in peak positions, line width and integrated intensity of the various internal modes. For better understanding of the nature of distribution of lithium atoms among tetrahedral and octahedral sites the Raman spectra of $\text{Li}_x\text{A}_3\text{B}_2\text{O}_{12}$ with $3 \leq x \leq 7.5$ measured in the range $200\text{--}500\text{ cm}^{-1}$ corresponding to that of the internal modes of LiO_6 and LiO_4 are shown in Fig. 3.11. Investigations on structure of the conventional cubic garnet $\text{Li}_3\text{Nd}_3\text{Te}_2\text{O}_{12}$ indicated that lithium housed exclusively on a filled tetrahedral site [114]. Hence, in the cubic garnet $\text{Li}_3\text{Y}_3\text{Te}_2\text{O}_{12}$ all the Li^+ are expected to occupy the tetrahedral $\text{Li}(1)$ 24d site and no ion in the octahedral $\text{Li}(2)$ sites, which is well reflected in the Raman spectrum of $\text{Li}_3\text{Y}_3\text{Te}_2\text{O}_{12}$ shown in Fig. 3.11(a). The relatively well defined sharp Raman bands observed at 421 cm^{-1} and 457 cm^{-1} in the expected LiO_4 internal mode region for the $\text{Li}_3\text{Y}_3\text{Te}_2\text{O}_{12}$ compared to that of the remaining investigated samples indicated the occupancy of Li only in the tetrahedral site [116].

As the Li^+ concentration i.e., the x value in these garnet-type ion conductors $\text{Li}_x\text{A}_3\text{B}_2\text{O}_{12}$ increases there is a redistribution of the Li^+ over the available $\text{Li}(1)$ and $\text{Li}(2)$ sites. Neutron diffraction studies on $\text{Li}_x\text{A}_3\text{B}_2\text{O}_{12}$ with $x = 5\text{--}6.6$ reveals the reduction in the occupancy of the tetrahedral site with an associated increase in the octahedral site along with the displacement off their original central 48g sites to the distorted 96h sites [222]. Percival et al. suggested that the distorted octahedral site may be described appropriately in terms of distorted tetrahedral arrangement with two longer bonds [121]. Hence, the Raman bands observed in the region $300\text{--}450\text{ cm}^{-1}$ may correspond to the expected internal modes of LiO_4 and distorted octahedral site for the samples $\text{Li}_5\text{La}_3\text{Ta}_2\text{O}_{12}$, $\text{Li}_6\text{La}_2\text{BaTa}_2\text{O}_{12}$ and $\text{Li}_{6.5}\text{La}_{1.5}\text{Ba}_{1.5}\text{Ta}_2\text{O}_{12}$. The presence of broad band in the region $300\text{--}450\text{ cm}^{-1}$ of the Raman spectra of $\text{Li}_5\text{La}_3\text{Ta}_2\text{O}_{12}$, $\text{Li}_6\text{La}_2\text{BaTa}_2\text{O}_{12}$ and $\text{Li}_{6.5}\text{La}_{1.5}\text{Ba}_{1.5}\text{Ta}_2\text{O}_{12}$ compared to $\text{Li}_3\text{Y}_3\text{Te}_2\text{O}_{12}$ in Fig. 3.11 supports this prediction [116].

The Raman spectrum of cubic phase $\text{Li}_7\text{La}_3\text{Zr}_2\text{O}_{12}$ shown in Fig. 3.11(e) indicates a broad band centered at around 370 cm^{-1} and a shoulder band at around 420 cm^{-1} . The Raman spectrum of $\text{Li}_{7.5}\text{La}_{2.5}\text{Sr}_{0.5}\text{Zr}_2\text{O}_{12}$ shown in Fig. 3.11(f) do not show any major change except a slight change in the position, decrease in intensity and increase in the broadness of the bands compared to that of $\text{Li}_7\text{La}_3\text{Zr}_2\text{O}_{12}$. The Raman spectra of $\text{Li}_7\text{La}_3\text{Zr}_2\text{O}_{12}$ (Fig. 3.11(e)) and $\text{Li}_{7.5}\text{La}_{2.5}\text{Sr}_{0.5}\text{Zr}_2\text{O}_{12}$ (Fig. 3.11(f)) indicated the changes in the nature of the lithium environment compared to that of the other investigated lithium garnets [116].

The major difference observed between the Raman spectra of the cubic ($Ia\bar{3}d$) and tetragonal ($I4_1/acd$) phase of LLZO is the presence of a larger number of Raman peaks or bands for tetragonal than that of the cubic phase particularly in the region $200\text{--}500\text{ cm}^{-1}$. The broad spectral features of the cubic garnet in the region $200\text{--}500\text{ cm}^{-1}$ might be due to the static or

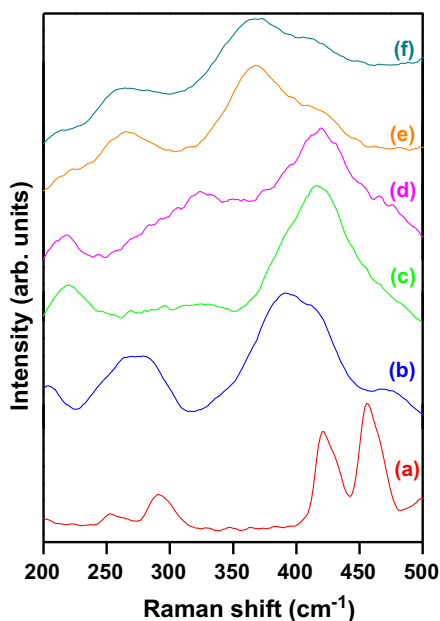


Fig. 3.11. Raman spectra of (a) $\text{Li}_3\text{Y}_3\text{Te}_2\text{O}_{12}$, (b) $\text{Li}_5\text{La}_3\text{Ta}_2\text{O}_{12}$, (c) $\text{Li}_6\text{La}_2\text{BaTa}_2\text{O}_{12}$, (d) $\text{Li}_{6.5}\text{La}_{1.5}\text{Ba}_{1.5}\text{Ta}_2\text{O}_{12}$, (e) $\text{Li}_7\text{La}_3\text{Zr}_2\text{O}_{12}$ and (f) $\text{Li}_{7.5}\text{La}_{2.5}\text{Sr}_{0.5}\text{Zr}_2\text{O}_{12}$ sintered at different elevated temperatures measured in the range $200\text{--}500\text{ cm}^{-1}$ [116].

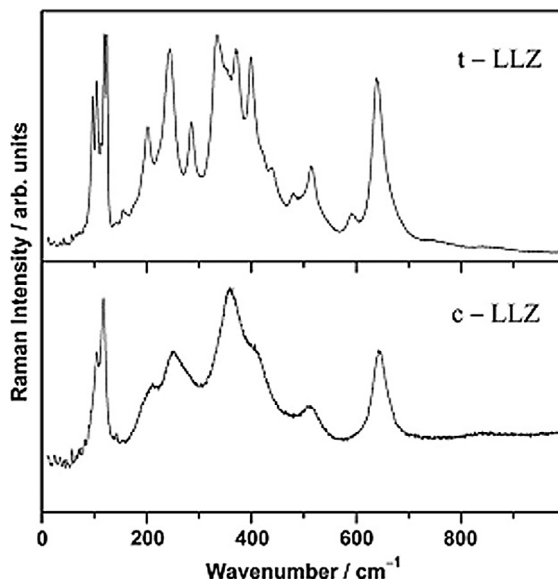


Fig. 3.12. Unpolarized micro-Raman spectra of tetragonal-LLZO and of cubic LLZO [237].

dynamic disorder of highly mobile Li^+ compared to the ordered arrangement in the tetragonal phase as shown in Fig. 3.12 [237]. The Raman spectrum in the intermediate-energy region of cubic LLZO exhibits a few broad and fairly overlapping bands associated with degenerate Raman modes, which turn out partly split in the tetragonal LLZO phase, due to its lower symmetry, thus originating a higher number of observed peaks. The weak intense band at 209 cm^{-1} , strong peak at 248 cm^{-1} , medium strong peak at 291 cm^{-1} , and strong intense peak at $346, 370,$ and 404 cm^{-1} are the characteristic Raman peaks observed for tetragonal LLZO. The medium intense broad band at 263 cm^{-1} , medium strong broad band at 366 cm^{-1} , and medium broad shoulder at 417 cm^{-1} are the characteristic Raman bands observed for the cubic LLZO.

Apart from high conductive cubic phase ($Ia\bar{3}d$) and tetragonal phase ($I4_1/acd$) there exist another phase in LLZO; The low temperature cubic phase. Raman spectra of both tetragonal and cubic phase LLZO (0.25 mol of Al added) revealed that the

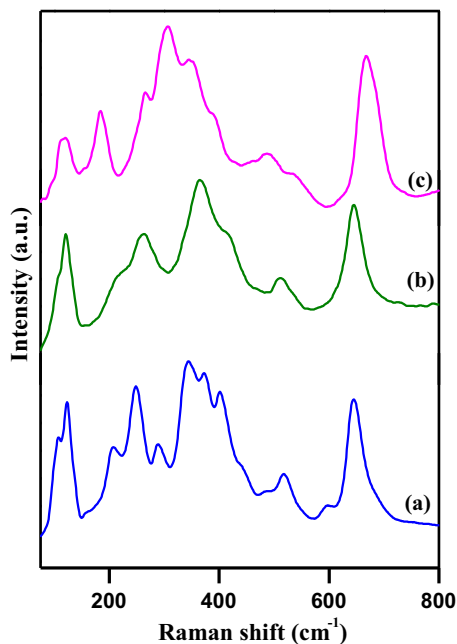


Fig. 3.13. Raman spectra of (a) tetragonal ($I4_1/acd$) phase LLZO, (b) high Li^+ conductive cubic ($Ia\bar{3}d$) phase LLZO and (c) low temperature cubic phase LLZO [148,176].

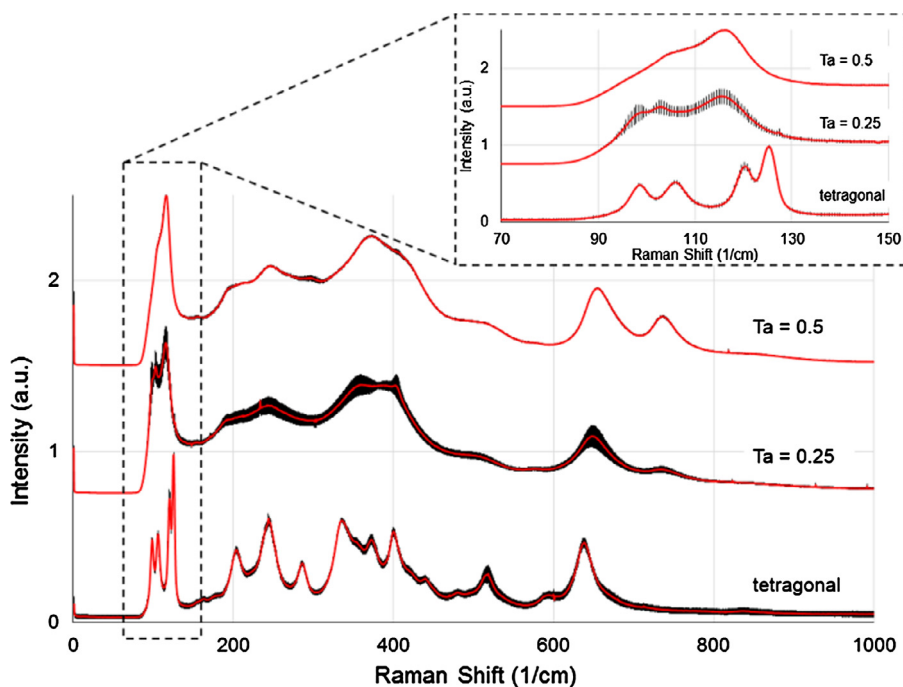


Fig. 3.14. Raman spectra for the sub-critically doped composition $\text{Li}_{6.75}\text{La}_3\text{Zr}_{1.75}\text{Ta}_{0.25}\text{O}_{12}$, and the critically doped composition $\text{Li}_{6.5}\text{La}_3\text{Zr}_{1.5}\text{Ta}_{0.5}\text{O}_{12}$. Inset shows the magnification of the bands near 110 cm^{-1} [239].

tetragonal phase or lithium-deficient lithium garnets were reported to be sensitive to humid conditions [238]. The formation of a low temperature cubic phase well below the usual tetragonal to cubic transition temperature is found to depend upon hydration mechanisms [238]. The nature of the high and low temperature cubic garnets is totally different: the one found above the phase transition (tetragonal to cubic) at higher temperature does not involve any major change in the stoichiometry, whereas the cubic phase formed at low temperature might be due to the effect of the insertion of water molecules and the protonation through the H^+/Li^+ exchange mechanism into the garnet structure.

The Raman spectra of tetragonal phase ($I4_1/acd$) LLZO, high Li^+ conductive cubic phase ($Ia\bar{3}d$) and low temperature cubic phase LLZO reported by Dhivya et al. [148,176] in the range $75\text{--}800\text{ cm}^{-1}$ are shown in Fig. 3.13(a)–(c), respectively. The Raman bands observed in the range $200\text{--}500\text{ cm}^{-1}$ (Fig. 3.13(b) and (c)) corresponding to the expected internal modes of LiO_4 and LiO_6 clearly revealed the major difference between the high Li^+ conductive cubic phase and low temperature cubic LLZO. The Raman spectrum of the low temperature cubic phase LLZO shown in Fig. 3.13(c) revealed strong intense peak at around 307 and 668 cm^{-1} , medium intense bands at around 120 , 184 , 263 , 344 and 380 cm^{-1} and a weak bands at around 487 and 534 cm^{-1} . The presence of relatively larger number of Raman modes in the region $200\text{--}500\text{ cm}^{-1}$ for the low temperature cubic phase LLZO might be due to the ordered arrangements of lithium in the crystal lattice [148,176]. In addition to the above difference in the Raman spectra of the low temperature cubic phase LLZO (Fig. 3.13(c)) and high Li^+ conductive cubic phase LLZO (Fig. 3.13(b)) an appreciable shift in the positions of vibrational stretching mode of ZrO_6 octahedral units is observed. The shift of approximately 23 cm^{-1} towards higher wave number for the $\text{Zr}\text{--O}$ stretching mode and sharpening of the Raman bands in the region of internal modes of LiO_4 and LiO_6 for the low temperature cubic phase as shown in Fig. 3.13(c) revealed an appreciable modification in the bonding nature of the low temperature cubic and high Li^+ conductive cubic phase LLZO [148,176].

Experimental observation with the substitution of Al^{3+} for Li in LLZO shows that a Li vacancy concentration of about $0.4\text{--}0.5$ atoms per formula unit is necessary to stabilize the cubic phase LLZO [239]. Similarly it is possible to create Li vacancy by substituting Zr^{4+} with that of Ta^{5+} and Nb^{5+} . Investigation on Raman spectroscopy of Al -free subcritically doped ($\text{Li}_{6.75}\text{La}_3\text{Zr}_{1.75}\text{Ta}_{0.25}\text{O}_{12}$) and critically doped ($\text{Li}_{6.5}\text{La}_3\text{Zr}_{1.5}\text{Ta}_{0.5}\text{O}_{12}$) compositions by Thompson et al. shown in Fig. 3.14 revealed that the Raman spectrum exhibited a mixture of cubic and tetragonal phases around the subcritically doped levels of 0.25 Li vacancies per formula unit [239]. It also supports the earlier predictions of $0.4\text{--}0.5$ Li vacancies required to stabilize the cubic phase [239].

4. Li^+ conductivity of lithium garnets

Observation of high Li^+ conductivity in $\text{Li}_5\text{La}_3\text{M}_2\text{O}_{12}$ ($\text{M} = \text{Nb}, \text{Ta}$) by Thangadurai et al. [90] stimulated significant research interest towards understanding the origin of high Li^+ conduction and conductivity optimizations by chemical substitutions

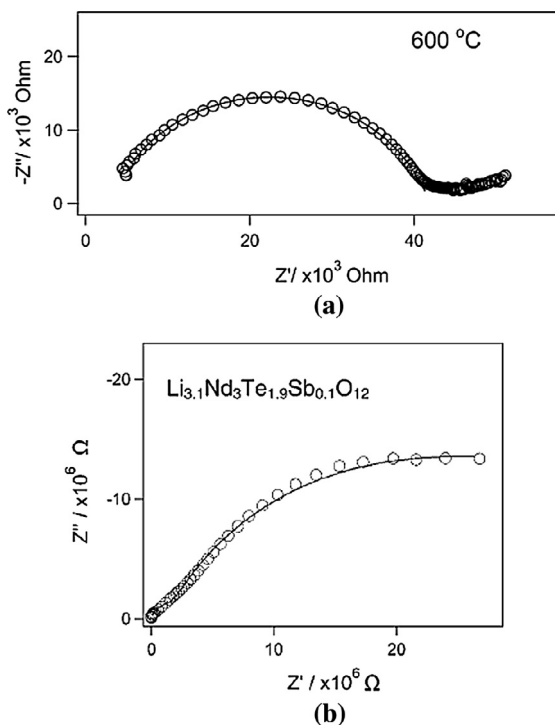


Fig. 4.1. AC impedance plots of (a) $\text{Li}_3\text{Nd}_3\text{Te}_2\text{O}_{12}$ measured using Pt ion-blocking electrodes at 600 °C [114] and (b) $\text{Li}_{3.1}\text{Nd}_3\text{Te}_{1.9}\text{Sb}_{0.1}\text{O}_{12}$ at 47 °C. The solid line represents the fit obtained to the data using an equivalent circuit model consisting of a constant phase element (CPE) in series with two CPE/resistor parallel components [96].

and structural modifications in lithium garnets [90,97,98,133,157]. AC impedance spectroscopy is a powerful technique for the study of Li^+ conduction in stuffed lithium garnets. Measurement of the electrical conductivity for polycrystalline materials using impedance spectroscopy provides information relating to the electrical behavior of both the grain interiors and the grain-boundary regions. Generally polycrystalline materials exhibit large grain-boundary resistance in addition to the

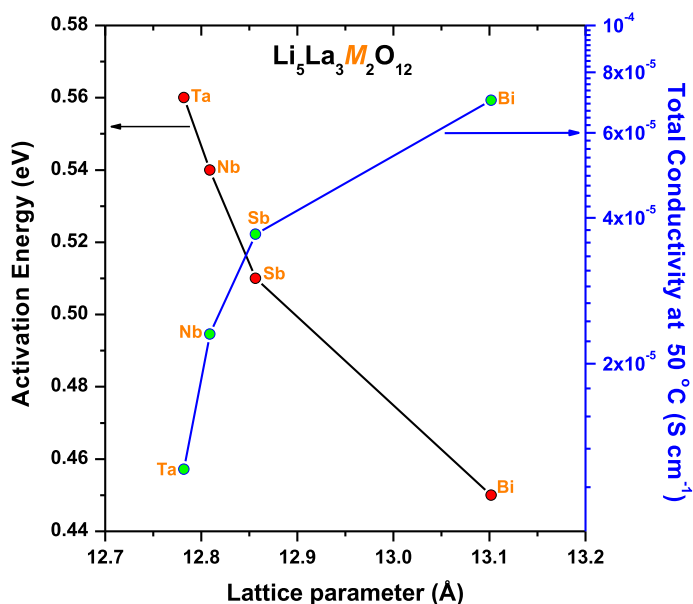


Fig. 4.2. Correlation between total (bulk + grain-boundary) Li^+ conductivity and activation energy vs lattice parameter of the $\text{Li}_5\text{La}_3\text{M}_2\text{O}_{12}$ (M = Ta, Nb, Sb and Bi) series [118].

bulk resistance. A number of studies have shown that the inter- and intra-grain conductivity found to be of the same order of magnitude in stuffed lithium garnets [90,97,98,133,157]. Moreover, at higher temperatures it is not possible to resolve these different processes. Hence for experimental and practical reasons of applications the ion transport in these systems has been described mostly using the total (bulk + grain-boundary) lithium ion conductivity.

Examination on the transport properties of ideal lithium garnet with nominal composition $\text{Li}_3\text{Nd}_3\text{Te}_2\text{O}_{12}$ indicated that the room temperature conductivity could not be measured accurately since the Li^+ mobility was abridged to more than a few orders of magnitude. An increase in the Li^+ conductivity was observed with an increase in the temperature and total (bulk + grain-boundary) Li^+ conductivity of $1 \times 10^{-5} \text{ S cm}^{-1}$ was observed at 600°C (Fig. 4.1(a)) with an activation energy (E_a) of 1.22 eV over the investigated temperature range [114].

It is possible to continuously change the lithium content in the garnet framework $\text{Li}_x\text{A}_3\text{B}_2\text{O}_{12}$ by the partial replacement of higher or lower oxidation state of either A or B cations. The partial replacement of hexavalent tellurium by pentavalent antimony in $\text{Li}_{3+x}\text{Nd}_3\text{Te}_{2-x}\text{Sb}_x\text{O}_{12}$ shows the variation of Li^+ conduction by two orders of magnitude ($1 \times 10^{-8} \text{ S cm}^{-1}$) with an increase in the lithium content even for a small doping of about 0.05 of Sb i.e., $\text{Li}_{3.05}\text{Nd}_3\text{Te}_{1.95}\text{Sb}_{0.05}\text{O}_{12}$ [222]. The observed enhancement in the Li^+ conductivity is due to an increase in the occupancy of the oxide octahedra with a simultaneous increase in the vacancy concentration of the tetrahedral site [96]. Relatively low value of activation energy of about 0.59 eV has been observed for $\text{Li}_{3.05}\text{Nd}_3\text{Te}_{1.95}\text{Sb}_{0.05}\text{O}_{12}$ which is two times smaller than that of the conventional $\text{Li}_3\text{Nd}_3\text{Te}_2\text{O}_{12}$ [96]. This observed step-change in the activation energy of $\text{Li}_{3+x}\text{Nd}_3\text{Te}_{2-x}\text{Sb}_x\text{O}_{12}$ indicates that the Li^+ conduction in the garnet structure increases with lithium content $x > 3$ in $\text{Li}_x\text{A}_3\text{B}_2\text{O}_{12}$. The AC impedance plot $\text{Li}_{3.1}\text{Nd}_3\text{Te}_{1.9}\text{Sb}_{0.1}\text{O}_{12}$ measured at 47°C is shown in Fig. 4.1(b).

Further increase in lithium content i.e., $\text{Li}_5\text{La}_3\text{M}_2\text{O}_{12}$ ($M = \text{Nb, Ta}$) exhibited total Li^+ conductivity of $\sim 10^{-6} \text{ S cm}^{-1}$ at 25°C [90]. Systematic studies on $\text{Li}_5\text{La}_3\text{M}_2\text{O}_{12}$ ($M = \text{Ta, Nb, Sb and Bi}$) by Murugan et al. [119,118] revealed that there exist a correlation between the lattice parameter and Li^+ conductivity. Li^+ conductivity increases with increase in the lattice parameter in the order $\text{Ta} < \text{Nb} < \text{Sb} < \text{Bi}$ [118]. The correlation between the Li^+ conductivity and activation energy vs lattice parameter of the $\text{Li}_5\text{La}_3\text{M}_2\text{O}_{12}$ ($M = \text{Ta, Nb, Sb and Bi}$) series are shown in Fig. 4.2 [118].

Chemical composition with the partial substitution of trivalent La^{3+} by K^+ and Nb^{5+} by In^{3+} in $\text{Li}_5\text{La}_3\text{Nb}_2\text{O}_{12}$ has been investigated by Thangadurai et al. to understand the relationship between compositions, structure and electrical properties [117]. The electrical conductivity of $\text{Li}_5\text{La}_3\text{Nb}_2\text{O}_{12}$ increased due to the replacement of In and K. In-substituted sample $\text{Li}_{5.5}\text{La}_3\text{Nb}_{1.75}\text{In}_{0.25}\text{O}_{12}$ prepared at 950°C exhibited the maximized bulk ionic conductivity of $1.8 \times 10^{-4} \text{ S cm}^{-1}$ at 50°C with the activation energy of 0.51 eV [117].

In order to understand the role of lithium concentration and the effect of the size of the other dopant ions a partial replacement of La^{3+} by divalent alkaline earth ions in $\text{Li}_5\text{La}_3\text{M}_2\text{O}_{12}$ ($M = \text{Nb, Ta}$) has been investigated [240]. This leads to a new series of lithium garnet with general formula $\text{Li}_6\text{La}_2\text{AM}_2\text{O}_{12}$ ($A = \text{Ca, Sr, Ba; M = Nb, Ta}$) [132,240]. Among the investigated materials in this series, the tantalum based compound with composition $\text{Li}_6\text{La}_2\text{BaTa}_2\text{O}_{12}$ exhibited maximized Li^+ conductivity of $4 \times 10^{-5} \text{ S cm}^{-1}$ at 22°C with activation energy of 0.40 eV as shown in Fig. 4.3 [240].

Impedance plot of $\text{Li}_6\text{SrLa}_2\text{Sb}_2\text{O}_{12}$ measured at 24°C using Au blocking electrode exhibited one semicircle at a higher frequency regime and a tail at lower frequency domain [119]. Careful analyses on the impedance spectra of $\text{Li}_6\text{SrLa}_2\text{Sb}_2\text{O}_{12}$ indicated that the observed semicircle is slightly compressed [119]. The experimental impedance data points of $\text{Li}_6\text{SrLa}_2\text{Sb}_2\text{O}_{12}$ measured at 24°C fitted with an equivalent circuit consisting of parallel resistance-constant phase element for bulk conduction. The total (bulk + grain-boundary) and bulk ionic conductivity of $\text{Li}_6\text{SrLa}_2\text{Sb}_2\text{O}_{12}$ was found to be in the order of 6.3×10^{-6} and $6.6 \times 10^{-6} \text{ S cm}^{-1}$, respectively at 24°C (Fig. 4.4(a)) [119]. The combined impedance and modulus plot of $\text{Li}_6\text{SrLa}_2\text{Sb}_2\text{O}_{12}$ emphasize the contribution of the grain-boundary to the total resistance. The presence of a single peak as shown in Fig. 4.4(b) indicates that electrical responses are due to the bulk and apparently the grain-boundary contribution is very small. The SEM investigation as shown in Fig. 4.4(c) revealed that $\text{Li}_6\text{SrLa}_2\text{Sb}_2\text{O}_{12}$ exhibited well crystallized grains and good contact area with the neighboring grains thereby reducing the grain-boundary contribution to the total resistance [119].

A systematic investigation on $\text{Li}_{5+x}\text{La}_{3-x}\text{Ba}_x\text{Ta}_2\text{O}_{12}$ ($x = 0, 0.25, 0.50, 1.00, 1.25, 1.50, 1.75, 2.00$) was carried out by Murugan et al. to explore the dependence of Li^+ conductivity with the lithium as well as the barium content [241]. The cubic lattice parameter found to be increased with an increase of x and reaches a maximum for composition $\text{Li}_6\text{La}_2\text{BaTa}_2\text{O}_{12}$ i.e., for $x = 1.0$ and then started to decrease with the further increase of lithium and barium content [241]. A further increase in lithium and barium content ($x = 1.5, 1.75$ and 2) leads the formation of the secondary phase together with the major garnet phase resulting in the reduction of the ionic conductivity with an associated increase in the activation energy. Among the investigated compounds, $\text{Li}_{6.25}\text{La}_{1.75}\text{Ba}_{1.25}\text{Ta}_2\text{O}_{12}$ exhibited the highest total (bulk + grain-boundary) and bulk ionic conductivity of $5 \times 10^{-5} \text{ S cm}^{-1}$ and $7.4 \times 10^{-5} \text{ S cm}^{-1}$, respectively, at 33°C [241].

Among the reported lithium garnets $\text{Li}_7\text{La}_3\text{Zr}_2\text{O}_{12}$ (LLZO) discovered by Murugan et al. has received much attention in recent times due to its relatively high Li^+ conductivity and chemical stability with lithium metal [97,98]. LLZO exhibited a bulk and total (bulk + grain-boundary) Li^+ conductivity of $5.11 \times 10^{-4} \text{ S cm}^{-1}$ and $7.74 \times 10^{-4} \text{ S cm}^{-1}$ respectively at 25°C with the activation energy for the Li^+ conductivity falls in the range 0.41 eV as shown in Fig. 4.5. The observed high Li^+ conductivity is comparable with the total (bulk + grain-boundary) Li^+ conductivity ($6.6 \times 10^{-4} \text{ S cm}^{-1}$ at 27°C) of polycrystalline Li_3N [34]. A comparison of Li^+ conductivity of $\text{Li}_7\text{La}_3\text{Zr}_2\text{O}_{12}$ with other well known fast Li^+ conductors is shown in Fig. 4.6 [97,98]. The LLZO was stable against the molten lithium [97,98]. Attempts to replace Zr^{4+} by means of other tetravalent cations led to a similar cubic phase system with composition $\text{Li}_7\text{La}_3\text{Hf}_2\text{O}_{12}$. The cubic phase $\text{Li}_7\text{La}_3\text{Hf}_2\text{O}_{12}$ exhibited a total (bulk + grain-boundary) Li^+ conductivity of around $5 \times 10^{-5} \text{ S cm}^{-1}$ [113].

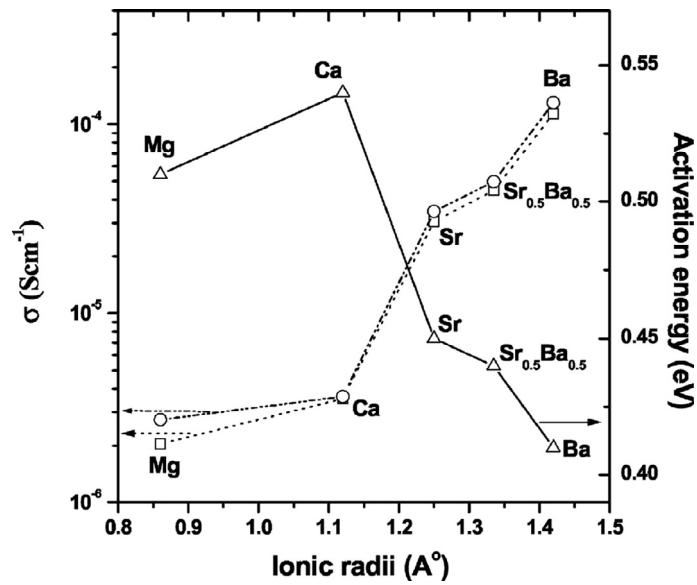


Fig. 4.3. Plot of total (bulk + grain-boundary) (indicated by open square) and bulk ionic conductivity (indicated by open circle) observed at 50 °C and activation energy (indicated by open triangle) vs the eight-coordinated ionic radii of the divalent Mg, Ca, Sr, $\text{Sr}_{0.5}\text{Ba}_{0.5}$ and Ba ions substituting a trivalent La in $\text{Li}_5\text{La}_3\text{Ta}_2\text{O}_{12}$ [240].

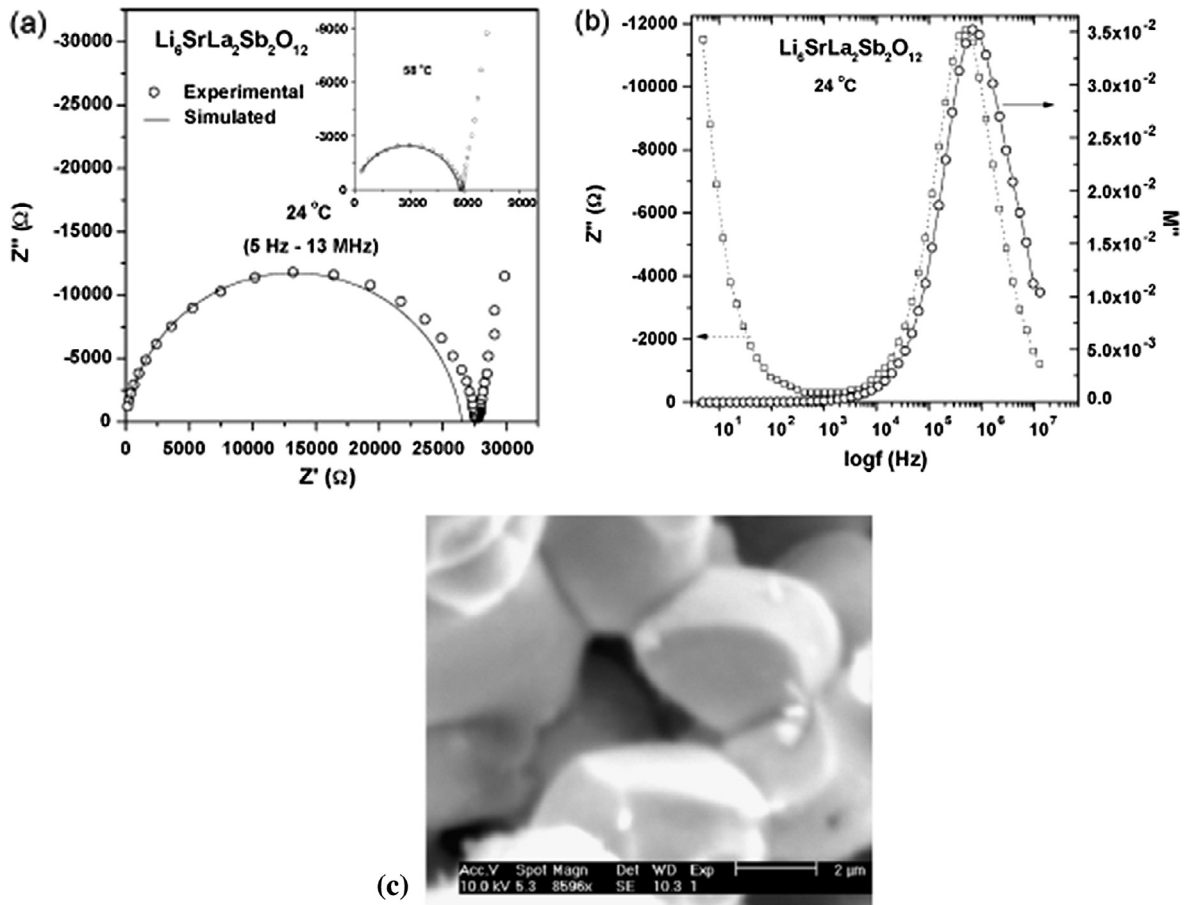


Fig. 4.4. (a) AC impedance and (b) spectroscopic plots of the imaginary components of the impedance Z'' and electric modulus M'' against $\log(\text{frequency})$ obtained at 24 °C and (c) magnified SEM image of $\text{Li}_6\text{SrLa}_2\text{Sb}_2\text{O}_{12}$ [119].

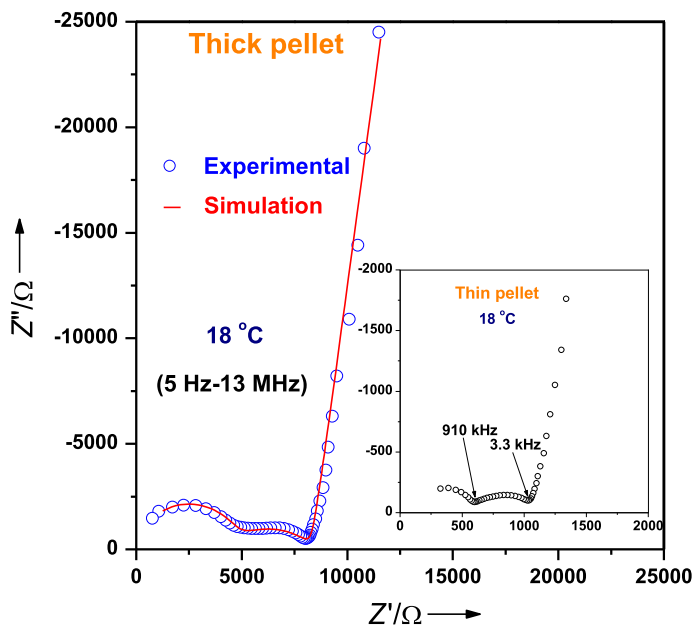


Fig. 4.5. AC impedance spectra of $\text{Li}_7\text{La}_3\text{Zr}_2\text{O}_{12}$ for the thick pellet (1.02 cm in thickness and 0.92 cm in diameter) [97,98]. The solid line represents simulated data with an equivalent circuit consisting of $(R_b Q_b)(R_{gb} Q_{gb})(Q_{el})$ (where R is the resistance, Q is the constant phase element, and the subscripts gb, and el refer to the grain, grain-boundary, and electrode) using the Equivalent program. The impedance plot measured in air at 18 °C for the thin pellet (0.18 cm in thickness and 0.98 cm in diameter) of $\text{Li}_7\text{La}_3\text{Zr}_2\text{O}_{12}$ is shown in the inset [97,98].

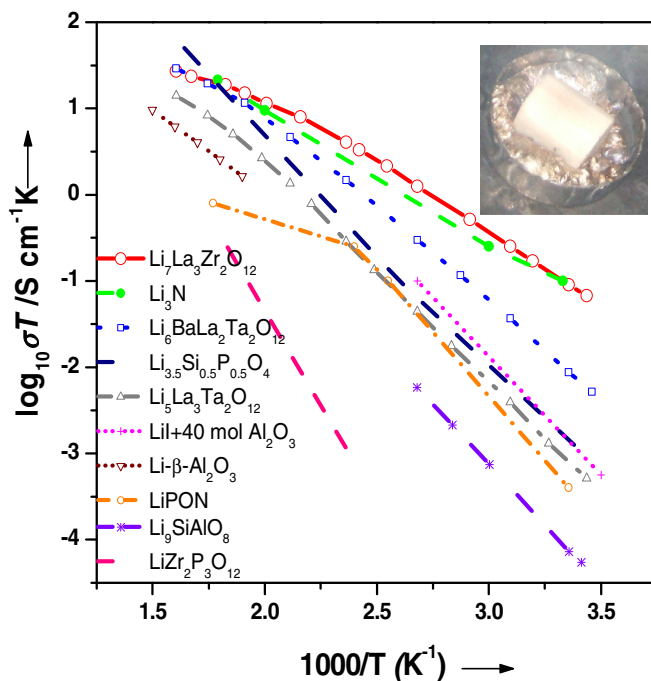


Fig. 4.6. The comparison of Li^+ conductivity of $\text{Li}_7\text{La}_3\text{Zr}_2\text{O}_{12}$ with other reported Li^+ conductors. The inset shows the stability of LLZO pellet against molten lithium in molybdenum crucible [97,98].

On the other hand tetragonal LLZO ($I4_1/acd$) reported by Awaka et al. exhibited a lower bulk Li^+ conductivity of $1.63 \times 10^{-6} \text{ S cm}^{-1}$. The reason for observed high Li^+ conductivity in cubic phase ($Ia\bar{3}d$) depends on certain criteria i.e., cubic phase exhibit short atomic displacement and the diffusion pathways are isotropic whereas tetragonal phase exhibit large atomic displacement and the diffusion pathways are anisotropic. This results in more static disorder of Li atom in cubic

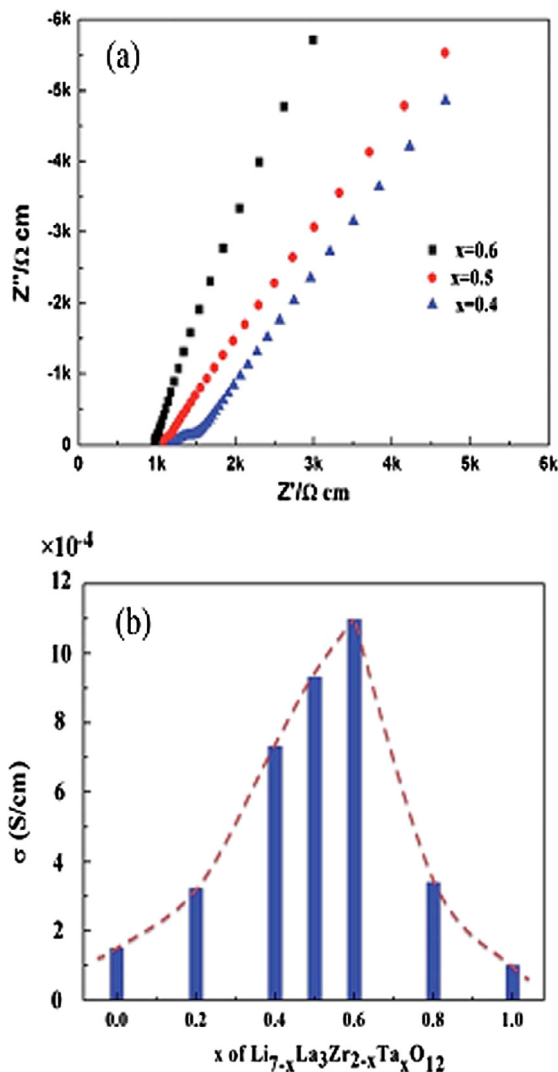


Fig. 4.7. (a) Impedance plot of $\text{Li}_{7-x}\text{La}_3\text{Zr}_{2-x}\text{Ta}_x\text{O}_{12}$ measured at 25 °C. (b) Variation in lithium conductivity with that of composition x in $\text{Li}_{7-x}\text{La}_3\text{Zr}_{2-x}\text{Ta}_x\text{O}_{12}$ [104].

phase LLZO than that of tetragonal phase LLZO [157,187,188]. Further investigation on stuffed lithium garnets leads to two related tetragonal systems with compositions $\text{Li}_7\text{La}_3\text{Sn}_2\text{O}_{12}$ [112] and $\text{Li}_7\text{La}_3\text{Hf}_2\text{O}_{12}$ [159]. $\text{Li}_7\text{La}_3\text{Sn}_2\text{O}_{12}$ has ordering of Li^+ in three fully occupied sites, leading to poor conductivity with high activation energy of about 0.79 eV. The tetragonal $\text{Li}_7\text{La}_3\text{Hf}_2\text{O}_{12}$ with space group $I4_1/acd$ exhibited bulk Li^+ conductivity of $9.85 \times 10^{-7} \text{ S cm}^{-1}$ and total (bulk + grain-boundary) Li^+ conductivity of $4.45 \times 10^{-7} \text{ S cm}^{-1}$ at 27 °C [159].

Based on various LLZO studies, it was suggested that the unintentional incorporation of Al^{3+} into LLZO from alumina crucible during the high-temperature (1230 °C) solid-state synthesis helps to stabilize the cubic phase against the tetragonal one [188,224,202]. Geiger et al. reported that Al contamination from the alumina crucible is the key aspect in stabilizing the high conductive cubic phase ($Ia\bar{3}d$) [188] Rangasamy et al. indicated that the optimized content of 0.24 mol of Al and 6.24 mol of lithium with nominal composition $\text{Li}_{6.24}\text{La}_3\text{Zr}_2\text{Al}_{0.24}\text{O}_{11.98}$ results a total Li^+ conductivity of $4 \times 10^{-4} \text{ S cm}^{-1}$ at room temperature with a relative density of 98% [100].

Ohta et al. report the successful improvement of the Li^+ conductivity by Nb doped $\text{Li}_{6.25}\text{La}_3\text{Zr}_{1.25}\text{Nb}_{0.75}\text{O}_{12}$ in the range of $8 \times 10^{-4} \text{ S cm}^{-1}$ at 25 °C [101]. Partial substitution of trivalent Y for a tetravalent Zr in LLZO with the nominal composition $\text{Li}_{7.06}\text{La}_3\text{Y}_{0.06}\text{Zr}_{1.94}\text{O}_{12}$ (LLYZ) using yttria stabilized ZrO_2 (3% YSZ) as reactant [105] indicated an increase in the bulk and total Li^+ conductivity of 9.56×10^{-4} and $8.10 \times 10^{-4} \text{ S cm}^{-1}$ at 25 °C with lower activation energy as 0.29 eV and 0.26 eV, respectively [105]. Further investigations were carried out on few lithium garnet systems to understand the optimum number of Li^+ concentration required to achieve maximized conductivity in these systems. Li et al. forecasted that the maximized Li^+ conductivity was achieved in the range $0.4 \leq x \leq 0.6$ for the samples $\text{Li}_{7-x}\text{La}_3\text{Zr}_{2-x}\text{Ta}_x\text{O}_{12}$ fired at 1140 °C in an alumina crucible

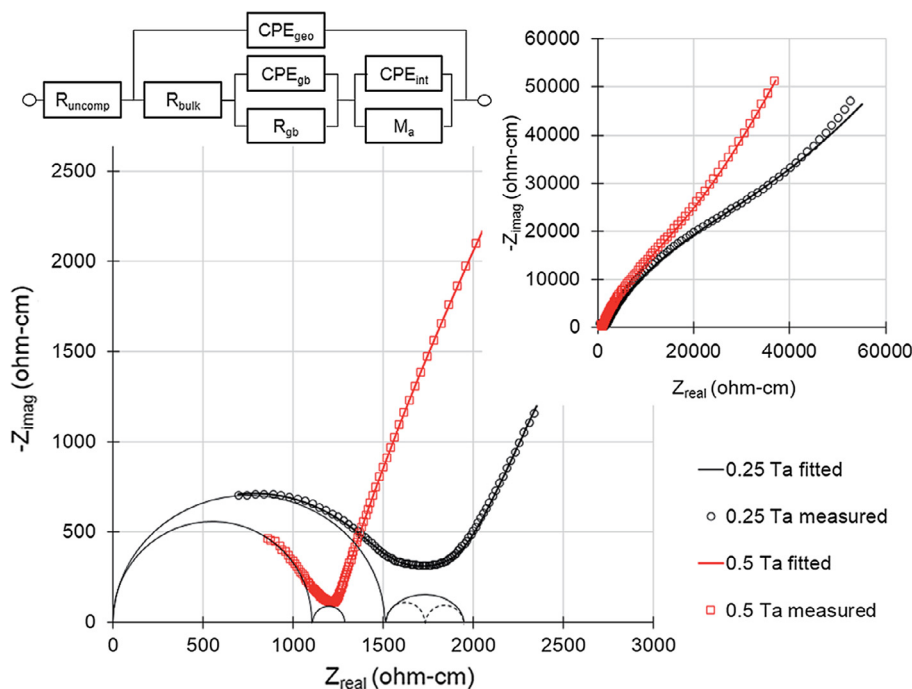


Fig. 4.8. AC impedance plots of $\text{Li}_{6.75}\text{La}_3\text{Zr}_{1.75}\text{Ta}_{0.25}\text{O}_{12}$ and $\text{Li}_{6.5}\text{La}_3\text{Zr}_{1.5}\text{Ta}_{0.5}\text{O}_{12}$ at room temperature. The open symbols correspond to the experimental data and the solid lines are the fitted results of the equivalent circuit. The equivalent circuit model is shown in the top left. The low frequency portion of the spectra is shown as inset [239].

[104]. A room-temperatures Li^+ conductivity of $1.0 \times 10^{-3} \text{ S cm}^{-1}$ with activation energy of 0.35 eV has been reported for the composition $\text{Li}_{6.4}\text{La}_3\text{Zr}_{1.4}\text{Ta}_{0.6}\text{O}_{12}$ [104]. The impedance plot of $\text{Li}_{7-x}\text{La}_3\text{Zr}_{2-x}\text{Ta}_x\text{O}_{12}$ measured in air at 25 °C and the change in the lithium conductivity with composition is given as Fig. 4.7(a) and (b).

Electrochemical impedance spectroscopy with an equivalent circuit modeling of subcritically doped $\text{Li}_{6.75}\text{La}_3\text{Zr}_{1.75}\text{Ta}_{0.25}\text{O}_{12}$ by Thompson et al. shown in Fig. 4.8 exhibited a depressed semicircle likely to be caused by the presence of more than one defect, viz., twinned tetragonal grains and grain-boundaries [239]. In other words, the subcritically doped $\text{Li}_{6.75}\text{La}_3\text{Zr}_{1.75}\text{Ta}_{0.25}\text{O}_{12}$ is a mixture of cubic and tetragonal phases [239].

Reports revealed that doping with elements such as Al, Y, Ce, Ga, Ge, In, Si, Nb, Ta, Sb, Te and W could stabilize the LLZO garnet in cubic phase ($Ia\bar{3}d$) with high Li^+ conductivity [100–103,105–110,137,242,243]. Thus searching for proper dopants has become an important topic in understanding the stabilization of LLZO in cubic phase and enhancing its Li^+ conduction properties. Doping of high valance cation results in decreasing lithium content in LLZO and thus enhances the Li^+ conductivity by creating more lithium vacancy [100]. In an attempt to increase the Li^+ conductivity, researchers have reported success with substitutions on the Zr^{4+} site in LLZO. The substitution of super-valent cation either Nb^{5+} or Ta^{5+} for Zr^{4+} in LLZO stabilize the high Li^+ conductive cubic phase relatively at lower sintering temperature and also enhances the Li^+ conductivity [101,104,242]. The results reported in literatures on doping with LLZO indicated a reduction in sintering temperature with La^{3+} site doping (Sr^{2+} or Ce^{4+}) [109,164] and improved conductivity by doping the Zr^{4+} site (Nb^{5+} or Ta^{5+}) [101,102,104]. Systematic Li^+ conductivity studies were also carried out regarding the simultaneous substitution on the La^{3+} and on the Zr^{4+} site in LLZO [148,244,245]. All these studies indicated the possibility of enhancement in the density and total Li^+ conductivity of LLZO through suitable and optimal amount of dopant for La and Zr along with optimal lithium concentration.

The ionically conducting solid electrolytes have been extensively studied and analyzed in terms of electrical modulus formalism [106–108,116,126]. Complex impedance spectra are dominated mostly by the resistive components of the sample whereas the modulus spectra highlight those with smaller capacitance. Complex modulus spectrum could distinguish against interfacial effect, electrode polarization and grain-boundary conduction and indicates the electrical phenomenon occurring in the dielectric spectrum [106–108,116,126]. The electric modulus studies on $\text{Li}_{5.5}\text{La}_3\text{Ta}_{1.75}\text{Y}_{0.25}\text{O}_{12}$, $\text{Li}_6\text{La}_3\text{Ta}_{1.5}\text{Y}_{0.5}\text{O}_{12}$ and $\text{Li}_{6.5}\text{La}_3\text{Ta}_{1.25}\text{Y}_{0.75}\text{O}_{12}$ shown in Fig. 4.9(a)–(c) indicated that, at lower temperatures, the modulus spectra of $\text{Li}_{5.5}\text{La}_3\text{Ta}_{1.75}\text{Y}_{0.25}\text{O}_{12}$ and $\text{Li}_6\text{La}_3\text{Ta}_{1.5}\text{Y}_{0.5}\text{O}_{12}$ exhibited a relaxation peak that can be ascribed to the charge re-orientation relaxation of Li^+ from one octahedral site to another octahedral site around an immobile Li^+ present in the tetrahedral site. With increasing temperature, the peak frequency shifts towards higher values indicating that the relaxation re-orientation of Li^+ is a thermally activated process [126].

Studies on the influence of Li^+ concentration on the structure and Li^+ transport properties of cubic lithium garnets $\text{Li}_x\text{A}_3\text{B}_2\text{O}_{12}$ ($A = \text{Y}^{3+}, \text{La}^{3+}, \text{Sr}^{2+}, \text{Ba}^{2+}$; $B = \text{Te}^{6+}, \text{Ta}^{5+}, \text{Zr}^{4+}$; $x = 3, 5, 6, 6.5, 7$ and 7.5) revealed that the Li^+ conductivity increase initially

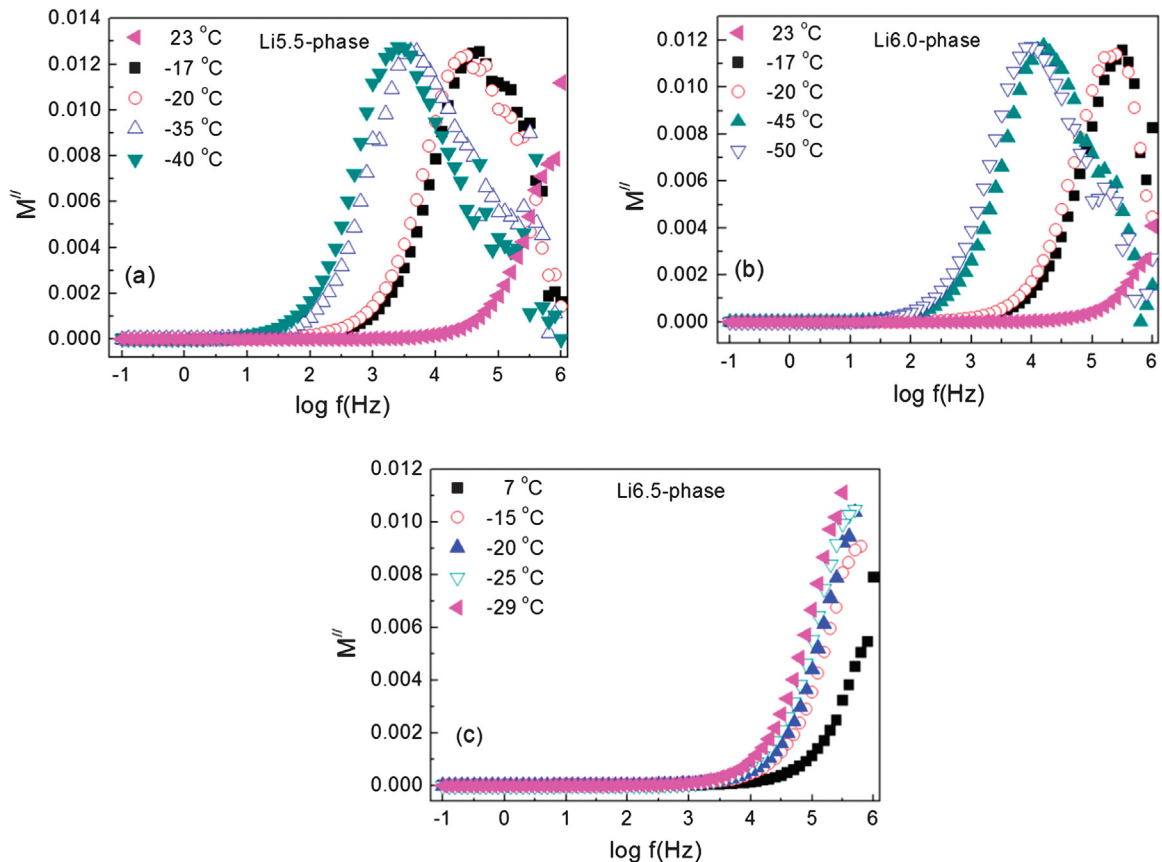


Fig. 4.9. Plots of imaginary part of M'' vs. log frequency of $\text{Li}_{5.5}\text{La}_3\text{Ta}_{1.75}\text{Y}_{0.25}\text{O}_{12}$, $\text{Li}_6\text{La}_3\text{Ta}_{1.5}\text{Y}_{0.5}\text{O}_{12}$ and $\text{Li}_{6.5}\text{La}_3\text{Ta}_{1.25}\text{Y}_{0.75}\text{O}_{12}$ [126].

with an increase of x in $\text{Li}_x\text{A}_3\text{B}_2\text{O}_{12}$ and reaches a maximized conductivity for $x = 7$, i.e., $\text{Li}_7\text{La}_3\text{Zr}_2\text{O}_{12}$ and then decreases with further increase of x [116]. In contrast the activation energy initially decreases with an increase of x and reaches a minimum of 0.32 eV for $x = 7$, i.e., $\text{Li}_7\text{La}_3\text{Zr}_2\text{O}_{12}$ and then increases with the further increase of x in $\text{Li}_x\text{A}_3\text{B}_2\text{O}_{12}$ as shown in Fig. 4.10 (a) and (b) [116].

The combined impedance Z'' and electrical modulus M'' against $\log(f)$ plots of $\text{Li}_5\text{La}_3\text{Ta}_2\text{O}_{12}$, $\text{Li}_6\text{La}_2\text{BaTa}_2\text{O}_{12}$ and $\text{Li}_{6.5}\text{La}_{1.5}\text{Ba}_{1.5}\text{Ta}_2\text{O}_{12}$ as shown in Fig. 4.11(a)–(c) indicates that, the difference in the peak frequencies of Z'' and M'' decrease in the order $\text{Li}_5\text{La}_3\text{Ta}_2\text{O}_{12} < \text{Li}_6\text{La}_2\text{BaTa}_2\text{O}_{12} < \text{Li}_{6.5}\text{La}_{1.5}\text{Ba}_{1.5}\text{Ta}_2\text{O}_{12}$, which indicates a reduction in the contribution of grain-boundary resistance to the total resistance with an increase of lithium content in $\text{Li}_x\text{A}_3\text{B}_2\text{O}_{12}$ [116].

It is possible to reduce the grain-boundary resistance of LLZO by utilizing suitable sintering aids that have low melting points. LLZO with high total Li^+ conductivity of $6.8 \times 10^{-4} \text{ S cm}^{-1}$ was reported as shown in Fig. 4.12 by the inclusion of appropriate amounts of Al and Si from the crucible and bowl of pulverizer, respectively [202].

Addition of various sintering additives like $\gamma\text{-Al}_2\text{O}_3$, Li_3BO_3 to LLZO and Li_3PO_4 , Li_2O to LLZOTO has been reported [144,143,152,161,202,203]. Addition of 6 wt.% of Li_2O into $\text{Li}_{6.75}\text{La}_3\text{Zr}_{1.75}\text{Ta}_{0.25}\text{O}_{12}$ (LLZOTO) additive leads to the formation of glassy-like phases at the grain-boundaries and thereby reduces the pores and enhances the Li^+ conductivity of $6.4 \times 10^{-4} \text{ S cm}^{-1}$ at room temperature with the relative density of 97.3% [143]. Inclusion of 1 wt.% of Li_3PO_4 into $\text{Li}_{7-x}\text{La}_3\text{Zr}_{2-x}\text{Ta}_x\text{O}_{12}$ reduced the sintering time from 36 h to 6 h and leads to the total lithium ion conductivity of about $7.2 \times 10^{-4} \text{ S cm}^{-1}$ in the sample [144].

Studies on the influence of sintering additives Li_3BO_3 , Li_3PO_4 and Li_4SiO_4 on the density and total (bulk + grain-boundary) Li^+ conductivity of $\text{Li}_{6.16}\text{Al}_{0.28}\text{La}_3\text{Zr}_2\text{O}_{12}$ (Al-LLZO) revealed that Al-LLZO added with 1 wt.% of Li_4SiO_4 sintered at 1200°C exhibited a room temperature (33°C) total (bulk + grain-boundary) Li^+ conductivity of $6.1 \times 10^{-4} \text{ S cm}^{-1}$ with a maximized density of 4.86 g cm^{-3} (relative density 96%) [176]. The variation in room temperature (33°C) bulk and total (bulk + grain-boundary) Li^+ conductivity and activation energy (total Li^+ conductivity) of Al-LLZO and Al-LLZO added with 1 wt.% of Li_3BO_3 , Li_3PO_4 and Li_4SiO_4 sintered at different elevated temperature depicted as Fig. 4.13 revealed that the total (bulk + grain-boundary) Li^+ conductivity is found to be maximum along with the minimum activation energy for the Al-LLZO added with 1 wt.% of Li_4SiO_4 sintered at 1200°C [176]. Similarly the inclusion of 1 wt.% of Li_4SiO_4 in Ta doped LLZO with nominal com-

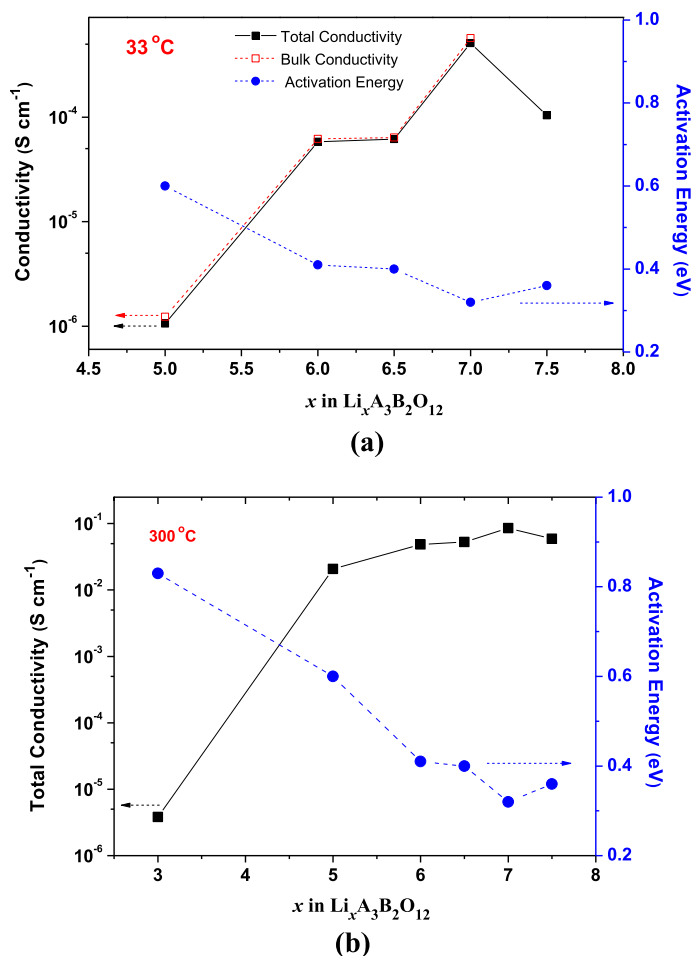


Fig. 4.10. (a) The composition dependencies of bulk (solid triangle) and total (solid square) Li^+ conductivity measured at 33 °C and activation energy (solid circle) for the composition $\text{Li}_x\text{A}_3\text{B}_2\text{O}_{12}$ with $5 \leq x \leq 7.5$. (b) The composition dependencies of total Li^+ conductivity (solid square) measured at 300 °C and activation energy (solid circle) for composition $\text{Li}_x\text{A}_3\text{B}_2\text{O}_{12}$ with $3 \leq x \leq 7.5$ [116].

position $\text{Li}_{6.4}\text{La}_3\text{Zr}_{1.4}\text{Ta}_{0.6}\text{O}_{12}$ exhibited a room temperature (33 °C) total (bulk + grain-boundary) Li^+ conductivity of $3.7 \times 10^{-4} \text{ S cm}^{-1}$ as shown in Fig. 4.14 [153].

5. Li^+ dynamics in lithium garnets

Lithium garnet frame work are grouped into three models viz., $\text{Li}_x\text{A}_3\text{B}_2\text{O}_{12}$; $x = 3, 5$ and 7. Examination on the neutron diffraction data for the three models revealed that the first model with chemical composition $\text{Li}_3\text{A}_3\text{B}_2\text{O}_{12}$ ($A = \text{Y, Pr, Nd, Sm-Lu}$; $B = \text{Te}$) [114] also known as conventional lithium garnet, had a cubic ordered structure ($Ia\bar{3}d$) in which the tetrahedral (24d) site are completely occupied, leaving the octahedral site (48g/96h) empty. The only plausible path for the Li^+ migration is to activate it from the occupied tetrahedral site to the neighboring unfilled octahedral site. This is not feasible at the room temperature. Moreover, the energy required for this Li^+ migration is quite high. The high occupancy of tetrahedral (24d) site and the lack of mobile Li^+ in octahedral (48g/96h) site are the reason for the low Li^+ conduction in $\text{Li}_x\text{A}_3\text{B}_2\text{O}_{12}$ with lithium concentration $x = 3$ [246].

The second model with chemical composition $\text{Li}_5\text{A}_3\text{B}_2\text{O}_{12}$ ($A = \text{La}$; $B = \text{Ta, Nb, Sb}$ and Bi) [90,118,222] in which the occupancy of octahedral takes place along with an increase in the vacancy concentration of the tetrahedral (24d) site. The detailed analysis on neutron diffraction reveals that the Li^+ occupying octahedral (48g) are displaced to new octahedral position (96h) due to the short Li-Li distance generated through large coulombic repulsion. Cussen et al. predicted that the additional lithium in lithium stuffed garnets (i.e., $x > 3$ in $\text{Li}_x\text{A}_3\text{B}_2\text{O}_{12}$) occupy the octahedral site (96h) that are empty in case of conventional garnets [220]. The octahedral site (96h) can accommodate a total of six lithium cations per formula unit. Later, Callaghan et al. with neutron diffraction studies on $\text{Li}_{5+x}\text{Ba}_x\text{La}_{3-x}\text{Ta}_2\text{O}_{12}$ ($x = 0-1.6$) reported that the displacement in lithium stuffed garnets are due to static disorder and there must exist a short Li...Li distance of 2.44 Å between the majority

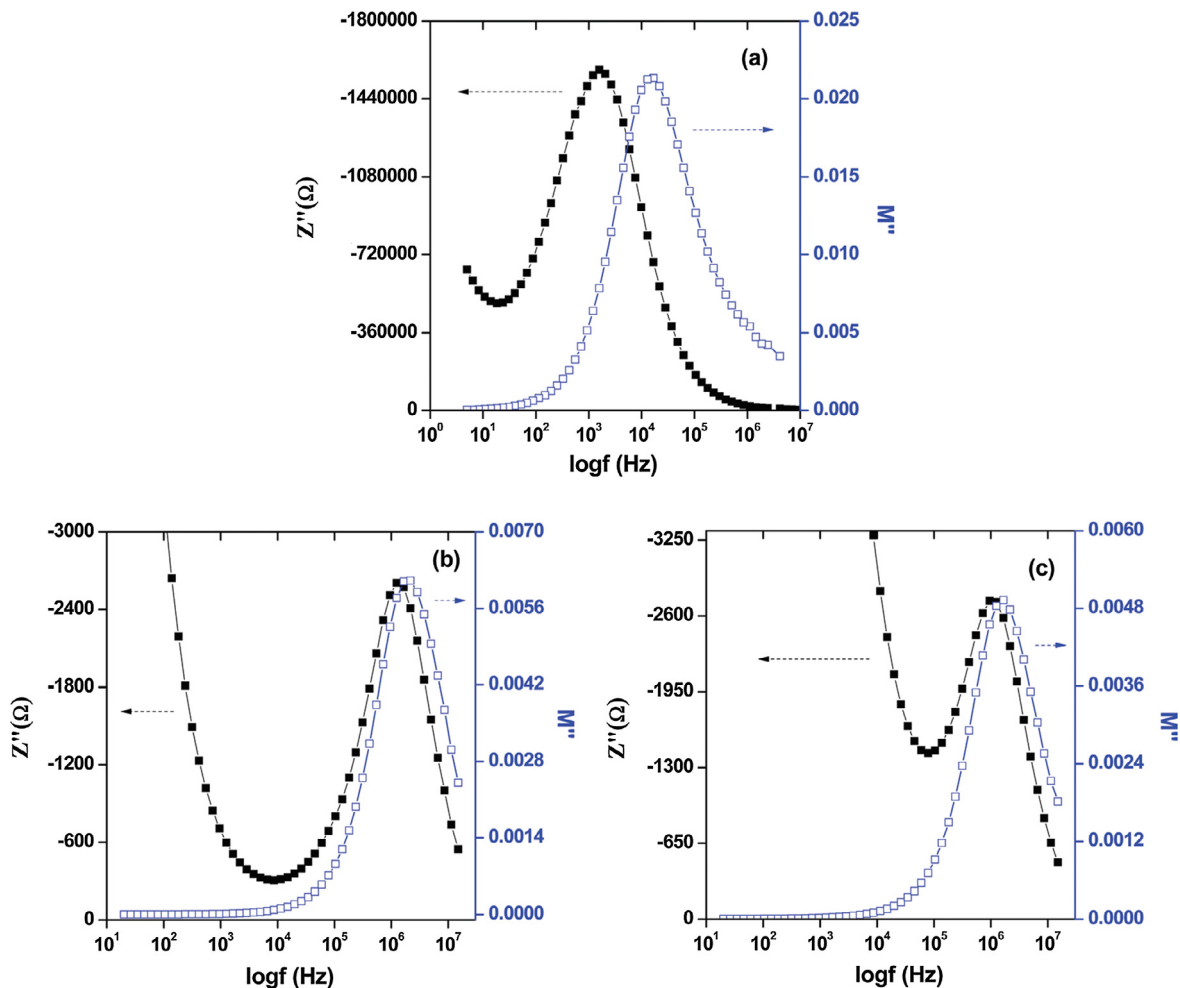


Fig. 4.11. Spectroscopic plots of the imaginary components of the impedance Z'' (solid square) and electric modulus M'' (open square) against log (frequency) obtained at 33 °C for (a) $\text{Li}_5\text{La}_3\text{Ta}_2\text{O}_{12}$, (b) $\text{Li}_6\text{La}_2\text{BaTa}_2\text{O}_{12}$ and (c) $\text{Li}_{6.5}\text{La}_{1.5}\text{Ba}_{1.5}\text{Ta}_2\text{O}_{12}$ [116].

occupied sites that promoting a high Li^+ mobility [222]. Moreover, the displacement of Li^+ at any of these site (octahedral (96h)/tetrahedral (24d)) would reflect a shift towards different neighboring Li site, provided the neighboring Li site must be empty [222]. It was found that the octahedral sites reach a maximum of 57%, with a tetrahedral vacancy of 14% for the composition $\text{Li}_{6.6}\text{Ba}_{1.6}\text{La}_{1.4}\text{Ta}_2\text{O}_{12}$ [222]. Reverse Monte Carlo (RMC) modeling and classical molecular dynamics studies on the local lithium structure and dynamics of garnet type $\text{Li}_5\text{La}_3\text{Ta}_2\text{O}_{12}$ predict that Li^+ hopping is not through the direct octahedral to octahedral movement but through a triangular bottle neck via 3D continuous network of tetrahedral (24d)/octahedral (96h) sites and thereby leads to fast ionic conduction [247]. The co-existence of mobile Li^+ and vacancies at octahedral (96h) makes the possible lithium migration through the interstice using the neighboring energy barrier route 48g/96h passing through their common tetrahedral (24d) site [246].

The third model is given for the composition $\text{Li}_7\text{A}_3\text{B}_2\text{O}_{12}$ ($\text{A} = \text{La}$; $\text{B} = \text{Zr}$ and Hf) [97,98,112,113]. Among them $\text{Li}_7\text{La}_3\text{Zr}_2\text{O}_{12}$ exhibited high Li^+ conductivity of $5 \times 10^{-4} \text{ S cm}^{-1}$ with cubic disordered structure ($Ia\bar{3}d$) in which both tetrahedral (24d) and octahedral (96h) sites were partially occupied [187]. However, the tetragonal ordered structure ($I4_1/acd$) with Li^+ conductivity of $1.63 \times 10^{-6} \text{ S cm}^{-1}$ in which tetrahedral (8a), octahedral (16f), and octahedral (32g) sites were fully occupied by lithium. Whereas, the tetrahedral (16e) sites were fully empty [157]. The occupancy of Li in cubic and tetragonal LLZO reported by Bernstein et al. is shown in Fig. 5.1 [248].

The mechanism observed in high Li^+ conductive cubic structure $\text{Li}_7\text{La}_3\text{Zr}_2\text{O}_{12}$ might be originated from the diffusion of mobile Li^+ through the border of 24d-96h and then climbing over other 24d-96h border and finally bypassing the empty octahedral site 48g site [246]. The presence of more mobile Li^+ in octahedral site and simultaneous vacancies in the tetrahedral site help to increase the transportation of Li^+ through the diffusion of Li^+ in the low energy barrier route 24d-96h-24d-96h [246]. The conduction pathway forecasted by Xu et al. based on DFT suggest that the occupancy of Li^+ in tetrahedral coordinated sites is reduced to ~50% with a simultaneous increase in the occupancy of octahedral sites to ~90% [246]. The Li^+

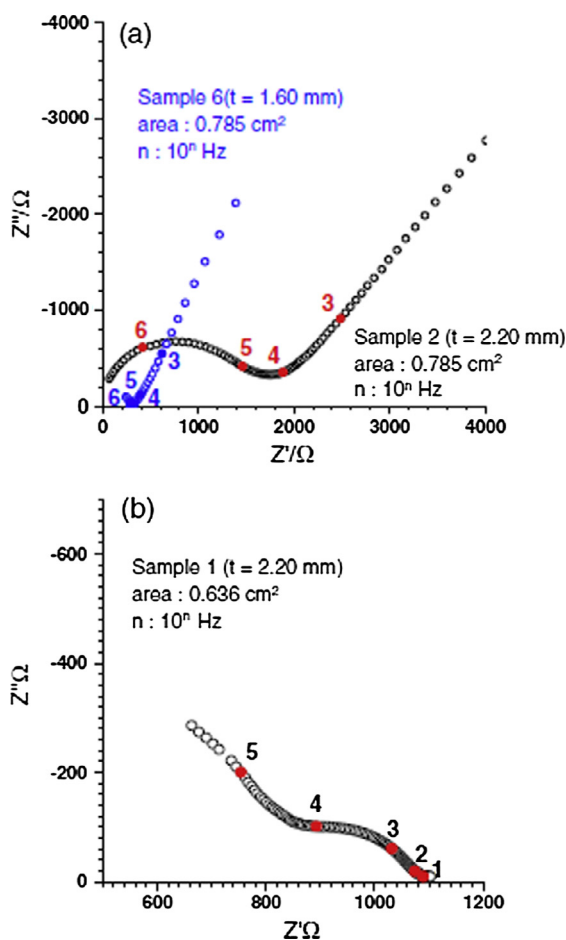


Fig. 4.12. Cole–Cole plots of (a) Pt/LLZO/Pt and (b) Li/LLZO/Li cell measured at room temperature [202].

migrate from one octahedral site ($48g/96h$) to the adjacent vacant octahedral site ($48g/96h$) through a common tetrahedral site ($24d$) [246]. Schematic representation for the occupancy of Li^+ with increasing lithium concentration in lithium garnets is shown in Fig. 5.2 [246].

Density-functional theory (DFT) studies on $\text{Li}_7\text{La}_3\text{Zr}_2\text{O}_{12}$ shows that the stability of tetragonal phase depends on two parameters (i) simultaneous ordering of the Li^+ on the Li sublattice and (ii) a volume-preserving tetragonal distortion that alleviate internal structural strain. Hence, doping supervalent cations leads to lithium vacancies thereby enables the possibility of stabilizing the cubic phase. Ab initio studies based on molecular dynamics within the cubic $\text{Li}_7\text{La}_3\text{Zr}_2\text{O}_{12}$ framework by Jalem et al. predicts that the distribution of Li^+ is high at octahedral site and the transportation of Li^+ takes place through a three dimensional distorted octahedral-tetrahedral-distorted octahedral diffusion path [249].

The determining factor in the formation of phase (cubic/tetragonal) was resolved when LLZO synthesized in Al-crucibles resulted in the cubic phase [188]. Subsequently experiments with intentional doping of Al confirmed that Al doping plays a major role in achieving high conductive cubic phase [100]. Computational results using density-functional theory and variable cell shape molecular dynamics simulations revealed that the supervalent Al^{3+} on the Li sublattice was charge compensated by the creation of two Li^+ vacancies [248]. The ordering of Li sublattice was destroyed by the creation of sufficient amount of these vacancies, and the resultant disorder along with the combination of lattice relaxation produced the high Li^+ conducting cubic symmetry. Moreover, the same vacancies are accountable for opening up previously blocked Li^+ hopping paths leading to an enhanced conductivity [248]. Comparison of theoretical investigation on the site occupancy of Al^{3+} in $\text{Li}_{7-3x}\text{Al}_{3+x}\text{La}_3\text{Zr}_2\text{O}_{12}$ using density functional theory with that of measured ^{27}Al NMR chemical shift reveals that Al^{3+} prefers the two different crystallographic sites i.e., tetrahedrally coordinated $24d$ site and a distorted 4-fold coordinated $96h$ site [250].

The cation doping within LLZO must exhibit high solubility and lead to change in the lithium concentration from 7 Li per formula unit. It has been shown that Al^{3+} is not uniquely necessary to achieve the high Li^+ conducting cubic phase and it is also possible to create the necessary Li vacancies by means of Ta^{5+} , Nb^{5+} , Al^{3+} , Ga^{3+} , In^{3+} , Sn^{4+} , Sb^{4+} , Y^{3+} , Ge^{4+} , Si^{4+} , Ca^{2+} , Sr^{2+} ,

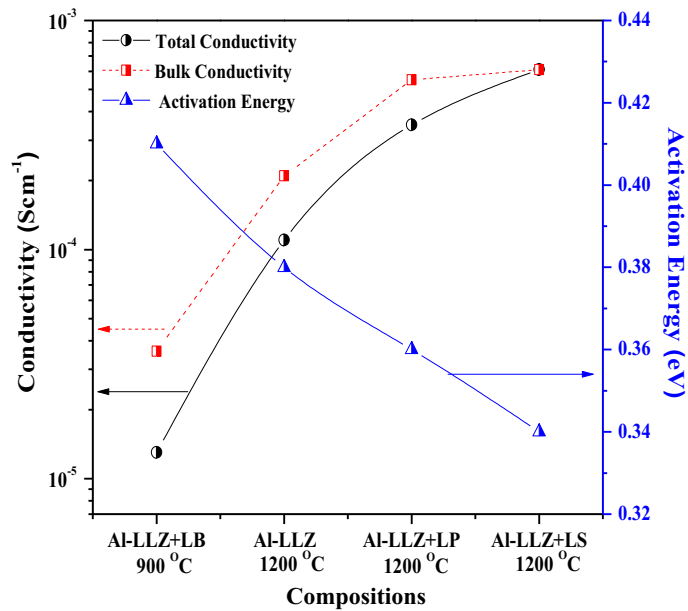


Fig. 4.13. The composition dependencies of bulk and total (bulk + grain-boundary) Li^+ conductivity measured at 33 °C and activation energy (total Li^+ conductivity) of Al-LLZO added with 1 wt.% of Li_3BO_3 sintered at 900 °C, Al-LLZO sintered at 1200 °C, Al-LLZO added with 1 wt.% of Li_3PO_4 sintered at 1200 °C and Al-LLZO added with 1 wt.% of Li_4SiO_4 sintered at 1200 °C [176].

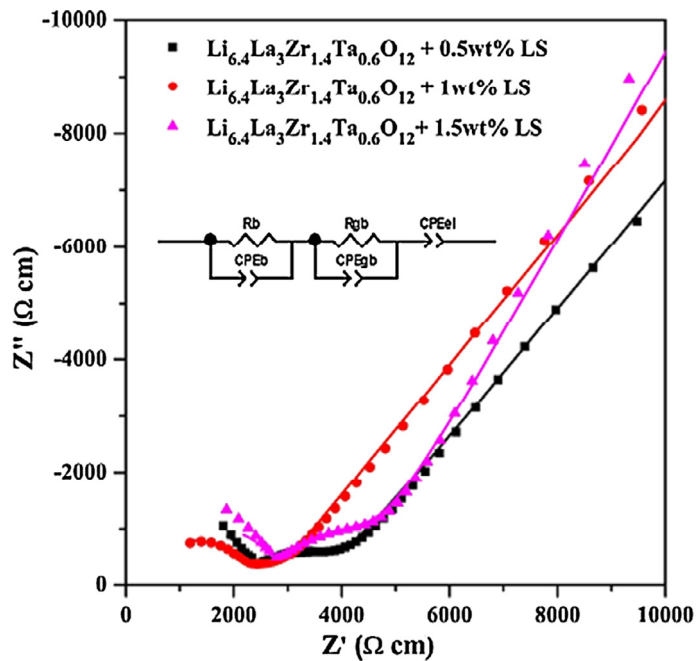


Fig. 4.14. Typical AC impedance plots of $\text{Li}_{6.4}\text{La}_3\text{Zr}_{1.4}\text{Ta}_{0.6}\text{O}_{12}$ added with 0.5 wt.%, 1 wt.% and 1.5 wt.% of Li_4SiO_4 (pellets sintered at 1200 °C) measured at room temperature (33 °C) using Li^+ blocking Au electrodes. The solid line represents the fitted data with an equivalent circuit [153].

Ba^{2+} , Hf^{4+} to obtain a cubic symmetry ($Ia\bar{3}d$) with increased conductivity [90,97,98,105–107,109,110,126,132,134,141,142,175,223,251].

DFT studies on multi doped LLZO using Al and Ta confirmed that the site occupancy of Al substituting a 24d Li site blocks the Li^+ conductive pathway in the garnet structure [252]. By an introduction of Ta into the LLZO framework there exhibited a shift in the majority of Al occupying from the 24d site to 96h Li sites resulting more open space for Li^+ transport with an increase in the amount of Li vacancy [252]. Molecular dynamics stimulation studies on the undoped LLZO, penta valent

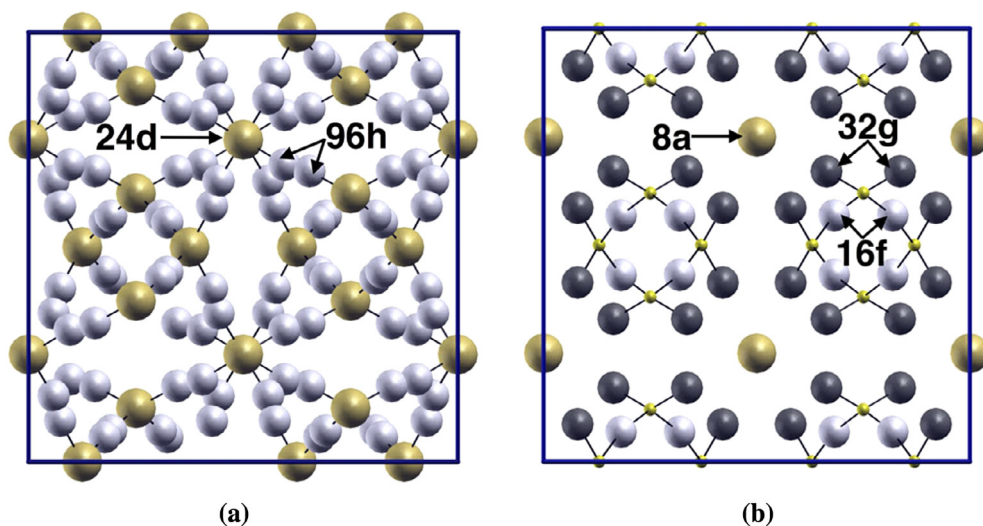


Fig. 5.1. (a) Li sublattice in the cubic phase of LLZO. (b) Li sublattice in the tetragonal phase of LLZO. The large gray (gold) balls represents the Li(1) atoms ($8a^+$ and $24d^c$), white balls represents Li(2) atoms ($16f^+$ and $96h^c$), and the dark gray balls represents Li(3) atoms ($32g^+$). The small (gold online) spheres represents the cubic Li(1) positions that becomes vacant upon transition to the ordered tetragonal structure ($16e^+$) [248].

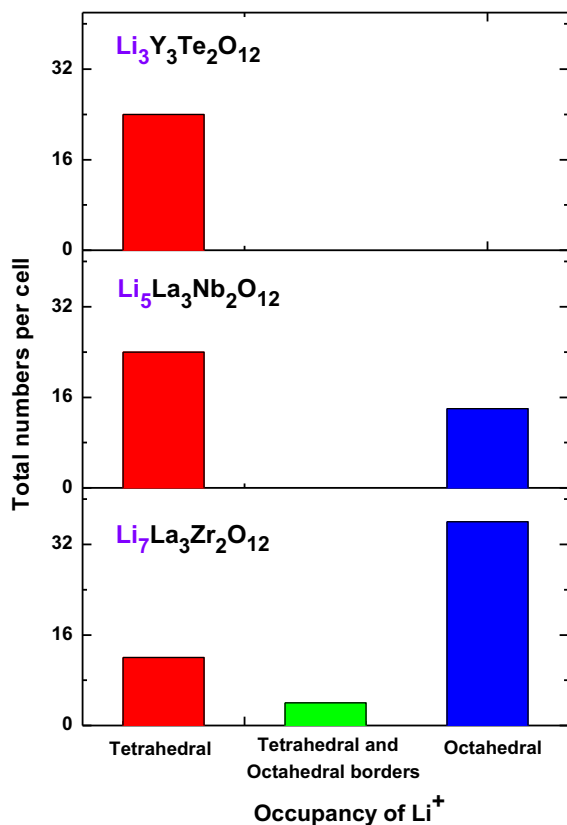


Fig. 5.2. Model showing the occupancy of Li⁺ with increasing lithium concentration in lithium garnets [246].

Ta⁵⁺/Nb⁵⁺ doped LLZO and trivalent Ga³⁺ or Al³⁺ doped LLZO revealed that the penta valent doping Ta⁵⁺, Nb⁵⁺ on LLZO increased the disorder and the vacancy concentration led to a more prominent conductivity enhancement than Al doping in Li ($24d$) [99]. On the other hand Ga doping on La site did not stabilize the cubic phase and did not affect the mobile charge carrier concentration [99]. Molecular dynamics studies on $\text{Li}_{7-x}\text{La}_3(\text{Zr}_{2-x}\text{M}_x)\text{O}_{12}$ ($\text{M} = \text{Ta}^{5+}, \text{Nb}^{5+}, x = 0, 0.25$) by Adams and

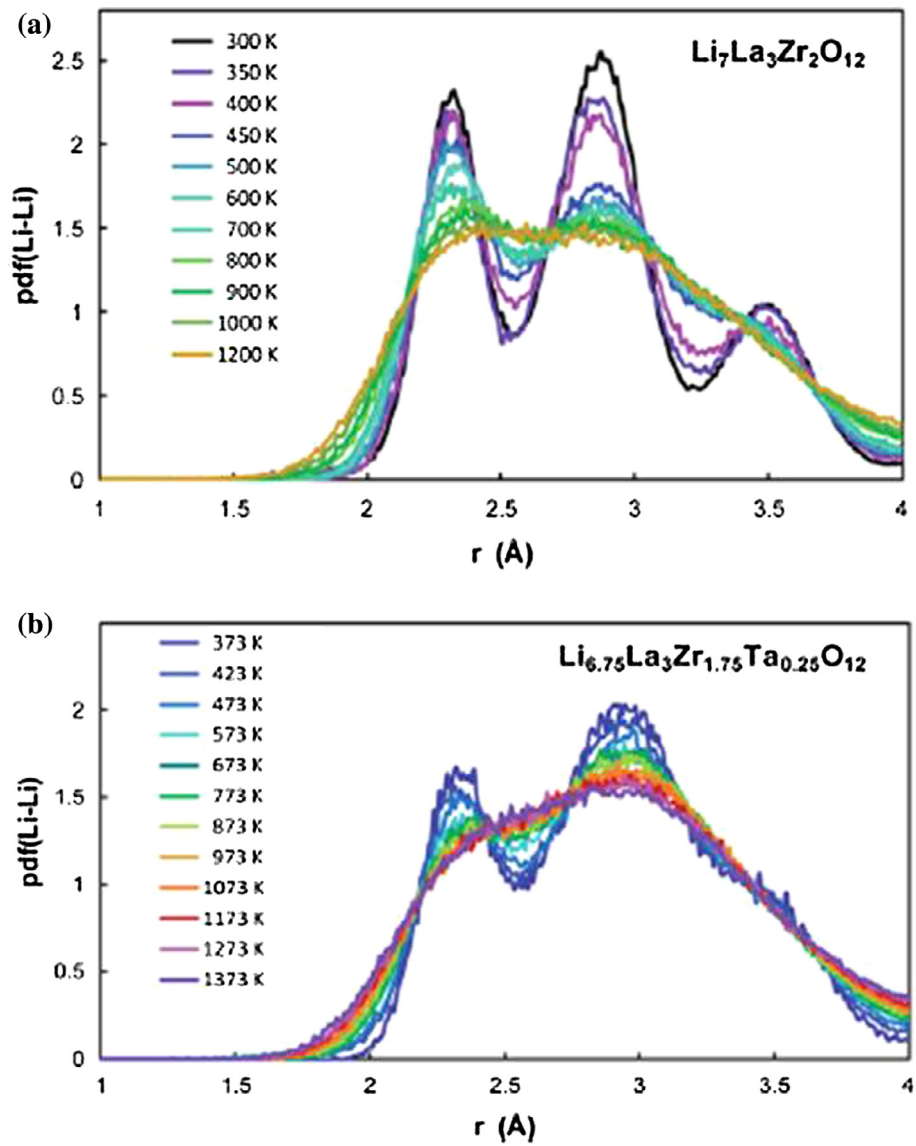


Fig. 5.3. Plots showing Li-Li pair distribution function at selected temperatures, as determined from molecular dynamics (MD) simulations, for (a) $\text{Li}_7\text{La}_3\text{Zr}_2\text{O}_{12}$ and (b) $\text{Li}_{6.75}\text{La}_3\text{Zr}_{1.75}\text{Ta}_{0.25}\text{O}_{12}$ [253].

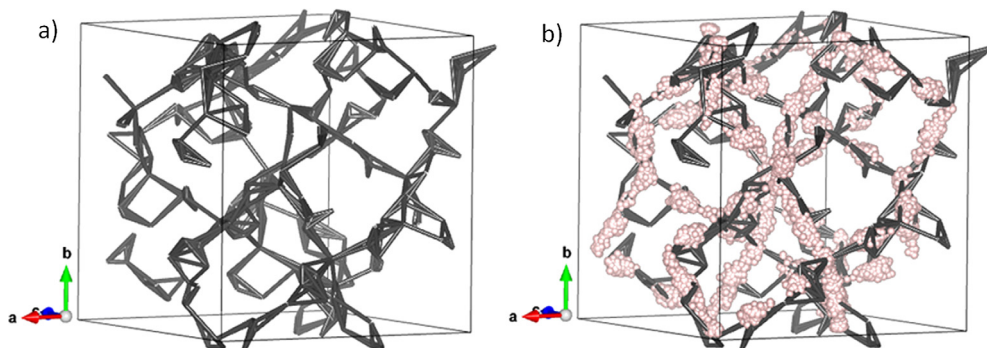


Fig. 5.4. (a) The migration pathway identified from topology analysis and (b) ab initio molecular dynamics (AIMD) trace at 600 K for cubic-LLZO showing that the predicted pathway from topology closely agrees with the AIMD trace, follow the Li(2)–Li(1)–Li(2) trajectory, no Li(2)–Li(2) hop [245].

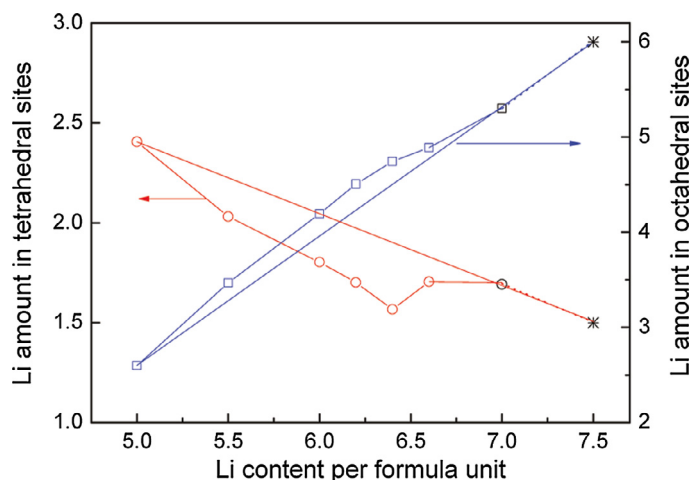


Fig. 5.5. Variation in the occupancy of tetrahedral 24d-A and bridging octahedral with Li concentration obtained from neutron diffraction data [254].

Stability of Dopants in $Li_7La_3Zr_2O_{12}$ Garnet

												13 IIIA	14 IVA	15 VA	16 VIA	17 VIIA	18 VIIIA	
1	1+ H 2.660											3+ B 2.210	4+ C 2.710	3+ N 3.950	O Oxygen	F Flourine	He Helium	
2	Li Lithium	2+ Be 1.020											3+ Al 1.360	4+ Si 2.350	3+ P 3.550	4+ S 2.640	5+ Cl 2.750	Ne Neon
3	1+ Na 2.340	2+ Mg 1.220											3+ Al 1.360	4+ Si 2.350	3+ P 3.550	4+ S 2.640	5+ Cl 2.750	Ar Argon
4	1+ K 2.360	2+ Ca 1.030	3+ Sc 0.760	4+ Ti 0.430	5+ V 2.000	3+ Cr 1.050	4+ Mn 0.530	3+ Fe 1.324	4+ Co 0.900	2+ Ni 1.270	2+ Cu 1.740	2+ Zn 1.320	3+ Ga 1.160	4+ Ge 1.110	5+ As 2.160	4+ Se 1.240	3+ Br 3.080	Kr Krypton
5	1+ Rb 1.290	2+ Sr 0.700	3+ Y 0.490	Zr Zirconium	5+ Nb 0.920	4+ Mo 0.130	4+ Tc -0.610	4+ Ru 0.310	3+ Rh 0.990	4+ Pd 0.220	1+ Ag 2.750	2+ Cd 1.090	3+ In 0.790	4+ Sn 0.310	5+ Sb 0.980	4+ Te 1.440	5+ I 0.980	Xe Xenon
6	1+ Cs 3.100	2+ Ba 1.260	La-Lu Lanthanide	4+ Hf 0.110	5+ Ta 0.940	4+ W 1.270	Re Rhenium	Os Osmium	4+ Ir -0.390	4+ Pt 0.270	2+ Au 2.390	3+ Hg 1.940	3+ Tl 1.110	4+ Pb 0.360	3+ Bi 0.700	Po Polonium	At Astatine	Rn Radon
7	Fr Francium	Ra Radium	Ac-Lr Actinide	Rf Rutherfordium	Db Dubnium	Sg Seaborgium	Bh Bohrium	Hs Hassium	Mt Meitnerium	Ds Darmstadtium	Rg Roentgenium	Uub Ununbium	Uut Ununtrium	Uuq Ununquadium	Uup Ununpentium	Uuh Ununhexium	Uus Ununseptium	Uuo Ununoctium
		La Lanthanum	4+ Ce 0.230	3+ Pr 0.220	3+ Nd 0.140	3+ Pm 0.260	3+ Sm 0.220	2+ Eu 1.530	3+ Gd 0.350	3+ Tb 0.440	3+ Dy 0.500	3+ Ho 0.560	3+ Er 0.660	3+ Tm 0.740	Yb Ytterbium	Lu Lutetium		
		Ac Actinium	3+ Th 1.050	4+ Pa 0.860	5+ U Uranium	4+ Np 17.30	5+ Pu 13.38	2+ Am Americium	3+ Cm Curium	3+ Bk Berkelium	3+ Cf Californium	3+ Es Einsteinium	3+ Fm Fermium	3+ Md Mendelevium	3+ No Nobelium	3+ Lr Lawrencium		

Fig. 5.6. Illustrations on the site and oxidation state preference for the dopant elements in LLZO. The colors indicate the most stable cation site (green for Li-site, red for La-site, and blue for Zr-site). The darker colors signify lower defect energy, such that Al^{3+} (Li) is darker than B^{3+} (Li). The box also indicates the preferred oxidation state and the defect energy (in eV) [255].

Rao revealed that the pentavalent doping (Ta^{5+} , Nb^{5+}) on LLZO reduce the local Li ordering and enhances the ionic conductivity [253]. A low energy pathway is observed through tetrahedral 24d sites [253]. Moreover, above the structural phase transition the distribution of lithium in the tetragonal phase is ordered with occupancy of 1/3 at tetrahedral 24d sites and half of the distorted octahedral 96h sites thereby avoiding the short Li–Li distances [253]. This is clearly reflected in the reduced relative intensity of the first peak in the radial distribution function as shown in Fig. 5.3 [253].

It is possible to increase the lithium content beyond $x = 7$ per formula unit in $Li_xA_3B_2O_{12}$ by doping Rb^+ on La^{3+} site. Ab initio molecular dynamics (AIMD) and topology investigation on Rb and Ta doped $Li_{7+2x-y}(La_{3-x}Rb_x)(Zr_{2-y}Ta_y)O_{12}$ ($0 \leq x \leq 0.375$, $0 \leq y \leq 1$) indicated that doping with neither Rb nor Ta on LLZO does not alter the topology of the migration pathway, rather change the lithium concentration. Moreover, the topology analysis revealed a three dimensional migration pathway $-96h-24d-96h$ – as shown in Fig. 5.4 [245].

Neutron diffraction studies by Xie et al. suggested that $x = 7.5$ in $Li_xA_3B_2O_{12}$ was the theoretical upper limit that a garnet framework can tolerate. However, this upper limit requires half occupancy of the tetrahedral (24d) sites with a complete

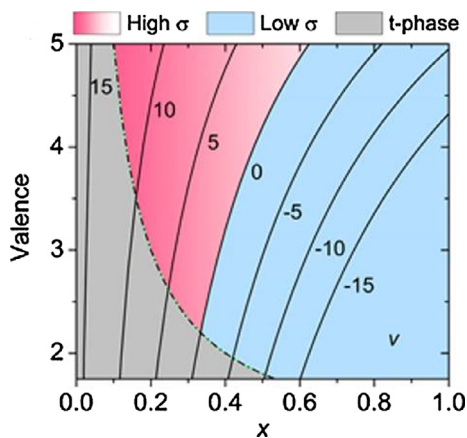


Fig. 5.7. Contour map indicates Li vacancy density (ν) as a function of the valence n and doping level x of M in the $\text{Li}_{7-6x}\text{M}_x\text{La}_3\text{Zr}_2\text{O}_{12}$ garnet [256].

occupancy of the octahedral sites (48g/96h). Moreover, they suggested that the highest Li^+ conductivity would be achieved for the lithium concentration $x = 6.4 \pm 0.1$ as depicted in Fig. 5.5 [254]. But the occupancy of octahedral sites (96h) reached a maximum ($\sim 90\%$) for the composition $x = 7$ i.e., $\text{Li}_7\text{La}_3\text{Zr}_2\text{O}_{12}$. Hence, further increase in the lithium concentration of garnet frame $\text{Li}_x\text{A}_3\text{B}_2\text{O}_{12}$, (i.e., for $x > 7$) led to an insufficient vacancies for the Li^+ migration [246].

DFT studies on defect energies and site preference on cation doping by Miara et al. suggested that Zn^{2+} and Mg^{2+} on the Li and Zr site, respectively, are found to be relatively stable [255]. Fig. 5.6 depicts site and oxidation state preference for the dopant elements in LLZO [255]. Apart from high Li^+ conductivity the enhancement of power density of all-solid-state rechargeable lithium batteries truly depends on the Li^+ transfer at the electrode/electrolyte interface. Results on the thermodynamic stability of electrolyte/cathode interface revealed that LLZO and LiCoO_2 exhibit a low driving force for decomposition in the charged state [255].

In order to reveal the mechanism of the high Li^+ conductivity in stuffed lithium garnets, two different dopants (Al^{3+} and Zn^{2+}) from two different groups (IIIA and IIB of periodic table) and valences (+3 and +2) with nominal compositions $\text{Li}_{6.28}\text{Al}_{0.24}\text{La}_3\text{Zr}_2\text{O}_{12}$ and $\text{Li}_{5.8}\text{Zn}_{0.6}\text{La}_3\text{Zr}_2\text{O}_{12}$ were investigated by Chen et al. [256]. Structural refinements revealed that both Al^{3+} and Zn^{2+} dopants redistribute the vacancies in the garnet framework by means of two different mechanisms i.e., the Li^+ migrate from octahedral sites to tetrahedral sites for Al^{3+} doped LLZO, in contrast the mechanism is reversed for Zn^{2+} doped LLZO [256]. Chen et al. suggested that the Li vacancy density (ν) in the active octahedral sites, which is determined by the valence and the content of aliovalent doping is the key factor for the ionic conductivity. If the value of $\nu > 0$, the number of vacancies in the active octahedral sites increases, thereby creating a fast Li^+ pathway bridging the two neighboring tetrahedral sites. If $\nu \leq 0$, the number of vacancies in the active octahedral sites becomes less, this is because all octahedral vacancies are trapped and deactivated at the influenced sites that are not able to contribute to Li^+ conduction. The immobile dopant ions do not block all of the possible pathways; however, it is the overwhelming slow pathways that limit the Li^+ conduction. In spite of large number of available vacancies in the tetrahedral site, the Li^+ mobility strongly depends on the accessibility of the octahedral bridges that converge on that site [256]. The relationship between ionic conductivity and aliovalent doping in LLZO is given in Fig. 5.7.

The concluding remarks of the systematic investigation by Chen et al. [256] for the doping optimization in garnet framework are:

- (i) Elements from IIA, IB, or IIB groups of the periodic table with +2 valency are not potentially suitable to increase the vacancy density (ν) in octahedral site.
- (ii) Metalloid dopants with high valence in IVA and VA groups (Si, Ge, Sn, As, and Sb) are capable to give larger ν , provided the dopants must be substituted in the accurate site of LLZO.
- (iii) Doping the elements from the same group such as Al^{3+} and Ga^{3+} led to similar Li^+ conductivity.

6. Application of lithium garnets in electrochemical devices

One of the major challenges in solid state batteries is the availability of a solid electrolyte which can satisfy criteria's simultaneously viz. good Li^+ conductivity at room temperature and good electrochemical stability with the potential electrodes. Although few solid electrolytes displayed higher Li^+ conductivity, such solid state electrolyte seems to have poor electrochemical stability against lithium metal negative electrode. This stability limitation restricts the choice of electrode materials to those of higher redox potential, which decreases the possible battery operating voltage. Moreover, electrode/electrolyte interfacial resistance can take up large values which would retard lithium insertion-extraction across the

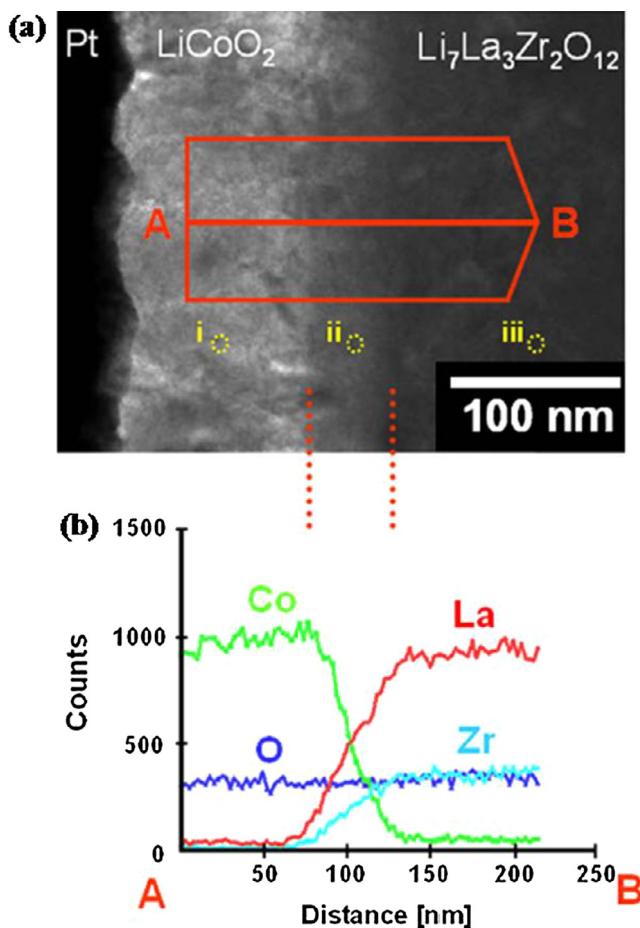


Fig. 6.1. (a) Cross-sectional TEM image of an LLZO/LiCoO₂ thin film interface. (b) corresponding EDS line profile obtained from the region indicated by the red arrow in the direction A–B. The reaction layer at the LLZO/LiCoO₂ interface is indicated by the broken red lines [257].

interface, resulting in a decreased power density. One of the uphill battles is to develop a solid electrolyte capable of meeting the requirements of high Li⁺ conductivity and good electrochemical stability simultaneously.

6.1. All-solid-state lithium battery

Despite the promises of reasonable high Li⁺ conductivity and stability against metallic lithium, all-solid-state Li-ion batteries based on cubic LLZO solid electrolytes have still challenges in realizing high practical performances due to their high electrode–electrolyte interfacial resistances. Reasonable electrochemical activities in all-solid-state Li⁺ batteries based on cubic LLZO solid electrolytes are so far only achieved by vacuum deposition of the cathode as thin films, because of the resulting good electrolyte–electrode contact.

A preliminary investigation on the electrochemical properties of LLZO was first carried out by Kotobuki et al. [160] in order to reveal the handiness of LLZO as a solid electrolyte for all-solid-state lithium batteries with Li metal as negative electrode and LiCoO₂ as positive electrode. The cyclic voltammogram (CV) of Li/LLZO/Li cell revealed the reversible dissolution and deposition of lithium. A full cell composed of Li metal negative electrode, LLZO solid electrolyte and LiCoO₂ exhibited an irreversible behavior at the first discharge and charge cycle due to possible reaction at the interface between LiCoO₂ and LLZO [160].

6.1.1. Interface engineering

An investigation to study the core reason behind the interfacial resistance was done by Kim et al. [257]. They prepared thin films of LiCoO₂ on LLZO pellets. Both analytical TEM and electrochemical measurements were carried out to characterize the interface. The TEM revealed the formation of an intermediate reaction layer consisting of La₂CoO₄, with thickness of around 50 nm at the LLZO/LiCoO₂ interface, as shown in Fig. 6.1 [257]. This reaction layer (which comprised varying concentrations of elements like Co, La and Zr) was ascribed as the prime reason for the high interfacial resistance, leading to poor

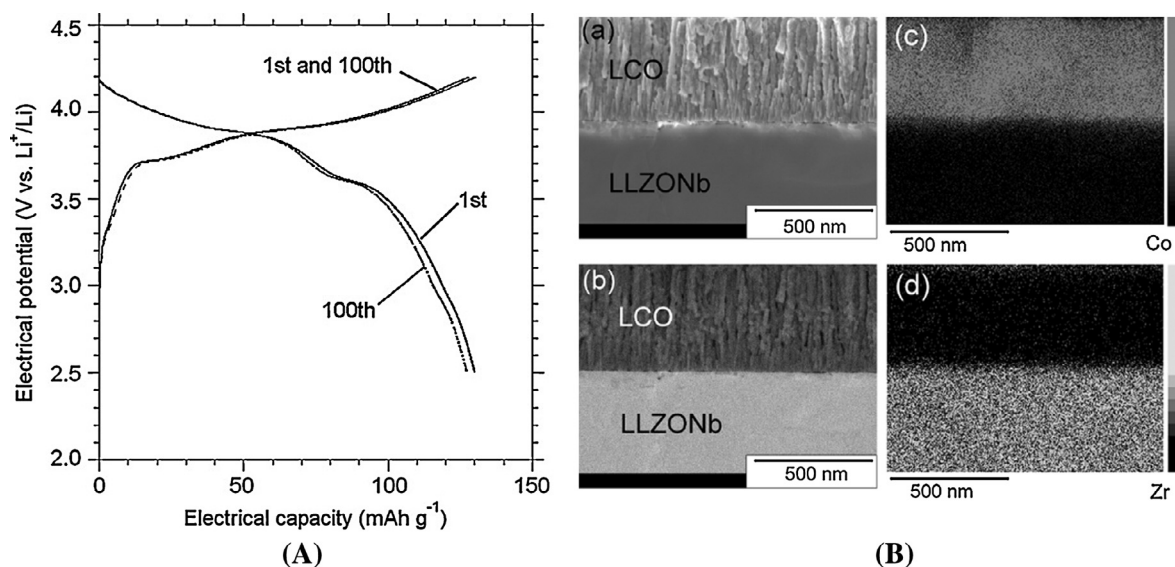


Fig. 6.2. (A) Charge-discharge curves for LiCoO₂/LLZONb/Li cell. The horizontal axis shows the capacity normalized by the weight of LiCoO₂ cathode. Solid lines indicate the 1st charge-discharge cycle and the dotted lines indicate the 100th charge-discharge cycles [258]. (B) Cross sectional FE-SEM image of the interface between LiCoO₂ and LLZONb after 100 charge-discharge cycles for (a) secondary electron and (b) backscattering electron. (c) and (d) Represents the EDX mapping for Co and Zr respectively [258].

lithium insertion-extraction behavior. Suppression of formation of such a reaction layer has become a prime necessity for the development of advanced solid state rechargeable lithium batteries with LLZO as solid electrolyte [257].

All-solid-state rechargeable lithium battery consisting of LiCoO₂ as positive electrode, Nb doped LLZO, Li_{6.75}La₃Zr_{1.75}Nb_{0.25}O₁₂ (LLZONb) as solid electrolyte and metallic lithium as negative electrode exhibited stable cycle performance, without any reaction phase at the interface even after 100 charge-discharge cycles [258]. The charge and discharge capacity of the battery at first cycle were 130 mAh g⁻¹ and 129 mAh g⁻¹, respectively, which comes around 90% of the theoretical capacity. Furthermore the charge and discharge capacity at 100th cycle were 127 mAh g⁻¹ and 130 mAh g⁻¹, respectively as shown in Fig. 6.2(A), which is 98% of the theoretical capacity [258]. Moreover, the interfacial resistance between LiCoO₂ and Li_{6.75}La₃Zr_{1.75}Nb_{0.25}O₁₂ at 25 °C was estimated to be 170 Ω cm², which is comparable to that for a Li⁺ battery with a liquid organic electrolyte [258].

This solid electrolyte with Nb additive exhibited stable cycle performance with no reaction phase or exfoliation at the interface even after 100 charge-discharge cycles which is clearly indicated in the FE-SEM and EDX mapping of the interface as shown in Fig. 6.2(B) [258]. Following this, in 2013 Ohta et al. [259] experimented on all-solid-state lithium ion batteries constructed using garnet type oxide Li_{6.75}La₃Zr_{1.75}Nb_{0.25}O₁₂ (LLZONb) as the solid electrolyte and Li₃BO₃ (LBO) as a solid electrolyte within the cathode layer. With the annealing process, LBO which has a low melting point (700 °C) acted as a bonding material at the interface by gradual melting. This melted LBO increased the interfacial contact between LLZONb and cathode layer which reduced the interfacial resistance between them [259]. The charge discharge capacity of the battery developed by this method was 74% of the theoretical value with high coulombic efficiency. The LBO helped to improve the good interfacial contact which enhanced the overall cell performance.

Although Ohta et al. [259] and Kotobuki et al. [160] showed it is feasible to cycle all solid state Li/LLZO/LiCoO₂ conversely, Ishiguro et al. [260] observed abrupt swings and a sudden drop in voltage during direct current (DC) polarization tests at ≥ 0.5 mA cm⁻² at room temperature. It was suggested that the short circuit could have resulted from Li dendrite formation and propagation.

In this decade, several approaches for the suppression of the lithium dendrite formation have been proposed and significant improvements have been reported for liquid electrolytes with a high concentration of lithium salts at high current density. However, the detailed performance under practical conditions such as long-term cycling performance at a high areal capacity has not been reported. As such, the mitigation of dendrite formation remains an important experimental and industrial challenge.

Monroe et al. predicted that the solid electrolyte must be approximately twice the shear modulus of metallic Li (4.2 GPa) to suppress Li dendrite initiation [261]. Using resonant ultrasound spectroscopy Jennifer et al. [262] determined the shear modulus of LLZO to be 61 GPa, which is more than adequate shear modulus to suppress Li dendrite initiation. It is believed that La and Zr in LLZO form a chemically stable atomic framework that is not decomposed upon contact with metallic Li.

Sharafi et al. demonstrated that temperature and current density significantly affect the Li-LLZO interface kinetics and stability [263]. The room temperature Li-LLZO interface resistance decreases dramatically by heating Li/LLZO/Li cells to 175 °C and cooling to room temperature. The interfacial resistance might be reduced because of the improved contact

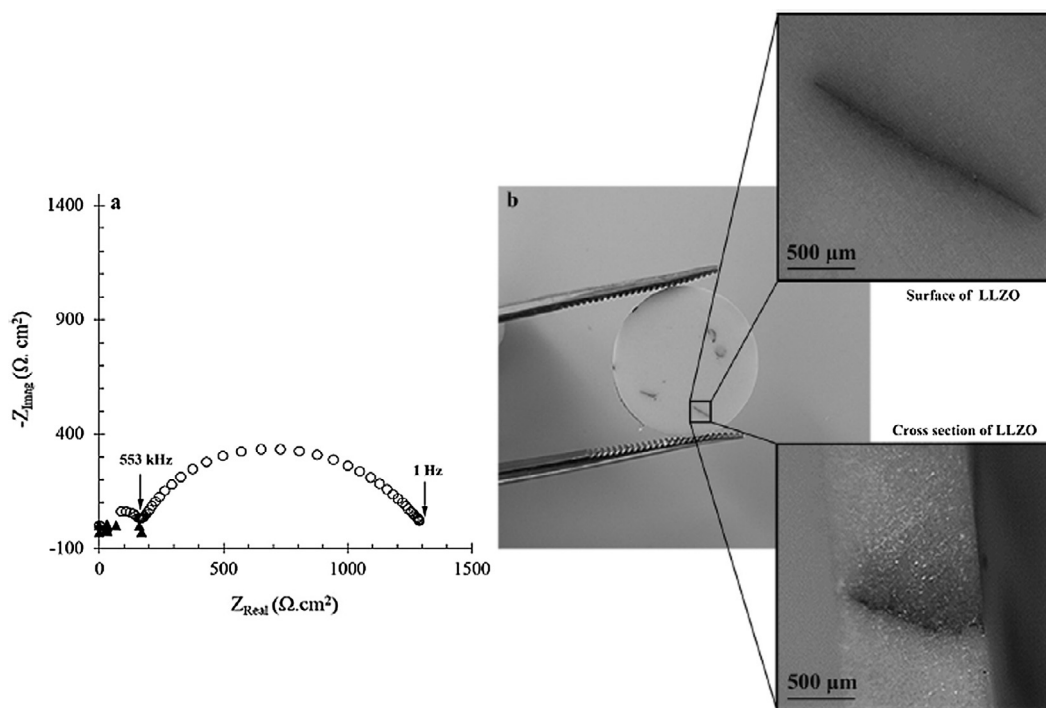


Fig. 6.3. (a) Nyquist plot of Li/LLZO/Li cell cycled at room temperature: before (○) and after the CCD was exceeded (▲) and (b) optical images showing the dark spots that appeared during cycling of LLZO pellet [263].

between Li and LLZO through heating under constant pressure. Also they demonstrated that the maximum sustainable current density (or critical current density - CCD) increases significantly with increasing temperature. Metallic Li spots were observed when the CCD was exceeded as shown in Fig. 6.3 [263].

Lithium dendrite formation has been reported for Nb-doped [260], Ta-doped [264] and Al-doped [265] garnet-type lithium ion conducting solid electrolytes. The mechanism for dendrite formation between lithium metal and the solid electrolyte has yet to be clarified, but the lithium diffusion kinetics at grain boundaries may be a key factor. Suzuki et al. [206] examined the lithium dendrite formation of transparent Al_2O_3 -doped $\text{Li}_7\text{La}_3\text{Zr}_2\text{O}_{12}$ prepared by hot isostatic pressing (HIP) at 127 MPa and 1160 °C for 2 h. The relative density of 1 wt.% Al_2O_3 -doped $\text{Li}_7\text{La}_3\text{Zr}_2\text{O}_{12}$ without HIP treatment was 91.5%, and with HIP treatment was increased to 99.1%. The HIP treated sample had approximately 1% white part near the grain-boundary [266].

Cell voltage vs. polarization period for Li/HIP treated 1 wt.% Al_2O_3 $\text{Li}_7\text{La}_3\text{Zr}_2\text{O}_{12}$ with white areas/Li and Li/HIP treated 1 wt.% Al_2O_3 $\text{Li}_7\text{La}_3\text{Zr}_2\text{O}_{12}$ without white areas/Li are shown in Fig. 6.4 [266]. The cell with the white parts in HIP treated 1 wt.% Al_2O_3 $\text{Li}_7\text{La}_3\text{Zr}_2\text{O}_{12}$ exhibited a sudden voltage drop after polarization for 100 s. However, the cell with HIP treated transparent 1 wt.% Al_2O_3 $\text{Li}_7\text{La}_3\text{Zr}_2\text{O}_{12}$ containing no white areas showed no sudden cell voltage drop, but instead the cell voltage increased gradually with the polarization period, which suggests that the grain-boundary-free $\text{Li}_7\text{La}_3\text{Zr}_2\text{O}_{12}$ suppresses lithium dendrite growth through the electrolyte [266].

Constant direct current measurements of HP-LLZO:Ta with a current density of 0.5 mA cm^{-2} by Tsai et al. revealed that the short circuit formation in lithium garnet was neither due to the low relative density of the samples nor the reduction of Li–Al glassy phase at grain boundaries but it was from Li dendrite formation inside, which took place along the grain boundaries [267]. The Li dendrite formation was mostly due to the inhomogeneous contact between LLZO solid electrolyte and Li electrodes as depicted in Fig. 6.5. By flattening the surface of the LLZO:Ta pellets and using thin layers of Au buffer between LLZO:Ta and Li electrodes, the interface resistance could be dramatically reduced, which results in short-circuit-free cells when running a current density of 0.5 mA cm^{-2} . The doggedness of the dendrite problem for higher current density by a proper microstructure engineering to provide good contact and eliminate the difference of conductivities for the grain and grain-boundary should be painstaking for future development of all solid-state Li batteries [267].

In order to improve the contact between lithium metal and LLZO solid electrolyte Luo et al., studied an effect of coating an ultrathin layer ($\sim 10 \text{ nm}$) of amorphous Si on the surface of garnet using plasma enhanced chemical vapor deposition (PECVD) [268]. An ultrathin coating of Si layer transforms the chemical properties of a garnet from “superlithiophobicity” to “super-lithiophilicity”. The symmetric cells composed of Li/Si-coated LLZO/Li displayed much lesser impedance and exceptional stability upon plating/stripping cycles with a small overpotential at 0.05 or 0.1 mA/cm^2 compared to Li/LLZO/Li cells as shown in Fig. 6.6(a)–(d) [268]. The over potential was found to be small for further increase of current density

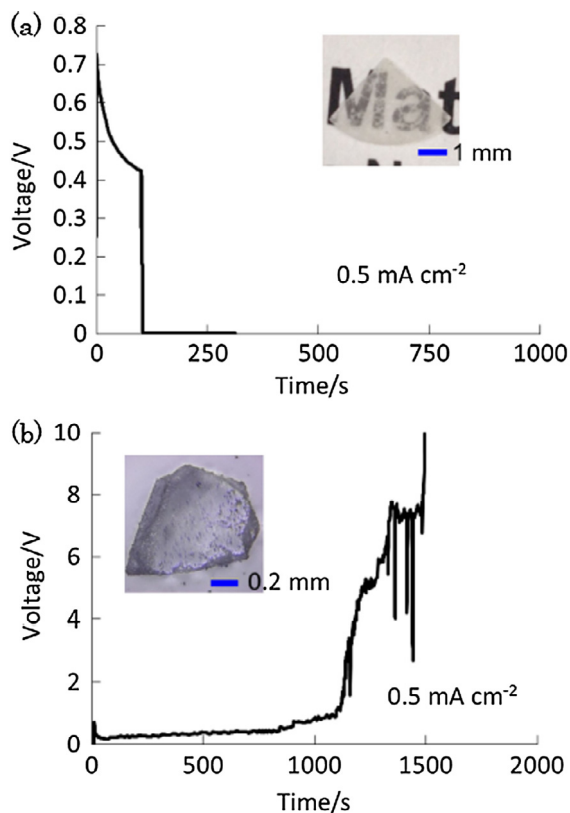


Fig. 6.4. Cell voltage vs. polarization period for Li/hot isostatically pressed 1 wt.% Al_2O_3 - $\text{Li}_7\text{La}_3\text{Zr}_2\text{O}_{12}$ /Li (a) with white areas and (b) without white areas [266].

to 0.2 mA/cm^2 , and the cell delivered stable cycling performance as shown in Fig. 6.6(e). The interfacial resistance between Li and LLZO dramatically decreased from $925 \text{ } \Omega \text{ cm}^2$ when lithiated Si was formed on the LLZO [268].

Ohta et al. explored the possibility of an all-solid-state battery with lithium garnet type oxide electrolyte, $\text{Li}_{6.8}(\text{La}_{2.95}, \text{Ca}_{0.05})(\text{Zr}_{1.75}, \text{Nb}_{0.25})\text{O}_{12}$ (LLZO-CaNb) with Al_2O_3 and Li_3BO_3 additives. By stacking the developed electrolyte on LiCoO_2 (LCO), it was co sintered at $790 \text{ } ^\circ\text{C}$ and then coated with Li metal negative electrode [269]. This design of LLZO-CaNb played a crucial role in suppressing the positive electrode-electrolyte reaction, showing a high Li^+ conductivity of 0.36 mS cm^{-1} at $25 \text{ } ^\circ\text{C}$ and a relative density of 90% even at low sintering temperature of $790 \text{ } ^\circ\text{C}$. It was suggested that the addition of Li_3BO_3

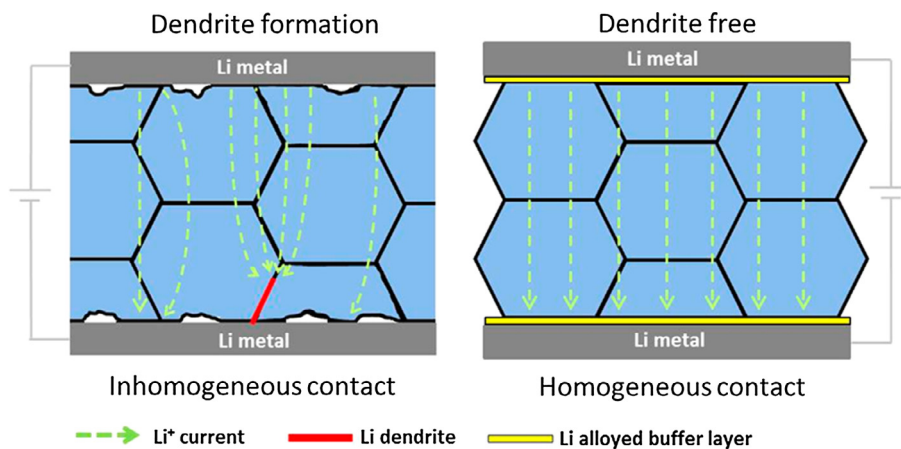


Fig. 6.5. Illustration of dendrite formation for inhomogeneous contact between LLZO solid electrolyte and Li electrodes and free from dendrite with homogeneous contact between LLZO solid electrolyte and Li electrodes [267].

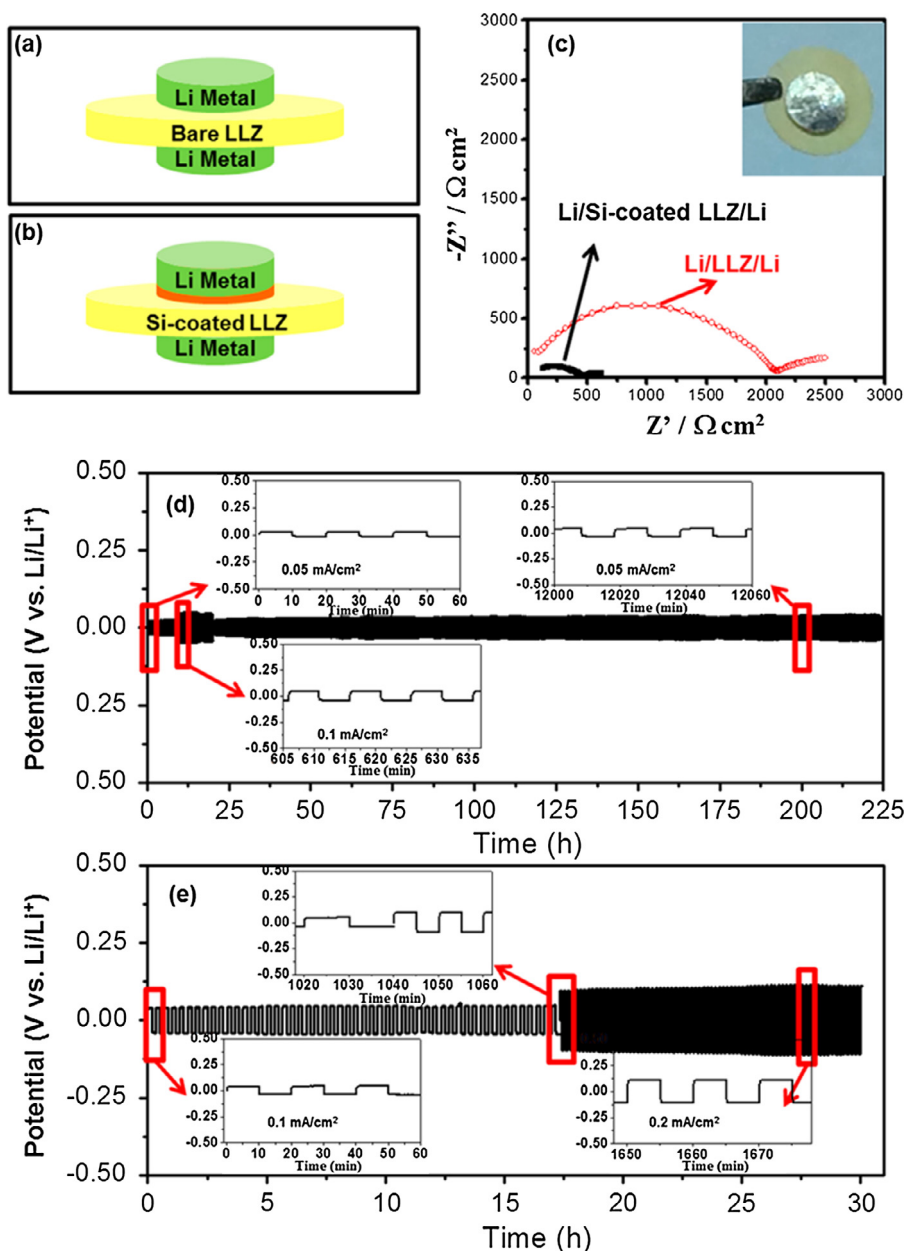


Fig. 6.6. (a) and (b) The schematic illustration of symmetrically stacked lithium cell containing bare LLZO and silicon coated LLZO, respectively. (c) Cole-Cole plots of lithium cells containing bare LLZO and silicon coated LLZO. The inset shows the photographic image of a symmetric cell containing Li/Silicon coated LLZO/Li. (d) and (e) Voltage vs. time profiles of symmetric cell containing Li/Silicon coated LLZO/Li at 0.05, 0.1 mA/cm² and 0.1, 0.2 mA/cm² current densities, respectively [268].

and Al₂O₃ was the prime reason for augmented sintering due to simultaneous inter diffusion of Al and Ca elements between garnet type oxide and additives [269]. A model battery designed with this developed electrolyte was confirmed to function well as a secondary battery with fairly good charge-discharge capacities of 98 mAh g⁻¹ and 78 mAh g⁻¹, respectively. These handsome properties indicate the possibility of fabricating all-solid-state lithium ion batteries with lithium garnets [269].

Modification of the electrode-electrolyte interface for all-solid-state lithium secondary batteries was done by Kato et al. by the deposition of a thin layer of Nb metal onto LLZO, producing a low resistivity-amorphous layer, with a thickness varying from 7 nm to 15 nm, by radio frequency magnetron sputtering in Ar atmosphere at room temperature [270]. The deposition of the thin layer of Nb metal onto LLZO resulted in lowering the interfacial resistance by one order of magnitude (from 2600 Ω/cm² to 150 Ω/cm²) depending on the thickness of the Nb metal layer as shown in Fig. 6.7 [270]. The CV

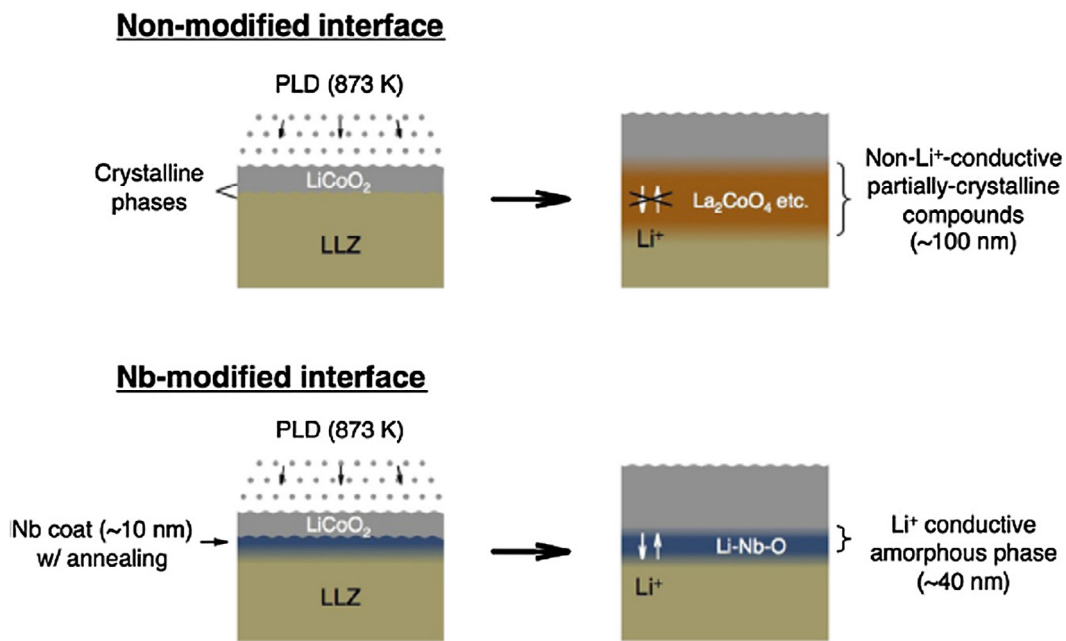


Fig. 6.7. Schematic representation of non-modified and Nb-modified LLZO/LiCoO₂ interfaces. Non-Li⁺-conductive phases such as a crystalline La₂CoO₄ phase produced by the mutual diffusion between LLZO and LiCoO₂ is suppressed by the Nb-modified LLZO/LiCoO₂ interface, thereby producing Li⁺ conductive amorphous phase [270].

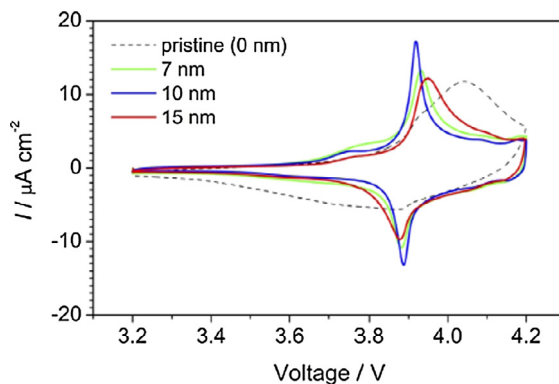


Fig. 6.8. CV of Li/LLZO/LiCoO₂ with and without Nb-modifications. The thicknesses of Nb layers between LLZO and LiCoO₂ are indicated by distinct colored lines: (black) 0 nm, (green) 7 nm, (blue) 10 nm, and (red) 15 nm. Scan rate = 0.1 mV/s [270].

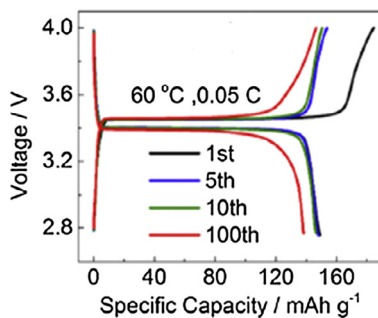


Fig. 6.9. Galvanostatic charge-discharge curves of the LFP:KB:Pvdf:LiTFSI/LLZOTO/Li batteries with 75% mass ratio of LiTFSI to LFP, measured at 0.05 C and 60 °C [271].

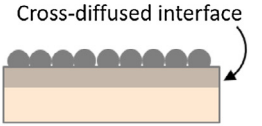
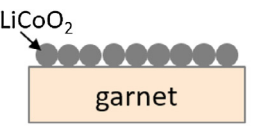
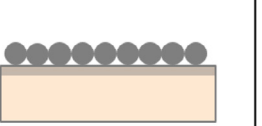
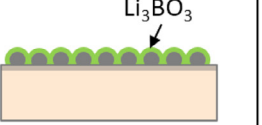
700-LCO/LLZO	RT-LCO/LLZO	RT-LCO/Co-LLZO	700-LCO-LBO/LLZO
			
Physical bonding ⊙	Physical bonding ×	Physical bonding ×	Physical bonding ⊙
Chemical interaction ⊙	Chemical interaction ×	Chemical interaction ⊙	Chemical interaction △
<i>LiCoO₂ coating on LLZO at 700°C</i>	<i>LiCoO₂ powder coating on pure LLZO at R.T.</i>	<i>LiCoO₂ powder coating on Co-diffused LLZO at R.T.</i>	<i>LiCoO₂/Li₃BO₃ coating on LLZO at 700°C</i>

Fig. 6.10. Schematic representation showing the physical bonding and the chemical interactions between LiCoO₂/LLZO cathode arrangements [278].

measurements revealed an improvement in the reaction rates for Li⁺ insertion/extraction reactions in voltage sweeping for the as modified Nb cell as shown in Fig. 6.8 [270].

Recently Du et al. fabricated all-solid-state lithium batteries, where highly conductive Ta doped Li_{6.4}La₃Zr_{1.4}Ta_{0.6}O₁₂ (LLZTO) served as the solid electrolyte. Polyvinylidene fluoride (PVdF): lithium bis(trifluoromethanesulfonyl)imide (LiTFSI), Ketjen Black (KB) and carbon coated LiFePO₄ (LFP) was chosen as the positive electrode and Li metal, the negative electrode [271]. At 60 °C, even after 100 cycles, the battery showed a first discharge capacity of 150 mAh g⁻¹ at 0.05 C, with capacity retention of 93% as shown in Fig. 6.9. The improved contact increased the charge transfer between the ceramic plate and the composite positive electrode [271].

Though garnet structured LLZO offers high Li⁺ conductivity comparable to other ceramic electrolytes, the determination of interfacial resistance at electrode/electrolyte is very much essential since it is considered to be the dominant contributor to the internal resistance of all-solid-state lithium batteries. Li⁺ mobility across the solid electrolyte and the positive electrode became intricate when the electrode undergoes large volume changes. During charging the volume change in positive electrode resulted in exfoliation and thereby limit the maximum thickness and area of the electrode. In order to overcome this issue there must be a good contact between electrode and solid electrolyte. Hence reducing the interfacial impedance across the solid electrolyte is crucial. So far there are many reports on stable Li⁺ transports across garnet solid electrolyte and LiCoO₂ positive electrode interfaces. Sputtering and pulsed laser deposition techniques were often used for the deposition of LiCoO₂ on LLZO. The major downside of direct deposition of LiCoO₂ on LLZO is that at high temperature i.e., >500 °C co-diffusion of Co from LiCoO₂ to LLZO was observed, alongside, La/Zr may also migrate from LLZO to LiCoO₂ [224,257,258]. Takada et al. reported that it is possible to suppress the formation of a space charge layer by an introduction of a nanoscale coating layer on LiCoO₂ using an electron-insulating and ion-conducting oxide materials such as LiNbO₃ [272], Li₄Ti₅O₁₂ [273], TaO₃ [274] and thereby could improve the power density of LiCoO₂ [275]. The presence of oxide coating on the positive electrode can limit the direct contact of the active material with the electrolyte, and thus preventing the cobalt infusion into the electrolyte [276,277]. Ohta et al., studied the effect of interface modification by an introduction of Li₃BO₃ between the LiCoO₂ and LLZO pellet [259]. The presence of Li₃BO₃ facilitates the conduction of Li⁺ in between LiCoO₂ and LLZO, moreover suppresses the co-diffusion across the positive electrode interface at high temperature. The LiCoO₂/Li₃BO₃ positive electrode composite on LLZO solid electrolyte delivered reversible capacities of ~80 mAh g⁻¹ for a few cycles [259]. Recently, Park et al., studied the physical and chemical interaction of LiCoO₂ and LLZO and reported that the formation of tetragonal phase LLZO at the interface of LiCoO₂ and LLZO at high temperature of 700 °C that affects the electrochemical performance and the cycle life [278]. LiCoO₂/LLZO cathode configurations with different degree of physical and chemical interactions are shown in Fig. 6.10 An irreversible electrochemical decomposition at >~3.0 V vs Li⁺/Li was observed. Whereas, the surface modification of LLZO by means of Co-diffused surface layer of Li₃BO₃ showed an improved physical bonding with a charge and discharge capacity of 79.9 mAh g⁻¹, 67.2 mAh g⁻¹, respectively, and Coulombic efficiency of 84.1% [278]. *In situ* experimental techniques and theoretical modeling are necessary to fully understand and mitigate the volume changes of positive electrode with garnet solid electrolyte [278]. One possible approach to overcome the issues related to positive electrode is to construct a composite electrode that consists of active material and solid-state electrolyte. The existence of large contact areas between active material and solid-state electrolyte in the composite particle assist the diffusion of Li⁺ at these interfaces. The advantage of composite electrode is that the particle has a granule structure consisting of nanoparticles, homogeneously dispersed and well connected. Composite electrodes therefore afford high capacity and high-packing density and are considered to be an appropriate electrode for all-solid-state lithium batteries.

Wakayama et al., developed a self-assembled block copolymer-templated synthesis of a 3D bicontinuous nanocomposite electrode material consisting of LiCoO₂ as the active cathode and LLZO as the solid electrolyte [279]. Li⁺ conductivity of 1.6 × 10⁻⁴ S cm⁻¹ was observed for the LLZO pellet. The 3D bicontinuous LCO/LLZO nanocomposite exhibited a high discharge capacity of 134 mAh g⁻¹ of cathode active material at the first cycle, which is 98% of the theoretical capacity

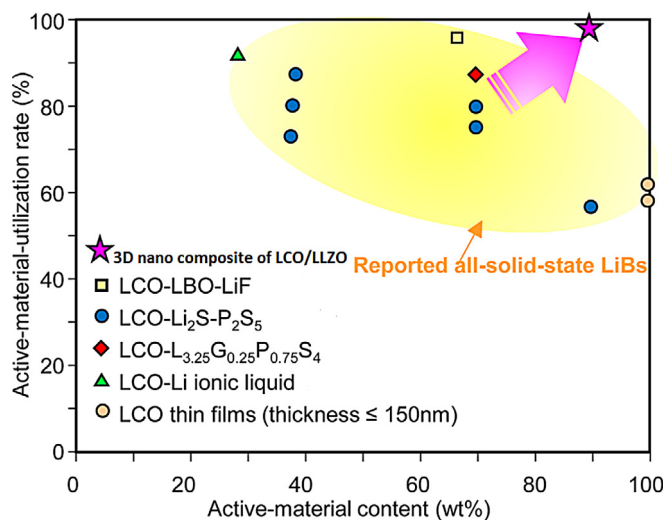


Fig. 6.11. Utilization rate vs. active-material content (wt.%) for 3D bicontinuous nanocomposite of LCO/LLZO and other reported all solid state lithium ion batteries [279].

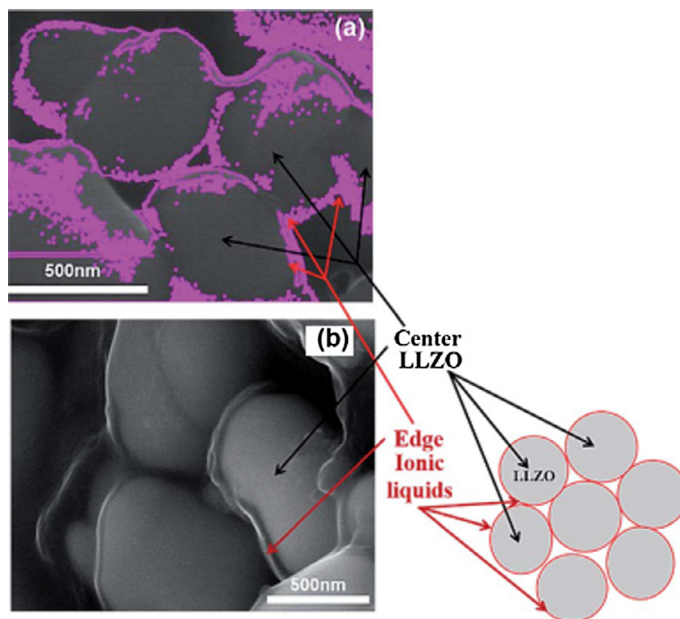


Fig. 6.12. (a) and (b) Depicts the FESEM image of LLZO particles enfolded by the ionic liquid and the LLZO particles contained within the ionic liquid. Figure (c) illustrates the schematic representation of the template developed by LLZO-ionic liquids (LiTFSI and Py14TFSI) [280].

(137 mAh g⁻¹). Fig. 6.11 shows the comparison of the utilization rate of the active materials vs content of the active material of 3D bicontinuous LCO/LLZO nanocomposite with other all-solid-state lithium battery. It can be clearly noted that the active material-utilization rate of 3D bicontinuous LCO/LLZO is around 98% (at an active-material content of 89.4 wt.%) which was higher than the rates for the other all-solid-state lithium battery [279].

Kim et al., proposed a hybrid solid electrolyte (HSE) that comprises 80% LLZO ceramic particle and ionic liquid -IL (19% Py14TFSI, and 1% lithium bis(trifluoromethanesulfonyl)imide) [280]. The presence of ionic liquid could minimize the interfacial resistance and thereby facilitate the Li⁺ conduction through both solid-liquid (LLZO-IL) and solid-liquid-solid (LLZO-IL-solid) interfaces. The FESEM image as shown in Fig. 6.12(a) and (b) indicates LLZO particles are sub-micrometer in size and are enfolded by the ionic liquid as a matrix. The HSE exhibited a total (bulk + grain-boundary) Li⁺ conductivity of 0.4 × 10⁻³ S cm⁻¹ with an electrochemical stability of 5.5 V against metallic lithium [280]. The charge discharge curves for the lithium cells and the image of the lithium cells before and after heating upto 150 °C for 30 min are shown as

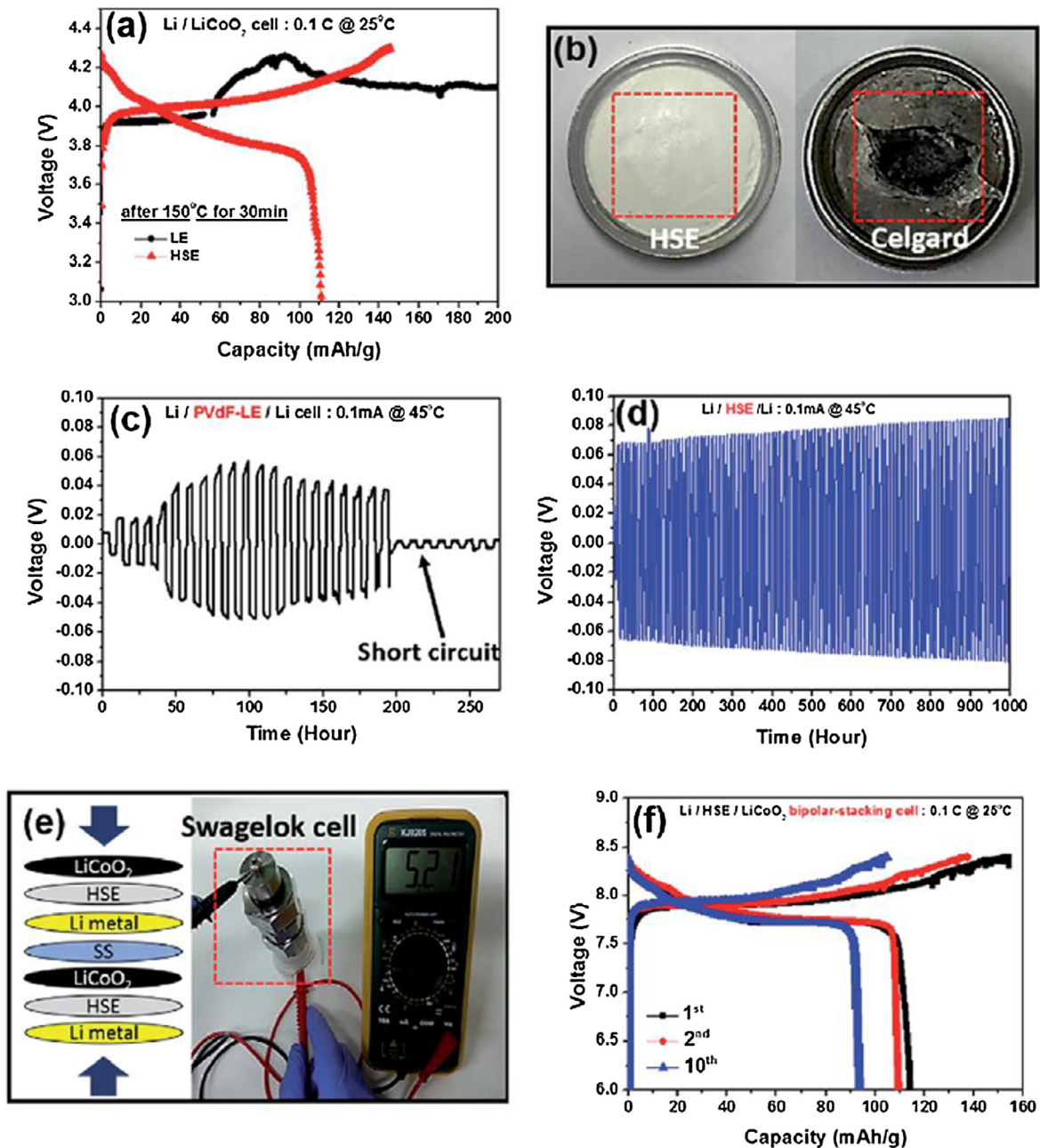


Fig. 6.13. (a) Charge-discharge curves for the lithium cells. (b) Picture of lithium cells before and after heating up to 150 °C for 30 min. (c) and (d) Voltage profile of lithium plating/stripping. (e) Photographic image of open circuit voltage after cell fabrication. (f) Charge-discharge curves for a bipolar stacked cell at a current density of 0.1 C [280].

Fig. 6.13(a) and (b). Compared with the conventional liquid electrolyte (LE) based $\text{Li}/\text{LE}/\text{LiCo}_2$ cell the fabricated $\text{Li}/\text{HSE}/\text{LiCo}_2$ showed a charge–discharge capacity of $140/130 \text{ mAh g}^{-1}$ with 99% capacity retention at the 150th cycle. Moreover, the $\text{Li}/\text{LE}/\text{LiCo}_2$ cell reacts with the electrode active species and caused undesirable chemical reactions as shown in Fig. 6.13 (c). In contrast the $\text{Li}/\text{HSE}/\text{LiCo}_2$ cell remained impervious towards the formation of lithium dendrite enhancing the charge-discharge capacities (Fig. 6.13(d)). The fabrication of high voltage ($> 8 \text{ V}$) pseudo-solid-state LIBs, ($\text{Li}/\text{HSE}/\text{LiCo}_2\text{-SS-Li}/\text{HSE}/\text{LiCo}_2$) using a stacked cell design (Swagelok-bipolar) 85 shown as Fig. 6.13(e), exhibited an open circuit voltage (OCV) of 5.21 V and the corresponding charge discharge curves for bipolar stacked cell measured at 0.1 C between 6.0 and 8.4 V is shown as Fig. 6.13(f) [280].

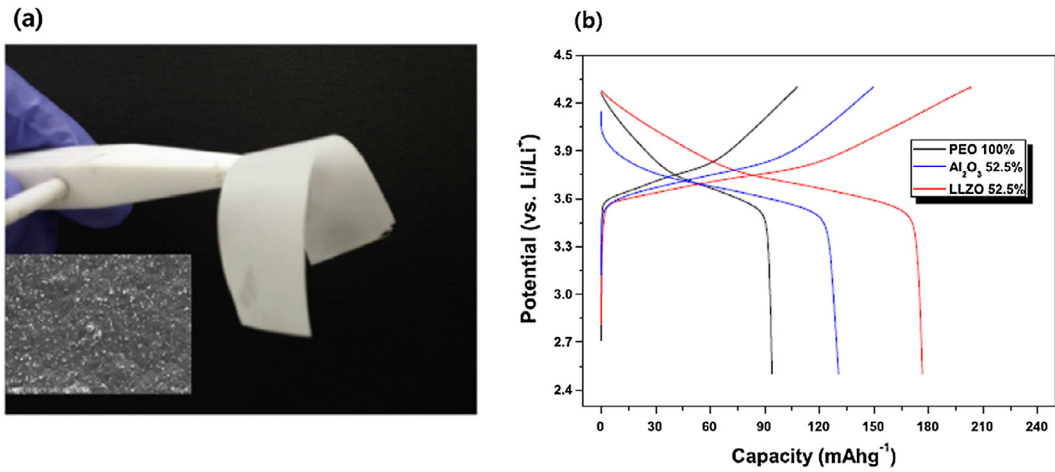


Fig. 6.14. (a) Photographic image of the membrane with 52.5% LLZO along with SEM image (inset) and (b) charge-discharge curve of coin cells containing various membranes in the 1st cycle measured at 55 °C [281].

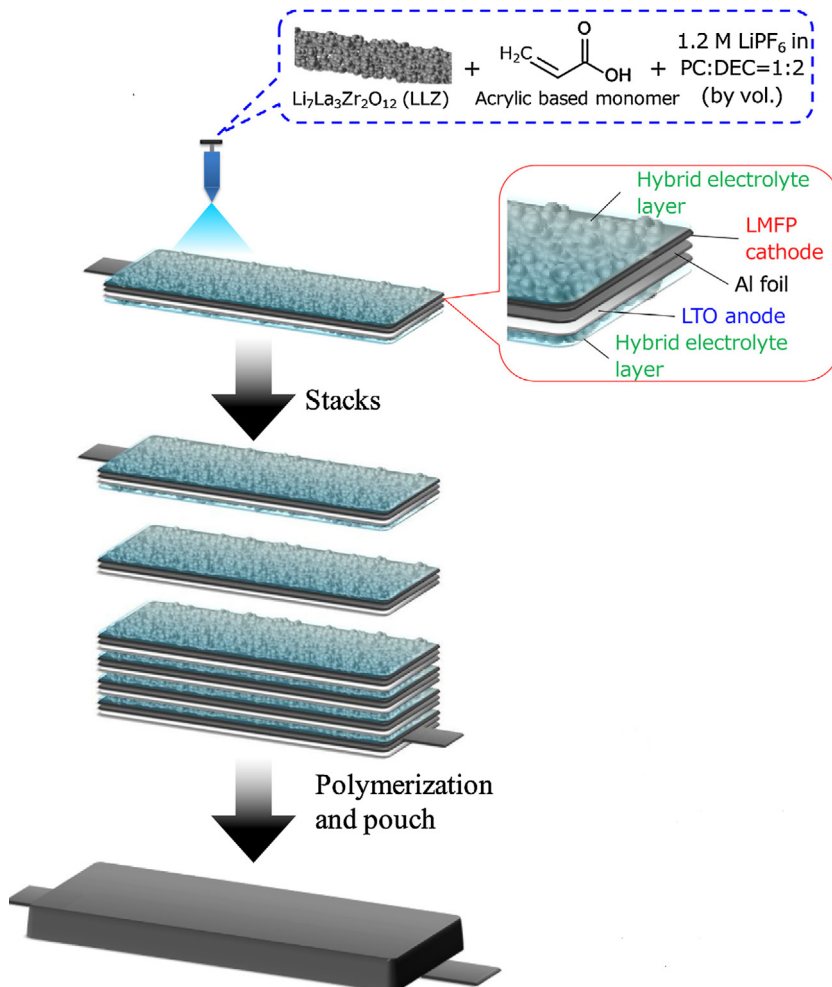


Fig. 6.15. Schematic procedure for the preparation of bipolar battery [282].

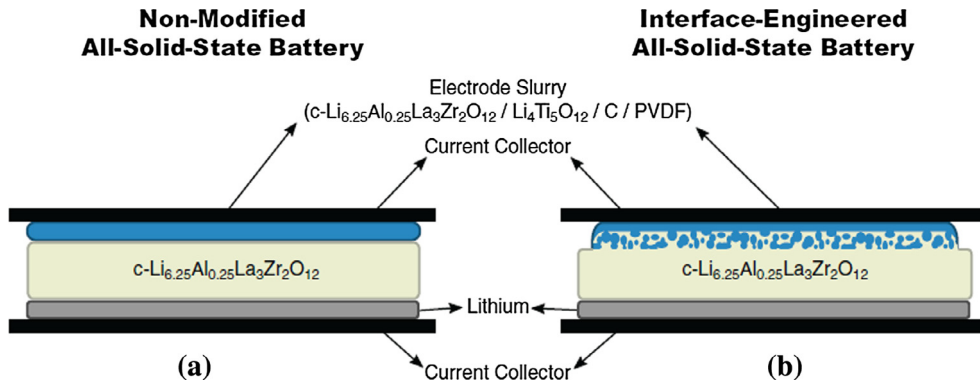


Fig. 6.16. Illustration of (a) nonmodified all-solid-state battery and (b) interface-engineered all-solid-state battery based on $c\text{-Li}_{6.25}\text{Al}_{0.25}\text{La}_3\text{Zr}_2\text{O}_{12}$ solid electrolyte with $\text{Li}_4\text{Ti}_5\text{O}_{12}$ and Li-metal electrodes [283].

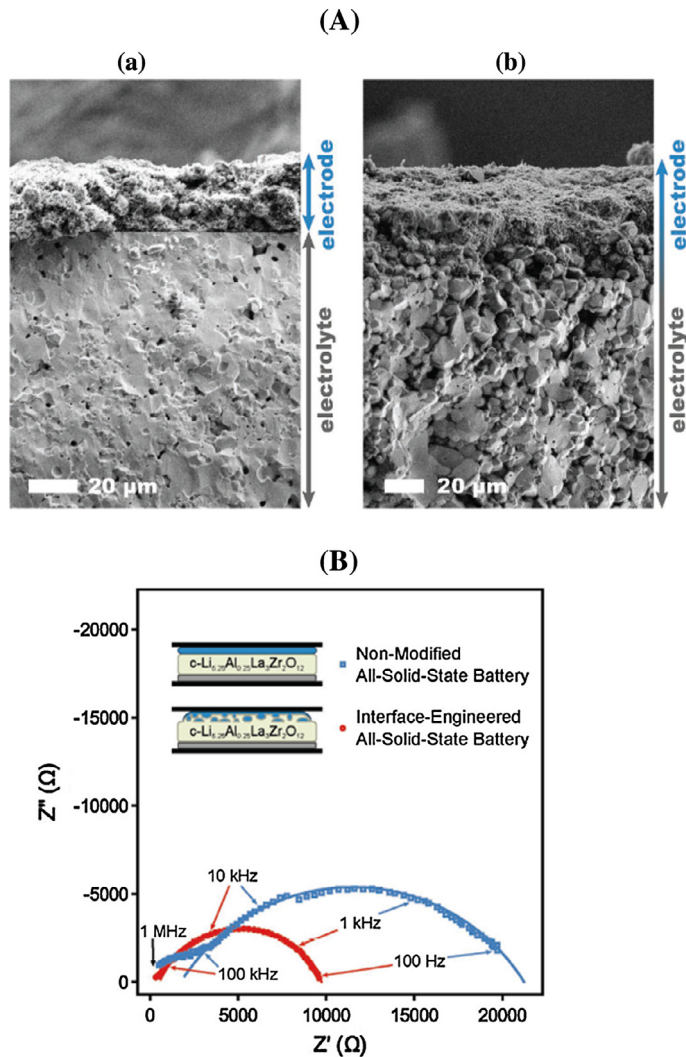


Fig. 6.17. (A) Cross sectional SEM images of pellets sintered with composite nano- $\text{Li}_4\text{Ti}_5\text{O}_{12}$ electrodes for (a) nonmodified and (b) interface-engineered pellets. (B) Cole-cole plot of nonmodified (blue) and interface-engineered (red) all-solid-state batteries based on $c\text{-Li}_{6.25}\text{Al}_{0.25}\text{La}_3\text{Zr}_2\text{O}_{12}$ with nanograined $\text{Li}_4\text{Ti}_5\text{O}_{12}$ and Li-metal electrodes measured at 95°C [283].

The interfacial resistance at the electrode electrolyte interfaces may be decreased by using a polymer electrolyte. Also dry electrolyte membranes based on polyethylene oxide (PEO) can be used in a freestanding form without modifying current battery fabrication processes. The low ionic conductivities of PEO-based membranes at room temperature can be enhanced by stabilizing the highly conductive amorphous matrix with inorganic filler (nano-sized SiO_2 , Al_2O_3 , BaTiO_3 , etc.). However, high ionic conductivities of around $10^{-4} \text{ S cm}^{-1}$ can only be obtained in these composites when they have very high filler contents (>30 wt.%), which result in poor mechanical properties.

Recently Choi et al. reported free-standing composite membrane with high ionic conductivity and good processability through the incorporation of garnet-type tetragonal phase LLZO solid electrolyte powder into a PEO polymer matrix and also assessed the feasibility of solid electrode designs that use oxide solid electrolyte powders [281]. The composite membrane with the maximum ionic conductivity ($4.42 \times 10^{-4} \text{ S cm}^{-1}$ at 55°C) was reported with 52.5%LLZO and 47.5% PEO. The hybridization of the organic and inorganic components of these membranes results in synergetic effects on their lithium ionic conductivity [281].

The photographic image of the membrane with 52.5% LLZO and charge-discharge characteristics of coin cells containing various membranes in the first cycle at 55°C are shown in Fig. 6.14(a). The tests of Li/composite membrane/ $\text{LiNi}_{0.6}\text{Co}_{0.2}\text{Mn}_{0.2}\text{O}_2$ half-cells indicated that the composite membrane containing LLZO exhibits superior kinetic properties to those of the other membranes (the PEO-only membrane and the membrane containing Al_2O_3) as shown in Fig. 6.14(b) [281].

Thin hybrid electrolytes composed of LLZ particles coated with 4 wt.% polyacrylonitrile (PAN)-based gel polymer electrolyte with a few micrometers thickness have been studied in order to be practically applied to 12 V-class bipolar battery with liquid-free and separator-free. The schematic procedure for preparation of bipolar battery is shown as Fig. 6.15 [282]. This hybrid electrolyte reduced the internal resistance of $\text{LiMn}_{0.8}\text{Fe}_{0.2}\text{PO}_4$ (LMFP)/ $\text{Li}_4\text{Ti}_5\text{O}_{12}$ (LTO) cells and enabled discharge at low temperatures. The fabricated 12 V-class bipolar battery with stacking cells in five series exhibited good discharge rate capability from 0.2 to 20 C and operated in the wide temperature range of -40°C to 80°C . The performance of 12 V-class bipolar battery using thin LLZ-based hybrid electrolyte was comparable to that of conventional lithium-ion batteries with a liquid electrolyte [282].

As dendrite formation in LLZO with Li metal anodes, especially at high current rates and lower pellet density, has been reported the investigation of alternative anode materials is also highly important. Broek et al. reported successful assembly of the anode material $\text{Li}_4\text{Ti}_5\text{O}_{12}$ in combination with $c\text{-Li}_{6.25}\text{Al}_{0.25}\text{La}_3\text{Zr}_2\text{O}_{12}$ garnet structures (Fig. 6.16) and reveal its battery operations to be employed in full ceramic all-solid-state batteries [283]. Broek et al. utilized novel strategies to design an interface-engineered all-solid-state battery based on a porous garnet electrolyte interface structure, in which the electrode

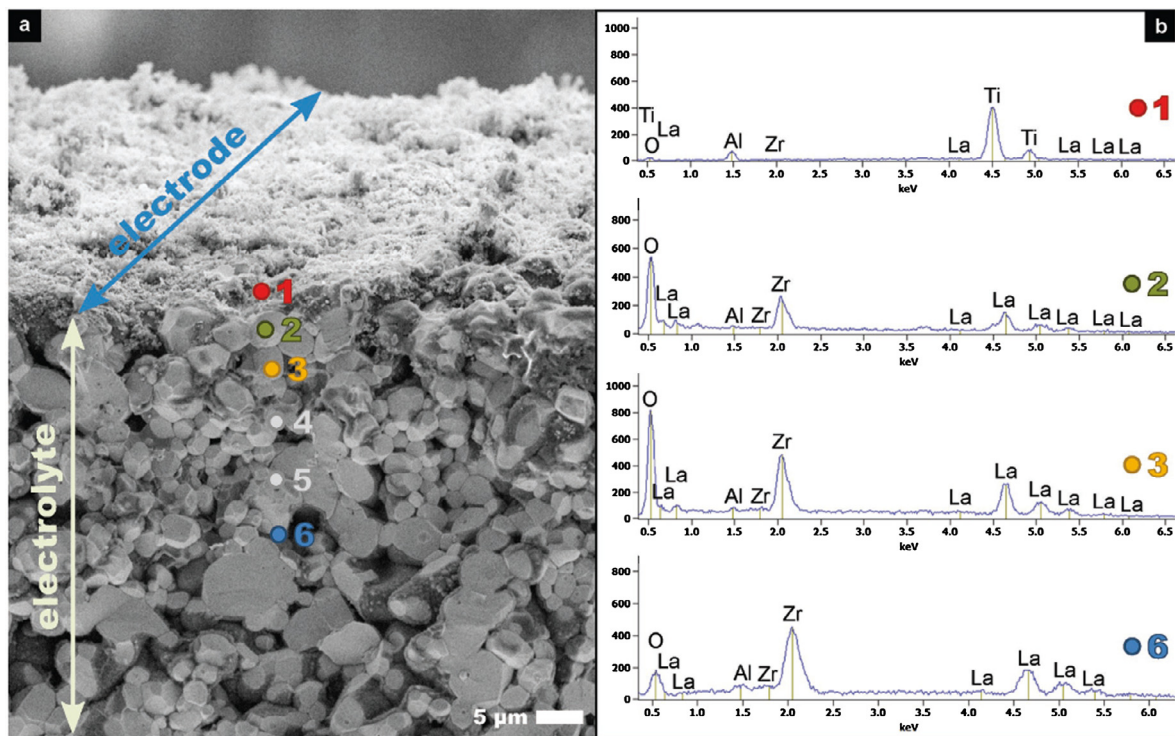


Fig. 6.18. (a) SEM image from an interface-engineered all-solid-state battery based on $c\text{-Li}_{6.25}\text{Al}_{0.25}\text{La}_3\text{Zr}_2\text{O}_{12}$ and nanogained $\text{Li}_4\text{Ti}_5\text{O}_{12}$ electrode obtained after 25 charge/discharge cycles. (b) Energy-dispersive X-ray spectra (EDX) data from the marked spots showing no additional phases at the electrode-electrolyte interphase [283].

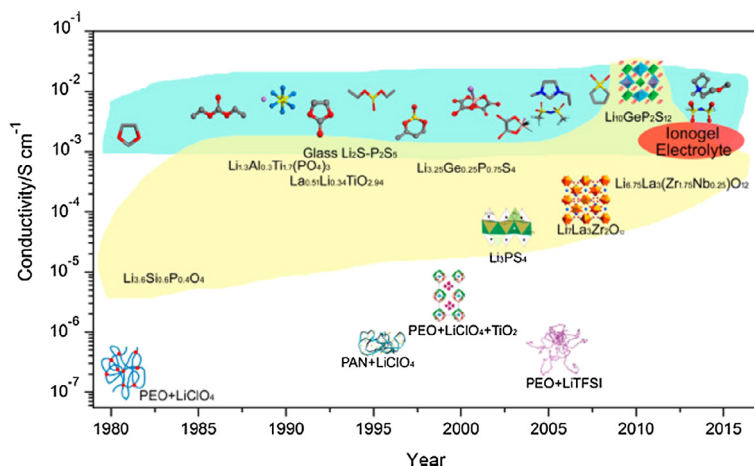


Fig. 6.19. Evolution over time of ionogel electrolytes (red area) with other inorganic solid electrolytes [31,32,81,97,98,275,285–288] (yellow area), organic liquid electrolytes [289–291] (blue area), ionic liquids [292–294] (blue area) and polymer electrolytes [295–298] [284].

material is intimately embedded [283]. The interface engineering is achieved through the sacrificial organic template on dense c - $\text{Li}_{6.25}\text{Al}_{0.25}\text{La}_3\text{Zr}_2\text{O}_{12}$ pellets, resulting in a porous interface after sintering into which the electrode slurry is cast. The scanning electron microscopy images and electrochemical impedance spectroscopy data shown as Fig. 6.17 revealed an intimate embedding of the nanograined $\text{Li}_4\text{Ti}_5\text{O}_{12}$ into the porous electrolyte interlayer and thereby drastically reduced cell resistances in the interface-engineered all-solid-state battery compared to nonmodified cells [283].

The SEM images and EDX spectra over the cross-section of interface-engineered all-solid-state battery after 25 charge/discharge cycles displayed as Fig. 6.18 did not reveal any new phases containing titanium at the electrode–electrolyte interface. Their results indicated the importance to engineer a suited ceramic interfacial structure with augmented contact points between the electrodes and the electrolyte to assure a proper Li^+ -transfer during charge and discharge cycles [283].

Owing to the high ionic conductivity stability in air and water, nonflammability and wide electrochemical window, ionic liquids have received much attention in the field of lithium batteries. However, immobilized ionic liquids within organic matrices used as polymer electrolyte membranes exhibit poor mechanical performance, and thermal stability is limited by the organic nature of the polymer. Wu et al. proposed an alternative route on the basis of immobilization of ionic liquids within a thermally stable inorganic matrix called “ionogels” [284]. The confinement of ionic liquids within organic and inorganic matrices makes it possible to keep their unique properties in the solid state, thus avoiding drawbacks related to shaping and risk of leakage. Ionogels are a unique class of stable solid-like electrolytes that combine the advantages of inorganic oxide and ionic liquid components. Lithium salts dissolved in an ionic liquid serve as the ionic-conducting phase, while the inorganic oxide solid matrices provide a physical barrier between the electrodes, thereby preventing short circuits. We believe that ionogel-based on garnet structured inorganic oxides energy storage devices may offer numerous advantages,

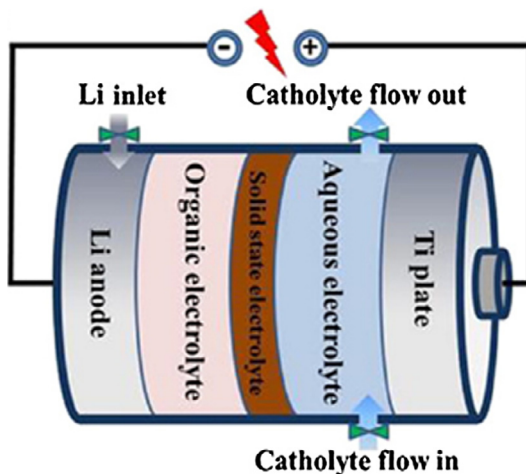


Fig. 6.20. Schematic illustrations of the $\text{Li-H}_2\text{O}_2$ semi fuel cell employing hybrid electrolyte [149].

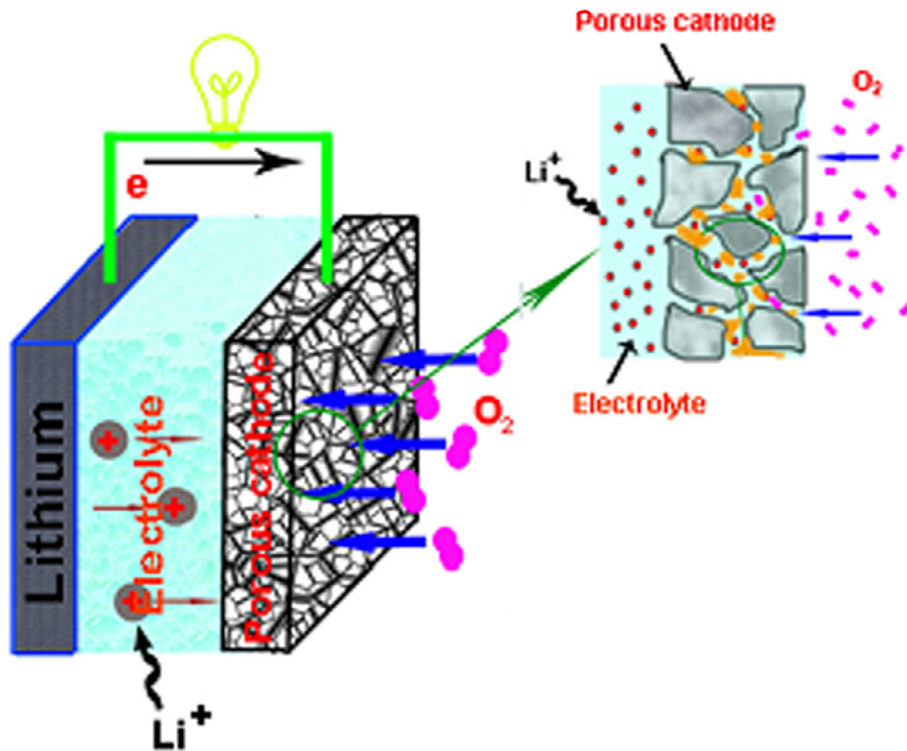


Fig. 6.21. Simplified sketch of a Li-air battery system [300].

including greater safety, lighter weight, and more flexibility for future application. The evolution over time of ionogel electrolytes (red area) with those of other inorganic solid electrolytes [31,32,81,97,98,275,285–288] (yellow area), organic liquid electrolytes [289–291] (blue area), ionic liquids [292–294] (blue area) and polymer electrolytes; [295–298] is shown as Fig. 6.19 [284].

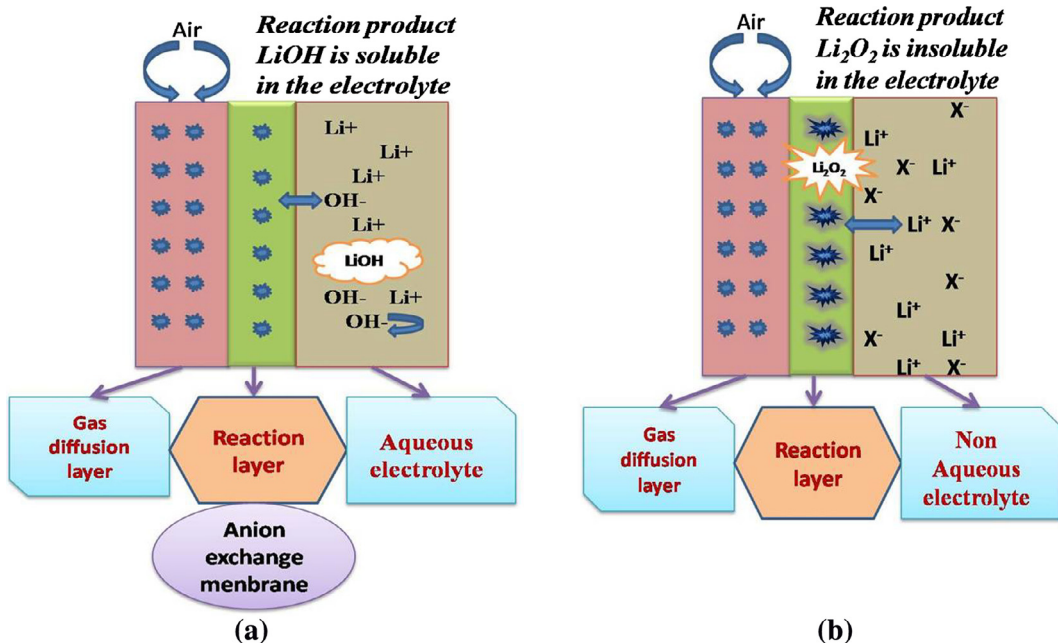


Fig. 6.22. Schematic representation showing the difference between the reaction product in (a) aqueous and (b) non-aqueous Li-air battery.

6.2. Fuel cell

An Al_2O_3 doped $\text{Li}_{6.4}\text{La}_3\text{Zr}_{1.4}\text{Ta}_{0.6}\text{O}_{12}$ (LLZTO) cylindrical pellet with the cubic garnet structure was prepared through solid state reaction with pressure less sintering by Liu et al. for the economical fabrication of lithium-hydrogen peroxide semi fuel cell [149]. Impedance spectroscopy measurements on LLZTO sheets (19 mm dia, 200 μm thickness), obtained by slicing the LLZTO cylinder showed a conductivity as high as $1.02 \times 10^{-3} \text{ S cm}^{-1}$ at room temperature. The relative density of LLZTO was found to be $\sim 94\%$. Schematic representation of the fabricated Li- H_2O_2 semi fuel cell using the hybrid electrolyte is shown in Fig. 6.20 [149]. The fabricated semi fuel cell with LLZO electrolyte exhibited lower interfacial resistance and high power density resulting in higher performance of the Li- H_2O_2 fuel cell. The discharge curves of the test showed a relative flat discharge voltage plateau with 82% of average lithium metal utilization in the negative electrode indicating a good stability of the thin LLZTO sheet in the cell. The dense LLZO provided reliable protection of Li metal against water/air in the cell, thereby preventing corrosion, capacity fade and lithium dendrite formation [149].

6.3. Li-air battery

Solid electrolyte with high Li^+ conductivity and excellent chemical stability against metallic lithium is expected to enhance the performance of high energy density lithium metal based batteries such as Li-air batteries. Rechargeable Li-air batteries, also called as the lithium-oxygen batteries (Li- O_2) established by Abraham et al. [299] possesses a very high energy density that instigate from the use of lithium metal as the negative electrode and the consumption of atmospheric oxygen at the positive electrode as shown in Fig. 6.21 [300]. The Li-air battery has been considered as a promising candidate for future generation of electric vehicles (EVs) because of its superior energy density 5200 Wh/kg including oxygen weight [301].

The Li-air batteries are categorized based on the types of electrolyte used such as: aprotic (organic) solvents, aqueous solvents, hybrid (non-aqueous/aqueous) solvents and all-solid-state electrolyte. In all these systems Li metal is used as the negative electrode and oxygen as the positive electrode. The primary electrochemical reaction mechanism for charge and discharge depends on the property of the electrolyte used in the Li-air battery.

The main difference between non-aqueous and aqueous electrolyte based Li-air battery is that the discharge product in the aqueous system is soluble LiOH (in alkaline medium) as shown in Fig. 6.22(a), while in the non-aqueous system, the discharge product is an insoluble insulator lithium peroxide (Li_2O_2) precipitated on the positive electrode as shown in Fig. 6.22 (b) [302]. The problem of positive electrode blockage is solved due to the soluble nature of the reaction products of LiOH in aqueous electrolyte, which continuously maintain the battery performance [303].

Due to the strong reaction between lithium metal and water, unlike conventional zinc-air batteries, the Li-air batteries cannot be operated with aqueous electrolytes without protection for the lithium metal negative electrode. Efforts have been made by various research groups to develop a suitable solid electrolyte to separate the metallic lithium negative electrode from the aqueous electrolyte. The commercial NASICON-type glass-ceramic $\text{Li}_{1+x+y}\text{Al}_x\text{Ti}_{2-x}\text{Si}_y\text{P}_{3-y}\text{O}_{12}$ (LTAP, Ohara Inc., Japan) solid electrolyte is considered as most prosperous for lithium-air battery applications. LTAP solid electrolyte has high Li^+ conductivity and better mechanical strength. Moreover, it is chemically stable in water, mild acids and bases. However

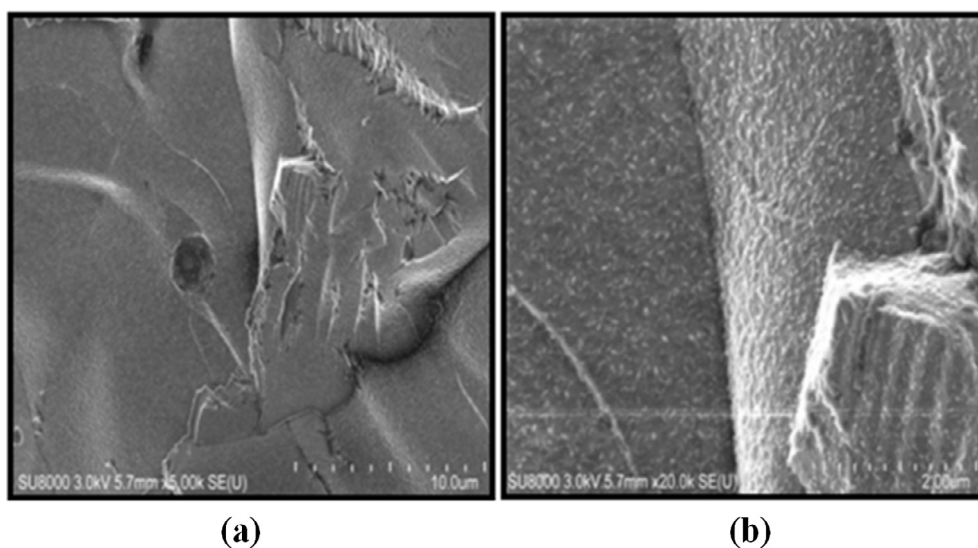


Fig. 6.23. (a) FE-SEM image of the fractured surface of $\text{Li}_7\text{La}_{2.75}\text{Y}_{0.25}\text{Zr}_2\text{O}_{12}$ pellets sintered at 1200 °C and (b) its corresponding magnified FE-SEM image [304].

the glass-ceramics LTAP is not the decisive solid electrolyte because of the unstable nature of LTAP in contact with metallic lithium. There emanated the necessity of an inclusion of a buffer layer between the electrolyte and that of the lithium metal that compromised the overall energy density. This buffer layer raised many technical problems which influenced the performance and stability of Li-air batteries.

Advanced Li-air battery architecture demands a high Li^+ conductive solid electrolyte membrane that is electrochemically stable against metallic lithium and aqueous electrolyte. The garnet structured $\text{Li}_7\text{La}_3\text{Zr}_2\text{O}_{12}$ (LLZO) has been widely considered in recent times for such applications because of its high Li^+ conductivity and good stability against lithium metal [97,98,187,202]. In addition to the high total (bulk + grain-boundary) Li^+ conductivity and electrochemical stability against lithium metal, the dense microstructure is also an essential factor for the successful application of LLZO as solid electrolyte membrane in rechargeable lithium and Li-air battery applications. The dense LLZO solid electrolyte membrane is expected to prevent the catholyte from reacting with metallic lithium and also to suppress lithium dendrite penetration. Also the grain boundaries were high interfacial energy regions for the reactions between LLZO and water/ CO_2 . Hence, the increasing density and reduced grain-boundary are not only helpful to enhance the Li^+ conductivity of LLZO, but also helpful in reducing the reactions between LLZO and water/ CO_2 .

The understanding of stability of the high Li^+ conductive solid electrolytes in different solutions with various pH is essential for possible application as a protective layer for lithium metal electrode and aqueous electrolytes. Shimonishi et al. reported that cubic LLZO was stable in saturated LiCl aqueous solution with respect to structure and electrical conductivity [175]. However, there are only few reports on studies of stability of garnet-type Li^+ conducting solid electrolyte in different aqueous solution. The preliminary results indicated that, high Li^+ conductive cubic phase LLZO would be a better solid electrolyte for Li-air batteries [175].

A systematic investigation has been carried out on the Li^+ conduction behavior and structural stability of $\text{Li}_7\text{La}_{3-x}\text{Y}_x\text{Zr}_2\text{O}_{12}$ ($x = 0.125, 0.25$ and 0.50) against aqueous solutions with different pH [304]. The SEM image of $\text{Li}_7\text{La}_{2.75}\text{Y}_{0.25}\text{Zr}_2\text{O}_{12}$ is shown as Fig. 6.23(a). The addition of Y in $\text{Li}_7\text{La}_{2.75}\text{Y}_{0.25}\text{Zr}_2\text{O}_{12}$ acted as the sintering aid during the sintering process and thereby helped to enhance the density. This is apparent in the magnified FE-SEM image of $\text{Li}_7\text{La}_{2.75}\text{Y}_{0.25}\text{Zr}_2\text{O}_{12}$, as shown in Fig. 6.18(b), which indicated the growth of relatively larger grains with better contact with the neighboring grains. Moreover, the $\text{Li}_7\text{La}_{2.75}\text{Y}_{0.25}\text{Zr}_2\text{O}_{12}$ pellets sintered at 1200°C exhibited relative density of 96% and a maximized room temperature total (bulk + grain-boundary) Li^+ conductivity of $3.21 \times 10^{-4} \text{ S cm}^{-1}$ [304].

The stability of high Li^+ conductive $\text{Li}_7\text{La}_{2.75}\text{Y}_{0.25}\text{Zr}_2\text{O}_{12}$ solid electrolyte in aqueous solutions was investigated in solutions of 1 M LiCl, dist. H_2O and 1 M LiOH solutions for 2 weeks at 50°C . The room temperature impedance profile of $\text{Li}_7\text{La}_{2.75}\text{Y}_{0.25}\text{Zr}_2\text{O}_{12}$ immersed in 1 M LiCl and dist. H_2O showed no remarkable change in Li^+ conductivity, i.e. it was in the same order ($10^{-4} \text{ S cm}^{-1}$) that of pristine $\text{Li}_7\text{La}_{2.75}\text{Y}_{0.25}\text{Zr}_2\text{O}_{12}$ [304]. This indicated that, the dense and high Li^+ conductive cubic phase solid electrolyte $\text{Li}_7\text{La}_{2.75}\text{Y}_{0.25}\text{Zr}_2\text{O}_{12}$ is stable and did not react with the solution of 1 M LiCl and dist. H_2O . However, $\text{Li}_7\text{La}_{2.75}\text{Y}_{0.25}\text{Zr}_2\text{O}_{12}$ immersed in 1 M LiOH at 50°C exhibited appreciable variation in the impedance profile as shown in Fig. 6.24. The degradation in the Li^+ conductivity might be due to the formation of secondary phase at the grain-boundary as a result of the reaction between $\text{Li}_7\text{La}_{2.75}\text{Y}_{0.25}\text{Zr}_2\text{O}_{12}$ and 1 M LiOH aqueous solution at 50°C [304].

Earlier reports indicated the Li^+/H^+ exchange reaction in several lithium garnets. Li^+/H^+ exchange rate depends on the pH of the solutions, and if it is intense, it may lead to a structural transformation or even decomposition. Consequently, it may degrade the Li^+ conductivity. However, $\text{Li}_7\text{La}_{2.75}\text{Y}_{0.25}\text{Zr}_2\text{O}_{12}$ preserved its high Li^+ conductive cubic structure ($Ia\bar{3}d$) against

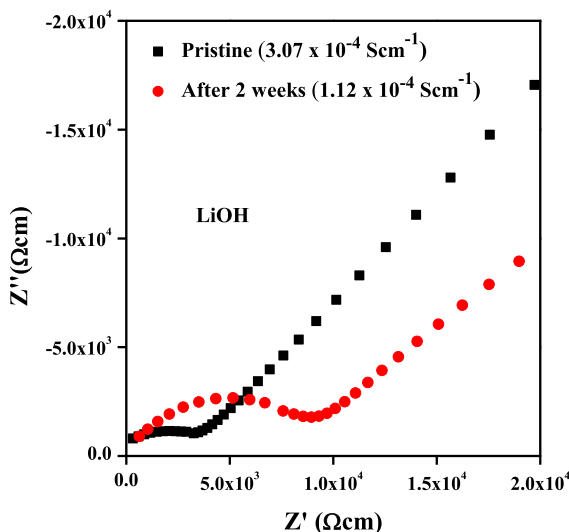


Fig. 6.24. Room temperature impedance (Cole-Cole) plot of $\text{Li}_7\text{La}_{2.75}\text{Y}_{0.25}\text{Zr}_2\text{O}_{12}$ immersed in 1 M LiOH solutions at 50°C for 2 weeks [304].

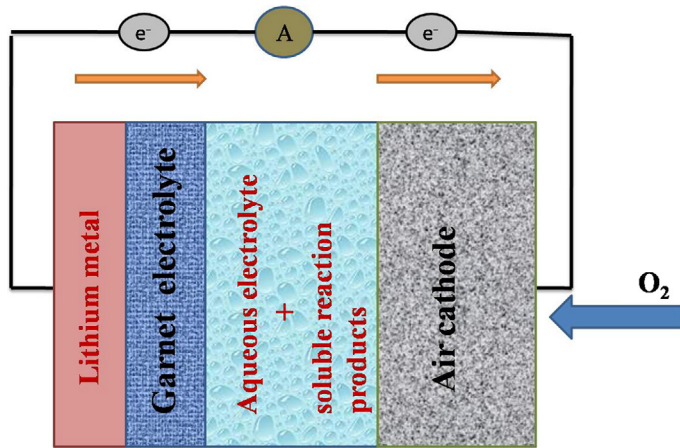


Fig. 6.25. Model architecture of Li-air battery with garnet structured solid electrolyte.

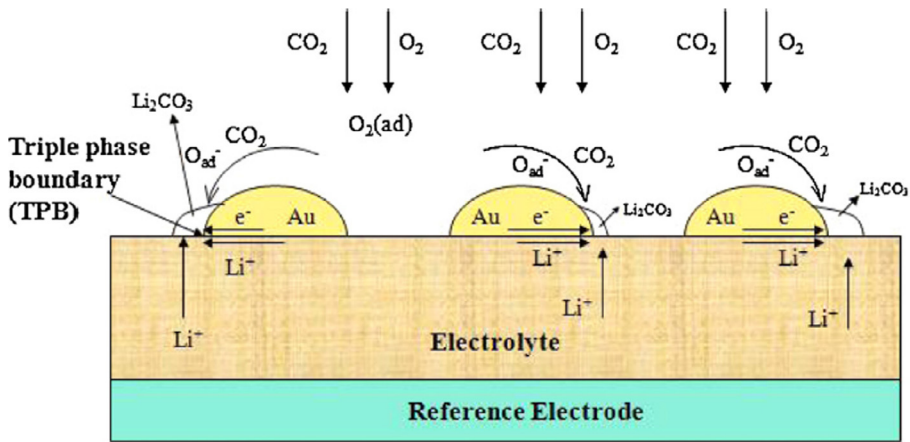


Fig. 6.26. Simplified sketch for the galvanic cell reaction processed for the formation of Li_2CO_3 in a CO_2 sensor [305].

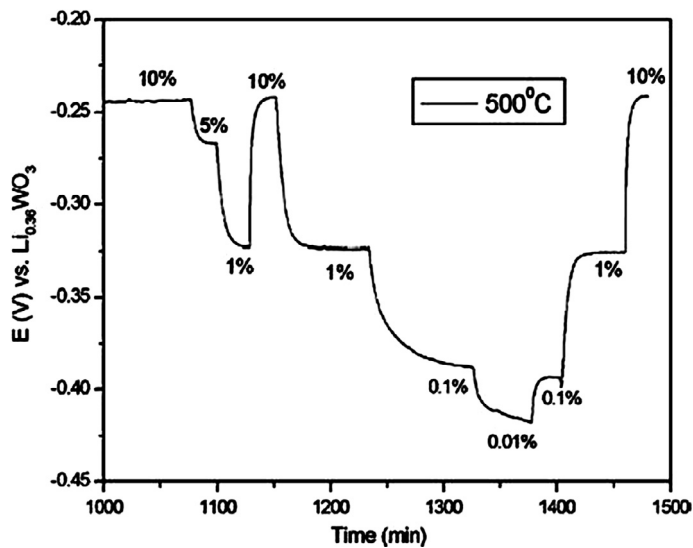


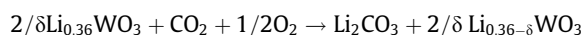
Fig. 6.27. Transient response of the cell to the changing CO_2 partial pressure at $500\text{ }^\circ\text{C}$ [305].

1 M LiCl and dist. H₂O and hence, it demonstrated no degradation in Li⁺ conductivity. The appearance of impurity phase and the degradation of Li⁺ conductivity in 1 M LiOH suggested that Li₇La_{2.75}Y_{0.25}Zr₂O₁₂ cannot be used with higher pH medium (strong alkaline medium) at elevated temperature for longer period of time [304].

The high Li⁺ conductivity, good thermal and chemical stability and ease of preparation of dense Li₇La_{2.75}Y_{0.25}Zr₂O₁₂ suggests that this partial yttrium-containing lithium garnet may be a promising solid ceramic electrolyte for all-solid-state lithium rechargeable batteries. The model Li-air battery architecture with LLZO lithium garnet shown in Fig. 6.25 is expected to deliver a high specific energy density.

6.4. Sensors

Zhu et al. [305] fabricated solid state potentiometric CO₂ sensor using Li₆BaLa₂Ta₂O₁₂ as solid electrolyte. Lithium tungsten oxide with nominal composition Li_{0.36}WO₃ was employed as the reference electrode and a blend of Li₂CO₃ and Au paste as the sensing electrode. When CO₂ gas is sensed, Li⁺ partially released from Li_{0.36}WO₃ migrate through the Li₆BaLa₂Ta₂O₁₂ solid state electrolyte. Meanwhile CO₂ molecules are easily diffused into porous auxiliary layer of the sensor leading to quick adsorption and desorption of CO₂ in the reactive sites as modeled in Fig. 6.26 [305]. This in turn equilibrates with the Li ions and the O₂ into Li₂CO₃ indicated by the following reaction:



By changing the CO₂ concentration from 0.01% to 10%, the EMF measurements were taken at 450 °C and 500 °C. Fig. 6.27 clearly shows a reproducible response with response time of less than 1 min [305].

The developed sensor showed a long life stable performance, a high sensitivity of 73 mV/decade, with the miniature structure lowering the heating temperature and subsequent reduction in the power consumption in comparison with the conventional tube type sensors [305]. One of the promising feature of this lithium electrolyte based CO₂ sensors are their fast response compared to any other alkali ion conducting materials.

7. Conclusions

Lithium batteries are expected to play an important role for the development of high performance batteries for future applications in e.g., electric vehicles, stationary energy storage and portable electronics. However, there are both scientific and practical compulsions to replace currently used flammable liquid electrolytes with safe solid electrolytes without trouncing of performance.

Crystalline garnet structured ceramic that contains mobile Li⁺ have the potential to combine the ionic mobility of liquid with the robust mechanical properties of solids. Systematic investigation through high resolution X-ray diffraction, neutron diffraction, nuclear magnetic resonance (NMR), Raman measurements, impedance spectroscopic measurements and various theoretical calculations shows that the structure and Li⁺ conductivity of lithium garnets are intimately related. The migration ability of Li⁺ via the vacancies plays a very crucial role in their conduction properties. Slight change in the ordering of lithium in lithium garnets ultimately has great influence on the Li⁺ conductivity due to the higher flexibility of crystal lattice and diffusion pathways.

Among numerous lithium garnets cubic phase LLZO offers multiple desirable properties like high ionic conductivities, stability against metallic lithium, a wide electrochemical operating window up to 6 V and pH stability around 7–11.5. In addition to the high Li⁺ conductivity and electrochemical stability, the dense microstructure is a critical issue for the successful application as an electrolyte membrane in high energy density battery. Field assisted sintering technique (FAST) is found to be a useful technique to prepare dense lithium garnets in a very short interval of time at relatively lower sintering temperature. The processing of dense (94 ± 1%) cubic phase LLZO thin (<30 μm) flexible films with high ambient ionic conductivities (0.2 ± 0.03 mS cm⁻¹) using conventional casting–sintering of flame made nanoparticles through careful control of the processing variables is an encouraging development. These c-LLZO membranes may greatly increase the choice of cell components and expected to simplify battery configurations. Further exploration of novel simple synthetic method and cost effective processing technology is required for the commercialization of garnet structured flexible thin films as electrolytes for electrochemical devices.

All-solid-state lithium batteries based on cubic LLZO solid electrolytes have still challenges in realizing high practical performances due to their high electrode–electrolyte interfacial resistances. Hence, it is of at most importance to form favorable contact between electrodes and the lithium garnet electrolyte. The interface modification will be a useful technique to improve the cycle stability and rate capability of charge discharge reaction. Further experimental research work on microstructure engineering may provide a solution to the dendrite problem for higher current density with metallic lithium as negative electrode. The issues related to positive electrode may be eliminated by constructing a composite electrode that consists of active material and solid-state electrolyte. Preparation of high Li⁺ conductive lithium garnet glass ceramic may solve the problem of dendrite growth and large interfacial resistance.

For electric vehicle applications, improvement of energy and power density is needed. It is not only decided by the properties of electrolyte, but also on the positive electrode and negative electrode and the battery configurations. Further

research activity on processing techniques and interface engineering are strongly required for the successful fabrication and commercialization of all solid state high energy density battery based on garnet structured electrolyte.

Acknowledgements

One of the author R.M. thank the German Science Foundation [DFG Grant WE 684/11-1], the DRDO [No: ERIP/E R/0804415/M/01/1183/4.11.2009], New Delhi, India, the CSIR [No. 03(1144)/09/EMR-II dated 12/11/2009], New Delhi, India, the Pondicherry University, Puducherry, India [PU/PC/Start-up Grant/2011-12/306], the DAE BRNS [No. 37(3)/14/42/2014-BRNS], Mumbai, India for the financial support and UGC, New Delhi, India for the Research Award [F.30-81/2015 (SA-II)] to carry out some of the research work presented in this review.

References

- [1] Braun PV, Cho J, Pikul JH, King WP, Zhang H. High power rechargeable batteries. *Curr Opin Solid State Mater Sci* 2012;16:186–98.
- [2] Tarascon JM, Armand M. Issues and challenges facing rechargeable lithium batteries. *Nature* 2001;414:359–67.
- [3] Zu CX, Li H. Thermodynamic analysis on energy densities of batteries. *Energy Environ Sci* 2011;4:2614–24.
- [4] Etacheri V, Marom R, Elazari R, Salitra G, Aurbach D. Challenges in the development of advanced Li-ion batteries: a review. *Energy Environ Sci* 2011;4:3243–62.
- [5] Scrosati B, Hassoun J, Sun YK. Lithium-ion batteries, a look into the future. *Energy Environ Sci* 2011;4:3287–95.
- [6] Mizushima K, Jones PC, Wiseman PJ, Goodenough JB. Li_xCoO_2 ($0 < x < -1$): a new cathode material for batteries of high energy density. *Mater Res Bull* 1980;15:783–9.
- [7] Linden D, Reddy TB. *Handbook of batteries*. 3rd ed. New York: McGraw-Hill; 2002.
- [8] Chagnon G, Allen P, Hensley K, Nechev K, Oweis S, Reynolds R, et al. Performance of SAFT Li-ion batteries for high power automotive application. In: *Proceedings of the electric vehicle symposium EVS-18*, Berlin.
- [9] Sloop SE, Pugh JK, Wang S, Kerr J, Kinoshita K. Chemical reactivity of PF_5 and LiPF_6 in ethylene carbonate/dimethyl carbonate solutions. *Electrochem Solid-State Lett* 2001;4:A42–4.
- [10] Rogers RD, Seddon KR. Chemistry ionic liquids-solvents of the future. *Science* 2003;302:792–3.
- [11] Stenger-Smith JD, Irvin JA. Ionic liquids for energy storage applications. *Mater Matters* 2009;4:103–5.
- [12] Gabriel S, Weiner J. Ueber einige abkömmlinge des propylamins. *Ber Dtsch Chem Ges* 1888;21:2669–79.
- [13] Sakaabe H, Matsumoto H. N-methyl-N-propylpiperidinium bis (trifluoromethanesulfonyl) imide (PP13-TFSI)–novel electrolyte base for Li battery. *Electrochem Commun* 2003;5:594–8.
- [14] Quartarone E, Mustarelli P. Electrolytes for solid-state lithium rechargeable batteries: recent advances and perspectives. *Chem Soc Rev* 2011;40:2525–40.
- [15] Lee JS, Bae JY, Lee H, Quan ND, Kim HS, Kim H. Ionic liquids as electrolytes for Li ion batteries. *J Ind Eng Chem* 2004;10:1086–9.
- [16] Sato T, Maruo T, Marukane S, Takagi K. Ionic liquids containing carbonate solvent as electrolytes for lithium ion cells. *J Power Sources* 2004;138:253–61.
- [17] Fenton DE, Parker JM, Wright PV. Complexes of alkali metal ions with poly (ethylene oxide). *Polymer* 1973;14:589.
- [18] Armand MB, Chabagno JM, Duclot M. Fast ion transport in solids: electrodes and electrolytes. In: Vashisha P, Mundy JN, Shenoy GK, editors. NY: North Holland; 1979. p. 131.
- [19] Wright PV. An anomalous transition to a lower activation energy for dc electrical conduction above the glass-transition temperature. *J Polym Sci Polym Phys Ed* 1976;14:955–7.
- [20] Grünebaum M, Hiller MM, Jankowsky S, Jeschke S, Pohl B, Schürmann T, et al. Synthesis and electrochemistry of polymer based electrolytes for lithium batteries. *Prog Solid State Chem* 2014;42:85–105.
- [21] Song JY, Wang YY, Wan CC. Review of gel-type polymer electrolytes for lithium-ion batteries. *J Power Sources* 1999;77:183–97.
- [22] Quartarone E, Mustarelli P, Magistris A. PEO-based composite polymer electrolytes. *Solid State Ionics* 1998;110:1–14.
- [23] Zhang P, Yang LC, Li LL, Ding ML, Wu YP, Holze R. Enhanced electrochemical and mechanical properties of P(VDF-HFP)-based composite polymer electrolytes with SiO_2 nanowires. *J Membr Sci* 2011;379:80–5.
- [24] Kumar D, Hashmi SA. Ion transport and ion-filler-polymer interaction in poly(methyl methacrylate)-based, sodium ion conducting, gel polymer electrolytes dispersed with silica nanoparticles. *J Power Sources* 2010;195:5101–8.
- [25] Pandey GP, Agrawal RC, Hashmi SA. Magnesium ion-conducting gel polymer electrolytes dispersed with nanosized magnesium oxide. *J Power Sources* 2009;190:563–72.
- [26] Ferrari S, Quartarone E, Mustarelli P, Magistris A, Fagnoni M, Protti S, et al. Lithium ion conducting P(VDF-HFP) composite gel electrolytes based on N-methoxyethyl-N-methylpyrrolidinium bis(trifluoromethanesulfonyl)-imide ionic liquid. *J Power Sources* 2010;195:559–66.
- [27] Tanaka R, Sakurai M, Sekiguchi H, Inoue M. Improvement of room-temperature conductivity and thermal stability of PEO-LiClO₄ systems by addition of a small proportion of polyethylenimine. *Electrochim Acta* 2003;48:2311–6.
- [28] Gray FM. *Solid polymer electrolytes: Fundamental and technological applications*. New York: VCH Publishers; 1991.
- [29] Appetecchi GB, Henderson W, Villano P, Berrettoni M, Passerini S. PEO-LiN(SO₂CF₂CF₃)₂ polymer electrolytes I. XRD, DSC, and ionic conductivity characterization. *J Electrochem Soc* 2001;148:A1171–8.
- [30] Irvine JTS, West AR. High conductivity ionic conductors, recent trends and application. In: Takahashi T, editor. *World Scientific Singapore*; 1989.
- [31] Aono H, Imanaka N, Adachi GY. High Li^+ conducting ceramics. *Acc Chem Res* 1994;27:265–70.
- [32] Adachi GY, Imanaka N, Aono H. Fast Li^+ conducting ceramic electrolytes. *Adv Mater* 1996;8:127–35.
- [33] Robertson AD, West AR, Ritchie AG. Review of crystalline lithium-ion conductors suitable for high temperature battery applications. *Solid State Ionics* 1997;104:1–11.
- [34] Alpen UV, Rabenau A, Talat GH. Ionic conductivity in Li_3N single crystals. *Appl Phys Lett* 1977;30:621–3.
- [35] Yao YFY, Kummer JT. Ion exchange properties of and rates of ionic diffusion in beta-alumina. *J Inorg Nucl Chem* 1967;29:2453–75.
- [36] Farrington GC, Dunn BS, Briant JL. Li^+ and divalent ion conductivity in beta and beta' alumina. *Solid State Ionics* 1981;3(4):405–8.
- [37] Wang B, Chakoumakos BC, Sales BC, Kwak BS, Bates JB. Synthesis crystal structure and ionic conductivity of a polycrystalline lithium phosphorus oxynitride with the $\gamma\text{-Li}_3\text{PO}_4$ structure. *J Solid State Chem* 1995;115:313–23.
- [38] Hong HYP. Crystal structure and ionic conductivity of $\text{Li}_{14}\text{Zn}(\text{GeO}_4)_4$ and other new Li^+ superionic conductors. *Mater Res Bull* 1978;13:117–24.
- [39] Murayama M, Kanno R, Irie M, Ito S, Hata T, Sonoyama N, et al. Synthesis of new lithium ionic conductor thio-LISICON-lithium silicon sulfides system. *J Solid State Chem* 2002;168:140–8.
- [40] Aono H, Sugimoto E, Sadaoka Y, Imanaka N, Adachi GY. The electrical properties of ceramic electrolytes for $\text{LiM}_x\text{Ti}_{2-x}(\text{PO}_4)_3 + y\text{Li}_2\text{O}$, M = Ge, Sn, Hf, and Zr systems. *J Electrochem Soc* 1993;140:1827–33.
- [41] Knauth P. Inorganic solid Li ion conductors: an overview. *Solid State Ionics* 2009;180:911–6.
- [42] Inaguma Y, Liqun C, Itoh M, Nakamura T, Uchida T, Ikuta H, et al. High ionic conductivity in lithium lanthanum titanate. *Solid State Commun* 1993;86:689–93.

- [43] Bohnke O, Bohnke C, Fourquet JL. Mechanism of ionic conduction and electrochemical intercalation of lithium into the perovskite lanthanum lithium titanate. *Solid State Ionics* 1996;91:21–31.
- [44] Birke P, Scharner S, Huggins RA, Weppner W. Electrolytic stability limit and rapid lithium insertion in the fast-ion-conducting $\text{Li}_{0.29}\text{La}_{0.57}\text{TiO}_3$ perovskite-type compound. *J Electrochem Soc* 1997;144:L167–9.
- [45] Zintl E, Brauer G. Konstitution des lithium nitrids. *Z Elektrochem Angew Phys Chem* 1935;41:102–7.
- [46] Rabenau A, Schulz H. Re-evaluation of the lithium nitride structure. *J Less Common Metals* 1976;50:155–9.
- [47] Rabenau A. Lithium nitride and related materials—case-study of the use of modern solid-state research techniques. *Solid State Ionics* 1982;6:277–93.
- [48] Gregory DH, O' Meara PM, Gordon AG, Hodges JP, Short S, Jorgensen JD. Structure of lithium nitride and transition-metal-doped derivatives, $\text{Li}_{3-x-y}\text{M}_x\text{N}$ (M = Ni, Cu): a powder neutron diffraction study. *Chem Mater* 2002;14:2063–70.
- [49] Bragg WL, Gottfried C, West J. The structure of β alumina. *Z Kristallogr* 1931;77:255–74.
- [50] Beevers CA, Ross MAS. The crystal structure of "Beta Alumina" $\text{Na}_2\text{O} \cdot 11\text{Al}_2\text{O}_3$. *Z Kristallogr* 1937;97:59–66.
- [51] Yamaguchi G, Suzuki K. On the structures of alkali polyaluminates. *Bull Chem Soc Jpn* 1968;41:93–9.
- [52] Bettman M, Peters CR. The crystal structure of $\text{Na}_2\text{O} \cdot \text{MgO} \cdot 5\text{Al}_2\text{O}_3$, with reference to $\text{Na}_2\text{O} \cdot 5\text{Al}_2\text{O}_3$ and other isotypal compounds. *J Phys Chem* 1969;73:1774–80.
- [53] Sudworth JL, Tilley AR. The sodium sulphur battery. London: Chapman and Hall; 1985.
- [54] Hong HYP. Crystal structures and crystal chemistry in the system $\text{Na}_{1+x}\text{Zr}_2\text{Si}_x\text{P}_{3-x}\text{O}_{12}$. *Mater Res Bull* 1976;11:173–82.
- [55] Goodenough JB, Hong HYP, Kafalas JA. Fast Na^+ ion transport in skeleton structures. *Mater Res Bull* 1976;11:203–20.
- [56] Bohnke O, Ronchetti S, Mazza D. From single-layer dispersions of molybdenum disulfide towards ternary metal sulfides: incorporating copper and silver into a MoS_2 matrix. *Solid State Ionics* 1999;122:137–44.
- [57] Alpen UV, Bell MF, Hofer HH. Ionic conductivity in $\text{Na}_4\text{ZrSi}_3\text{O}_{16}$. *Solid State Ionics* 1982;7:345–8.
- [58] Alamo J, Roy R. Crystal chemistry of the $\text{NaZr}_2(\text{PO}_4)_3$, NZP or CTP, structure family. *J Mater Sci* 1986;21:444–50.
- [59] Ivanov-Schitz AK, Bykov AB. Ionic conductivity of the $\text{NaZr}_2(\text{PO}_4)_3$ single crystals. *Solid State Ionics* 1997;100:153–5.
- [60] Cretin M, Fabry P. Comparative study of lithium ion conductors in the system $\text{Li}_{1+x}\text{Al}_x\text{A}_{2-x}\text{IV}(\text{PO}_4)_3$ with $\text{A}^{\text{IV}} = \text{Ti}$ or Ge and $0 \leq x \leq 0.7$ for use as Li^+ sensitive membranes. *J Eur Ceram Soc* 1999;19:2931–40.
- [61] Aono H, Sugimoto E, Sadaoka Y, Imanaka N, Adachi G. Ionic conductivity of the lithium titanium phosphate ($\text{Li}_{1+x}\text{Al}_x\text{Ti}_{2-x}(\text{PO}_4)_3$), ($\text{Li}_{1+x}\text{Sc}_x\text{Ti}_{2-x}(\text{PO}_4)_3$), ($\text{Li}_{1+x}\text{Y}_x\text{Ti}_{2-x}(\text{PO}_4)_3$), ($\text{Li}_{1+x}\text{La}_x\text{Ti}_{2-x}(\text{PO}_4)_3$) systems. *J Electrochem Soc* 1989;136:590–1.
- [62] Geng H, Lan J, Mei A, Lin Y, Nan CW. Effect of sintering temperature on microstructure and transport properties of $\text{Li}_{3-x}\text{La}_{2/3-x}\text{TiO}_3$ with different lithium contents. *Electrochim Acta* 2011;56:3406–14.
- [63] Ion Transport in NASICON Solids. <<http://www.iitg.ernet.in/physics/fac/padmakumar/nasicon.htm>>.
- [64] Bruce PG, West AR. Phase diagram of the LISICON, solid electrolyte system $\text{Li}_4\text{GeO}_4\text{-Zn}_2\text{GeO}_4$. *Mat Res Bull* 1980;15:379–85.
- [65] Plattner E, Vollenkle H. Die kristallstruktur der verbindung $\text{Li}_3\text{Zn}_{0.5}\text{GeO}_4$. *Monat Chem* 1979;110:693–8.
- [66] Abrahams I, Bruce PG, David WIF, West AR. A re-examination of the lisicon structure using high-resolution powder neutron diffraction: evidence for defect clustering. *Acta Crystallogr* 1989;B45:457–62.
- [67] Abrahams I, Bruce PG, West AR, David WIF. Structure determination of LISICON solid solutions by powder neutron diffraction. *J Solid State Chem* 1988;75:390–66.
- [68] Saiful Islam M. Recent atomistic modelling studies of energy materials: batteries included. *Phil Trans R Soc A* 2010;368:3255–67.
- [69] Holzwarth NAW, Du YA. Li ion diffusion mechanisms in the crystalline electrolyte $\gamma\text{-Li}_3\text{PO}_4$ batteries and energy storage. *J Electrochem Soc* 2007;154:A999–A1004.
- [70] Murayama M, Kanno R, Kawamoto Y, Kamiyama T. Structure of the thio-LISICON, Li_4GeS_4 . *Solid State Ionics* 2002;154:789–94.
- [71] Bruce PG, Abraham I. A defect cluster model for ion migration in solid electrolytes. *J Solid State Chem* 1991;95:74–82.
- [72] Ryoji K, Murayama M, Irie M, Shinya Ito W, Hata T, Sonoyama N, et al. Synthesis of new lithium ionic conductor thio-lisicon lithium silicon sulfides system. *J Solid State Chem* 2002;168:140–8.
- [73] Ryoji K, Homma K, Yonemura M, Kobayashi T, Nagao M, Hirayama M. Crystal structure and phase transitions of the lithium ionic conductor Li_3PS_4 . *Solid State Ionics* 2011;182:53–8.
- [74] West PAR, Glasser PF. Preparation and crystal chemistry of some tetrahedral L&PO-type compounds. *J Solid State Chem* 1972;4:20–8.
- [75] Zhang S, Deng C, Fu BL, Yang SY, Ma L. Doping effects of magnesium on the electrochemical performance of $\text{Li}_2\text{FeSiO}_4$ for lithium ion batteries. *Electroanal Chem* 2010;644:150–4.
- [76] Deng C, Zhang S, Fu BL, Yang SY, Ma L. Effects of Cr doping on the electrochemical properties of $\text{Li}_2\text{FeSiO}_4$ cathode material for lithium-ion batteries. *Electrochim Acta* 2010;55:8482–9.
- [77] Bruce PG, West AR. Ionic conductivity of LISICON solid solutions, $\text{Li}_{2+2x}\text{Zn}_{1-x}\text{GeO}_4$. *J Solid State Chem* 1982;44:354–65.
- [78] Kuwano J, West AR. New Li^+ ion conductors in the system, $\text{Li}_4\text{GeO}_4\text{-Li}_3\text{VO}_4$. *Mat Res Bull* 1980;15:1661–7.
- [79] Khorassani A, West AR. Li^+ ion conductivity in the System $\text{Li}_4\text{SiO}_4\text{-Li}_3\text{VO}_4$. *J Solid State Chem* 1984;53:369–75.
- [80] Yamaki J, Ohtsuka H, Shodai T. Rechargeable lithium thin film cells with inorganic electrolytes. *Solid State Ionics* 1996;86–88:1279–84.
- [81] Kanno R, Murayama M. Lithium ionic conductor thio-LISICON: the $\text{Li}_2\text{S-GeS}_2\text{-P}_2\text{S}_5$ system. *J Electrochem Soc* 2001;148:A742–6.
- [82] Galasso FS. Structure, properties and preparation of perovskite-type compounds. Oxford: Pergamon Press; 1969.
- [83] Bhalla AS, Guo R, Roy R. The perovskite structure—a review of its role in ceramic science and technology. *Mater Res Innov* 2000;4:3–26.
- [84] Thangadurai V, Weppner W. Synthesis and electrical properties of K^- and Pr^- substituted LaGaO_3 and LaInO_3 perovskites. *J Electrochem Soc* 2001;148:1294–301.
- [85] Harada Y, Ishigaki T, Kawai H, Kuwano J. Lithium ion conductivity of polycrystalline perovskite $\text{La}_{0.67-x}\text{Li}_x\text{TiO}_3$ with ordered and disordered arrangements of the A-Site ions. *Solid State Ionics* 1998;108:407–13.
- [86] Harada Y, Hirakoso Y, Kawai H, Kuwano J. Order-disorder of the A-site ions and lithium ion conductivity in the perovskite solid solution $\text{La}_{0.67-x}\text{Li}_x\text{TiO}_3$ ($x = 0.11$). *Solid State Ionics* 1999;121:245–51.
- [87] Catti M. Local structure of the $\text{Li}_{1/8}\text{La}_{5/8}\text{TiO}_3$ (LLTO) ionic conductor by theoretical simulations. *J Phys* 2008;117:1–8.
- [88] Bates JB, Dudney NJ, Neudecker B, Ueda A, Evans CD. Thin-film lithium and lithium-ion batteries. *Solid State Ionics* 2000;135:33–45.
- [89] Wolfenstine J. Electrical and mechanical properties of hot-pressed versus sintered $\text{LiTi}_2(\text{PO}_4)_3$. *Solid State Ionics* 2009;180:961–7.
- [90] Thangadurai V, Kaack H, Weppner W. Novel fast lithium ion conduction in garnet-type $\text{Li}_5\text{La}_3\text{M}_2\text{O}_{12}$ (M = Nb, Ta). *J Am Ceram Soc* 2003;86:437–40.
- [91] Wells AF. Structural inorganic chemistry. 5th ed. Oxford: Oxford Science Publications: Clarendon Press; 1984.
- [92] Cussen EJ, Yip TWS. A neutron diffraction study of the d^0 and d^{10} lithium garnets $\text{Li}_3\text{Nd}_3\text{W}_2\text{O}_{12}$ and $\text{Li}_3\text{La}_3\text{Sb}_2\text{O}_{12}$. *J Solid State Chem* 2007;180:1832–9.
- [93] Siegmán A. Lasers. Mill Valley, CA: University Science Books; 1986.
- [94] Wyckoff RWG. Crystal structures: inorganic compounds $\text{R}_x(\text{MX})_y$, $\text{R}_x(\text{MnXp})_y$, hydrates and ammoniates. 2nd ed. New York: Interscience Publishers; 1960.
- [95] Hyooma H, Hayashi K. Crystal structures of $\text{La}_3\text{Li}_5\text{M}_2\text{O}_{12}$ (M = Nb, Ta). *Mater Res Bull* 1988;23:1399–407.
- [96] O'Callaghan MP, Powell AS, Titman JJ, Chen GZ, Cussen EJ. Switching on fast lithium ion conductivity in garnets: the structure and transport properties of $\text{Li}_{3+x}\text{Nd}_3\text{Te}_{2-x}\text{Sb}_2\text{O}_{12}$. *Chem Mater* 2008;20:2360–9.
- [97] Murugan R, Thangadurai V, Weppner W. Fast lithium ion conduction in garnet-type $\text{Li}_7\text{La}_3\text{Zr}_2\text{O}_{12}$. *Angew Chem Int Ed* 2007;46:7778–81.
- [98] Murugan R, Thangadurai V, Weppner W. Schnelle lithiumionenleitung in granatartigem $\text{Li}_7\text{La}_3\text{Zr}_2\text{O}_{12}$. *Angew Chem* 2007;119:7925–8.
- [99] Gu W, Ezhiri M, Prasada Rao R, Avdeev M, Adams S. Effects of penta- and trivalent dopants on structure and conductivity of $\text{Li}_7\text{La}_3\text{Zr}_2\text{O}_{12}$. *Solid State Ionics* 2015;274:100–5.

- [100] Rangasamy E, Wolfenstine J, Sakamoto J. The role of Al and Li concentration on the formation of cubic garnet solid electrolyte of nominal composition $\text{Li}_7\text{La}_3\text{Zr}_2\text{O}_{12}$. *Solid State Ionics* 2012;206:28–32.
- [101] Ohta S, Kobayashi T, Asaoka T. High lithium ionic conductivity in the garnet-type oxide $\text{Li}_{7-x}\text{La}_3(\text{Zr}_{2-x}\text{Nb}_x)\text{O}_{12}$ ($x = 0-2$). *J Power Sources* 2011;196:3342–5.
- [102] Wang Y, Lai W. High ionic conductivity lithium garnet oxides of $\text{Li}_{7-x}\text{La}_3\text{Zr}_{2-x}\text{Ta}_x\text{O}_{12}$ compositions. *Electrochem Solid-State Lett* 2012;15:A68–71.
- [103] Buschmann H, Berends S, Mogwitz B, Janek J. Lithium metal electrode kinetics and ionic conductivity of the solid lithium ion conductors “ $\text{Li}_7\text{La}_3\text{Zr}_2\text{O}_{12}$ ” and $\text{Li}_{7-x}\text{La}_3\text{Zr}_{2-x}\text{Ta}_x\text{O}_{12}$ with garnet-type structure. *J Power Sources* 2012;206:236–44.
- [104] Li Y, Han JT, Wang C, Xie H, Goodenough JB. Optimizing Li^+ conductivity in a garnet framework. *J Mater Chem* 2012;22:15357–61.
- [105] Murugan R, Ramakumar S, Janani N. High conductive yttrium doped $\text{Li}_7\text{La}_3\text{Zr}_2\text{O}_{12}$ cubic lithium garnet. *Electrochem Commun* 2011;13:1373–5.
- [106] Ramakumar S, Satyanarayana L, Manorama SV, Murugan R. Structure and Li^+ dynamics of Sb-doped $\text{Li}_7\text{La}_3\text{Zr}_2\text{O}_{12}$ fast lithium ion conductors. *Phys Chem Chem Phys* 2013;15:11327.
- [107] Dhivya L, Janani N, Palanivel B, Murugan R. Li^+ transport properties of W substituted $\text{Li}_7\text{La}_3\text{Zr}_2\text{O}_{12}$ cubic lithium garnets. *AIP Adv* 2013;3:082115–82121.
- [108] Deviannapoorani C, Dhivya L, Ramakumar S, Murugan R. Lithium ion transport properties of high conductive tellurium substituted $\text{Li}_7\text{La}_3\text{Zr}_2\text{O}_{12}$ cubic lithium garnets. *J Power Sources* 2013;240:18–25.
- [109] Rangasamy E, Wolfenstine J, Allen J, Sakamoto J. The effect of 24c-site (A) cation substitution on the tetragonal-cubic phase transition in $\text{Li}_{7-x}\text{La}_{3-x}\text{A}_x\text{Zr}_2\text{O}_{12}$ garnet-based ceramic electrolyte. *J Power Sources* 2013;230:261–6.
- [110] Huang M, Dumon A, Nan C. Effect of Si, In and Ge doping on high ionic conductivity of $\text{Li}_7\text{La}_3\text{Zr}_2\text{O}_{12}$. *Electrochem Commun* 2012;21:62–4.
- [111] Howard MA, Clemens O, Kendrick E, Knight KS, Apperley DC, Anderson PA, et al. Effect of Ga incorporation on the structure and Li ion conductivity of $\text{La}_3\text{Zr}_2\text{Li}_7\text{O}_{12}$. *Dalton Trans* 2012;41:12048–53.
- [112] Percival J, Kendrick E, Smith RI, Slater PR. Cation ordering in Li containing garnets: synthesis and structural characterisation of the tetragonal system, $\text{Li}_7\text{La}_3\text{Sn}_2\text{O}_{12}$. *Dalton Trans* 2009;26:5177–81.
- [113] Zaiß T, Ortner M, Murugan R, Weppner W. Fast ionic conduction in cubic hafnium garnet $\text{Li}_7\text{La}_3\text{Hf}_2\text{O}_{12}$. *Ionics* 2010;16:855–8.
- [114] O’Callaghan MP, Lynham DR, Cussen EJ, Chen GZ. Structure and ionic-transport properties of lithium-containing garnets $\text{Li}_3\text{Ln}_3\text{Te}_2\text{O}_{12}$ (Ln = Y, Pr, Nd, Sm–Lu). *Chem Mater* 2006;18:4681–9.
- [115] Cussen EJ, Yip TWS, O’Neill G, O’Callaghan MP. A comparison of the transport properties of lithium-stuffed garnets and the conventional phases $\text{Li}_3\text{Ln}_3\text{Te}_2\text{O}_{12}$. *J Solid State Chem* 2011;184:470–5.
- [116] Ramakumar S, Janani N, Murugan R. Influence of lithium concentration on the structure and Li^+ transport properties of cubic phase lithium garnets. *Dalton Trans* 2015;44:539–52.
- [117] Thangadurai V, Weppner W. Effect of sintering on the ionic conductivity of garnet-related structure $\text{Li}_5\text{La}_3\text{Nb}_2\text{O}_{12}$ and In- and K-doped $\text{Li}_5\text{La}_3\text{Nb}_2\text{O}_{12}$. *J Solid State Chem* 2006;179:974–84.
- [118] Murugan R, Weppner W, Beurmann PS, Thangadurai V. Structure and lithium ion conductivity of bismuth containing lithium garnets $\text{Li}_5\text{La}_3\text{Bi}_2\text{O}_{12}$ and $\text{Li}_6\text{SrLa}_2\text{Bi}_2\text{O}_{12}$. *Mater Sci Eng B* 2007;143:14–20.
- [119] Murugan R, Weppner W, Beurmann PS, Thangadurai V. Structure and lithium ion conductivity of garnet-like $\text{Li}_5\text{La}_3\text{Sb}_2\text{O}_{12}$ and $\text{Li}_6\text{SrLa}_2\text{Sb}_2\text{O}_{12}$. *Mater Res Bull* 2008;43:2579–91.
- [120] Murugan R, Weppner W, Thangadurai V. Effect of lithium ion content on the lithium ion conductivity of the garnet-like structure $\text{Li}_{5+x}\text{BaLa}_2\text{Ta}_2\text{O}_{11.5} + 0.5x$ ($x = 0-2$). *Appl Phys A* 2008;91:615–20.
- [121] Percival J, Kendrick E, Slater PR. Synthesis and characterisation of the garnet-related Li ion conductor, $\text{Li}_5\text{Nd}_3\text{Sb}_2\text{O}_{12}$. *Mater Res Bull* 2008;43:765–70.
- [122] Narayanan S, Thangadurai V. Effect of Y substitution for Nb in $\text{Li}_5\text{La}_3\text{Nb}_2\text{O}_{12}$ on Li^+ conductivity of garnet-type solid electrolytes. *J Power Sources* 2011;196:8085–90.
- [123] Truong L, Colter J, Thangadurai V. Chemical stability of Li-stuffed garnet-type $\text{Li}_{5+x}\text{Ba}_x\text{La}_{3-x}\text{Ta}_2\text{O}_{12}$ ($x = 0, 0.5, 1$) in water: a comparative analysis with the Nb analogue. *Solid State Ionics* 2013;247–248:1–7.
- [124] Nemori H, Matsuda Y, Matsui M, Yamamoto O, Takeda Y, Imanishi N. Relationship between lithium content and ionic conductivity in the $\text{Li}_{5+2x}\text{La}_3\text{Nb}_{2-x}\text{Sc}_x\text{O}_{12}$ system. *Solid State Ionics* 2014;266:9–12.
- [125] Pinzaru D, Thangadurai V. Synthesis, structure and Li ion conductivity of garnet-like $\text{Li}_{5+2x}\text{La}_3\text{Nb}_{2-x}\text{Sm}_x\text{O}_{12}$ ($0 \leq x \leq 0.7$). *J Electrochem Soc* 2014;161:A2060–7.
- [126] Baral AK, Sumaletha N, Farshid R, Thangadurai V. Evaluation of fundamental transport properties of Li-excess garnet-type $\text{Li}_{5+2x}\text{La}_3\text{Ta}_{2-x}\text{Y}_x\text{O}_{12}$ ($x = 0.25, 0.5$ and 0.75) electrolytes using AC impedance and dielectric spectroscopy. *Phys Chem Chem Phys* 2014;16:11356–65.
- [127] Wang D, Zhong G, Dolotko O, Li Y, McDonald MJ, Mi J, et al. The synergistic effects of Al and Te on the structure and Li^+ – mobility of the garnet-type solid electrolytes. *J Mater Chem A* 2014;2:20271–9.
- [128] Nemori H, Matsuda Y, Mitsuoka S, Matsui M, Yamamoto O, Takeda Y, et al. Stability of garnet-type solid electrolyte $\text{Li}_x\text{La}_3\text{A}_{2-y}\text{B}_y\text{O}_{12}$ (A = Nb or Ta, B = Sc or Zr). *Solid State Ionics* 2015;282:7–12.
- [129] Wang D, Zhong G, Pang WK, Guo Z, Li Y, McDonald MJ, et al. Toward understanding the lithium transport mechanism in garnet-type solid electrolytes: Li^+ ion exchanges and their mobility at octahedral/tetrahedral sites. *Chem Mater* 2015;27:6650–9.
- [130] Narayanan S, Ramezanipour F, Thangadurai V. Dopant concentration–porosity–Li-ion conductivity relationship in garnet-type $\text{Li}_{5+2x}\text{La}_3\text{Ta}_{2-x}\text{Y}_x\text{O}_{12}$ ($0.05 \leq x \leq 0.75$) and their stability in water and 1 M LiCl. *Inorg Chem* 2015;54:6968–77.
- [131] Li Y, Wang Z, Cao Y, Du F, Chen C, Cui Z, et al. W-Doped $\text{Li}_7\text{La}_3\text{Zr}_2\text{O}_{12}$ ceramic electrolytes for solid state Li-ion batteries. *Electrochim Acta* 2015;180:37–42.
- [132] Thangadurai V, Weppner W. $\text{Li}_6\text{ALa}_2\text{Nb}_2\text{O}_{12}$ (A = Ca, Sr, Ba): a new class of fast lithium ion conductors with garnet-like structure. *J Am Ceram Soc* 2005;88:411–8.
- [133] Thangadurai V, Weppner W. $\text{Li}_6\text{ALa}_2\text{Ta}_2\text{O}_{12}$ (A = Sr, Ba): novel garnet-like oxides for fast lithium ion conduction. *Adv Funct Mater* 2005;15:107–12.
- [134] Thangadurai V, Weppner W. Investigations on electrical conductivity and chemical compatibility between fast lithium ion conducting garnet-like $\text{Li}_6\text{BaLa}_2\text{Ta}_2\text{O}_{12}$ and lithium battery cathodes. *J Power Sources* 2005;142:339–44.
- [135] Percival J, Slater PR. Identification of the Li sites in the Li ion conductor, $\text{Li}_6\text{SrLa}_2\text{Nb}_2\text{O}_{12}$, through neutron powder diffraction studies 2007. *Solid State Commun* 2007;142:355–7.
- [136] Awaka J, Kijima N, Takahashi Y, Hayakawa H, Akimoto J. Synthesis and crystallographic studies of garnet-related lithium-ion conductors $\text{Li}_6\text{CaLa}_2\text{Ta}_2\text{O}_{12}$ and $\text{Li}_6\text{BaLa}_2\text{Ta}_2\text{O}_{12}$. *Solid State Ionics* 2009;180:602–6.
- [137] Li Y, Wang CA, Xie H, Cheng J, Goodenough JB. High lithium ion conduction in garnet-type $\text{Li}_6\text{La}_3\text{ZrTaO}_{12}$. *Electrochem Commun* 2011;13:1289–92.
- [138] Narayanan S, Ramezanipour F, Thangadurai V. Enhancing Li ion conductivity of garnet-type $\text{Li}_5\text{La}_3\text{Nb}_2\text{O}_{12}$ by Y- and Li-codoping: synthesis, structure, chemical stability and transport properties. *J Phys Chem C* 2012;116:20154–62.
- [139] Xie H, Li Y, Han J, Dong Y, Paranthaman MP, Wang L. $\text{Li}_6\text{La}_3\text{SnMO}_{12}$ (M = Sb, Nb, Ta), a family of lithium garnets with high Li-ion conductivity. *J Electrochem Soc* 2012;159:A1148–51.
- [140] Narayanan S, Epp V, Wilkening M, Thangadurai V. Macroscopic and microscopic Li^+ transport parameters in cubic garnet-type “ $\text{Li}_{6.5}\text{La}_{2.5}\text{Ba}_{0.5}\text{ZrTaO}_{12}$ ” as probed by impedance spectroscopy and NMR. *RSC Adv* 2012;2:2553–61.
- [141] Asha G, Murugan R, Paranthaman PM, Bi Z, Bridges CA, Nakanishi M, et al. Optimum lithium-ion conductivity in cubic $\text{Li}_{7-x}\text{La}_3\text{Hf}_{2-x}\text{Ta}_x\text{O}_{12}$. *J Power Sources* 2012;209:184–8.
- [142] Allen JL, Wolfenstine J, Rangasamy E, Sakamoto J. Effect of substitution (Ta, Al, Ga) on the conductivity of $\text{Li}_7\text{La}_3\text{Zr}_2\text{O}_{12}$. *J Power Sources* 2012;206:315–9.

- [143] Li Y, Cao Y, Guo X. Influence of lithium oxide additives on densification and ionic conductivity of garnet-type $\text{Li}_{6.75}\text{La}_3\text{Zr}_{1.75}\text{Ta}_{0.25}\text{O}_{12}$ solid electrolytes. *Solid State Ionics* 2013;253:76–80.
- [144] Yang C, Qiu LY, Xiang-Xin G. Densification and lithium ion conductivity of garnet-type $\text{Li}_{7-x}\text{La}_3\text{Zr}_{2-x}\text{Ta}_x\text{O}_{12}$ ($x = 0.25$) solid electrolytes. *Chin Phys B* 2013;22:078201–78205.
- [145] Zhong Y, Zhou Q, Guo Y, Li Z, Qiang Y. The ionic conductivity of $\text{Li}_6\text{BaLa}_2\text{M}_2\text{O}_{12}$ with coexisting Nb and Ta on the M sites. *Ionics* 2013;19:697–700.
- [146] Zeier WG, Zhou S, Bermudez BL, Page K, Melot BC. Dependence of the Li-ion conductivity and activation energies on the crystal structure and ionic radii in $\text{Li}_6\text{MLa}_2\text{Ta}_2\text{O}_{12}$. *Appl Mater Interfaces* 2014;6:10900–7.
- [147] Zhen-Zhu CAO, Wei R, Jin-Rong L, Guo-Rong L, Yan-Fang G, Ming-Hao F, et al. Microstructure and ionic conductivity of Sb-doped $\text{Li}_7\text{La}_3\text{Zr}_2\text{O}_{12}$ ceramics. *J Inorg Mater* 2014;29:220–4.
- [148] Dhivya L, Murugan R. Effect of simultaneous substitution of Y and Ta on the stabilization of cubic phase, microstructure and Li^+ conductivity of $\text{Li}_7\text{La}_3\text{Zr}_2\text{O}_{12}$ lithium garnet. *Appl Mater Interfaces* 2014;6:17606–15.
- [149] Liu K, Wang CA. Garnet-type $\text{Li}_{6.4}\text{La}_3\text{Zr}_{1.4}\text{Ta}_{0.6}\text{O}_{12}$ thin sheet: fabrication and application in lithium-hydrogen peroxide semi-fuel cell. *Electrochem Commun* 2014;48:147–50.
- [150] Liu K, Ma JT, Wang CA. Excess lithium salt functions more than compensating for lithium loss when synthesizing $\text{Li}_{6.5}\text{La}_3\text{Ta}_{0.5}\text{Zr}_{1.5}\text{O}_{12}$ in alumina crucible. *J Power Sources* 2014;260:109–14.
- [151] Inada R, Kusakabe K, Tanaka T, Kudo S, Sakurai Y. Synthesis and properties of Al-free $\text{Li}_{7-x}\text{La}_3\text{Zr}_{2-x}\text{Ta}_x\text{O}_{12}$ garnet related oxides. *Solid State Ionics* 2014;262:568–72.
- [152] Li Y, Wang Z, Li C, Cao Y, Guo X. Densification and ionic-conduction improvement of lithium garnet solid electrolytes by flowing oxygen sintering. *J Power Sources* 2014;248:642–6.
- [153] Janani N, Ramakumar S, Kannan S, Murugan R. Optimization of lithium content and sintering aid for maximized Li^+ conductivity and density in Ta-doped $\text{Li}_7\text{La}_3\text{Zr}_2\text{O}_{12}$. *J Am Ceram Soc* 2015;98:2039–46.
- [154] Deviannapoorani C, Ramakumar S, Janani N, Murugan R. Synthesis of lithium garnets from $\text{La}_2\text{Zr}_2\text{O}_7$ pyrochlore. *Solid State Ionics* 2015;283:123–30.
- [155] Li Y, Han JT, Vogel SC, Wang CA. The reaction of $\text{Li}_{6.5}\text{La}_3\text{Zr}_{1.5}\text{Ta}_{0.5}\text{O}_{12}$ with water. *Solid State Ionics* 2015;269:57–61.
- [156] Tong X, Thangadurai V, Wachsman ED. Highly conductive Li garnets by a multielement doping strategy. *Inorg Chem* 2015;54:3600–7.
- [157] Awaka J, Kijima N, Hayakawa H, Akimoto J. Synthesis and structure analysis of tetragonal $\text{Li}_7\text{La}_3\text{Zr}_2\text{O}_{12}$ with the garnet-related type structure. *J Solid State Chem* 2009;182:2046–52.
- [158] Wang WG, Wang XP, Gao YX, Fang QF. Lithium-ionic diffusion and electrical conduction in the $\text{Li}_7\text{La}_3\text{Ta}_2\text{O}_{13}$ compounds. *Solid State Ionics* 2009;180:1252–6.
- [159] Awaka J, Kijima N, Kataoka K, Hayakawa H, Ohshima K, Akimoto J. Neutron powder diffraction study of tetragonal $\text{Li}_7\text{La}_3\text{Hf}_2\text{O}_{12}$ with the garnet-related type structure. *J Solid State Chem* 2010;183:180–5.
- [160] Kotobuki M, Munakata H, Kanamura K, Sato T, Yoshid Y. Compatibility of $\text{Li}_7\text{La}_3\text{Zr}_2\text{O}_{12}$ solid electrolyte to all-solid-state battery using Li metal anode. *J Electrochem Soc* 2010;157:A1076–9.
- [161] Buschmann H, Dolle J, Berendts S, Kuhn A, Bottke P, Wilkening M, et al. Structure and dynamics of the fast lithium ion conductor $\text{Li}_7\text{La}_3\text{Zr}_2\text{O}_{12}$. *Phys Chem Chem Phys* 2011;13:19378–92.
- [162] Tan J, Tiwar A. Synthesis of cubic phase $\text{Li}_7\text{La}_3\text{Zr}_2\text{O}_{12}$ electrolyte for solid-state lithium-ion batteries. *Electrochem Solid State Lett* 2012;15:A37–9.
- [163] Il'ina EA, Andreev OL, Antonov BD, Batalov NN. Morphology and transport properties of the solid electrolyte $\text{Li}_7\text{La}_3\text{Zr}_2\text{O}_{12}$ prepared by the solid-state and citrate-nitrate methods. *J Power Sources* 2012;201:169–73.
- [164] Dumon A, Huang M, Shen Y, Nan CW. High Li ion conductivity in strontium doped $\text{Li}_7\text{La}_3\text{Zr}_2\text{O}_{12}$ garnet. *Solid State Ionics* 2013;243:36–41.
- [165] Mariappan CR, Gnanasekar KI, Jayaraman V, Gnanasekaran T. Lithium ion conduction in $\text{Li}_5\text{La}_3\text{Ta}_2\text{O}_{12}$ and $\text{Li}_7\text{La}_3\text{Ta}_2\text{O}_{13}$ garnet-type materials. *J Electro Ceram* 2013;30:258–65.
- [166] Howard M, Clemens O, Knight K, Anderson P, Hafiz S, Panchmatia PM, et al. Synthesis, conductivity and structural aspects of $\text{Nd}_3\text{Zr}_2\text{Li}_{7-3x}\text{Al}_x\text{O}_{12}$. *J Mater Chem A* 2013;1:14013–22.
- [167] Hitz GT, Wachsman ED, Thangadurai V. Highly Li-stuffed garnet-type $\text{Li}_{7+x}\text{La}_3\text{Zr}_{2-x}\text{Y}_x\text{O}_{12}$ batteries and energy storage. *J Electrochem Soc* 2013;160:A1248–55.
- [168] Cai L, Yin WZ, Kun R. High ionic conductivity in garnet-type F-doped $\text{Li}_7\text{La}_3\text{Zr}_2\text{O}_{12}$. *J Inorg Mater* 2015;30:995–1001.
- [169] Jin Y, McGinn PJ. $\text{Li}_7\text{La}_3\text{Zr}_2\text{O}_{12}$ Electrolyte stability in air and fabrication of a $\text{Li}/\text{Li}_7\text{La}_3\text{Zr}_2\text{O}_{12}/\text{Cu}_{0.1}\text{V}_2\text{O}_5$ solid-state battery. *J Power Sources* 2013;239:326–31.
- [170] Cheng L, Crumlin EJ, Chen W, Qiao R, Hou H, Lux SF, et al. The origin of high electrolyte–electrode interfacial resistances in lithium cells containing garnet type solid electrolytes. *Phys Chem Chem Phys* 2014;16:18294–300.
- [171] Xia W, Xu B, Duan H, Guo Y, Kang H, Li H, et al. Ionic conductivity and air stability of Al-doped $\text{Li}_7\text{La}_3\text{Zr}_2\text{O}_{12}$ sintered in alumina and Pt crucibles. *ACS Appl Mater Interfaces* 2016;8:5335–42.
- [172] Cheng L, Chen W, Kunz M, Persson K, Tamura N, Chen G, et al. Effect of surface microstructure on electrochemical performance of garnet solid electrolytes. *ACS Appl Mater Interfaces* 2015;7:2073–81.
- [173] Cheng L, Wu CH, Jarry A, Chen W, Ye Y, Zhu J, et al. Interrelationships among grain size, surface composition, air stability, and interfacial resistance of Al-substituted $\text{Li}_7\text{La}_3\text{Zr}_2\text{O}_{12}$ solid electrolytes. *ACS Appl Mater Interfaces* 2015;7:17649–55.
- [174] Kokal I, Somer M, Notten PHL, Hintzen HT. Sol-gel synthesis and lithium ion conductivity of $\text{Li}_7\text{La}_3\text{Zr}_2\text{O}_{12}$ with garnet-related type structure. *Solid State Ionics* 2011;185:42–6.
- [175] Shimonishi Y, Toda A, Zhang T, Hirano A, Imanishi N, Yamamoto O, et al. Synthesis of garnet-type $\text{Li}_{7-x}\text{La}_3\text{Zr}_2\text{O}_{12-1/2x}$ and its stability in aqueous solutions. *Solid State Ionics* 2011;183:48–53.
- [176] Janani N, Deviannapoorani C, Dhivya L, Murugan R. Influence of sintering additives on densification and Li^+ conductivity of Al doped $\text{Li}_7\text{La}_3\text{Zr}_2\text{O}_{12}$ lithium garnet. *RSC Adv* 2014;4:51228–38.
- [177] Gao YX, Wang XP, Wang WG, Fang QF. Sol-gel synthesis and electrical properties of $\text{Li}_5\text{La}_3\text{Ta}_2\text{O}_{12}$ lithium ionic conductors. *Solid State Ionics* 2010;181:33–6.
- [178] Gao YX, Wang XP, Wang WG, Zhuang Z, Zhang DM, Fang QF. Synthesis, ionic conductivity and chemical compatibility of garnet-like lithium ionic conductor $\text{Li}_5\text{La}_3\text{Bi}_2\text{O}_{12}$. *Solid State Ionics* 2010;181:1415–9.
- [179] Janani N, Ramakumar S, Dhivya L, Deviannapoorani C, Saranya K, Murugan R. Synthesis of cubic $\text{Li}_7\text{La}_3\text{Zr}_2\text{O}_{12}$ by modified sol-gel process. *Ionics* 2011;17:575–80.
- [180] Jin Y, McGinn PJ. Al-doped $\text{Li}_7\text{La}_3\text{Zr}_2\text{O}_{12}$ synthesized by a polymerized complex method. *J Power Sources* 2011;196:8683–7.
- [181] Dhivya L, Karthik K, Ramakumar S, Murugan R. Facile synthesis of high lithium ion conductive cubic phase lithium garnets for electrochemical energy storage devices. *RSC Adv* 2015;5:96042–51.
- [182] Afyon S, Krumeich F, Rupp JLM. A shortcut to garnet-type fast Li-ion conductors for all-solid state batteries. *J Mater Chem A* 2015;3:18636–48.
- [183] Shao C, Liu H, Yu Z, Zheng Z, Sun N, Diao C. Structure and ionic conductivity of cubic $\text{Li}_7\text{La}_3\text{Zr}_2\text{O}_{12}$ solid electrolyte prepared by chemical coprecipitation method. *Solid State Ionics* 2016;287:13–6.
- [184] Roof IP, Smith MD, Cussen EJ, Zur Loye HC. Crystal growth of a series of lithium garnets $\text{Ln}_3\text{Li}_5\text{Ta}_2\text{O}_{12}$ ($\text{Ln} = \text{La, Pr, Nd}$) structural properties, Alexandrite effect and unusual ionic conductivity. *J Solid State Chem* 2009;182:295–300.
- [185] Steffen G. Farbe und Lumineszenz von Mineralien: Einführung in die kristall chemischen und kristall physikalischen Ursachen. Enke im Georg-Thieme-Verl; 2000.
- [186] Xiao X, Wagata H, Hayashi F, Onodera H, Yubuta K, Zettsu N, et al. Unique growth manner of $\text{Li}_5\text{La}_3\text{Ta}_2\text{O}_{12}$ crystals from lithium hydroxide flux at low temperature. *Cryst Growth Des* 2015;15:4863–8.

- [187] Awaka J, Takashima A, Kataoka A, Kijima N, Idemoto Y, Akimoto J. Crystal structure of fast lithium-ion-conducting cubic $\text{Li}_7\text{La}_3\text{Zr}_2\text{O}_{12}$. *Chem Lett* 2011;40:60–2.
- [188] Geiger CA, Alekseev E, Lazic B, Fisch M, Armbruster T, Langner T, et al. Crystal chemistry and stability of $\text{Li}_7\text{La}_3\text{Zr}_2\text{O}_{12}$ garnet: a fast lithium-ion conductor. *Inorg Chem* 2011;50:1089–97.
- [189] Kalita DJ, Lee SH, Lee KS, Ko DH, Yoon YS. Ionic conductivity properties of amorphous Li–La–Zr–O solid electrolyte for thin film batteries. *Solid State Ionics* 2012;229:14–9.
- [190] Lobe S, Dellen C, Finsterbusch M, Gehrke HG, Sebold D, Tsai CL, et al. Radio frequency magnetron sputtering of $\text{Li}_7\text{La}_3\text{Zr}_2\text{O}_{12}$ thin films for solid-state batteries. *J Power Sources* 2016;307:684–9.
- [191] Reinacher J, Berendts S, Janek J. Preparation and electrical properties of garnet-type $\text{Li}_6\text{BaLa}_2\text{Ta}_2\text{O}_{12}$ lithium solid electrolyte thin films prepared by pulsed laser deposition. *Solid State Ionics* 2014;258:1–7.
- [192] Tan J, Tiwari A. Fabrication and characterization of $\text{Li}_7\text{La}_3\text{Zr}_2\text{O}_{12}$ thin films for lithium ion battery. *ECS Solid-State Lett* 2012;1:Q57–60.
- [193] Kim S, Hirayama M, Taminato S, Kanno R. Epitaxial growth and lithium ion conductivity of lithium-oxide garnet for an all solid-state battery electrolyte. *Dalton Trans* 2013;42:13112–7.
- [194] Park JS, Cheng L, Zorba V, Mehta A, Cabana J, Chen G, et al. Effects of crystallinity and impurities on the electrical conductivity of Li–La–Zr–O thin films. *Thin Solid Films* 2015;576:55–60.
- [195] Katsui H, Goto T. Preparation of cubic and tetragonal $\text{Li}_7\text{La}_3\text{Zr}_2\text{O}_{12}$ film by metal organic chemical vapor deposition. *Thin Solid Films* 2015;584:130–4.
- [196] Quinlan FT, Vidu R, Predoana L, Zaharescu M, Gartner M, Groza J, et al. Lithium cobalt oxide (LiCoO_2) nanocoatings by sol-gel methods. *Ind Eng Chem Res* 2004;43:2468–77.
- [197] MK Kim, Chung HT, Park YJ, Kim JG, Son JT, Park KS, et al. Fabrication of LiCoO_2 thin films by sol-gel method and characterisation as positive electrodes for Li/LiCoO₂ cells. *J Power Sources* 2001;99:34–40.
- [198] Chen RJ, Huang M, Huang WZ, Shen Y, Lin YH, Nan CW. Sol-gel derived Li–La–Zr–O thin films as solid electrolytes for lithium-ion batteries. *J Mater Chem A* 2014;2:13277–82.
- [199] Djenadic R, Botros M, Benel C, Clemens O, Indris S, Choudhary A, et al. Nebulized spray pyrolysis of Al-doped $\text{Li}_7\text{La}_3\text{Zr}_2\text{O}_{12}$ solid electrolyte for battery applications. *Solid State Ionics* 2014;263:49–56.
- [200] Yi E, Wang W, Kieffer J, Laine RM. Flame made nanoparticles permit processing of dense, flexible, Li^+ conducting ceramic electrolyte thin films of cubic- $\text{Li}_7\text{La}_3\text{Zr}_2\text{O}_{12}$ (c-LLZO). *J Mater Chem A* 2016;12947–54.
- [201] Yang T, Gordon ZD, Li Y, Chan CK. Nanostructured garnet-type solid electrolytes for lithium batteries: electrospinning synthesis of $\text{Li}_7\text{La}_3\text{Zr}_2\text{O}_{12}$ nanowires and particle size-dependent phase transformation. *J Phys Chem C* 2015;119:14947–53.
- [202] Kumazaki S, Iriyama Y, Kim KH, Murugan R, Tanabe K, Yamamoto K. High lithium ion conductive $\text{Li}_7\text{La}_3\text{Zr}_2\text{O}_{12}$ by inclusion of both Al and Si. *J Electrochem Commun* 2011;13:509–12.
- [203] Takano R, Tadanaga K, Hayashi A, Tatsumisago M. Low temperature synthesis of Al-doped $\text{Li}_7\text{La}_3\text{Zr}_2\text{O}_{12}$ solid electrolyte by a sol-gel process. *Solid State Ionics* 2014;255:104–7.
- [204] Tadanaga K, Takano R, Ichinose T, Mori S, Hayashi A, Tatsumisago M. Low temperature synthesis of highly ion conductive $\text{Li}_7\text{La}_3\text{Zr}_2\text{O}_{12}$ - Li_3BO_3 composites. *J Electrochem Commun* 2013;33:51–4.
- [205] Wolfenstine J, Sakamoto J, Allen JL. Electron microscopy characterization of hot-pressed Al substituted $\text{Li}_7\text{La}_3\text{Zr}_2\text{O}_{12}$. *J Mater Sci* 2012;47:4428–31.
- [206] Suzuki Y, Kami K, Watanabe K, Watanabe A, Saito N, Ohnishi T, et al. Transparent cubic garnet-type solid electrolyte of Al_2O_3 -doped $\text{Li}_7\text{La}_3\text{Zr}_2\text{O}_{12}$. *Solid State Ionics* 2015;278:172–6.
- [207] Amores M, Ashton TE, Baker PJ, Cussen EJ, Corr SA. Fast microwave-assisted synthesis of Li-stuffed garnets and insights into Li diffusion from muon spin spectroscopy. *J Mater Chem A* 2016;4:1729–36.
- [208] Mukhopadhyay A, Basu B. Consolidation-microstructure-property relationships in bulk nanoceramics and ceramic nanocomposites: a review. *Int Mater Rev* 2007;52:257–88.
- [209] Omori M. Sintering, consolidation, reaction and crystal growth by the spark plasma system (SPS). *Mater Sci Eng A* 2000;287:183–8.
- [210] Groza JR, Zavaliangos A. Sintering activation by external electrical field. *Mater Sci Eng A* 2000;287:171–7.
- [211] Nygren M, Shen Z. On the preparation of bio-, nano- and structural ceramics and composites by spark plasma sintering. *Solid State Sci* 2003;5:125–31.
- [212] Orru R, Licheri R, Locci AM, Cincotti A, Cao G. Consolidation/synthesis of materials by electric current activated/assisted sintering. *Mater Sci Eng R* 2009;63:127–287.
- [213] Kali R, Mukhopadhyay A. Spark plasma sintered/synthesized dense and nanostructured materials for solid-state Li-ion batteries: overview and perspective. *J Power Sources* 2014;247:920–31.
- [214] Baek SW, Lee JM, Kim TY, Song MS, Park Y. Garnet related lithium ion conductor processed by spark plasma sintering for all solid state batteries. *J Power Sources* 2014;249:197–206.
- [215] Räthel J, Herrmann M, Beckert W. Temperature distribution for electrically conductive and non-conductive materials during field assisted sintering (FAST). *J Eur Ceram Soc* 2009;29:1419–25.
- [216] Zhang Y, Chen F, Tu R, Shen Q, Zhang L. Field assisted sintering of dense Al-substituted cubic phase $\text{Li}_7\text{La}_3\text{Zr}_2\text{O}_{12}$ solid electrolytes. *J Power Sources* 2014;268:960–4.
- [217] Fu K, Gong Y, Dai J, Gong A, Han X, Yao Y, et al. Flexible, solid-state, ion-conducting membrane with 3D garnet nanofiber networks for lithium batteries. *PNAS Early Edition* 2016:1–6.
- [218] Hellner E, Gerlich R, Koch E, Fischer W. The oxygen framework in garnet and its occurrence in the structures of $\text{Na}_3\text{Al}_2\text{Li}_3\text{F}_{12}$, $\text{Ca}_3\text{Al}_2(\text{OH})_{12}$, RhBi_4 and Hg_3TeO_6 in: physics data. In: Behrens H, Ebel G, editors. *Fachinformationszentrum Energie, Physik, Mathematik Karlsruhe* 1979;16–1:1–16.
- [219] Mazza D. Remarks on a ternary phase in the La_2O_3 - Me_2O_5 - Li_2O system (Me = Nb, Ta). *Mater Lett* 1988;7:205–7.
- [220] Cussen EJ. The structure of lithium garnets: cation disorder and clustering in a new family of fast Li^+ conductors. *Chem Commun* 2006;4:412–3.
- [221] Percival J, Kendrick E, Slater PR. Synthesis and conductivities of the garnet-related Li ion conductors, $\text{Li}_5\text{Ln}_3\text{Sb}_2\text{O}_{12}$ (Ln = La, Pr, Nd, Sm, Eu). *Solid State Ionics* 2008;179:1666–9.
- [222] O'Callaghan MP, Cussen EJ. Lithium dimer formation in the Li-conducting garnets $\text{Li}_{5+x}\text{Ba}_x\text{La}_{3-x}\text{Ta}_2\text{O}_{12}$ ($0 < x \leq 1.6$). *Chem Commun* 2007;20:2048–50.
- [223] Galven C, Fourquet JL, Crosnier-Lopez MP, Le Berre F. Instability of the lithium garnet $\text{Li}_7\text{La}_3\text{Sn}_2\text{O}_{12}$: Li^+/H^+ exchange and structural study. *Chem Mater* 2011;23:1892–900.
- [224] Kotobuki M, Kanamura K, Sato Y, Yoshida T. Fabrication of all-solid-state lithium battery with lithium metal anode using Al_2O_3 -added $\text{Li}_7\text{La}_3\text{Zr}_2\text{O}_{12}$ solid electrolyte. *J Power Sources* 2011;196:7750–4.
- [225] Howard MA, Clemens O, Kendrick E, Knight KS, Apperley DC, Anderson PA, et al. Effect of Ga incorporation on the structure and Li ion conductivity of $\text{Li}_7\text{La}_3\text{Zr}_2\text{O}_{12}$. *Dalton Trans* 2012;41:12048–53.
- [226] Retenwänder D, Welzl A, Cheng L, Fleig J, Musso M, Suard E, et al. Synthesis, crystal chemistry and electrochemical properties of $\text{Li}_{7-2x}\text{La}_3\text{Zr}_{2-x}\text{Mo}_x\text{O}_{12}$ ($x = 0.1-0.4$): stabilization of the cubic garnet polymorph via substitution of Zr^{4+} by Mo^{6+} . *Inorg Chem* 2015;54:10440–9.
- [227] Wullen LV, Echelmeyer T, Meyer HW, Wilmer D. The mechanism of Li-ion transport in the garnet $\text{Li}_5\text{La}_3\text{Nb}_2\text{O}_{12}$. *PCCP* 2007;9:3298–303.
- [228] Kuhn A, Narayanan S, Spencer L, Goward G, Thangadurai V, Wilkening M. Li self-diffusion in garnet-type $\text{Li}_7\text{La}_3\text{Zr}_2\text{O}_{12}$ as probed directly by diffusion-induced ^7Li spin-lattice relaxation NMR spectroscopy. *Phys Rev B* 2011;83:094302–94311.
- [229] Duvel A, Khun A, Robben L, Wilkening M, Heitjans P. Mechanosynthesis of solid electrolytes: preparation, characterization and Li ion transport properties of garnet-type Al-doped $\text{Li}_7\text{La}_3\text{Zr}_2\text{O}_{12}$ crystallizing with cubic symmetry. *J Phys Chem C* 2012;116:15192–202.
- [230] Hubaud AA, Schroeder DJ, Key B, Ingram BJ, Dogan F, Vaughey JT. Low temperature stabilization of cubic ($\text{Li}_{7-x}\text{Al}_{x/3}$) $\text{La}_3\text{Zr}_2\text{O}_{12}$: role of aluminum during formation. *J Mater Chem A* 2013;1:8813–8.

- [231] Bottke P, Rettenwander D, Schmidt W, Amthauer G, Wilkening M. Ion dynamics in solid electrolytes: NMR reveals the elementary steps of Li^+ hopping in the garnet $\text{Li}_{6.5}\text{La}_3\text{Zr}_{2.75}\text{Mo}_{0.25}\text{O}_{12}$. *Chem Mater* 2015;27:6571–82.
- [232] Rettenwander D, Geiger CA, Tribus M, Tropper P, Amthauer G. A synthesis and crystal chemical study of the fast ion conductor $\text{Li}_{7-3x}\text{Ga}_x\text{La}_3\text{Zr}_2\text{O}_{12}$ with $x = 0.08$ to 0.84. *Inorg Chem* 2014;53:6264–9.
- [233] Bernuy-Lopez C, Manalastas Jr W, Lopez del Amo JM, Aguadero A, Aguesse F, Kilner JA. Atmosphere controlled processing of Ga-substituted garnets for high Li-ion conductivity ceramics. *Chem Mater* 2014;26:3610–7.
- [234] Rettenwander D, Reinhard Wagner, Julia Langer, Maria Elisabeth Maier, Martin Wilkening, Georg Amthauer. Crystal chemistry of “ $\text{Li}_7\text{La}_3\text{Zr}_2\text{O}_{12}$ ” garnet doped with Al, Ga, and Fe: a short review of NMR and Mössbauer spectroscopy studies. *Eur J Mineral* 2015.
- [235] Julien C. 4-V cathode materials for rechargeable lithium batteries wet-chemistry synthesis, structure and electrochemistry. *Ionics* 2000;6:30–46.
- [236] Julien CM, Massot M. Lattice vibrations of materials for lithium rechargeable batteries. *Mater Sci Eng B* 2003;100:69–78.
- [237] Tietz F, Wegener T, Gerhards MT, Giarola M, Mariotto G. Synthesis and Raman micro-spectroscopy investigation of $\text{Li}_7\text{La}_3\text{Zr}_2\text{O}_{12}$. *Solid State Ionics* 2013;230:77–82.
- [238] Larraz G, Orera A, Sanjuan ML. Cubic phases of garnet type $\text{Li}_7\text{La}_3\text{Zr}_2\text{O}_{12}$: the role of hydration. *J Mater Chem A* 2013;1:11419–28.
- [239] Thompson T, Wolfenstine J, Allen JL, Johannes M, Huq A, David IN, et al. Tetragonal vs. cubic phase stability in Al – free Ta doped $\text{Li}_7\text{La}_3\text{Zr}_2\text{O}_{12}$ (LLZO). *J Mater Chem A* 2014;2:13431–6.
- [240] Murugan R, Thangadurai V, Weppner W. Lattice parameter and sintering temperature dependence of bulk and grain-boundary conduction of garnet-like solid lithium-electrolytes. *J Electro Chem Soc* 2008;155:A90–A101.
- [241] Murugan R, Thangadurai V, Weppner W. Lithium ion conductivities of $\text{Li}_{5+x}\text{Ba}_x\text{La}_{3-x}\text{Ta}_2\text{O}_{12}$ ($x = 0-2$) with garnet-related structure in dependence of the barium content. *Ionics* 2007;13:195–203.
- [242] Janani N, Ramakumar S, Murugan R. Fast lithium ion conduction in zirconium containing garnet structured ceramic electrolyte. In: 3rd International Congress on Ceramics (ICC3), Osaka, Japan; 2010. p. S9A-P017.
- [243] Logeat A, Koehler T, Eisele U, Stiaszny B, Harzer A, Tovar M, et al. From order to disorder: the structure of lithium-conducting garnets $\text{Li}_{7-x}\text{La}_3\text{Ta}_x\text{Zr}_{2-x}\text{O}_{12}$ ($x = 0-2$). *Solid State Ionics* 2012;206:33–8.
- [244] Kihira Y, Ohta S, Imagawa H, Asaoka T. Effect of simultaneous substitution of alkali earth metals and Nb in $\text{Li}_7\text{La}_3\text{Zr}_2\text{O}_{12}$ on lithium-ion conductivity. *ECS Electrochem Lett* 2013;2:A56–9.
- [245] Miara LJ, Ong SP, Mo Y, Richards WD, Park Y, Lee JM, et al. Effect of Rb and Ta doping on the ionic conductivity and stability of the garnet $\text{Li}_{7+2x-y}(\text{La}_{3-x}\text{Rb}_x(\text{Zr}_{2-y}\text{Ta}_y)\text{O}_{12})$ ($0 \leq x \leq 0.375$, $0 \leq y \leq 1$) superionic conductor: a first principles investigation. *Chem Mater* 2013;25:3048–55.
- [246] Xu M, Park MS, Lee JM, Kim TY, Park YS, Ma E. Mechanisms of Li^+ transport in garnet-type cubic $\text{Li}_{3+x}\text{La}_3\text{M}_2\text{O}_{12}$ ($M = \text{Te}, \text{Nb}, \text{Zr}$). *Phys Rev B* 2012;85:052301–52305.
- [247] Wang Y, Klenk M, Page K, Lai W. Local structure and dynamics of lithium garnet ionic conductors: a model material $\text{Li}_5\text{La}_3\text{Ta}_2\text{O}_{12}$. *Chem Mater* 2014;26:5613–24.
- [248] Bernstein N, Johannes MD, Hoang K. Origin of the structural phase transition in $\text{Li}_7\text{La}_3\text{Zr}_2\text{O}_{12}$. *Phys Rev Lett* 2012;109:205702.
- [249] Jalem R, Yamamoto Y, Shiiba H, Nakayama M, Munakata H, Kasuga T, et al. Concerted migration mechanism in the Li ion dynamics of garnet-type $\text{Li}_7\text{La}_3\text{Zr}_2\text{O}_{12}$. *Chem Mater* 2013;25:425–30.
- [250] Rettenwander D, Blaha P, Laskowski R, Schwarz K, Bottke P, Wilkening M, et al. DFT study of the role of Al^{3+} in the fast ion-conductor $\text{Li}_{7-3x}\text{Al}_{3+x}\text{La}_3\text{Zr}_2\text{O}_{12}$ garnet. *Chem Mater* 2014;26:2617–23.
- [251] Wolfenstine J, Ratchford J, Rangasamy E, Sakamoto J, Allen JL. Synthesis and high Li-ion conductivity of Ga-stabilized cubic $\text{Li}_7\text{La}_3\text{Zr}_2\text{O}_{12}$. *Mater Chem Phys* 2012;134:571–5.
- [252] Shin DO, Oh K, Kim KM, Park KY, Lee B, Lee YG, et al. Synergistic multi-doping effects on the $\text{Li}_7\text{La}_3\text{Zr}_2\text{O}_{12}$ solid electrolyte for fast lithium ion conduction. *Sci Rep* 2015;5:18053.
- [253] Adams S, Prasada Rao R. Ion transport and phase transition in $\text{Li}_{7-x}\text{La}_3(\text{Zr}_{2-x}\text{M}_x)\text{O}_{12}$ ($M = \text{Ta}^{5+}, \text{Nb}^{5+}$, $x = 0, 0.25$). *J Mater Chem* 2012;22:1426–34.
- [254] Xie H, Alonso JA, Li Y, Fernandez-Diaz MT, Goodenough JB. Lithium distribution in aluminum-free cubic $\text{Li}_7\text{La}_3\text{Zr}_2\text{O}_{12}$. *Chem Mater* 2011;23:3587–9.
- [255] Miara LJ, Richards WD, Wang YE, Ceder G. First-principles studies on cation dopants and electrolyte cathode interphases for lithium garnets. *Chem Mater* 2015;27:4040–7.
- [256] Chen Y, Rangasamy E, Liang C, An K. Origin of high Li^+ conduction in doped $\text{Li}_7\text{La}_3\text{Zr}_2\text{O}_{12}$ garnets. *Chem Mater* 2015;27:5491–4.
- [257] Kim KH, Iriyama Y, Yamamoto K, Kumazak S, Asaka T, Tanabe K, et al. Characterization of the interface between LiCoO_2 and $\text{Li}_7\text{La}_3\text{Zr}_2\text{O}_{12}$ in an all-solid-state rechargeable lithium battery. *J Power Sources* 2011;196:764–7.
- [258] Ohta S, Kobayashi T, Seki J, Asaoka T. Electrochemical performance of an all-solid-state lithium ion battery with garnet-type oxide electrolyte. *J Power Sources* 2012;202:332–5.
- [259] Ohta S, Komagata S, Seki J, Saeki T, Morishita S, Asaoka T. All-solid-state lithium ion battery using garnet-type oxide and Li_3BO_3 solid electrolytes fabricated by screen-printing. *J Power Sources* 2013;238:53–6.
- [260] Ishiguro K, Nakata Y, Matsui M, Uechi I, Takeda Y, Yamamoto O, et al. Stability of Nb-doped cubic $\text{Li}_7\text{La}_3\text{Zr}_2\text{O}_{12}$ with lithium metal batteries and energy storage. *J Electrochem Soc* 2013;160:A1690–3.
- [261] Monroe C, Newman J. The impact of elastic deformation on deposition kinetics at lithium/polymer interfaces. *J Electrochem Soc* 2005;152:A396–404.
- [262] Jennifer EN, Elden DC, Sakamoto JS, Rangasamy E, Wolfenstine JB. Room temperature elastic moduli and Vickers hardness of hot-pressed LLZO cubic garnet. *J Mater Sci* 2012;47:7978–85.
- [263] Sharafi A, Meyer HM, Nanda J, Wolfenstine J, Sakamoto J. Characterizing the Li- $\text{Li}_7\text{La}_3\text{Zr}_2\text{O}_{12}$ interface stability and kinetics as a function of temperature and current density. *J Power Sources* 2016;302:135–9.
- [264] Ishiguro K, Nemori H, Sunahiro S, Nakata Y, Sudo R, Matsui M, et al. Ta-doped $\text{Li}_7\text{La}_3\text{Zr}_2\text{O}_{12}$ for water-stable lithium electrode of lithium-air batteries. *J Electrochem Soc* 2014;161:A668–74.
- [265] Sudo R, Nakata Y, Ishiguro K, Matsui M, Hirano A, Takeda Y, et al. Interface behavior between garnet-type lithium conducting solid electrolyte and lithium metal. *Solid State Ionics* 2014;262:151–4.
- [266] Takeda Y, Yamamoto O, Imanishi N. Lithium dendrite formation on a lithium metal anode from liquid, polymer and solid electrolytes. *Electrochemistry* 2016;84(4):210–8.
- [267] Tsai C-L, Roddatis V, VinodChandran C, Ma Q, Uhlenbruck S, Bram M, et al. $\text{Li}_7\text{La}_3\text{Zr}_2\text{O}_{12}$ interface modification for Li dendrite prevention. *Appl Mater Interfaces* 2016;8:10617–26.
- [268] Luo W, Gong Y, Zhu Y, Kelvin Fu K, Dai J, et al. Transition from superlithiophobicity to superlithiophilicity of garnet solid-state electrolyte. *J Am Chem Soc* 2016;138:12258–62.
- [269] Ohta S, Seki J, Yagi Y, Kihira Y, Tani T, Asaoka T. Co-sinterable lithium garnet-type oxide electrolyte with cathode for all-solid-state lithium ion battery. *J Power Sources* 2014;265:40–4.
- [270] Kato T, Hamanaka T, Yamamoto K, Hirayama T, Sagane F, Motoyama M, et al. In-situ $\text{Li}_7\text{La}_3\text{Zr}_2\text{O}_{12}/\text{LiCoO}_2$ interface modification for advanced all-solid-state battery. *J Power Sources* 2014;260:292–8.
- [271] Du F, Zhao N, Li Y, Chen C, Liu Z, Guo X. All solid state lithium batteries based on lamellar garnet-type ceramic electrolytes. *J Power Sources* 2015;300:24–8.
- [272] Ohta N, Takada K, Sakaguchi I, Zhang L, Ma R, Fukuda K. LiNbO_3 -coated LiCoO_2 as cathode material for all solid-state lithium secondary batteries. *Electrochem Commun* 2007;9:1486–90.
- [273] Ohta N, Takada K, Zhang L, Ma R, Osada M, Sasaki T. Enhancement of the high-rate capability of solid-state lithium batteries by nanoscale interfacial modification. *Adv Mater* 2006;18:2226–9.

- [274] Xu X, Takada K, Fukuda K, Ohnishi T, Akatsuka K, Osada M, et al. Tantalum oxide nanomesh as self-standing one nanometre thick electrolyte. *Energy Environ Sci* 2011;4:3509–12.
- [275] Takada K. Progress and perspective of solid-state lithium batteries. *Acta Mater* 2013;61:759–70.
- [276] Wang Z, Wu C, Liu L, Wu F, Chen L, Huang X. Electrochemical evaluation and structural characterization of commercial LiCoO₂ surfaces modified with MgO for lithium-ion batteries. *J Electrochem Soc* 2002;149:A466–71.
- [277] Wang Z, Liu L, Chen L, Huang X. Structural and electrochemical characterizations of surface-modified LiCoO₂ cathode materials for Li-ion batteries. *Solid State Ionics* 2002;148:335–42.
- [278] Park K, Yu BC, Jung JW, Li Y, Zhou W, Gao H, et al. Electrochemical nature of the cathode interface for a solid-state lithium-ion battery: interface between LiCoO₂ and garnet-Li₇La₃Zr₂O₁₂. *Chem Mater* 2016;8051–9.
- [279] Wakayama H, Yonekura H, Kawai Y. Three-dimensional bicontinuous nanocomposite from a self-assembled block copolymer for a high-capacity all-solid-state lithium battery cathode. *Chem Mater* 2016;28:4453–9.
- [280] Kim HW, Manikandan P, Jun Lim Y, Hong Kim J, Nam S, Kim Y. Hybrid solid electrolyte with the combination of Li₇La₃Zr₂O₁₂ ceramic and ionic liquid for high voltage pseudo-solid-state Li-ion batteries. *J Mater Chem A* 2016;17025–32.
- [281] Choi J-H, Lee C-H, Yu JH, Doh CH, Lee SM. Enhancement of ionic conductivity of composite membranes for all-solid-state lithium rechargeable batteries incorporating tetragonal Li₇La₃Zr₂O₁₂ into a polyethylene oxide matrix. *J Power Sources* 2015;274:458–63.
- [282] Yoshima K, Harada Y, Takami N. Thin Hybrid electrolyte based on garnet-type lithium ion conductor Li₇La₃Zr₂O₁₂ for 12V- class bipolar batteries. *J Power sources* 2016;302:283–90.
- [283] Broek JVD, Afyon S, Jennifer Rupp LM. Interface-engineered all-solid-state Li-ion batteries based on garnet-type fast Li⁺ conductors. *Adv Energy Mater* 2016;1600736–46.
- [284] Wu F, Chen N, Chen R, Zhu Q, Qian J, Li Li. "Liquid-in-solid" and "solid-in-liquid" electrolytes with high rate capacity and long cycling life for lithium-ion batteries. *Chem Mater* 2016;28:848–56.
- [285] Mizuno F, Hayashi A, Tadanaga K, Tatsumisago M. New highly ion-conductive crystals precipitated from Li₂S–P₂S₅ glasses. *Adv Mater* 2005;17:918–21.
- [286] Murayama M, Sonoyama N, Yamada A, Kanno R. Material design of new lithium ionic conductor, thio-lesion in the Li₂S–P₂S₅ System. *Solid State Ionics* 2004;170:173–80.
- [287] Kamaya N, Homma K, Yamakawa Y, Hirayama M, Kanno R, Yonemura M, et al. A lithium superionic conductor. *Nat Mater* 2011;10:682–6.
- [288] Yi E, Wang W, Mohanty S, Kieffer J, Tamaki R, Laine RM. Materials that can replace liquid electrolytes in li batteries: superionic conductivities in Li_{1.7}Al_{0.3}Ti_{1.7}Si_{0.4}P_{2.6}O₁₂ processing combustion synthesized nanopowders to free standing thin films. *J Power Sources* 2014;269:577–88.
- [289] Chen R, Zhu L, Wu F, Li L, Zhang R, Chen S. Investigation of a novel ternary electrolyte based on dimethyl sulfite and lithium difluoromono(oxalato) borate for lithium ion batteries. *J Power Sources* 2014;245:730–8.
- [290] Chen R, Wu F, Li L, Guan Y, Qiu X, Chen S, et al. Butylene sulfite as a film-forming additive to propylene carbonate-based electrolytes for lithium ion batteries. *J Power Sources* 2007;172:395–403.
- [291] Xiang J, Wu F, Chen R, Li L, Yu H. High voltage and safe electrolytes based on ionic liquid and sulfone for lithium-ion batteries. *J Power Sources* 2013;233:115–20.
- [292] Jin Y, Fang S, Yang L, Hirano SI, Tachibana K. Functionalized ionic liquids based on guanidinium cations with two ether groups as new electrolytes for lithium battery. *J Power Sources* 2011;196:10658–66.
- [293] Thakur VK, Ding G, Ma J, Lee PS, Lu X. Hybrid materials and polymer electrolytes for electrochromic device applications. *Adv Mater* 2012;24:4071–96.
- [294] Armand M, Endres F, MacFarlane DR, Ohno H, Scrosati B. Ionic-liquid materials for the electrochemical challenges of the future. *Nat Mater* 2009;8:621–9.
- [295] Vallee A, Besner S, Prud Homme J. Comparative study of poly(ethylene oxide) electrolytes made with LiN(CF₃SO₂)₂, LiCF₃SO₃ and LiClO₄: thermal properties and conductivity behaviour. *Electrochim Acta* 1992;37:1579–83.
- [296] Croce F, Appetecchi GB, Persi L, Scrosati B. Nanocomposite Polymer electrolytes for lithium batteries. *Nature* 1998;394:456–8.
- [297] Edman L, Ferry A, Doeff MM. Slow recrystallization in the polymer electrolyte system Poly(ethylene oxide)_n-LiN(CF₃SO₂)₂. *J Mater Res* 2000;15:1950–4.
- [298] Agubra VA, Fergus JW. The formation and stability of the solid electrolyte interface on the graphite anode. *J Power Sources* 2014;268:153–62.
- [299] Abraham KM, Jiang Z. A polymer electrolyte-based rechargeable lithium/oxygen battery. *J Electrochem Soc* 1996;143:1–5.
- [300] Sandhu S, Brutchon G, Fellner J. Lithium/air cell: preliminary mathematical formulation and analysis. *J Power Sources* 2007;170:196–209.
- [301] Girishkumar G, McCloskey B, Luntz AC, Swanson S, Wilcke W. Lithium-air battery: promise and challenges. *J Phys Chem Lett* 2010;1:2193–203.
- [302] Christensen J, Albertus P, Sanchez-Carrera RS, Lohmann T, Kozinsky B, Liedtke R, et al. A critical review of Li/air batteries. *J Electrochem Soc* 2012;159: R1–R30.
- [303] He P, Wang Y, Zhou H. A Li-air fuel cell with recycle aqueous electrolyte for improved stability. *Electrochem Commun* 2010;12:1686–9.
- [304] Deviannapoorani C, Shankar LS, Ramakumar S, Murugan R. Investigation on lithium ion conductivity and structural stability of yttrium substituted Li₇La₃Zr₂O₁₂. *Ionics* 2016;283:123–30.
- [305] Zhu Y, Thangadurai V, Weppner W. Garnet-like solid state electrolyte Li₆BaLa₂Ta₂O₁₂ based potentiometric CO₂ gas sensor. *Sens Actuat B: Chem* 2013;176:284–9.